

THE UNIVERSITY OF CALGARY

AMPLITUDE-VERSUS-OFFSET ANALYSIS USING  
VERTICAL SEISMIC PROFILING AND  
WELL-LOG DATA

by

Craig A. Coulombe

A THESIS

SUBMITTED TO THE FACULTY OF GRADUATE STUDIES  
IN PARTIAL FULFILLMENT OF THE REQUIREMENTS FOR THE  
DEGREE OF MASTER OF SCIENCE

DEPARTMENT OF GEOLOGY AND GEOPHYSICS

CALGARY, ALBERTA

AUGUST, 1993

© Craig A. Coulombe 1993



National Library  
of Canada

Acquisitions and  
Bibliographic Services Branch

395 Wellington Street  
Ottawa, Ontario  
K1A 0N4

Bibliothèque nationale  
du Canada

Direction des acquisitions et  
des services bibliographiques

395, rue Wellington  
Ottawa (Ontario)  
K1A 0N4

*Your file    Votre référence*

*Our file    Notre référence*

The author has granted an irrevocable non-exclusive licence allowing the National Library of Canada to reproduce, loan, distribute or sell copies of his/her thesis by any means and in any form or format, making this thesis available to interested persons.

L'auteur a accordé une licence irrévocable et non exclusive permettant à la Bibliothèque nationale du Canada de reproduire, prêter, distribuer ou vendre des copies de sa thèse de quelque manière et sous quelque forme que ce soit pour mettre des exemplaires de cette thèse à la disposition des personnes intéressées.

The author retains ownership of the copyright in his/her thesis. Neither the thesis nor substantial extracts from it may be printed or otherwise reproduced without his/her permission.

L'auteur conserve la propriété du droit d'auteur qui protège sa thèse. Ni la thèse ni des extraits substantiels de celle-ci ne doivent être imprimés ou autrement reproduits sans son autorisation.

ISBN 0-315-88476-2

Canada

Name Craig Anthony Coulombe

*Dissertation Abstracts International* is arranged by broad, general subject categories. Please select the one subject which most nearly describes the content of your dissertation. Enter the corresponding four-digit code in the spaces provided.

Geophysics

SUBJECT TERM

0373

SUBJECT CODE

U·M·I

## Subject Categories

### THE HUMANITIES AND SOCIAL SCIENCES

#### COMMUNICATIONS AND THE ARTS

Architecture ..... 0729  
Art History ..... 0377  
Cinema ..... 0900  
Dance ..... 0378  
Fine Arts ..... 0357  
Information Science ..... 0723  
Journalism ..... 0391  
Library Science ..... 0399  
Mass Communications ..... 0708  
Music ..... 0413  
Speech Communication ..... 0459  
Theater ..... 0465

#### EDUCATION

General ..... 0515  
Administration ..... 0514  
Adult and Continuing ..... 0516  
Agricultural ..... 0517  
Art ..... 0273  
Bilingual and Multicultural ..... 0282  
Business ..... 0688  
Community College ..... 0275  
Curriculum and Instruction ..... 0727  
Early Childhood ..... 0518  
Elementary ..... 0524  
Finance ..... 0277  
Guidance and Counseling ..... 0519  
Health ..... 0680  
Higher ..... 0745  
History of ..... 0520  
Home Economics ..... 0278  
Industrial ..... 0521  
Language and Literature ..... 0279  
Mathematics ..... 0280  
Music ..... 0522  
Philosophy of ..... 0998  
Physical ..... 0523

Psychology ..... 0525  
Reading ..... 0535  
Religious ..... 0527  
Sciences ..... 0714  
Secondary ..... 0533  
Social Sciences ..... 0534  
Sociology of ..... 0340  
Special ..... 0529  
Teacher Training ..... 0530  
Technology ..... 0710  
Tests and Measurements ..... 0288  
Vocational ..... 0747

#### LANGUAGE, LITERATURE AND LINGUISTICS

Language  
  General ..... 0679  
  Ancient ..... 0289  
  Linguistics ..... 0290  
  Modern ..... 0291  
Literature  
  General ..... 0401  
  Classical ..... 0294  
  Comparative ..... 0295  
  Medieval ..... 0297  
  Modern ..... 0298  
  African ..... 0316  
  American ..... 0591  
  Asian ..... 0305  
  Canadian (English) ..... 0352  
  Canadian (French) ..... 0355  
  English ..... 0593  
  Germanic ..... 0311  
  Latin American ..... 0312  
  Middle Eastern ..... 0315  
  Romance ..... 0313  
  Slavic and East European ..... 0314

#### PHILOSOPHY, RELIGION AND THEOLOGY

Philosophy ..... 0422  
Religion  
  General ..... 0318  
  Biblical Studies ..... 0321  
  Clergy ..... 0319  
  History of ..... 0320  
  Philosophy of ..... 0322  
Theology ..... 0469

#### SOCIAL SCIENCES

American Studies ..... 0323  
Anthropology  
  Archaeology ..... 0324  
  Cultural ..... 0326  
  Physical ..... 0327  
Business Administration  
  General ..... 0310  
  Accounting ..... 0272  
  Banking ..... 0770  
  Management ..... 0454  
  Marketing ..... 0338  
Canadian Studies ..... 0385  
Economics  
  General ..... 0501  
  Agricultural ..... 0503  
  Commerce-Business ..... 0505  
  Finance ..... 0508  
  History ..... 0509  
  Labor ..... 0510  
  Theory ..... 0511  
Folklore ..... 0358  
Geography ..... 0366  
Gerontology ..... 0351  
History  
  General ..... 0578

Ancient ..... 0579  
Medieval ..... 0581  
Modern ..... 0582  
Black ..... 0328  
African ..... 0331  
Asia, Australia and Oceania ..... 0332  
Canadian ..... 0334  
European ..... 0335  
Latin American ..... 0336  
Middle Eastern ..... 0333  
United States ..... 0337  
History of Science ..... 0585  
Law ..... 0398  
Political Science  
  General ..... 0615  
  International Law and  
    Relations ..... 0616  
  Public Administration ..... 0617  
Recreation ..... 0814  
Social Work ..... 0452  
Sociology  
  General ..... 0626  
  Criminology and Penology ..... 0627  
  Demography ..... 0938  
  Ethnic and Racial Studies ..... 0631  
  Individual and Family  
    Studies ..... 0628  
  Industrial and Labor  
    Relations ..... 0629  
  Public and Social Welfare ..... 0630  
  Social Structure and  
    Development ..... 0700  
  Theory and Methods ..... 0344  
Transportation ..... 0709  
Urban and Regional Planning ..... 0999  
Women's Studies ..... 0453

### THE SCIENCES AND ENGINEERING

#### BIOLOGICAL SCIENCES

Agriculture  
  General ..... 0473  
  Agronomy ..... 0285  
  Animal Culture and  
    Nutrition ..... 0475  
  Animal Pathology ..... 0476  
  Food Science and  
    Technology ..... 0359  
  Forestry and Wildlife ..... 0478  
  Plant Culture ..... 0479  
  Plant Pathology ..... 0480  
  Plant Physiology ..... 0817  
  Range Management ..... 0777  
  Wood Technology ..... 0746  
Biology  
  General ..... 0306  
  Anatomy ..... 0287  
  Biostatistics ..... 0308  
  Botany ..... 0309  
  Cell ..... 0379  
  Ecology ..... 0329  
  Entomology ..... 0353  
  Genetics ..... 0369  
  Limnology ..... 0793  
  Microbiology ..... 0410  
  Molecular ..... 0307  
  Neuroscience ..... 0317  
  Oceanography ..... 0416  
  Physiology ..... 0433  
  Radiation ..... 0821  
  Veterinary Science ..... 0778  
  Zoology ..... 0472  
Biophysics  
  General ..... 0786  
  Medical ..... 0760

#### EARTH SCIENCES

Biogeochemistry ..... 0425  
Geochemistry ..... 0996

Geodesy ..... 0370  
Geology ..... 0372  
Geophysics ..... 0373  
Hydrology ..... 0388  
Mineralogy ..... 0411  
Paleobotany ..... 0345  
Paleoecology ..... 0426  
Paleontology ..... 0418  
Paleozoology ..... 0985  
Palynology ..... 0427  
Physical Geography ..... 0368  
Physical Oceanography ..... 0415

#### HEALTH AND ENVIRONMENTAL SCIENCES

Environmental Sciences ..... 0768  
Health Sciences  
  General ..... 0566  
  Audiology ..... 0300  
  Chemotherapy ..... 0992  
  Dentistry ..... 0567  
  Education ..... 0350  
  Hospital Management ..... 0769  
  Human Development ..... 0758  
  Immunology ..... 0982  
  Medicine and Surgery ..... 0564  
  Mental Health ..... 0347  
  Nursing ..... 0569  
  Nutrition ..... 0570  
  Obstetrics and Gynecology ..... 0380  
  Occupational Health and  
    Therapy ..... 0354  
  Ophthalmology ..... 0381  
  Pathology ..... 0571  
  Pharmacology ..... 0419  
  Pharmacy ..... 0572  
  Physical Therapy ..... 0382  
  Public Health ..... 0573  
  Radiology ..... 0574  
  Recreation ..... 0575

Speech Pathology ..... 0460  
Toxicology ..... 0383  
Home Economics ..... 0386

#### PHYSICAL SCIENCES

##### Pure Sciences

Chemistry  
  General ..... 0485  
  Agricultural ..... 0749  
  Analytical ..... 0486  
  Biochemistry ..... 0487  
  Inorganic ..... 0488  
  Nuclear ..... 0738  
  Organic ..... 0490  
  Pharmaceutical ..... 0491  
  Physical ..... 0494  
  Polymer ..... 0495  
  Radiation ..... 0754  
Mathematics ..... 0405  
Physics  
  General ..... 0605  
  Acoustics ..... 0986  
  Astronomy and  
    Astrophysics ..... 0606  
  Atmospheric Science ..... 0608  
  Atomic ..... 0748  
  Electronics and Electricity ..... 0607  
  Elementary Particles and  
    High Energy ..... 0798  
  Fluid and Plasma ..... 0759  
  Molecular ..... 0609  
  Nuclear ..... 0610  
  Optics ..... 0752  
  Radiation ..... 0756  
  Solid State ..... 0611  
Statistics ..... 0463

##### Applied Sciences

Applied Mechanics ..... 0346  
Computer Science ..... 0984

Engineering  
  General ..... 0537  
  Aerospace ..... 0538  
  Agricultural ..... 0539  
  Automotive ..... 0540  
  Biomedical ..... 0541  
  Chemical ..... 0542  
  Civil ..... 0543  
  Electronics and Electrical ..... 0544  
  Heat and Thermodynamics ..... 0348  
  Hydraulic ..... 0545  
  Industrial ..... 0546  
  Marine ..... 0547  
  Materials Science ..... 0794  
  Mechanical ..... 0548  
  Metallurgy ..... 0743  
  Mining ..... 0551  
  Nuclear ..... 0552  
  Packaging ..... 0549  
  Petroleum ..... 0765  
  Sanitary and Municipal ..... 0554  
  System Science ..... 0790  
Geotechnology ..... 0428  
Operations Research ..... 0796  
Plastics Technology ..... 0795  
Textile Technology ..... 0994

#### PSYCHOLOGY

General ..... 0621  
Behavioral ..... 0384  
Clinical ..... 0622  
Developmental ..... 0620  
Experimental ..... 0623  
Industrial ..... 0624  
Personality ..... 0625  
Physiological ..... 0989  
Psychobiology ..... 0349  
Psychometrics ..... 0632  
Social ..... 0451



Nom \_\_\_\_\_

*Dissertation Abstracts International* est organisé en catégories de sujets. Veuillez s.v.p. choisir le sujet qui décrit le mieux votre thèse et inscrire le code numérique approprié dans l'espace réservé ci-dessous.

SUJET



CODE DE SUJET

## Catégories par sujets

### HUMANITÉS ET SCIENCES SOCIALES

#### COMMUNICATIONS ET LES ARTS

Architecture .....	0729
Beaux-arts .....	0357
Bibliothéconomie .....	0399
Cinéma .....	0900
Communication verbale .....	0459
Communications .....	0708
Danse .....	0378
Histoire de l'art .....	0377
Journalisme .....	0391
Musique .....	0413
Sciences de l'information .....	0723
Théâtre .....	0465

#### ÉDUCATION

Généralités .....	515
Administration .....	0514
Art .....	0273
Collèges communautaires .....	0275
Commerce .....	0688
Économie domestique .....	0278
Éducation permanente .....	0516
Éducation préscolaire .....	0518
Éducation sanitaire .....	0680
Enseignement agricole .....	0517
Enseignement bilingue et multiculturel .....	0282
Enseignement industriel .....	0521
Enseignement primaire .....	0524
Enseignement professionnel .....	0747
Enseignement religieux .....	0527
Enseignement secondaire .....	0533
Enseignement spécial .....	0529
Enseignement supérieur .....	0745
Évaluation .....	0288
Finances .....	0277
Formation des enseignants .....	0530
Histoire de l'éducation .....	0520
Langues et littérature .....	0279

Lecture .....	0535
Mathématiques .....	0280
Musique .....	0522
Orientation et consultation .....	0519
Philosophie de l'éducation .....	0998
Physique .....	0523
Programmes d'études et enseignement .....	0727
Psychologie .....	0525
Sciences .....	0714
Sciences sociales .....	0534
Sociologie de l'éducation .....	0340
Technologie .....	0710

#### LANGUE, LITTÉRATURE ET

##### LINGUISTIQUE

Langues	
Généralités .....	0679
Anciennes .....	0289
Linguistique .....	0290
Modernes .....	0291
Littérature	
Généralités .....	0401
Anciennes .....	0294
Comparée .....	0295
Médiévale .....	0297
Moderne .....	0298
Africaine .....	0316
Américaine .....	0591
Anglaise .....	0593
Asiatique .....	0305
Canadienne (Anglaise) .....	0352
Canadienne (Française) .....	0355
Germanique .....	0311
Latino-américaine .....	0312
Moyen-orientale .....	0315
Romane .....	0313
Slave et est-européenne .....	0314

#### PHILOSOPHIE, RELIGION ET

##### THÉOLOGIE

Philosophie .....	0422
Religion	
Généralités .....	0318
Clergé .....	0319
Études bibliques .....	0321
Histoire des religions .....	0320
Philosophie de la religion .....	0322
Théologie .....	0469

#### SCIENCES SOCIALES

Anthropologie	
Archéologie .....	0324
Culturelle .....	0326
Physique .....	0327
Droit .....	0398
Économie	
Généralités .....	0501
Commerce-Affaires .....	0505
Économie agricole .....	0503
Économie du travail .....	0510
Finances .....	0508
Histoire .....	0509
Théorie .....	0511
Études américaines .....	0323
Études canadiennes .....	0385
Études féministes .....	0453
Folklore .....	0358
Géographie .....	0366
Gérontologie .....	0351
Gestion des affaires	
Généralités .....	0310
Administration .....	0454
Banques .....	0770
Comptabilité .....	0272
Marketing .....	0338
Histoire	
Histoire générale .....	0578

Ancienne .....	0579
Médiévale .....	0581
Moderne .....	0582
Histoire des noirs .....	0328
Africaine .....	0331
Canadienne .....	0334
États-Unis .....	0337
Européenne .....	0335
Moyen-orientale .....	0333
Latino-américaine .....	0336
Asie, Australie et Océanie .....	0332
Histoire des sciences .....	0585
Loisirs .....	0814
Planification urbaine et régionale .....	0999
Science politique	
Généralités .....	0615
Administration publique .....	0617
Droit et relations internationales .....	0616
Sociologie	
Généralités .....	0626
Aide et bien-être social .....	0630
Criminologie et établissements pénitentiaires .....	0627
Démographie .....	0938
Études de l'individu et de la famille .....	0628
Études des relations interethniques et des relations raciales .....	0631
Structure et développement social .....	0700
Théorie et méthodes .....	0344
Travail et relations industrielles .....	0629
Transports .....	0709
Travail social .....	0452

### SCIENCES ET INGÉNIERIE

#### SCIENCES BIOLOGIQUES

Agriculture	
Généralités .....	0473
Agronomie .....	0285
Alimentation et technologie alimentaire .....	0359
Culture .....	0479
Élevage et alimentation .....	0475
Exploitation des pâturages .....	0777
Pathologie animale .....	0476
Pathologie végétale .....	0480
Physiologie végétale .....	0817
Sylviculture et faune .....	0478
Technologie du bois .....	0746
Biologie	
Généralités .....	0306
Anatomie .....	0287
Biologie (Statistiques) .....	0308
Biologie moléculaire .....	0307
Botanique .....	0309
Cellule .....	0379
Écologie .....	0329
Entomologie .....	0353
Génétique .....	0369
Limnologie .....	0793
Microbiologie .....	0410
Neurologie .....	0317
Océanographie .....	0416
Physiologie .....	0433
Radiation .....	0821
Science vétérinaire .....	0778
Zoologie .....	0472
Biophysique	
Généralités .....	0786
Médicale .....	0760

Géologie .....	0372
Géophysique .....	0373
Hydrologie .....	0388
Minéralogie .....	0411
Océanographie physique .....	0415
Paléobotanique .....	0345
Paléocécologie .....	0426
Paléontologie .....	0418
Paléozoologie .....	0985
Palynologie .....	0427

#### SCIENCES DE LA SANTÉ ET DE L'ENVIRONNEMENT

Économie domestique .....	0386
Sciences de l'environnement .....	0768
Sciences de la santé	
Généralités .....	0566
Administration des hôpitaux .....	0769
Alimentation et nutrition .....	0570
Audiologie .....	0300
Chimiothérapie .....	0992
Dentisterie .....	0567
Développement humain .....	0758
Enseignement .....	0350
Immunologie .....	0982
Loisirs .....	0575
Médecine du travail et thérapie .....	0354
Médecine et chirurgie .....	0564
Obstétrique et gynécologie .....	0380
Ophtalmologie .....	0381
Orthophonie .....	0460
Pathologie .....	0571
Pharmacie .....	0572
Pharmacologie .....	0419
Physiothérapie .....	0382
Radiologie .....	0574
Santé mentale .....	0347
Santé publique .....	0573
Soins infirmiers .....	0569
Toxicologie .....	0383

#### SCIENCES DE LA TERRE

Biogéochimie .....	0425
Géochimie .....	0996
Géodésie .....	0370
Géographie physique .....	0368

#### SCIENCES PHYSIQUES

##### Sciences Pures

Chimie	
Généralités .....	0485
Biochimie .....	0487
Chimie agricole .....	0749
Chimie analytique .....	0486
Chimie minérale .....	0488
Chimie nucléaire .....	0738
Chimie organique .....	0490
Chimie pharmaceutique .....	0491
Physique .....	0494
Polymères .....	0495
Radiation .....	0754
Mathématiques .....	0405
Physique	
Généralités .....	0605
Acoustique .....	0986
Astronomie et astrophysique .....	0606
Électronique et électricité .....	0607
Fluides et plasma .....	0759
Météorologie .....	0608
Optique .....	0752
Particules (Physique nucléaire) .....	0798
Physique atomique .....	0748
Physique de l'état solide .....	0611
Physique moléculaire .....	0609
Physique nucléaire .....	0610
Radiation .....	0756
Statistiques .....	0463

##### Sciences Appliquées Et Technologie

Informatique .....	0984
Ingénierie	
Généralités .....	0537
Agricole .....	0539
Automobile .....	0540

Biomédicale .....	0541
Chaleur et ther modynamique .....	0348
Conditionnement (Emballage) .....	0549
Génie aérospatial .....	0538
Génie chimique .....	0542
Génie civil .....	0543
Génie électronique et électrique .....	0544
Génie industriel .....	0546
Génie mécanique .....	0548
Génie nucléaire .....	0552
Ingénierie des systèmes .....	0790
Mécanique navale .....	0547
Métallurgie .....	0743
Science des matériaux .....	0794
Technique du pétrole .....	0765
Technique minière .....	0551
Techniques sanitaires et municipales .....	0554
Technologie hydraulique .....	0545
Mécanique appliquée .....	0346
Géotechnologie .....	0428
Matériaux plastiques (Technologie) .....	0795
Recherche opérationnelle .....	0796
Textiles et tissus (Technologie) .....	0794

#### PSYCHOLOGIE

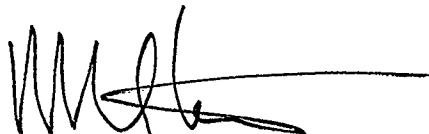
Généralités .....	0621
Personnalité .....	0625
Psychobiologie .....	0349
Psychologie clinique .....	0622
Psychologie du comportement .....	0384
Psychologie du développement .....	0620
Psychologie expérimentale .....	0623
Psychologie industrielle .....	0624
Psychologie physiologique .....	0989
Psychologie sociale .....	0451
Psychométrie .....	0632



# THE UNIVERSITY OF CALGARY

## FACULTY OF GRADUATE STUDIES

The undersigned certify that they have read, and recommend to the Faculty of Graduate Studies for acceptance, a thesis entitled "Amplitude-Versus-Offset Analysis Using Vertical Seismic Profiling and Well-Log Data" submitted by Craig Anthony Coulombe in partial fulfillment of the requirements for the degree of Master of Science.



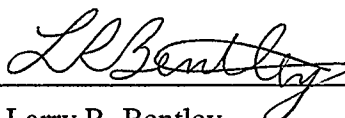
---

Supervisor, Dr. Robert R. Stewart  
Dept. of Geology and Geophysics



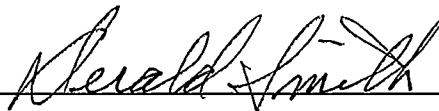
---

Dr. R. James Brown  
Dept. of Geology and Geophysics



---

Dr. Larry R. Bentley  
Dept. of Geology and Geophysics



---

Dr. Derald G. Smith  
Dept. of Geography

August 26, 1993

# ABSTRACT

A multioffset VSP (vertical seismic profiling) geometry is used in this thesis to acquire data for AVO (amplitude-versus-offset) analysis of a reservoir zone. The VSP geometry consists of ten surface source positions and eleven downhole receiver positions. The downhole receivers are placed immediately above the reservoir zone. A zero-offset and an offset VSP were also acquired and analysed.

A three-component processing flow is developed, and tested here using synthetic data, to extract the true seismic amplitudes from VSP data. AVO analysis of the multioffset VSP data suggests a lower  $P$ -wave velocity in the reservoir zone based on forward modeling. Well-log interpretation indicates that the reservoir zone is a gas-bearing dolomite with porosities as high as 18 %.

Generalized-linear-inversion methods are developed to invert the zero-offset VSP corridor stack for the acoustic impedance, and to invert the multioffset VSP  $P$ - $P$  and  $P$ - $SV$  reflectivity traces jointly for the elastic parameters  $V_p$ ,  $V_s$ , and  $\rho$ . The zero offset inversion resulted in an inverted impedance curve that matched the higher frequency trends but failed to match the low frequency trends of the initial-guess impedance curve. The joint  $P$ - $P$ / $P$ - $SV$  inversion is found to update the elastic parameters in a realistic manner; however there is some residual error. The resulting  $P$ -wave velocity in the reservoir is higher than the initial guess which is the opposite of the forward modeling results.

# **ACKNOWLEDGEMENTS**

There are many people who have contributed to and enhanced this thesis. The people in the CREWES Project have all helped provide a positive research environment. Specifically, I have enjoyed and grown from many technical discussions with Don Easley. Rob Stewart, my thesis advisor, has made many positive contributions towards my emergence as a graduate scientist. Rob has offered many helpful suggestions to this work that have helped me clarify the important areas of this research.

I owe a great deal of gratitude to Perry Katapodis and Michael Jones of Schlumberger of Canada for introducing me to the data used in this thesis. Schlumberger of Canada has supported me with the use of their VSP processing software, and computer time. Mike Jones has provided me with many stimulating conversations regarding VSP data processing and inversion, and many useful suggestions regarding these areas.

Finally, my wife Val has been a pillar of strength and stood behind me through all the long hours spent at school. Thank you for your patience and understanding during this research.

# TABLE OF CONTENTS

<b>Approval Page .....</b>	<b>ii</b>
<b>Abstract .....</b>	<b>iii</b>
<b>Acknowledgements .....</b>	<b>iv</b>
<b>Table of Contents .....</b>	<b>v</b>
<b>List of Tables .....</b>	<b>vii</b>
<b>List of Figures .....</b>	<b>viii</b>
<b>List of Symbols and Notations .....</b>	<b>xi</b>
<b>1 Introduction .....</b>	<b>1</b>
1.1 Amplitude versus Offset .....	1
1.1.1 Historical Review of AVO .....	1
1.1.2 Current AVO Applications .....	3
1.2 Vertical Seismic Profiling .....	4
1.2.1 VSP Geometry for AVO Analysis .....	6
1.3 Study Objectives .....	7
<b>2 VSP Acquisition and Processing .....</b>	<b>9</b>
2.1 Introduction .....	9
2.2 VSP Acquisition .....	9
2.3 VSP Processing .....	13
2.3.1 Zero-Offset VSP Processing .....	13
2.3.2 Offset VSP Processing .....	26
2.3.3 Multioffset VSP Processing - Synthetic Data .....	44
2.3.4 Multioffset VSP Processing - Field Data .....	50
<b>3 VSP Interpretation .....</b>	<b>58</b>
3.1 Introduction .....	58
3.2 Well Log/Zero-Offset VSP Interpretation .....	58
3.2.1 Well A Log Blocking .....	59
3.2.2 Well A Log Interpretation .....	60
3.2.3 VSP/Well Log Correlation .....	66
3.3 Integrated VSP Interpretation .....	71
3.4 AVO Interpretation and Modeling .....	74
<b>4 VSP Inversion .....</b>	<b>86</b>
4.1 Introduction .....	86
4.2 1-D Generalized Linear Inversion .....	86
4.2.1 Synthetic Data Examples .....	91
4.2.2 Real Data Example .....	100
4.3 Joint P-P/P-SV AVO Inversion .....	103
4.3.1 AVO Inversion GLI Algorithm .....	103
4.3.2 Synthetic Data Inversion .....	110
4.3.3 Field Data Inversion .....	128



<b>5 Conclusions .....</b>	<b>140</b>
5.1 Thesis Summary .....	140
5.2 Future Work .....	142
<b>References .....</b>	<b>143</b>
<b>Appendix A Well B AVO Analysis .....</b>	<b>147</b>

# LIST OF TABLES

Table 2.1. Well A geophone locations .....	12
Table 3.1. Average log values in zone of interest .....	60
Table 3.2. VSP and perturbed velocities .....	84

# LIST OF FIGURES

1.1.	Schematic plot of the variation of reflection coefficient with angle-of-incidence .....	2
1.2.	AVO VSP geometry .....	7
2.1.	Map of Alberta .....	10
2.2.	Stratigraphic column .....	11
2.3.	Plan view of the Well A multioffset VSP survey geometry .....	12
2.4.	Raw vertical channel of the zero-offset VSP .....	15
2.5.	First-arrival time-depth curve from the zero-offset VSP .....	16
2.6.	Enhanced downgoing <i>P</i> waves .....	18
2.7.	Subtraction of the enhanced downgoing <i>P</i> waves .....	19
2.8.	Enhanced upgoing <i>P</i> waves .....	20
2.9.	Downgoing <i>P</i> waves flattened at 200 ms before waveshaping deconvolution .....	21
2.10.	Waveshaping deconvolved downgoing <i>P</i> waves flattened at 200 ms .....	21
2.11.	Waveshaping deconvolution applied to the upgoing <i>P</i> waves .....	22
2.12.	(a) Upgoing <i>P</i> waves shifted to two-waytime. (b) Corridor stack of the upgoing <i>P</i> waves .....	25
2.13.	Raw vertical channel .....	28
2.14.	Raw radial channel .....	29
2.15.	Raw transverse channel .....	30
2.16.	Downgoing <i>P</i> wavefield after wavefield separation .....	31
2.17.	Downgoing <i>S</i> wavefield after wavefield separation .....	32
2.18.	Upgoing <i>P</i> wavefield after wavefield separation .....	33
2.19.	Upgoing <i>S</i> wavefield after wavefield separation .....	34
2.20.	Downgoing <i>P</i> wavefield before waveshaping deconvolution .....	35
2.21.	Downgoing <i>P</i> wavefield after waveshaping deconvolution .....	36
2.22.	Upgoing <i>P</i> wavefield after waveshaping deconvolution .....	38
2.23.	Upgoing <i>S</i> wavefield after waveshaping deconvolution .....	39
2.24.	NMO-corrected upgoing <i>P</i> wavefield after median filtering .....	40
2.25.	NMO-corrected upgoing <i>S</i> wavefield after median filtering .....	41
2.26.	Corridor stack and VSPCDP map of upgoing <i>P</i> wavefield .....	42
2.27.	Corridor stack and VSPCCP map of upgoing <i>S</i> wavefield .....	43
2.28.	Velocity model used to generate the synthetic test data .....	45
2.29.	Raw synthetic data from the 400 m offset .....	46
2.30.	The results of wavefield separation for the 400 m offset .....	47
2.31.	Waveshaping deconvolved downgoing <i>P</i> wavefield, and upgoing <i>P-P</i> and <i>P-SV</i> wavefields .....	48
2.32.	Final processed synthetic <i>P-P</i> and <i>P-SV</i> reflectivity gathers .....	49
2.33.	Picked amplitudes of the top of gas-sand event .....	49
2.34.	Multioffset VSP three-component processing flow .....	50
2.35.	Raw vertical, radial, and transverse channels of 2000 m offset VSP. ....	51
2.36.	Output of wavefield separation .....	53
2.37.	Waveshaping deconvolved downgoing <i>P</i> and upgoing <i>P</i> and <i>S</i> wavefields. ....	54
2.38.	Flattened upgoing <i>P</i> and <i>S</i> wavefields .....	55
2.39.	Stacked and gathered <i>P-P</i> and <i>P-SV</i> reflectivity traces .....	56
2.40.	<i>P-P</i> and <i>P-SV</i> reflectivities shifted back to the correct traveltimes .....	57
2.41.	NMO corrected <i>P-P</i> and <i>P-SV</i> reflectivity traces .....	57

3.1.	Raw well logs in zone of interest.....	61
3.2.	Raw and blocked well logs .....	62
3.3.	Photoelectric cross-section log .....	63
3.4.	Blocked-sonic and VSP velocities .....	65
3.5.	Comparison of the synthetic seismogram and the VSP corridor-stack trace.....	68
3.6.	Raw and blocked well logs in zone of interest in time .....	69
3.7.	Comparison of 1-D seismic with the acoustic-impedance log in time .....	70
3.8.	Composite plot of sonic log, zero-offset VSP, and the zero-offset VSP corridor stack .....	72
3.9.	Correlation of 5 Events across the VSP corridor stack, <i>P</i> -wave gather, offset VSP <i>P</i> -wave corridor stack, <i>S</i> -wave gather, and offset VSP <i>S</i> -wave corridor stack .....	73
3.10.	Single Interface Zoeppritz equation solution for <i>P-P</i> and <i>P-SV</i> waves.....	76
3.11.	Correlation of multilayer forward modeled <i>P-P</i> and <i>P-SV</i> gathers with the field <i>P-P</i> and <i>P-SV</i> gathers .....	78
3.12.	<i>P-P</i> forward models.....	81
3.13.	<i>P-SV</i> forward models.....	82
3.14.	<i>P-P</i> multilayer forward models and field data comparison .....	84
3.15.	<i>P-SV</i> multilayer forward models and field data comparison .....	85
4.1.	Schematic diagram of a stack of layers and the resulting forward modeled seismic trace.....	87
4.2.	Flow chart of the GLI inversion method .....	88
4.3.	Synthetic data inversion results for spiked data traces .....	93
4.4.	Synthetic data inversion results for VSP wavelet traces .....	94
4.5.	Synthetic data inversion results for initial incorrect top impedance.....	95
4.6.	Synthetic data inversion results for event at the wrong traveltime.....	96
4.7.	Synthetic data inversion results with random noise added .....	98
4.8.	Synthetic data inversion results with random noise added .....	99
4.9.	Field data inversion results .....	102
4.10.	<i>P-P</i> and <i>P-SV</i> reflection-coefficient curves for changing layer parameters .....	108
4.11.	Partial derivatives of the Zoeppritz equations .....	109
4.12.	Synthetic AVO model data .....	111
4.13.	Initial-guess, inverted and true model parameter curves .....	112
4.14.	Initial-guess, inverted and true model parameter curves for incorrect upper layer initial guess .....	112
4.15.	Initial-guess, inverted and true model parameter curves for rounded angles of incidence.....	114
4.16.	Initial-guess, inverted and true model parameter curves for random noise added to incident angles.....	114
4.17.	Model parameter curves for noise added to the test data .....	115
4.18.	Model parameter curves for noise added to the test data .....	116
4.19.	<i>P-P</i> reflectivity synthetic traces.....	118
4.20.	<i>P-SV</i> reflectivity synthetic traces.....	119
4.21.	Partial derivative matrix <i>A</i> .....	120
4.22.	Initial-guess, inverted and true model parameter curves for the inversion with a spike wavelet.....	121
4.23.	Initial-guess, inverted and true model parameter curves for the inversion with the VSP wavelet.....	123
4.24.	Synthetic real and initial-guess <i>P-P</i> reflectivity traces.....	124
4.25.	Synthetic real and initial-guess <i>P-SV</i> reflectivity traces.....	125

4.26.	Synthetic real and inverted $P$ - $P$ reflectivity traces .....	126
4.27.	Synthetic real and inverted $P$ - $SV$ reflectivity traces .....	127
4.28.	Initial-guess and inverted model parameter curves .....	129
4.29.	Real and initial-guess $P$ - $P$ reflectivity traces.....	130
4.30.	Real and inverted $P$ - $P$ reflectivity traces .....	132
4.31.	Real and initial-guess $P$ - $SV$ reflectivity traces.....	133
4.32.	Real and inverted $P$ - $SV$ reflectivity traces .....	134
4.33.	Initial-guess and inverted model parameter curves .....	135
4.34.	Real and inverted $P$ - $P$ reflectivity traces .....	136
4.35.	Real and inverted $P$ - $SV$ reflectivity traces .....	136
4.36.	Initial-guess and inverted model parameter curves .....	138
4.37.	Real and inverted $P$ - $P$ reflectivity traces .....	138
A.1.	Plan view of the multioffset VSP geometry .....	148
A.2.	Processed $P$ - $P$ and $P$ - $SV$ reflectivity traces .....	149
A.3.	Blocked well logs through the zone of interest .....	150
A.4.	Synthetic $P$ - $P$ and $P$ - $SV$ reflectivity traces .....	151
A.5.	Picked $P$ - $P$ amplitudes of the top and base of porosity events .....	153
A.6.	Picked $P$ - $SV$ amplitudes of the top and base of porosity events .....	154

# LIST OF SYMBOLS AND NOTATIONS

AVO	Amplitude Versus Offset.
Composite plot	A plot of the VSP in depth and time and a well log in depth allowing direct corelation of VSP events in time with the well logs in depth.
$f$	Frequency.
Hz	A frequency unit of Hertz.
$k$	Wavenumber.
Offset VSP	A VSP acquired with a single source offset from the well bore.
Multioffset VSP	A VSP acquired over the same geophone levels with several source positions at differencet offsets from the well bore.
$P$ - $P$	$P$ -wave reflection or transmission event.
$P$ - $SV$	Mode-converted shear-wave transmission or reflection.
$P$ - $SV$ - $SV$	$S$ -wave reflection that originated as a $P$ wave, mode converted to a downgoing $S$ wave and reflected as a $S$ wave.
VSP	Vertical seismic profile.,
Zero-offset VSP	A VSP acquired with the source very near the well bore.
$P$ wave	A seismic compressional wave.
$S$ wave	A seismic shear wave.
$V_p$	$P$ -wave velocity.
$V_s$	$S$ -wave velocity.
$V_p/V_s$	The ratio of the $P$ -wave velocity to the $S$ -wave velocity.
s	A time unit of seconds.
ms	A time unit of milliseconds.
$\phi$	Porosity.
$\rho$	Density.
$\rho_b$	Bulk density.
$\rho_f$	Fluid density.
$\rho_{ma}$	Matrix density.

# Chapter 1

## Introduction

### 1.1 Amplitude versus Offset

Amplitude-versus-offset (AVO) analysis has been considered as a useful exploration procedure for some time (Ostrander, 1984; Chacko, 1989; Rutherford and Williams, 1989; Burnett, 1990). The main goal of AVO analysis is to estimate the Poisson's ratio (or equivalently the  $V_p/V_s$  ratio) in a subsurface zone using conventional surface seismic data. Poisson's ratio is important to explorationists because it can be diagnostic of both gas saturation and gross lithology (Tatham and Krug, 1985).

#### 1.1.1 Historical Review of AVO

The theory behind AVO has been known for some time. The original papers deriving the equations for reflection and refraction of harmonic elastic waves at an interface between isotropic homogeneous elastic solids were published by C.G. Knott in 1899, and K. Zoeppritz in 1919 (Young and Braille, 1976). Early work in understanding these equations and hence understanding seismic reflections was done by Muskat and Meres (1940). They concluded that reflected energy from various elastic interfaces will decrease with increasing angle of incidence, but the magnitude of the effect is small for the angles of incidence used (less than 10 degrees). They use these findings to justify the assumption of normal incidence for offset traces. It should be noted that they assumed a constant Poisson's ratio of 0.25.

Koefoed (1955) tested the effects of varying the Poisson's ratio in the medium above and below an interface on the reflection amplitudes of planar  $P$  waves. Koefoed's results are important when considering AVO. Koefoed derived several rules for the

reflection coefficient versus angle-of-incidence curves that are shown schematically in Figure 1.1. These rules are generalizations for a limited number of observations and for angles of incidence less than 30 degrees, but they are generally true for reflection-coefficient curves. Koefoed also stated that in the remote future, it may be possible to interpret the lithological nature of rock strata from the shapes of reflection coefficient curves. This statement could be used today as a definition of AVO analysis.

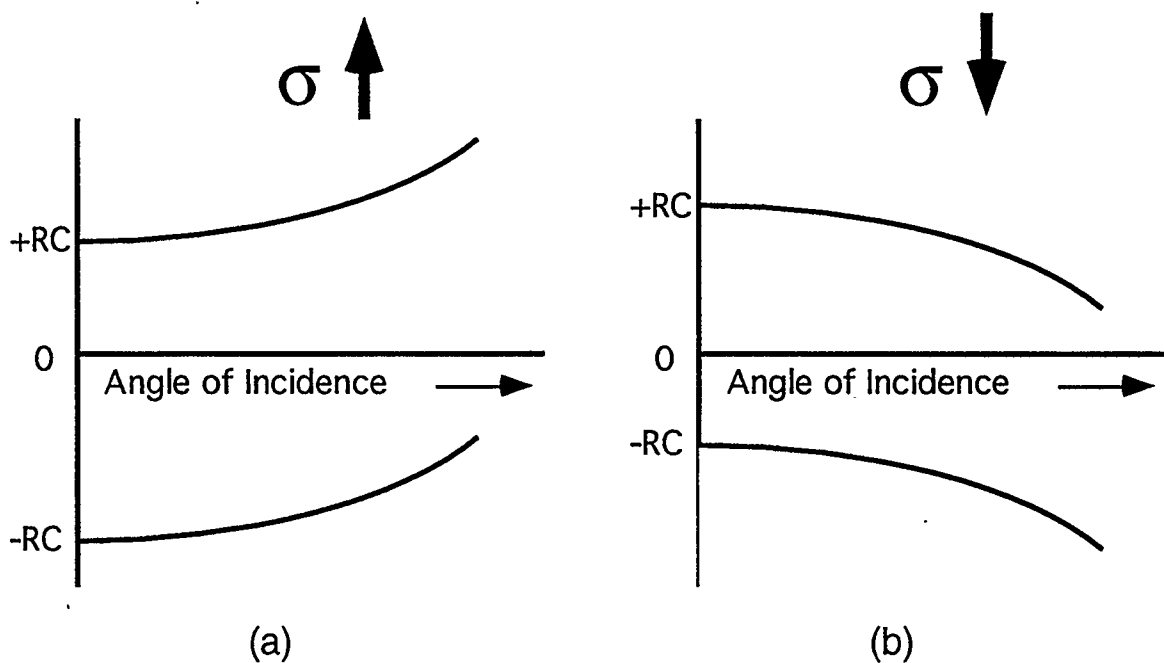


FIG 1.1. Schematic plot of the variation of reflection coefficient with angle-of-incidence; (a) for an increase in Poisson's ratio ( $\sigma$ ) across an interface, and (b) for a decrease in Poisson's ratio across an interface.

Ostrander (1984) introduced a practical application of the AVO phenomenon. He used the Zoeppritz amplitude equations (e.g., Aki and Richards, 1980) to analyze the reflection coefficient versus angle-of-incidence curves for a simple three-layer, gas-sand model. The model consisted of a sand layer encased in two shale layers. By using published values of Poisson's ratio for shale, brine-saturated sandstone, and gas-saturated sandstone, he determined that there is a sufficient difference in reflection coefficient versus angle of incidence to allow discrimination between gas-saturated and brine-



saturated sandstones. He tested his theoretical observations with field seismic data and showed that AVO can be used to detect gas sands.

### **1.1.2 Current AVO Applications**

Current AVO methods are applied in various sedimentary basins with differing lithologies. Chacko (1989) documented an example of how AVO was used for porosity identification in South Sumatra. Chacko found that tight and porous limestone facies had different AVO responses, and that these different facies could be identified based on this difference. Burnett (1990) found that seismic amplitudes and the AVO responses corresponded well with production zones in the Mestena Grande Field in Texas. However, forward modeling failed to predict the observed AVO responses in the field data. The forward modeling failure was attributed to a lack of shear-wave velocity information and to structural complexities. Burnett also found it surprising that AVO effects are visible in the thinly interbedded, sand-shale sequence, with a total sand thickness of 9 m given that the seismic wavelengths were over 90 m. Morris and MacGregor (1991) presented a paper outlining the use of AVO to delineate the transition between basinal and tight bank facies in the Caroline field in Alberta, Canada. Swan (1991) showed the errors caused by different processing and acquisition factors on AVO measurements. Spherical-spreading losses, source directivity, velocity estimation errors, thin-bed interference, anisotropy, and wavelet stretch can all have significant effects on AVO measurements. Mazotti (1991) used complex-trace analysis to compute the amplitude-, phase-, and frequency-versus-offset responses for synthetic and field data. This analysis helped to detect critical angle and interference phenomena. Walden (1991) illustrated that the standard AVO method of using gradient and intercept traces generally ignores any type of quality control, and proposed a statistically robust AVO gradient and intercept calculation scheme. Ross (1992) documented how complexities due to salt

structures can obscure the correct AVO response. Lawton and Nazar (1992) used  $P$ - $P$  and  $P$ - $SV$  AVO modeling to explain a discrepancy in  $P$ - $P$  and  $P$ - $SV$  stacked seismic character of a reservoir zone. Frazier and Zaengle (1992) use  $P$ - $P$  and  $P$ - $SV$  reflections, rock physics, and  $P$ -wave AVO to provide interval  $V_p/V_s$  ratios that correlate with known lithologies in producing fields. Therefore, it might be argued that while the theory of AVO is well understood, the practical applications and limitations of AVO analysis are still being developed and documented.

## 1.2 Vertical Seismic Profiling

The VSP can be used to gain insight into wavefield propagation (Lee and Balch, 1983; Gaiser et al. 1984; and Dankbaar, 1987). Three components of the seismic wavefield can be recorded in situ over a range of depth levels. With the VSP geometry, upgoing and downgoing seismic events can be identified at different points of their propagation path in depth and time. Furthermore, many wavefield propagation effects can be observed: seismic attenuation can be measured by comparing the amplitude spectra of the downgoing wavefield at different depth levels; on offset VSPs both reflected and transmitted mode-converted  $S$ -waves can be observed (confirming the Zoeppritz equations); and multiples can be identified and removed. Thus using the VSP in interpretation and analysis generally leads to a well-defined solution that is independent of many of the uncertainties that can plague surface seismic data.

Although there are many advantages in using VSP data, there are also limitations: a well must be available for VSP acquisition; VSP data are limited in subsurface coverage; and the VSP may have a substantial cost.

When considering AVO, there are several aspects of the VSP that can be used to an advantage. The downgoing wavefield is recorded, and can be used to design a deconvolution operator that eliminates many of the wavefield propagation effects (such

as multiples) between the source and receiver. Essentially, the downgoing wavefield can be shaped to a desired wavelet of known phase. The operator used to shape the downgoing wavefield is applied to the upgoing wavefield. The result is the reflection coefficient series convolved with the desired wavelet as shown by Gaiser et al. (1984). Additionally, the amplitudes of the seismic wavefield are recorded, and can be used to obtain a good estimate of the reflection coefficient of an interface by taking the ratio of the incident and reflected amplitudes. A similar technique was used recently by Cheng et al. (1992), and many years ago by Jolly (1953). Furthermore, the incident and reflected amplitudes can be measured immediately above the interface, eliminating most wavefield propagation effects, and resulting in the true amplitude seismic response. A additional feature of the VSP is that three-component acquisition and processing can be used to obtain mode-converted  $P$ - $SV$  reflections. The result is that both  $P$ - $P$  and  $P$ - $SV$  reflections can be used jointly in an AVO study to help understand the subsurface rock properties. Thus the additional information in the converted wave reflections should enhance the interpretation and analysis of the seismic wavefield.

In summary, the main advantages of the VSP are that seismic waves are measured in situ near reflecting boundaries, resulting in the possibility of true-amplitude seismic processing, the seismic wavelet is known, and many of the multiples can be eliminated from the data. Also, VSP data generally have a higher bandwidth than comparable surface seismic data due to the shorter travel path, and the signal-to-noise ratio is generally higher than that of surface seismic data because the borehole environment is quite and there is strong borehole coupling.

### 1.2.1 VSP Geometry for AVO Analysis

A multioffset VSP geometry (Figure 1.2) is used in this study to record data specifically for AVO analysis of a reservoir zone. The fundamental aspects of this geometry are the source and receiver positions. Several source positions are located at increasing distances (offsets) from the borehole to obtain reflection coefficients for a range of  $P$ -wave angles of incidence. A number of 3-component geophones (receivers) are placed immediately above the zone of interest so the reflection point of a given interface remains near the borehole as the source is moved away from the borehole. Therefore, approximately the same subsurface point is imaged for all the source positions. It is necessary to record at several depth levels above the reservoir zone to accommodate multichannel wavefield separation algorithms used to separate the seismic wavefield into the different propagation modes.

The true seismic amplitudes can be obtained by taking the ratio of the incident and reflected wave amplitudes. A  $P$ -wave direct-arrival ray path and a  $P$ -wave reflection raypath for an arbitrary interface are shown in Figure 1.2. When the geophone is near the interface, the amplitude of the recorded  $P$ -wave direct arrival and the amplitude of the  $P$ -wave incident on the interface are approximately equal. So, the ratio between recorded upgoing (reflected) and downgoing  $P$ -wave amplitudes is the  $P$ - $P$  reflection coefficient of the interface. The ratio is independent of most wave propagation effects (attenuation, transmission losses, multiples, and spherical spreading) because the travel path of the reflected wave is small, and the travel paths of the two downgoing  $P$  waves are nearly the same. This ratio process also minimizes uncertainties caused by source directivity and source or receiver coupling.

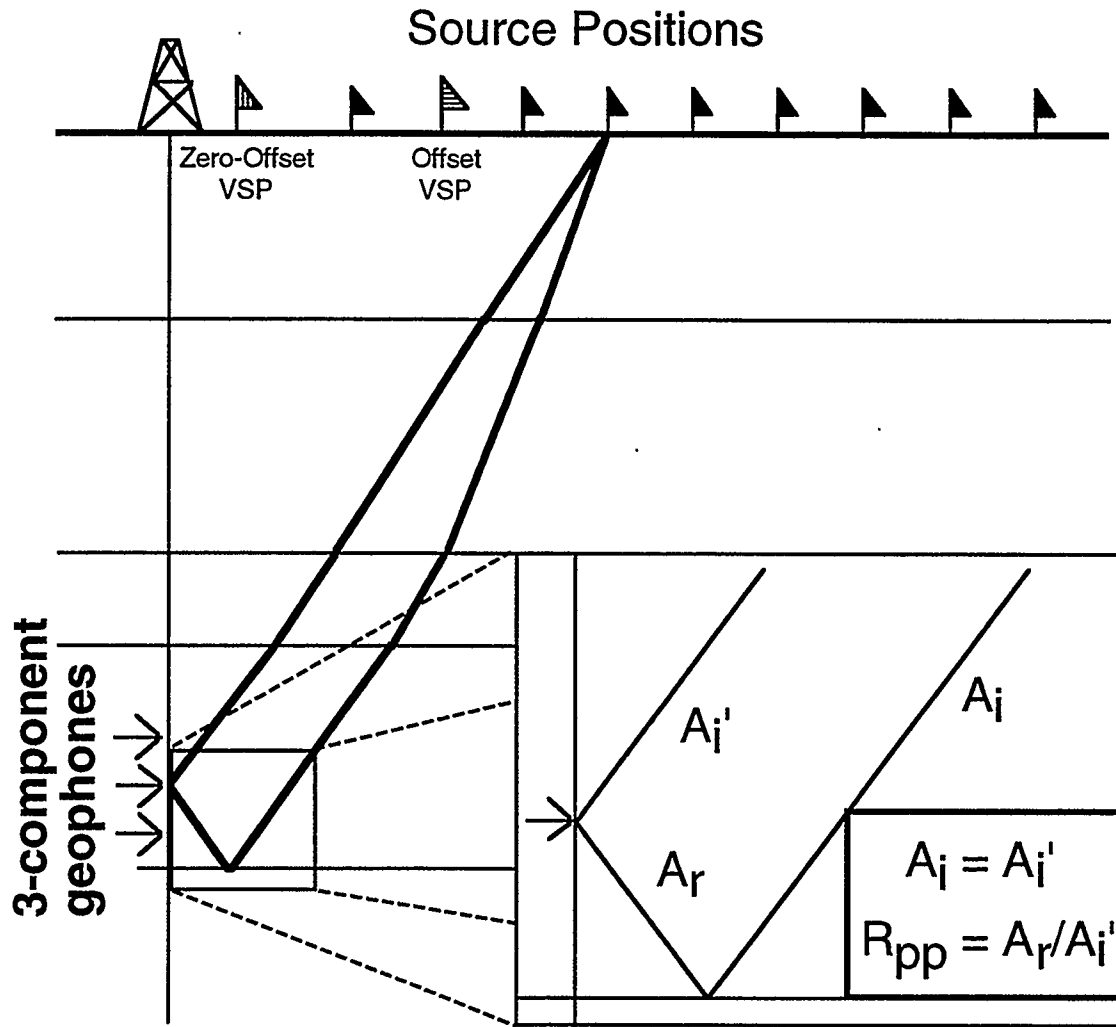


FIG 1.2. AVO VSP geometry outlining the positions of the sources and the receivers. The source positions for the zero offset and offset VSPs are also displayed. Where  $A_i$  and  $A_i'$  are the downgoing wave amplitudes,  $A_r$  is the reflected wave amplitudes, and  $R_{pp}$  is the  $P$ -wave reflection coefficient for the interface.

### 1.3 Study Objectives

The main objective of this thesis is to use the multioffset VSP geometry to analyze the AVO behavior and estimate the rock properties of a subsurface reservoir zone. In meeting the main goal several procedures and algorithms, such as data processing, data interpretation, forward modeling, and inversion, are developed.

In order to apply the VSP geometry to the AVO problem, the geometry must be well understood. The aspects of the VSP which can be exploited in terms of the AVO problem are identified and explained. It is important to test each processing step to be certain the seismic amplitudes are not distorted. Once a processing flow is developed, the data are interpreted. The purpose is to determine if a coherent interpretation can be made using all the available data (well logs, zero-offset VSP, offset VSP, and AVO multioffset VSP). Following the initial interpretation, forward modeling is used to compare synthetic seismograms generated from the Earth model with the VSP field data. This match is determined qualitatively, and leads to a quantitative method of determining the Earth model that best represents the field seismic data. A joint  $P$ - $P/P$ - $SV$  least-squares inversion scheme is developed to determine quantitatively the best match of the model data to the field VSP data.

This modular approach to understanding and solving the problem is used because each module forms the background of the next module, forming a well-defined path to understanding the seismic response and thus the AVO behavior of the subsurface reservoir zone.

# Chapter 2

## VSP Acquisition and Processing

### 2.1 Introduction

The multioffset VSP geometry shown in Figure 1.2 outlines the AVO technique. The specifics of the geometry can vary depending on the target depth and the overall survey objective. The VSP survey consists of three VSP types; a zero-offset VSP, an offset VSP, and a multioffset VSP. Each VSP survey is acquired for a different purpose, and requires a different processing flow. Processing the zero-offset VSP results in a true *P*-wave time-to-depth correlation and a normal-incidence, zero-phase, largely multiple-free seismic trace. The offset VSP is processed to image the *P-P* and *P-SV* reflectivities away from the borehole, and to obtain an *S*-wave time-to-depth correlation. Processing the multioffset VSP results in true amplitude *P-P* and *P-SV* reflectivities for subsequent AVO analysis.

### 2.2 VSP Acquisition

The VSP data were acquired using the 4-9-97-11W6 well bore in North West Alberta shown in Figure 2.1. The purpose of the VSP survey was to evaluate the seismic response of the gas-bearing Slave Point formation. The stratigraphy of the Slave Point in this area is shown in Figure 2.2. The Slave Point in this area is predominantly limestone with localized porosity enhanced by dolomitization. The Slave Point is overlain by the Beaverhill Lake, a shaly limestone, and underlain by the Watt Mountain, a shale unit. The reservoir zone is within the Slave Point Formation with production from a dolomitized zone. The reservoir zone is permeable with both vugular and intergranular porosity. In permeable zones, there are often uncertainties in well-log measurements

caused by fluid invasion; for example, the sonic log can measure the response of the invaded zone instead of the unaltered reservoir zone. The VSP survey was acquired to help in understanding the seismic response of the reservoir, given the limitations of forward modeling caused by these uncertainties. The zero-offset VSP was acquired to provide a normal-incidence seismic trace at the well bore, and the  $P$ -wave VSP interval velocities. The 750-m offset VSP was acquired for  $S$ -wave VSP interval velocities. There was an AVO anomaly observed on the surface seismic data, and the multioffset VSP was acquired to confirm the observed AVO anomaly.

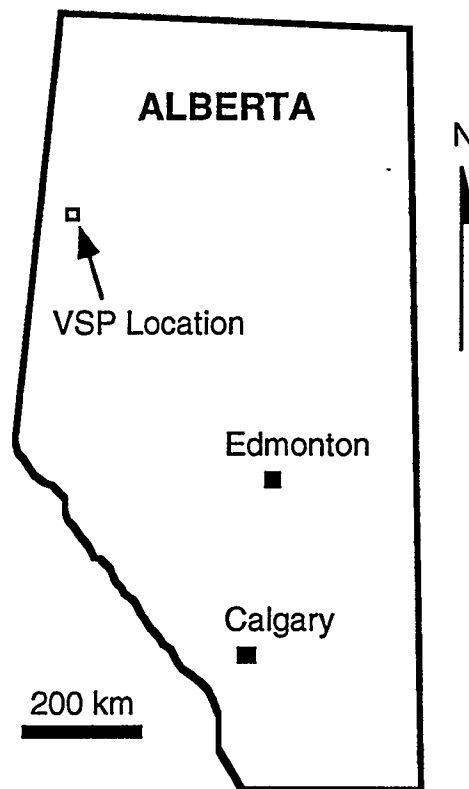


FIG 2.1. Map of Alberta showing the location of the VSP survey.



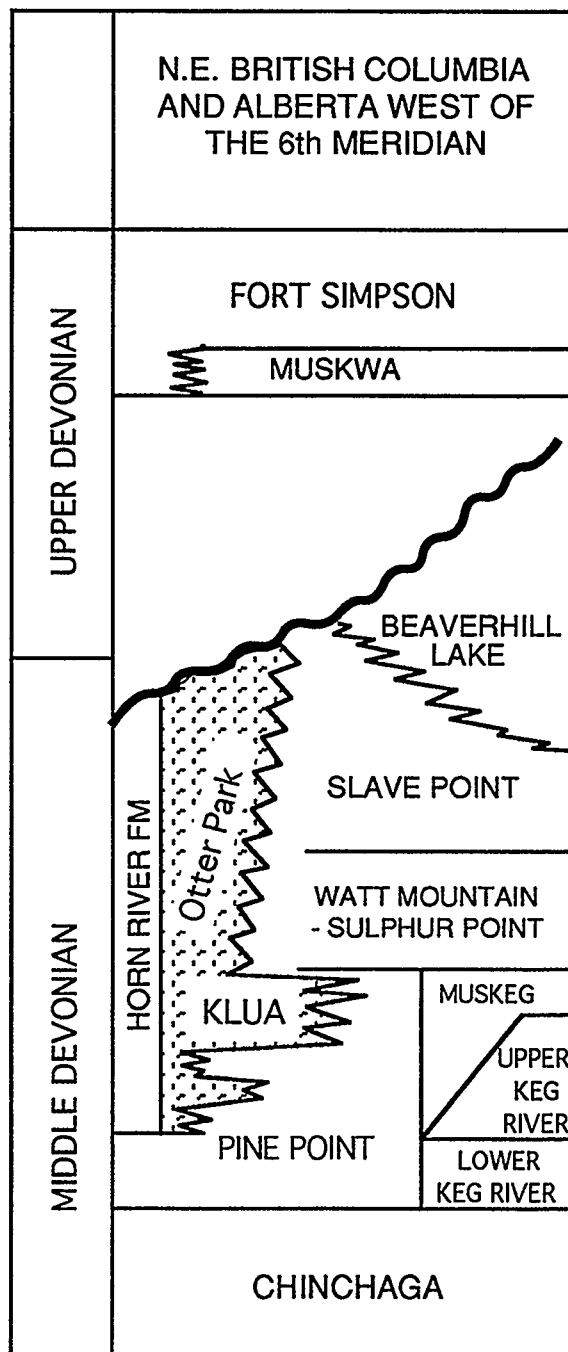


FIG 2.2. Stratigraphic column of the Devonian section in the study area (modified from Ferry, 1989)

The source positions of the VSP survey are shown in plan view in Figure 2.3. The receiver positions are outlined in Table 2.1 for each VSP survey type. The target

depth for the survey is approximately 2500 m. The receiver was a single-level 3-component mechanically-clamped geophone, and the data were acquired in open hole conditions (the borehole was not cased). The source consisted of two Mertz-25 vibrators, and a 12-s sweep from 10 to 90 Hz was used. The logistics of the survey were to acquire data at all the receiver positions for a given source position, and then move the source to the next position.

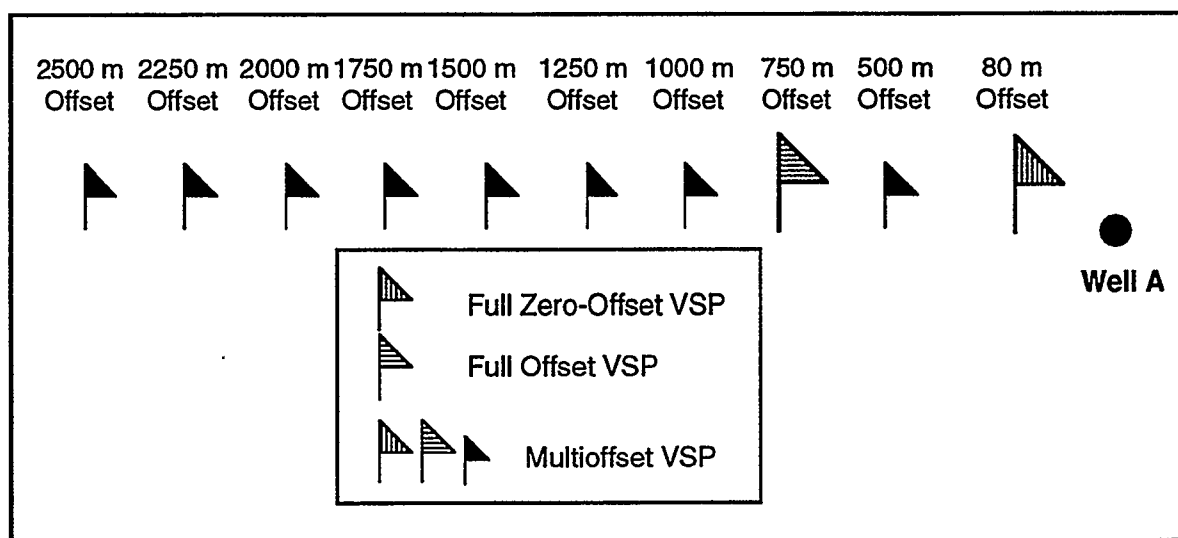


FIG 2.3. Plan view of the Well A multioffset VSP survey geometry. Three VSP surveys are diagrammed; a zero-offset VSP at 80 m from the borehole, an offset VSP at 750 m from the borehole, and a multioffset VSP with 10 offsets ranging from 80 to 2500 m from the borehole.

Table 2.1. Well A geophone locations.

Source Offset (m)	Number of Levels	Bottom Level (m)	Top Level (m)	Level Spacing (m)
80	75	2625	400	25
500	11	2525	2325	20
750	81	2525	905	20
1000	11	2525	2325	20
1250	11	2525	2325	20
1500	11	2525	2325	20
1750	11	2525	2325	20
2000	11	2525	2325	20
2250	11	2525	2325	20
2500	11	2525	2325	20

## 2.3 VSP Processing

Each VSP shown in Figure 2.3 contains different information. Each VSP yields a true time-to-depth correlation which is one of the important advantages of VSP data. The arrival times of the  $P$ -wave direct arrival from the zero-offset VSP can be used in a travelttime inversion algorithm to obtain the  $P$ -wave interval velocities (Stewart, 1984). Similarly the arrival times of the  $S$ -wave direct arrival or a near-surface mode-converted  $S$  wave can be used to obtain the shear-wave interval velocities. Thus a good estimate of the  $P$ - and  $S$ -wave velocities can be obtained from the zero-offset and offset VSPs. There is also considerable information in the reflected (upgoing) wavefields of the VSP data. The corridor stack from the zero-offset VSP can be used in an composite plot to help correlate seismic events with well logs (Stewart and DiSiena, 1989). The offset VSP can be used to correlate  $P$ - $P$  and  $P$ - $SV$  reflections (Geis et al., 1990). The multioffset VSP contains the  $P$ - $P$  and  $P$ - $SV$  reflection amplitudes for a range of  $P$ -wave angles of incidence to be used for AVO analysis.

### 2.3.1 Zero-Offset VSP Processing

The zero-offset VSP has been processed using a conventional processing flow including the following steps: median filter for separation of the upgoing and downgoing waves; waveshaping deconvolution using the downgoing  $P$  waves to design the deconvolution operator to be applied to the upgoing  $P$  waves; amplitude recovery by applying an exponential gain; and shift to two-way time by doubling the first-break time of the upgoing  $P$  waves.

The raw vertical channel of the zero-offset VSP is shown in Figure 2.4. These data are plotted in trace-normalized form (each trace in the plot is scaled independently) with the level number plotted along the horizontal axis. The discontinuities along the first breaks are due to gaps in the geophone depth levels. There is a large change in the

slope of the first breaks at the upper levels (shallower depths) of the survey due to a change in level spacing from 25 m to 100 m. These upper levels were acquired mainly for the velocity information in the first-break traveltimes and not for reflections, so these levels are not used in further processing.

Several events can be identified in these data. The downgoing  $P$  wavefield and a reflected upgoing  $P$ -wave are labeled  $P$  and  $P-P$  respectively. So, both downgoing and upgoing events can be identified in these data, and further processing is necessary to enhance these events. Also plotted in Figure 2.4 are the first-break traveltimes of the downgoing  $P$  waves. As a vibroseis source was used in this survey, the resulting direct-arrival  $P$  waves appear near zero-phase. The first-break time is picked as the first strong trough in the downgoing  $P$  waves. A plot of the first-break traveltime versus depth is shown in Figure 2.5. The first-break traveltimes are important: they give the true time-to-depth correlation of the VSP data, they are used to flatten the direct arrivals in the up and downgoing wave-separation process, and they are used to shift the data to two-way time.

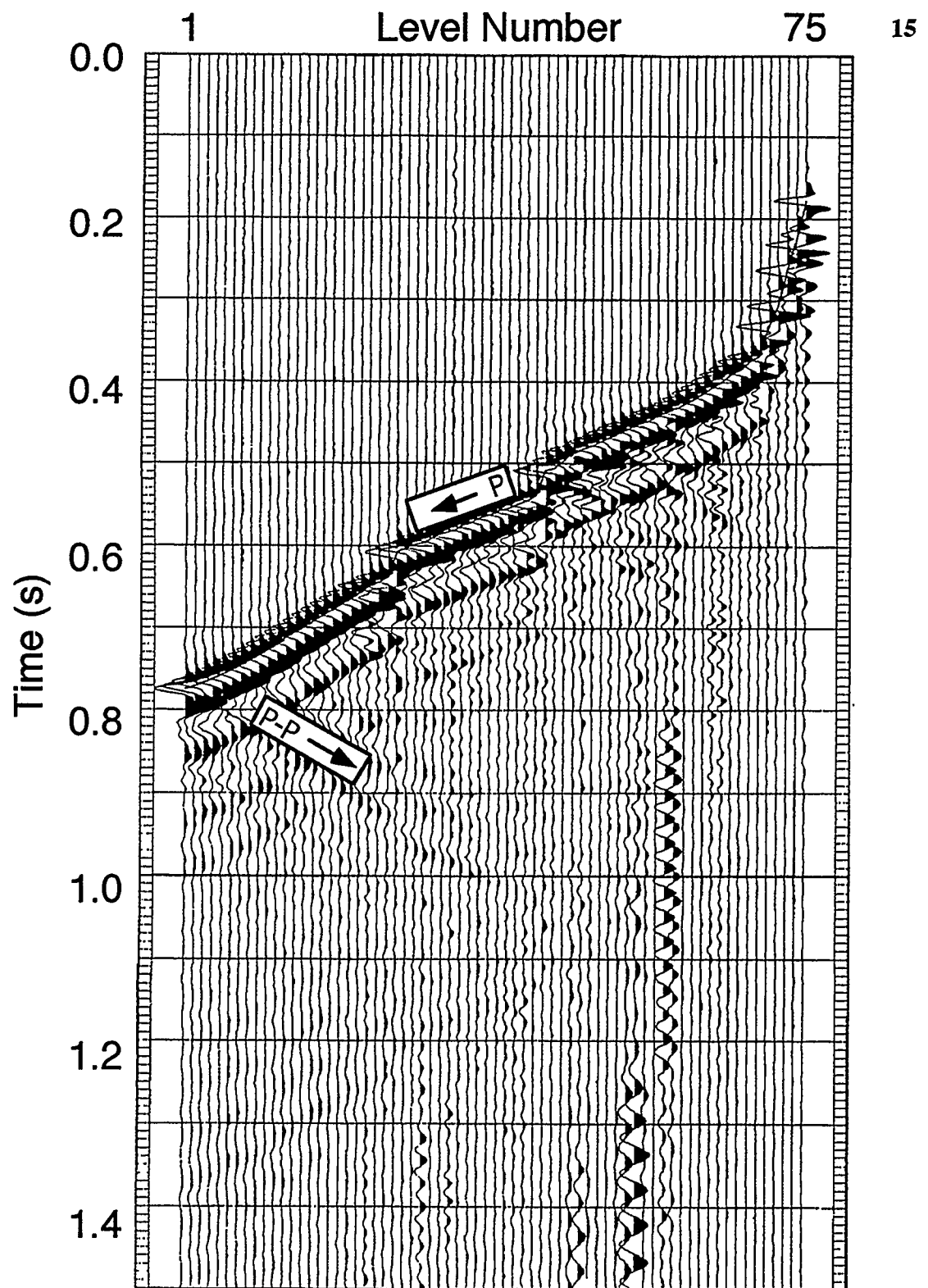


FIG 2.4. Raw vertical channel of the zero-offset VSP. Data are plotted trace-normalized.

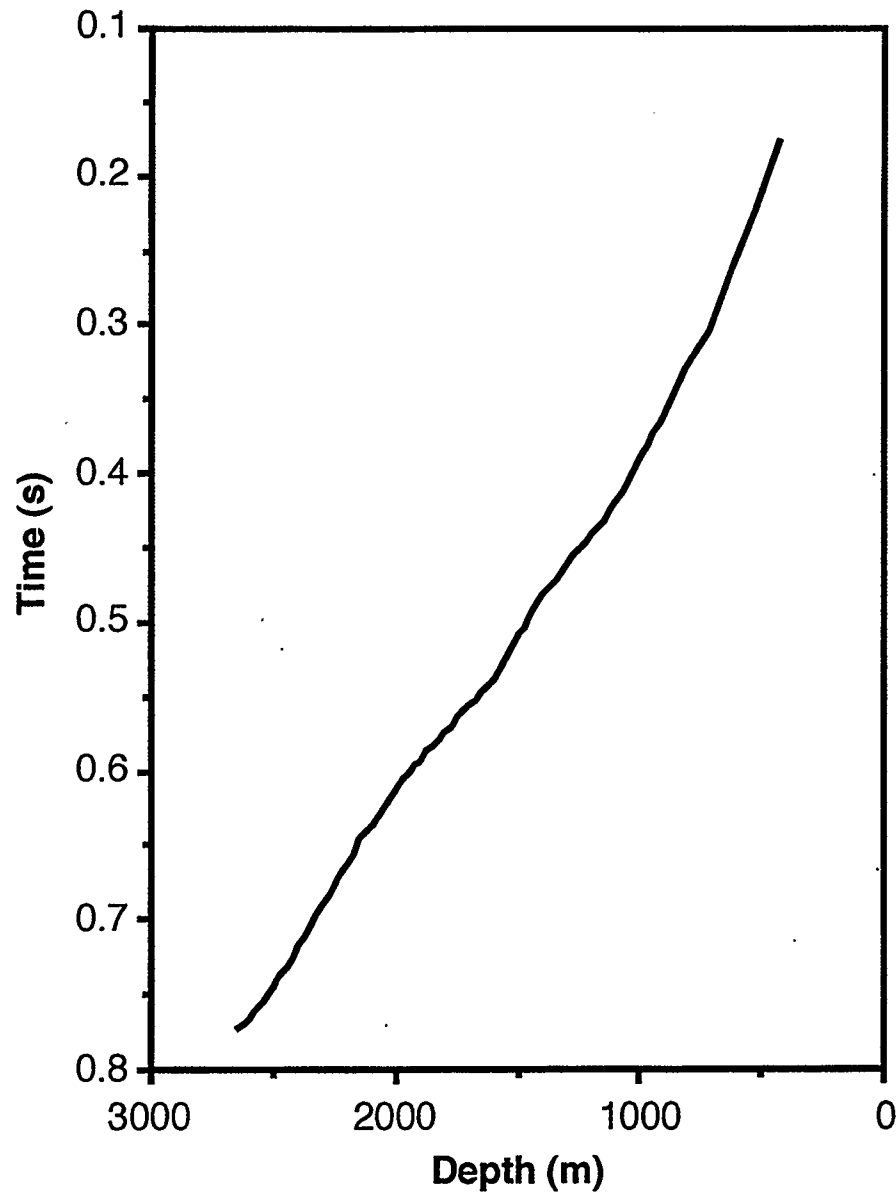


FIG 2.5. First-arrival time-depth curve from the zero-offset VSP.

The next step in the processing flow is to separate the data into upgoing and downgoing  $P$  waves. There are several methods used for this process,  $f-k$  (frequency-wavenumber) filtering and median filtering are two. The median filter has been shown to be a very robust method for the upgoing-downgoing wave separation (Stewart, 1985), and is used here. An eleven-trace median filter was used to enhance the downgoing  $P$  waves in the raw data. The results are shown in Figure 2.6. These data are plotted such

that a single scalar is applied to all the traces in the plot (file normalized). The enhanced downgoing *P* waves are then subtracted from the raw data. The data after subtraction are the upgoing *P* waves (Figure 2.7). The upgoing *P* waves are then enhanced using a seven-trace median filter. The results are shown in Figure 2.8. Note the increase in coherency and decrease in random noise in the upgoing *P* waves after median filtering. Thus the median filtering process both separates the upgoing and downgoing *P* waves and increases the signal-to-noise ratio of the data in this case.

The next step in processing these data is to trace equalize the energy of the downgoing *P* waves along the first-break traveltimes. A 200 ms window was used to calculate the equalization factor, starting 40 ms before the first breaks and ending 160 ms after the first breaks. This process corrects for spherical spreading and transmission losses along the downgoing *P*-wave travel path.

The data are then processed to zero phase using a waveshaping-deconvolution technique. In this process each of the downgoing *P*-wave traces is shaped to a 5th-order zero-phase Butterworth wavelet with a 10 - 90 Hz frequency band. The operator designed for each of the downgoing *P*-wave traces is applied to the upgoing *P*-wave traces. Following the argument developed in Section 1.2, this process shapes the embedded wavelet in the upgoing energy to a 5th-order zero-phase Butterworth wavelet. The downgoing *P* waves (Figure 2.9) are flattened at 200 ms before waveshaping deconvolution and trace equalization. Note the amplitude decay as the wave travels down the borehole, and what is interpreted as a near-surface multiple at approximately 0.270 s. The downgoing *P* waves after waveshaping deconvolution are shown in Figure 2.10. The waveshaping process eliminates many of the multiples in the data. This can be observed by noting that the reverberations in the downgoing *P* waves occurring after the first breaks are collapsed into a single peak wavelet after waveshaping deconvolution. The upgoing *P* waves after waveshaping deconvolution are shown in Figure 2.11.

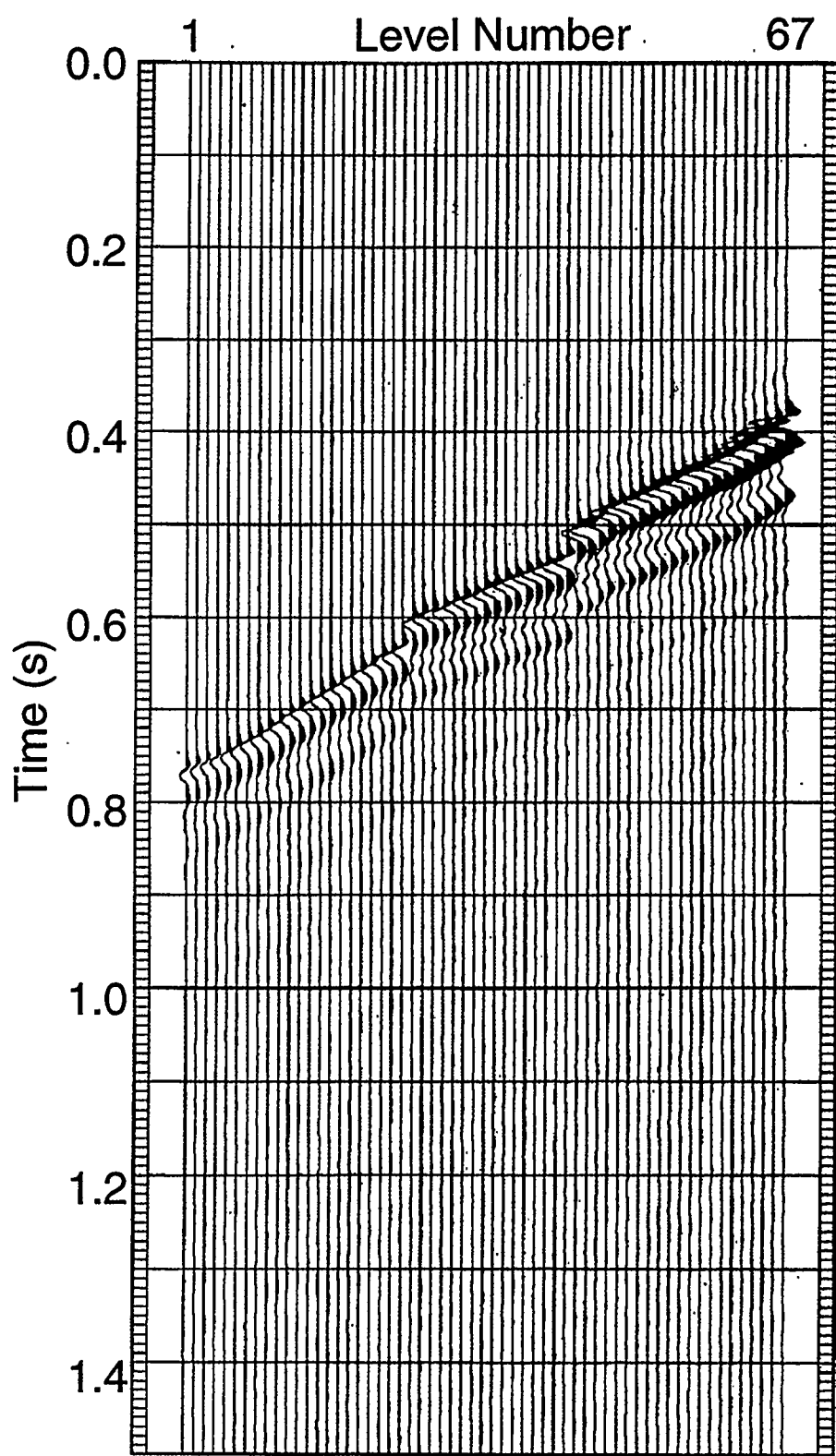


FIG 2.6. Enhanced downgoing  $P$  waves from the zero-offset VSP. The waves were enhanced using an eleven-trace median filter. The data are plotted file-normalized.



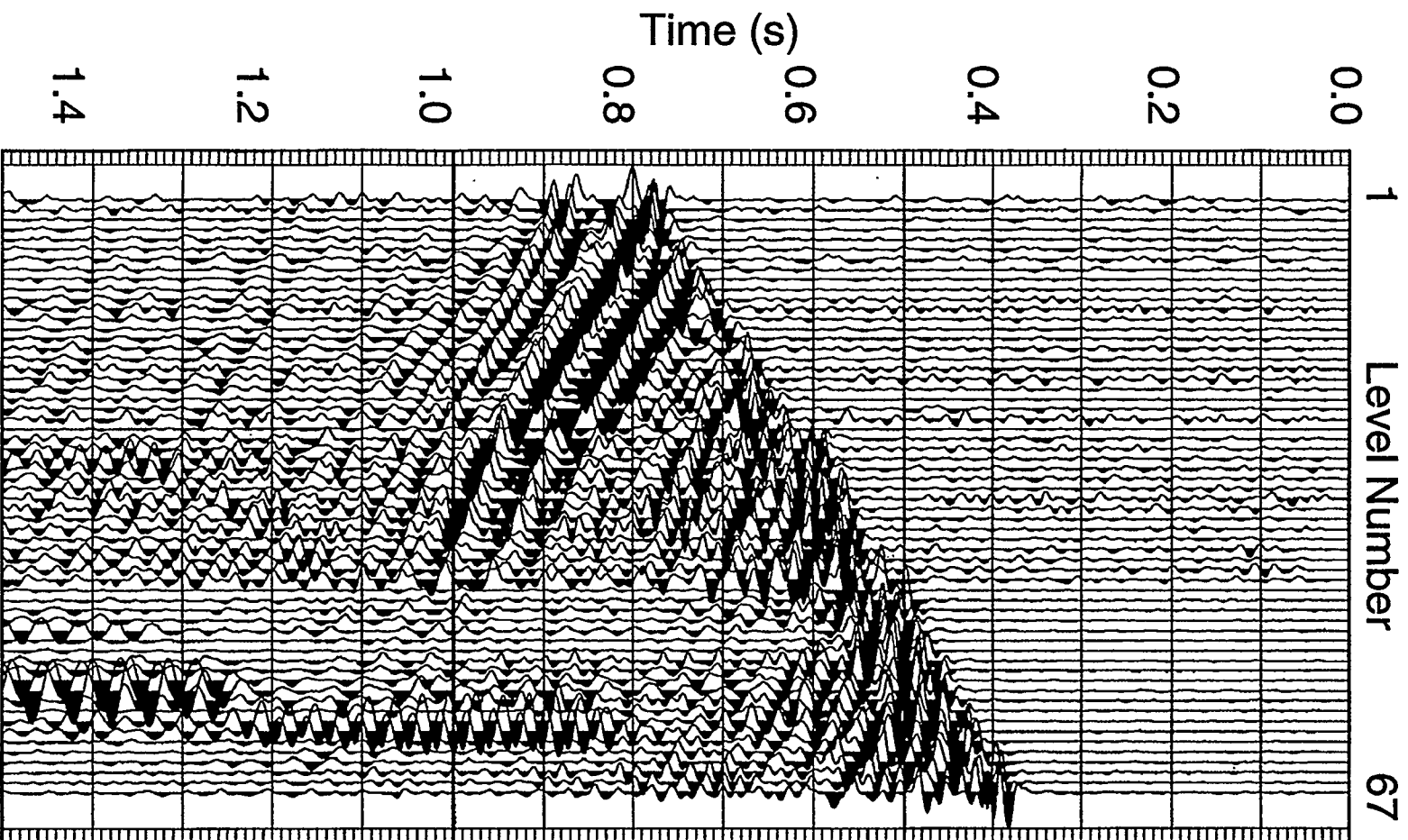


FIG 2.7. Subtraction of the enhanced downgoing  $P$  waves from the raw zero-offset VSP, resulting in the upgoing  $P$  waves. The data are plotted trace-normalized.

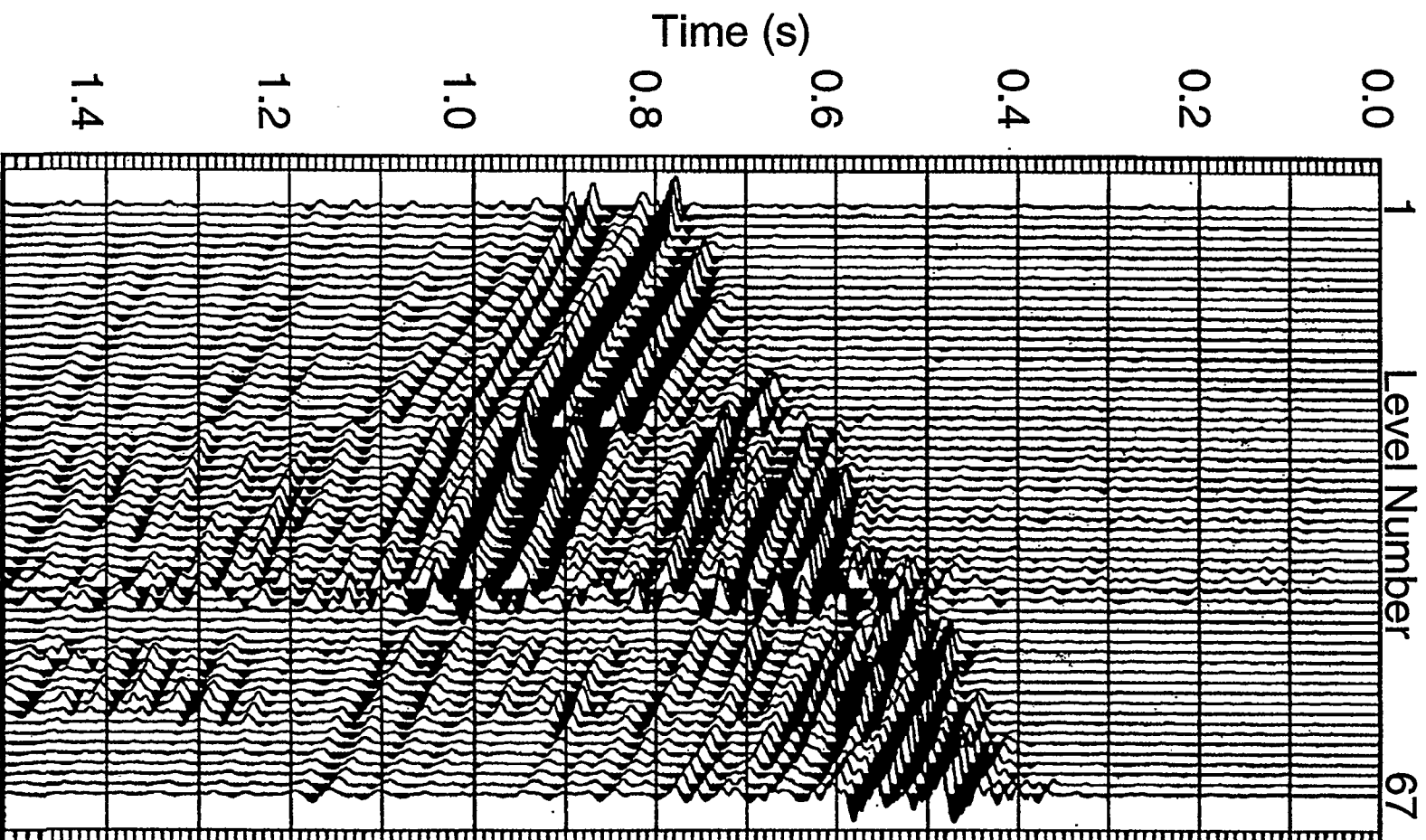


FIG 2.8. Enhanced upgoing  $P$  waves using a seven-trace median filter. The data are plotted trace-normalized.

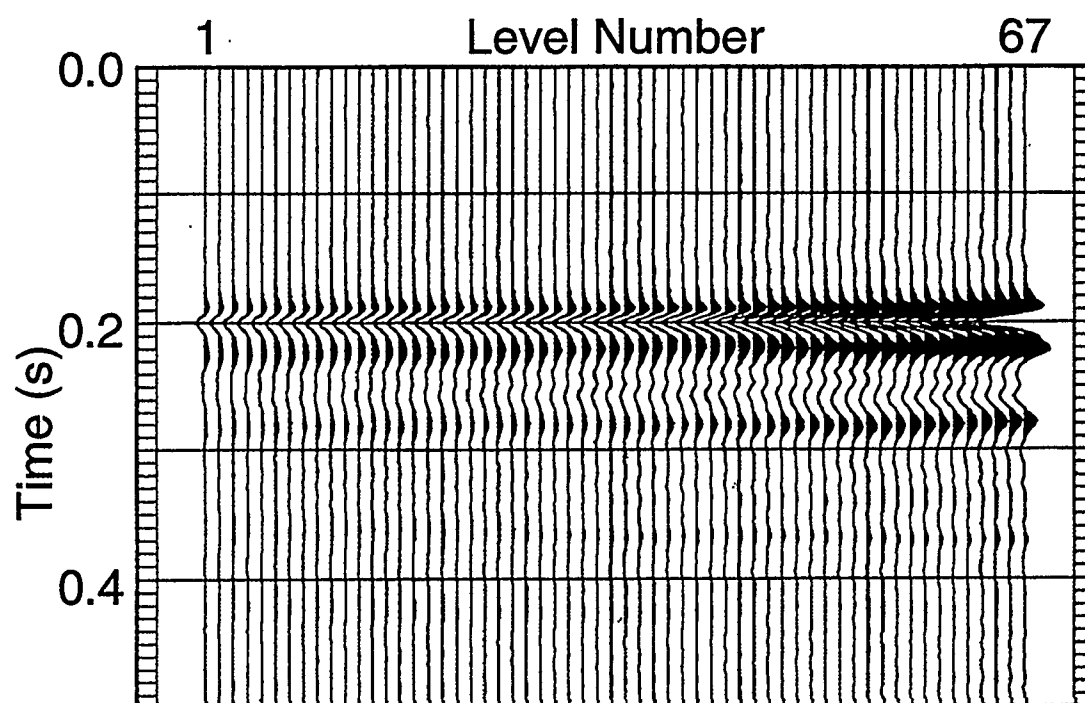


FIG 2.9. Downgoing  $P$  waves flattened at 200 ms before waveshaping deconvolution. The data are plotted file-normalized.

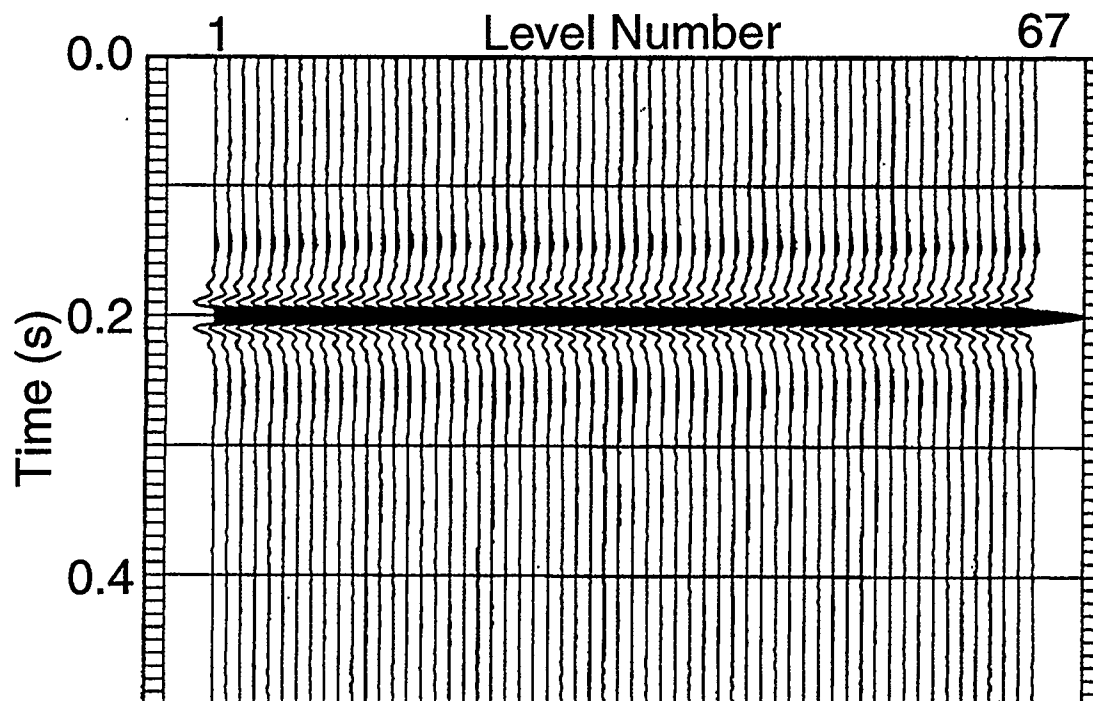


FIG 2.10. Waveshaping deconvolved downgoing  $P$  waves flattened at 200 ms, and shaped to a 5th-order Butterworth wavelet. The data are plotted file-normalized.

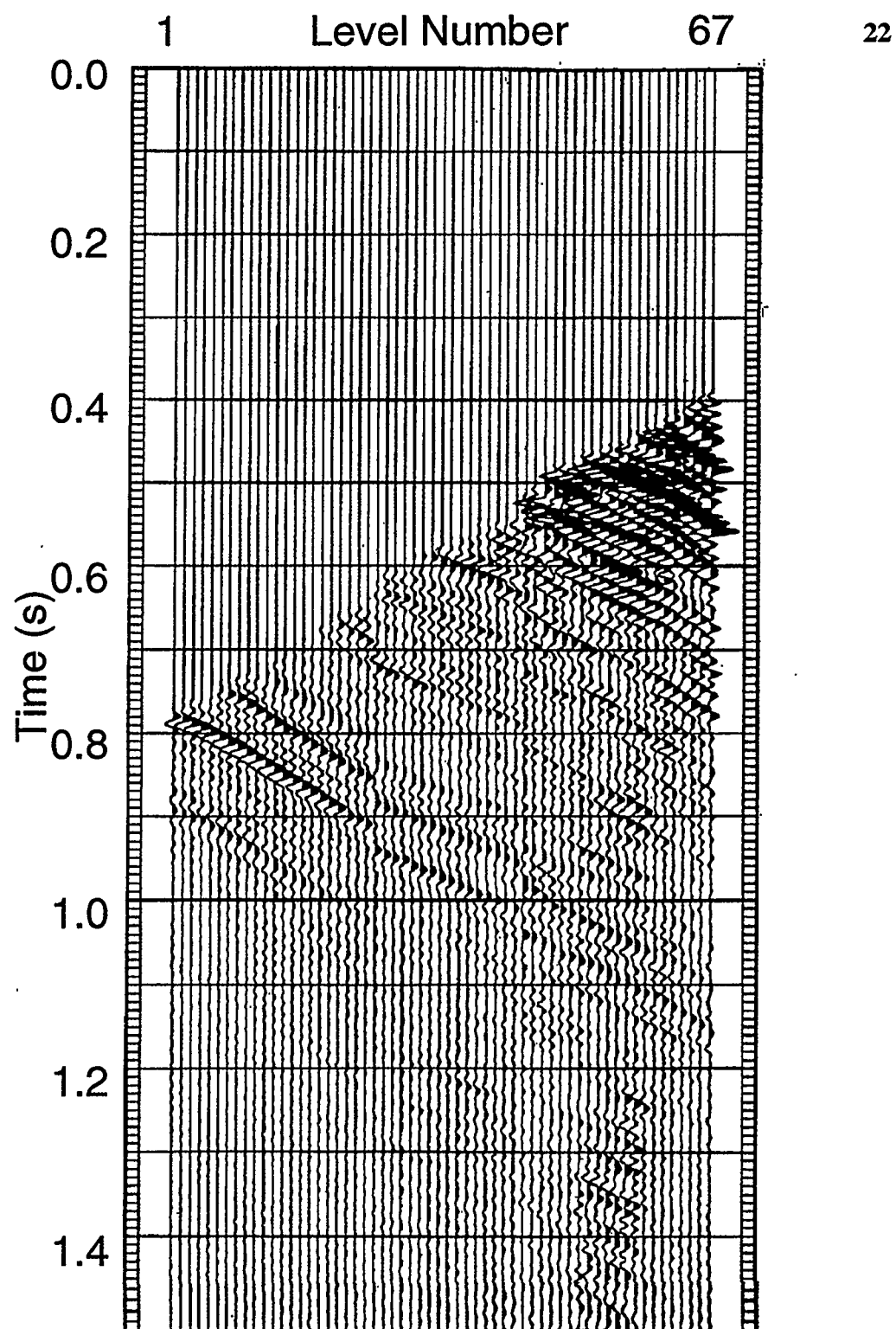


FIG 2.11. Waveshaping deconvolution applied to the upgoing  $P$  waves. The data are plotted file-normalized.

After waveshaping deconvolution the data are scaled to true reflection amplitudes. The data are then corrected for spherical spreading and transmission losses. True reflection amplitude is defined here as the amplitude of the seismic events resulting from convolution of a wavelet that has a peak amplitude of 1.0 with the reflection coefficient series. The data are scaled to true reflection amplitudes by taking the ratio of the upgoing and the downgoing amplitudes. Before waveshaping deconvolution the downgoing *P* waves were trace equalized to correct for downward propagation losses and to prepare the data so that the waveshaping deconvolution operators designed from the downgoing *P* wave traces does not introduce any trace-to-trace amplitude changes in the data. So, because the downgoing amplitudes have been equalized, the upgoing amplitudes must also be adjusted by the same amount. This is achieved by scaling each of the waveshaping deconvolved upgoing *P*-wave traces by the factor used to equalize the downgoing *P*-wave traces.

It should be noted that if the waveshaping deconvolution operator collapsed the downgoing *P* waves into a wavelet with a peak amplitude of 1.0, the equalization and upgoing-to-downgoing ratio steps would be unnecessary. These procedures were required because of uncertainty in the exact formulation of the waveshaping deconvolution operator.

Obtaining the true seismic amplitudes in this manner is only valid for reflections within a short time period of the first-break curve. As the waves travel back up the borehole, the waves experience transmission losses and spherical spreading as well as other propagation phenomena (such as attenuation). To correct for the losses along the upward travel path, a  $T^n$  scaling function is applied to the upgoing *P* waves, where  $T$  is the time from the first-break curve, and  $n$  is a constant. An  $n$  value of 1.70 was found to balance the amplitudes of events originating near the bottom of the well bore and traveling up the borehole.

The final process applied is to shift the data to two-way time. The zero-offset VSP geometry simplifies this process. The first-break traveltimes corresponds to the one-way vertical *P*-wave traveltimes from the source to the receiver. The upgoing *P* wave traveltimes are shifted to two-way time by shifting each trace by the first-break time. The shifted data are shown in Figure 2.12. The reflected events are now flattened, and the amplitudes along the events are generally constant. The abrupt shifts along the first-breaks in Figure 2.12 are due to gaps in the geophone recording levels, as mentioned previously. A corridor extending from the first-break time down 100 ms is extracted from the upgoing *P* waves and stacked to obtain the final VSP trace (Figure 2.12). The corridor for the bottom 10 traces extends to the end of the data to include reflections from below the well. A corridor of the VSP data is used because as the reflected energy travels back up the borehole, it becomes contaminated with intra-bed multiples and other wave phenomena which can not be controlled in processing. So, the most accurately processed data are near the first breaks. An example of this is in the zone of interest. Note the character change between 1.50 and 1.54 s from level 1 to level 67. This is largely due to multiple energy contaminating the primary events. This also illustrates the advantages of the VSP over surface seismic data where the seismic reflections are recorded in situ where they occur as opposed to being recorded at the surface as in the surface-seismic case.

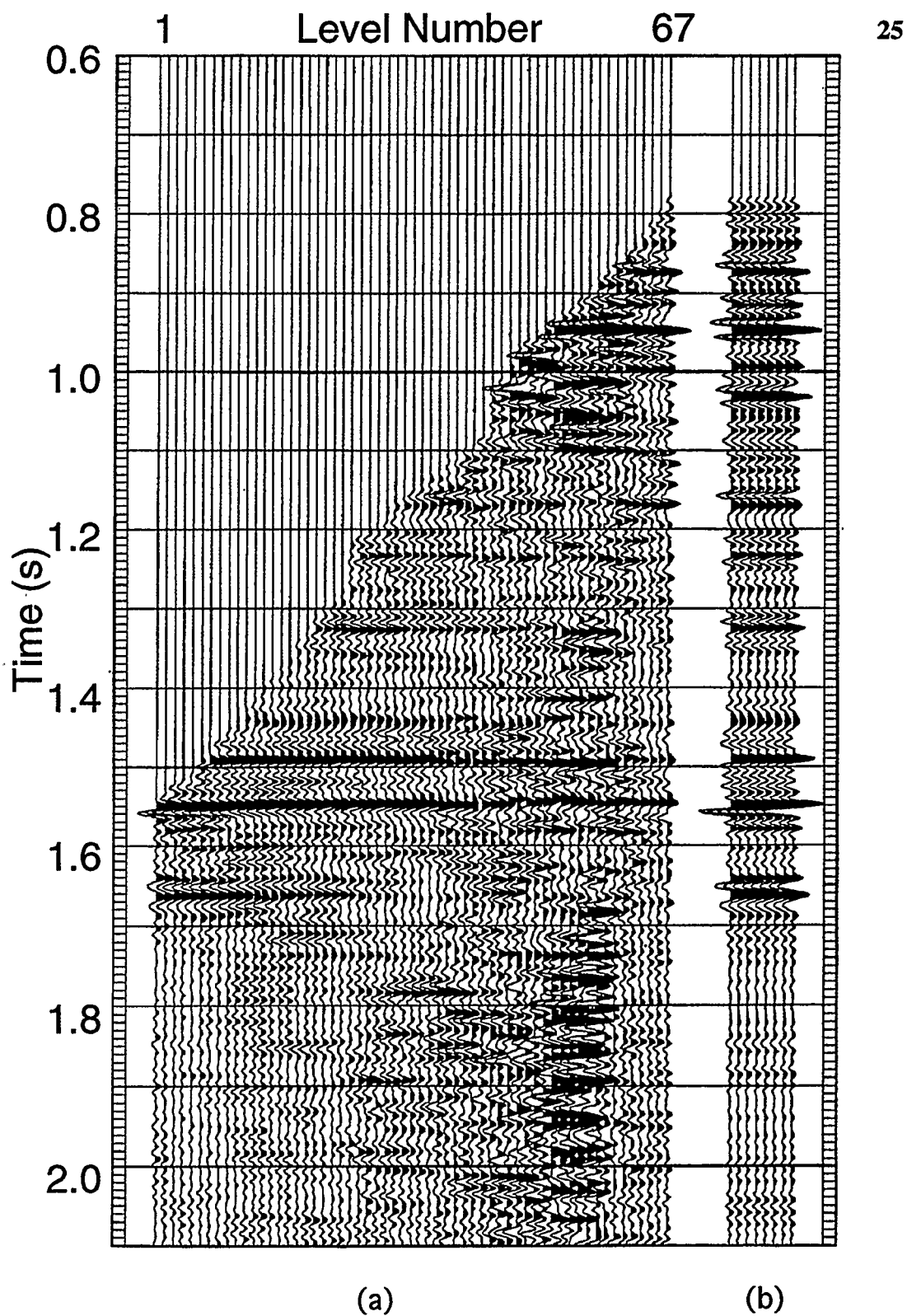


FIG 2.12. (a) Upgoing *P* waves shifted to two-way time to match the traveltimes of surface seismic data. (b) Corridor stack of the upgoing *P* waves using a 100 ms corridor. The stacked trace is repeated eight times.

### 2.3.2 Offset VSP Processing

The 750 m offset VSP (shown in Figure 2.3) has been processed using a three-component processing flow. The flow is designed to extract the  $P$ - $P$  and mode-converted  $P$ - $SV$  reflections from the data. The extracted  $P$ - $P$  and  $P$ - $SV$  reflectivities are used for  $P$ - $P/P$ - $SV$  event correlations and further processed to create  $P$ - $P$  and  $P$ - $SV$  offset images.

The raw vertical channel of the offset VSP is shown in Figure 2.13. The data quality is good, and both downgoing and upgoing events can be identified. The downgoing  $P$  waves are labeled  $P$ , and the reflected upgoing  $P$  waves are labeled  $P$ - $P$ . There are discontinuities along the first-break curve (Figure 2.13) that are due to missing geophone levels in the recording geometry.

The horizontal channels must be preprocessed to correct for tool rotation that occurs as the geophone is pulled up the borehole. The two horizontal channels are rotated at each depth level to determine the direction of maximum  $P$ -wave direct-arrival energy, in a manner similar to DiSiena et al. (1984). The rotated horizontal component of the seismic wavefield with the maximum direct-arrival  $P$ -wave energy is defined as the radial channel. The transverse channel is defined as the component perpendicular to the direction of maximum  $P$ -wave direct-arrival energy. The downgoing  $P$ -wave energy was maximized in a 40 ms window beginning 10 ms before the first breaks and ending 30 ms after the first breaks. The rotated radial channel is shown in Figure 2.14 and the rotated transverse channel is shown in Figure 2.15. The  $P$ -wave direct arrival (labeled  $P$ ) and downgoing  $S$ -wave energy (labeled  $P$ - $S$ ) are identified on the radial channel. Note that there is more noise before the first breaks on the radial channel than on the vertical channel. This suggests that the horizontal component of the seismic wavefield is smaller than the vertical component for this geometry.

The transverse channel (Figure 2.15) is displayed mainly for quality control of the horizontal rotations. There is little if any coherent energy on this channel indicating that



the horizontal rotation algorithm performed well. However, there is more energy beyond the first breaks of the  $P$ -wave direct arrival. This could be due to small errors in the horizontal rotations, or possibly due to complex wave phenomena such as anisotropy. Although the tranverse channel does bring up some interesting questions, the main goal of processing the offset VSP is to extract the  $P$ - $P$  and  $P$ - $SV$  reflections from the vertical and radial channels.

After the correction for tool rotation, the vertically and radially sampled seismic wavefield is separated into upgoing and downgoing compressional- and shear-wave modes. A parametric inversion technique developed by Leaney and Esmersoy (1989) was used for this separation. In the parametric inversion, the data are modeled as a superposition of  $P$  waves and  $SV$  waves. The local  $P$  and  $S$  velocities, angles of incidence, and waveforms are the model parameters. A least-squares match between the observed data and model-generated data is used to estimate the model parameters. This method was chosen for its ability to recover accurate wavefield amplitudes, and its proven robustness when applied to other data of similar geometry and geologic setting. The results of this algorithm are the four separate wave-propagation modes of the seismic wavefield: the downgoing  $P$  wavefield (Figure 2.16); the downgoing  $S$  wavefield (Figure 2.17); the upgoing  $P$  wavefield (Figure 2.18); and the upgoing  $S$  wavefield (Figure 2.19). Overall, the method produced a good separation of the seismic wavefield into the four wave propagation modes.

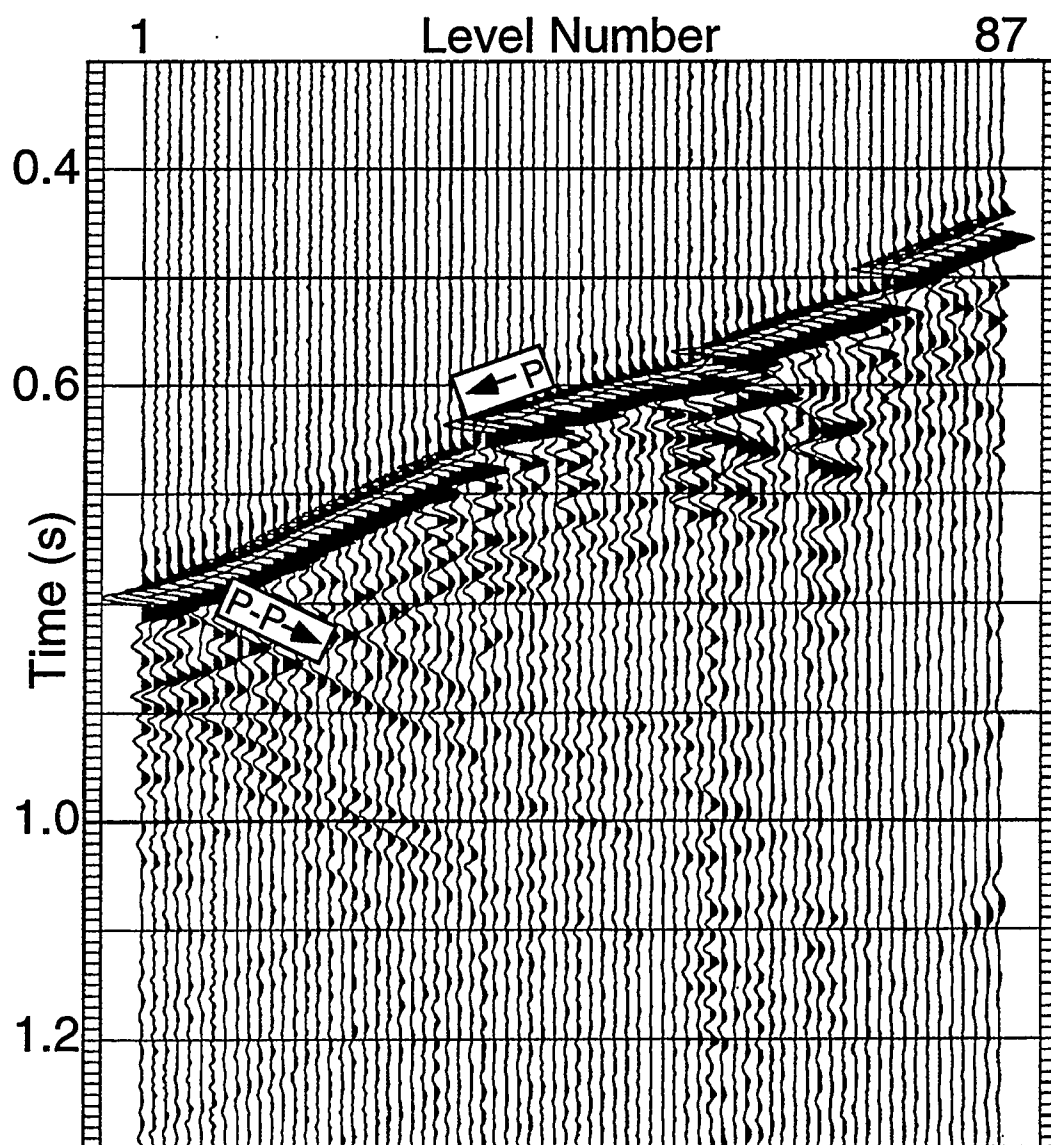


FIG 2.13. Raw vertical channel plotted trace-normalized. There is strong downgoing  $P$ -wave energy (labeled  $P$ ), and strong upgoing  $P$ -wave energy (labeled  $P-P$ ).

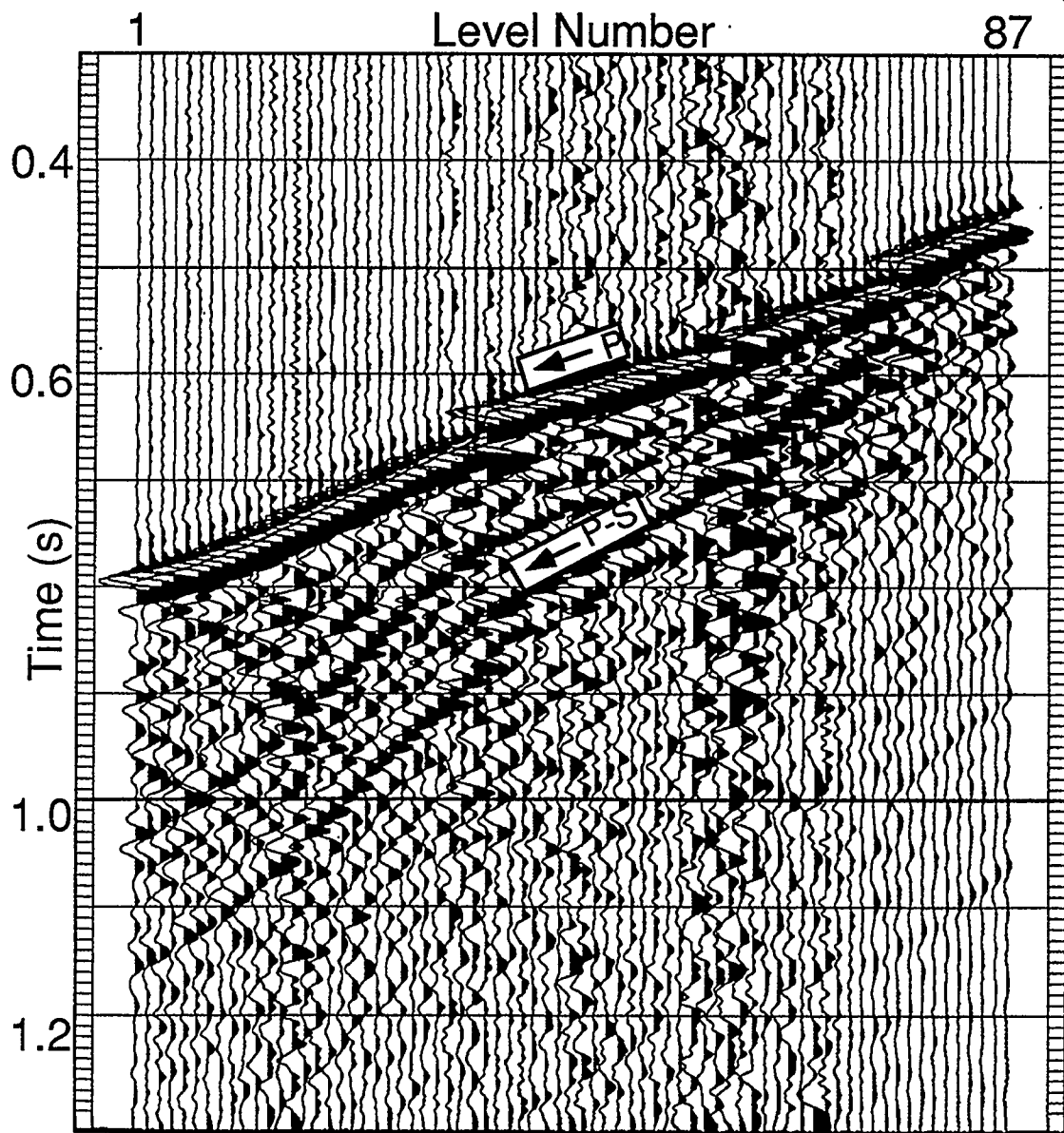


FIG 2.14. Raw radial channel plotted trace-normalized. There is strong downgoing  $P$ -wave energy (labeled  $P$ ), and strong mode-converted downgoing  $S$ -wave energy (labeled  $P$ - $S$ ).

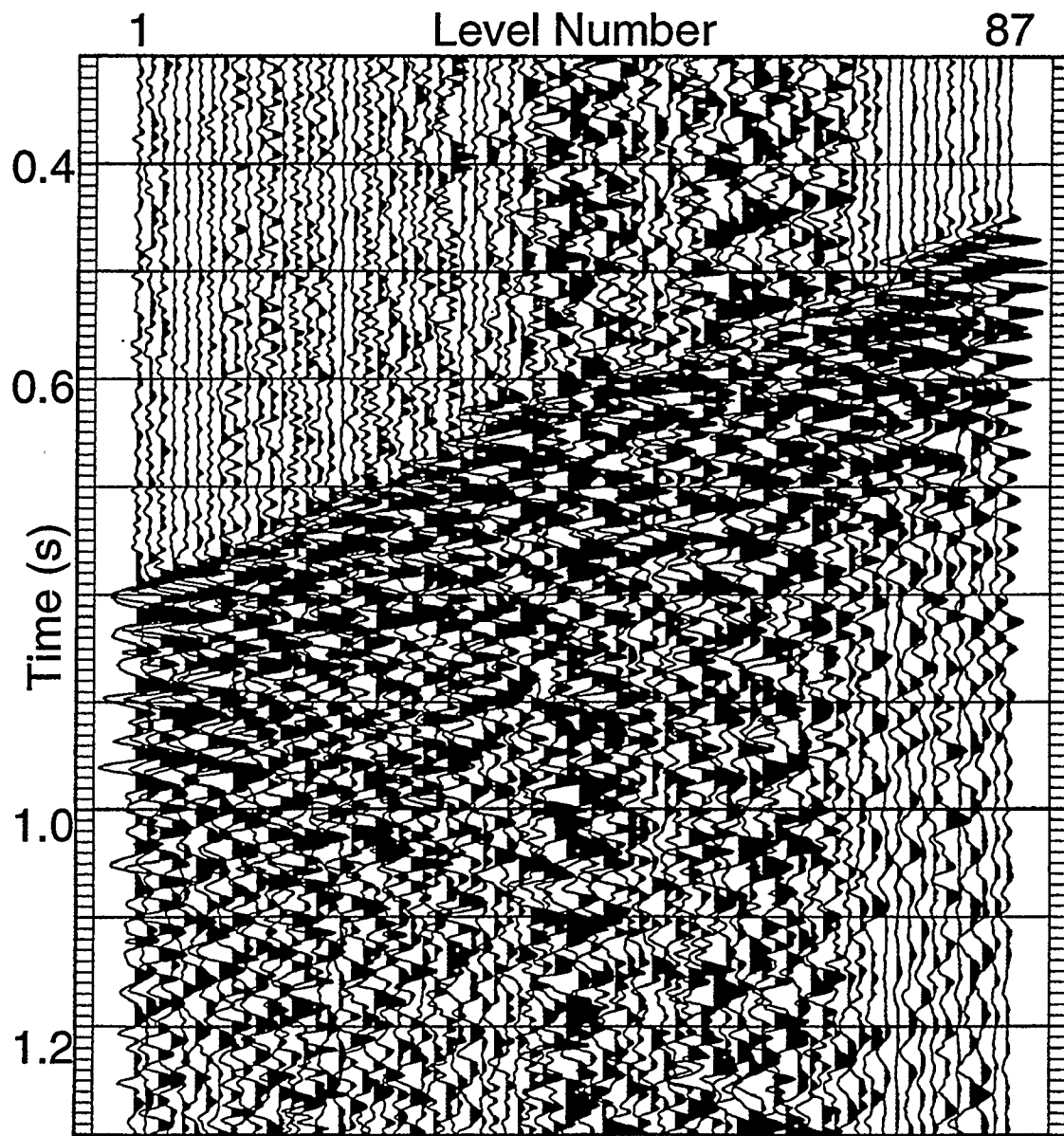


FIG 2.15. Raw transverse channel plotted trace-normalized.

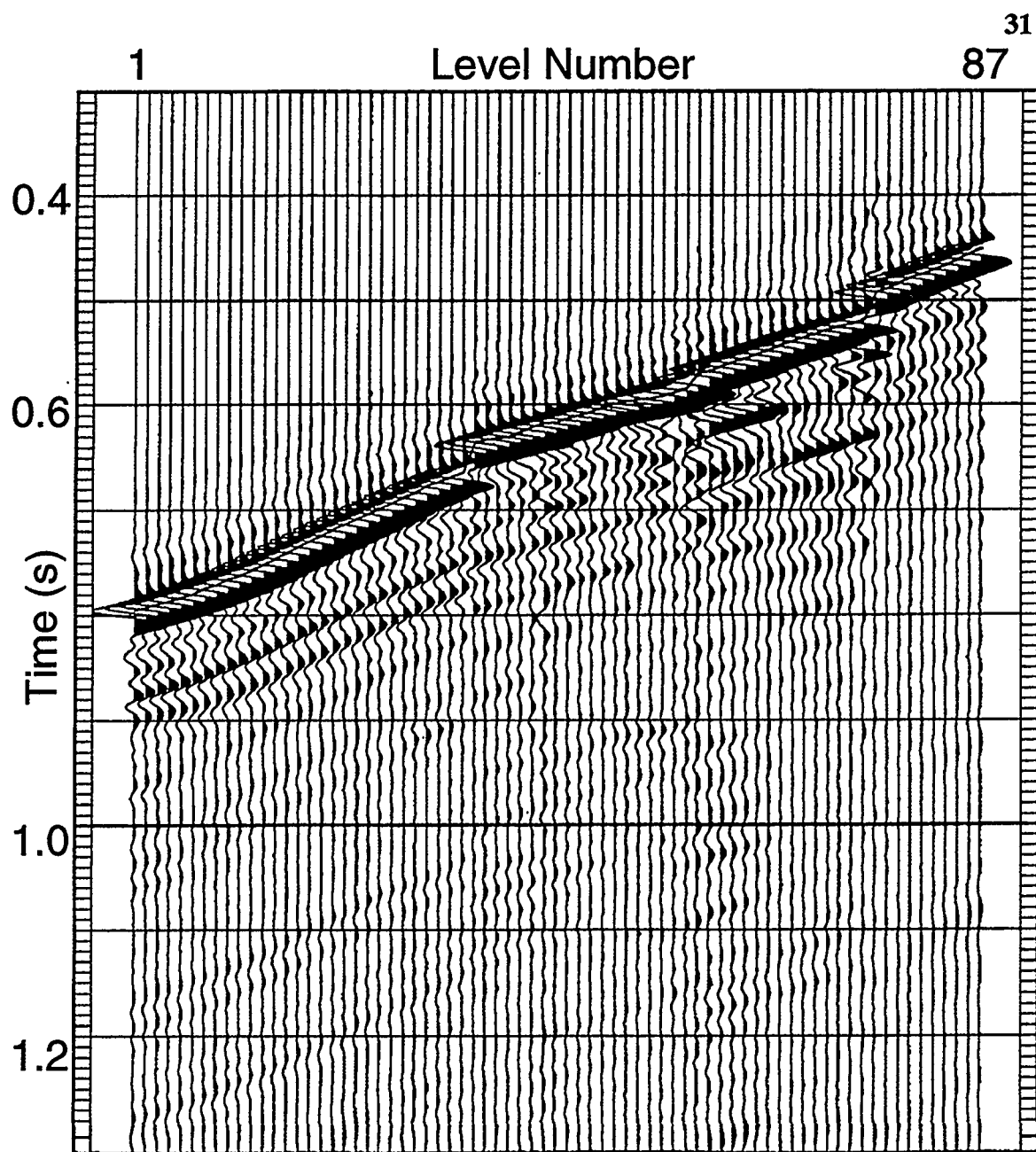


FIG 2.16. Downgoing  $P$  wavefield after wavefield separation; plotted trace-normalized.

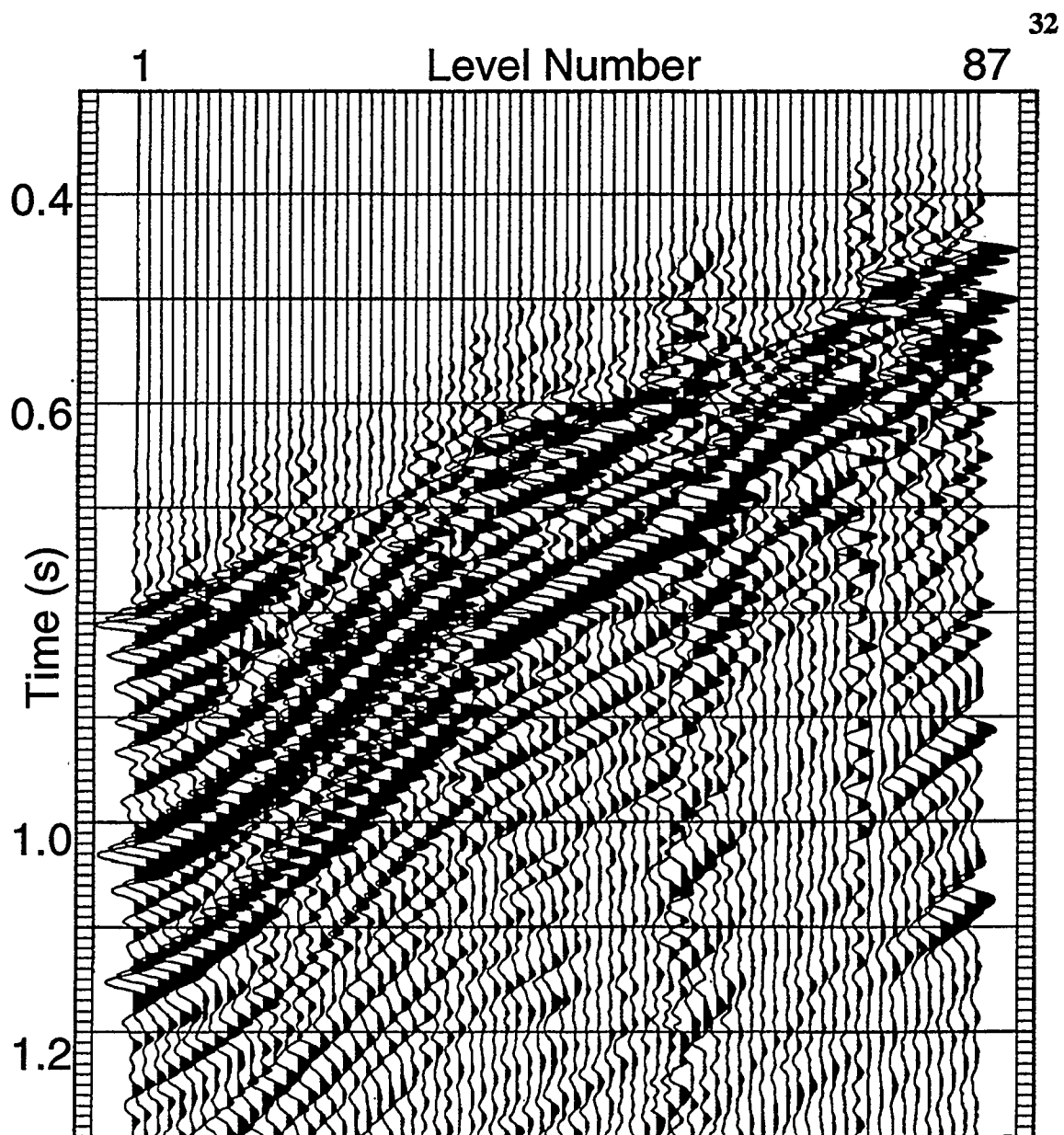


FIG 2.17. Downgoing  $S$  wavefield after wavefield separation; plotted file-normalized.

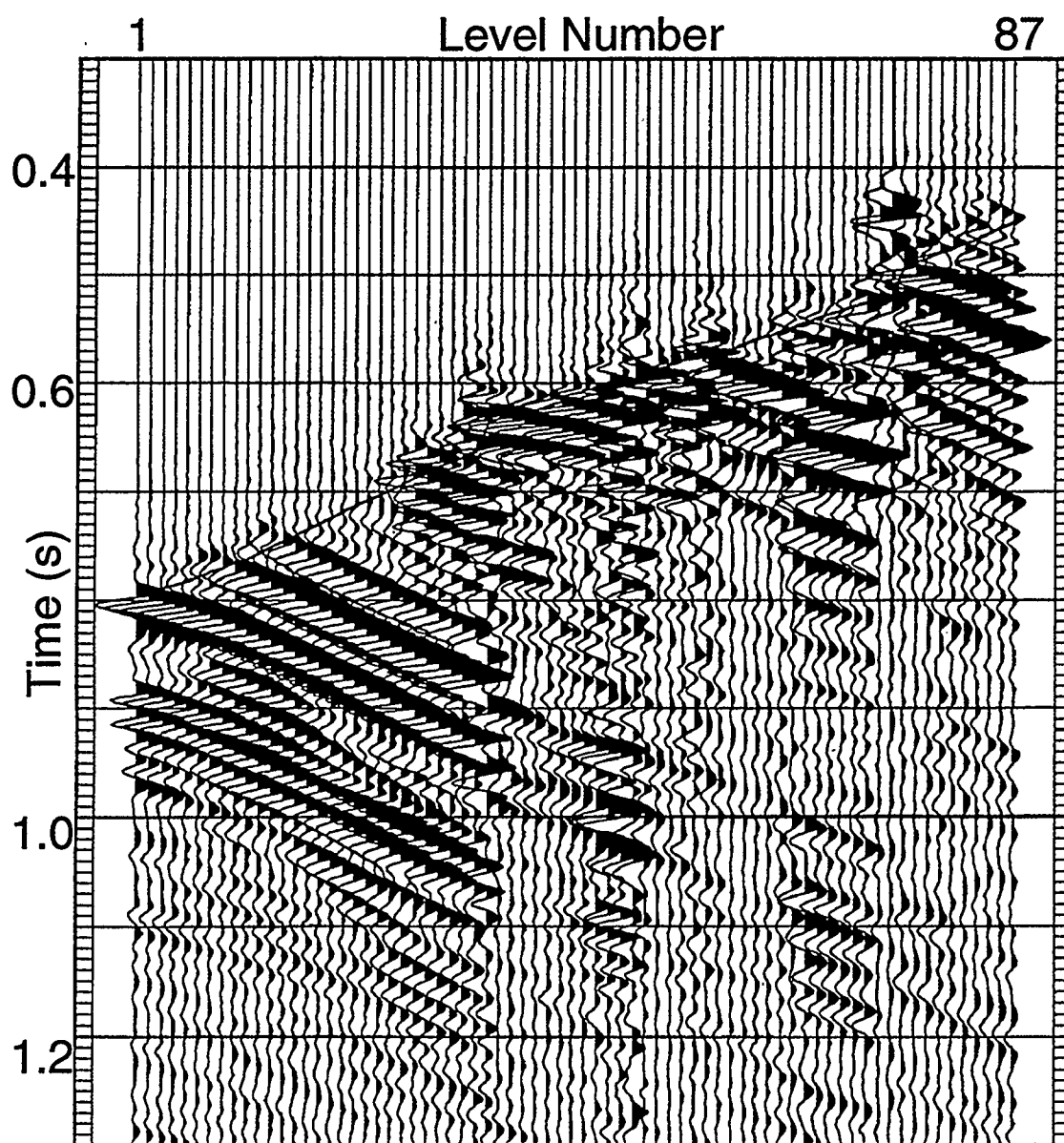


FIG 2.18. Upgoing  $P$  wavefield after wavefield separation; plotted trace-normalized.

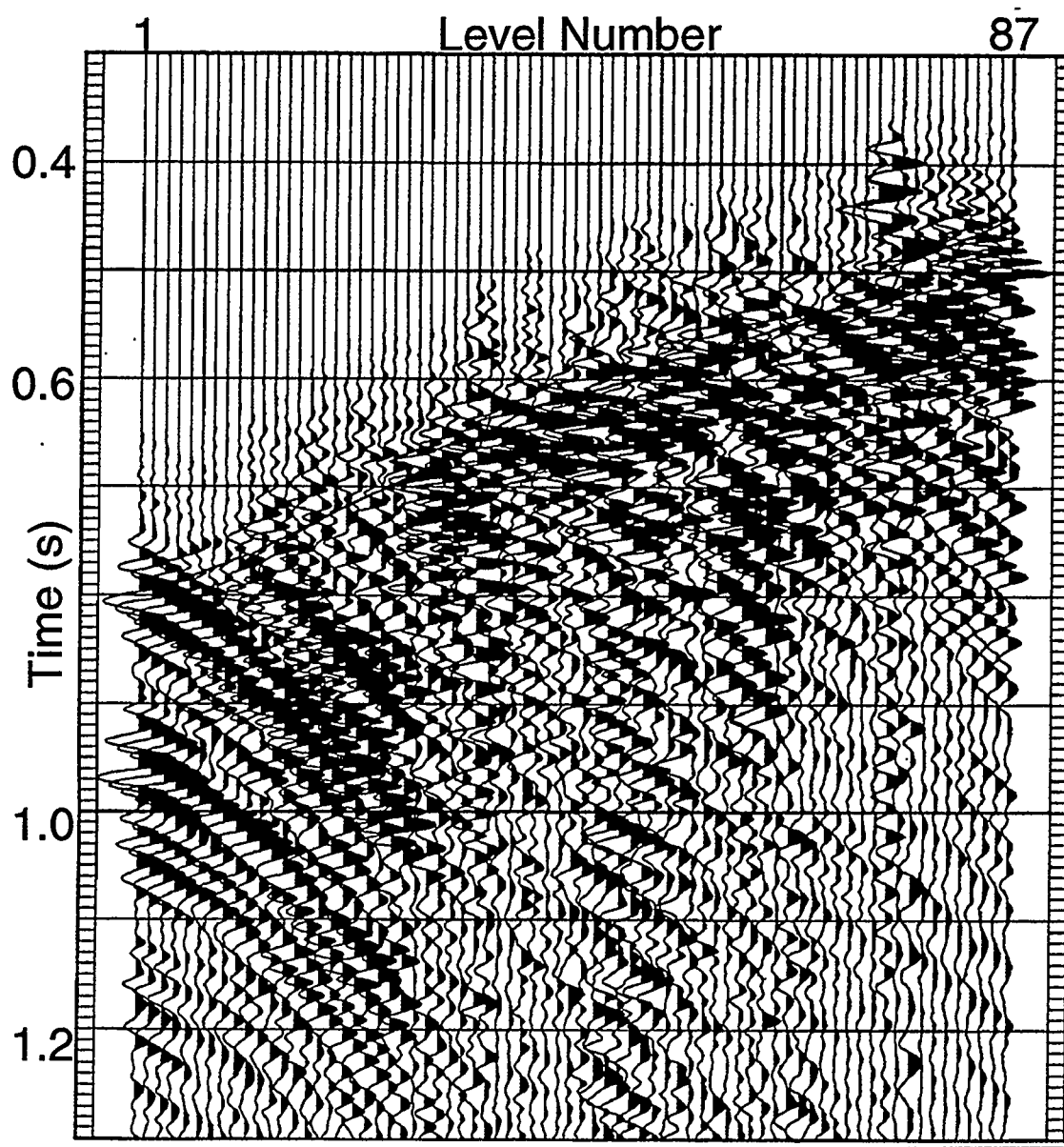


FIG 2.19. Upgoing  $S$  wavefield after wavefield separation plotted trace normalized.

Following the wavefield separation process, waveshaping deconvolution was applied to the data. Prior to waveshaping deconvolution, the downgoing  $P$  wavefield was trace equalized to correct for propagation losses along the downward travel path of the wavefield. This process assures that a constant-amplitude deconvolution operator is calculated from the downgoing  $P$  wavefield. Again, as in the zero-offset case, the



operator is designed from the downgoing  $P$  wavefield, and then applied to the upgoing  $P$  wavefield. The same operator designed from the downgoing  $P$  wavefield is also applied to the upgoing  $S$  wavefield because the latter consists largely of mode-converted shear waves generated by the former. The downgoing  $P$  wavefield flattened at 200 ms is shown before waveshaping deconvolution in Figure 2.20, and after waveshaping deconvolution in Figure 2.21. Note again that the reverberations in the downgoing  $P$  wavefield have been collapsed into a single peak that is a 5th-order zero-phase Butterworth wavelet.

After waveshaping deconvolution, the upgoing  $P$  and  $S$  wavefields are scaled by the same factor used to trace equalize the downgoing  $P$  wavefield. A gain-recovery function is then applied to the data to correct for spherical spreading and transmission losses. For these data a  $T^n$  gain function is applied starting at the first-break times of the downgoing  $P$  wavefield. Again an  $n$  value of 1.70 was found to balance the amplitudes of the upgoing  $P$  and  $S$  wavefields across the array of receivers.

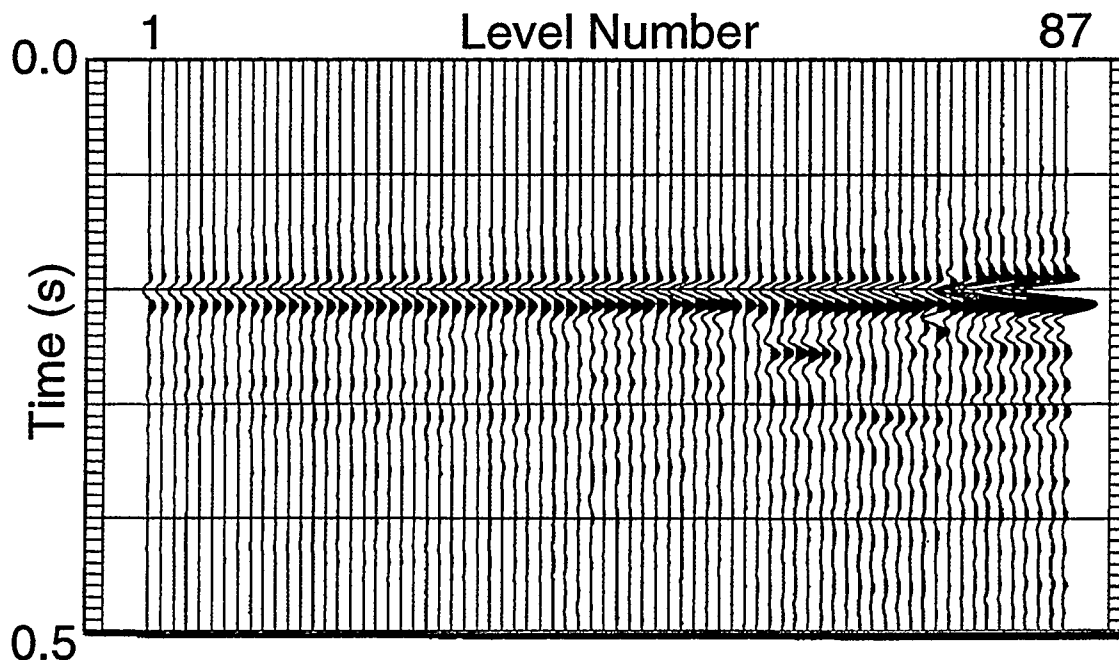


FIG 2.20. Downgoing  $P$  wavefield before waveshaping deconvolution flattened at 200 ms; plotted file-normalized.

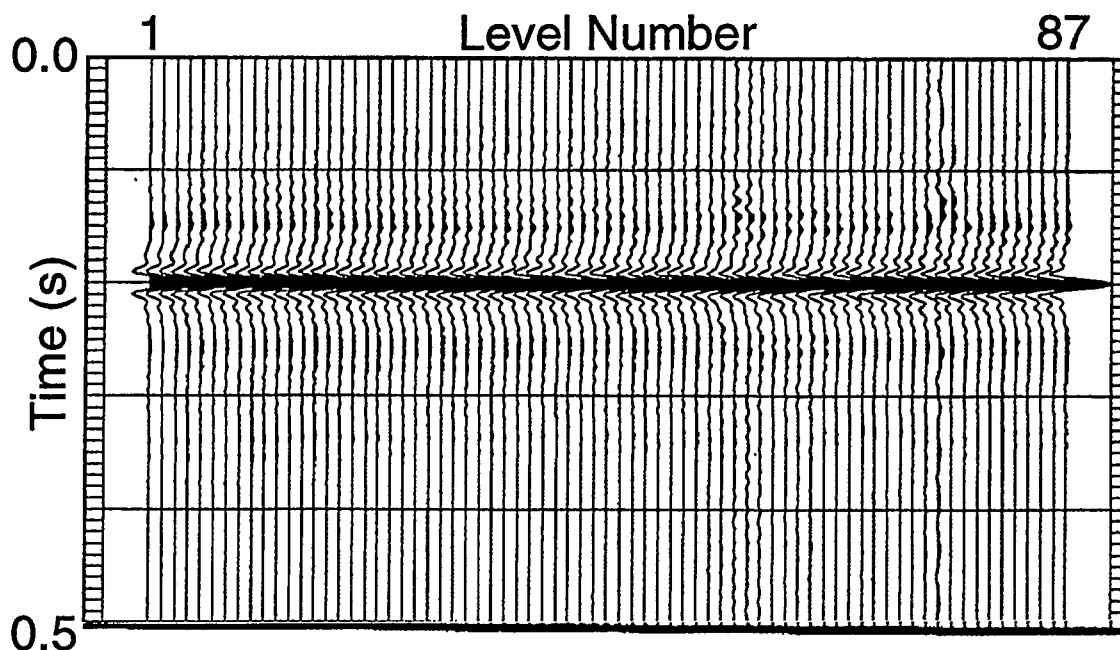


FIG 2.21. Downgoing  $P$  wavefield after waveshaping deconvolution flattened at 200 ms; plotted file normalized.

The next step was to correct the upgoing wavefields for normal moveout (NMO). A procedure similar to that outlined by Geis et al. (1990) is used for the NMO correction. The NMO traveltimes are calculated by ray tracing through a velocity model. The velocity model is determined using the first-break traveltimes from the zero-offset VSP and the downgoing shear-wave traveltimes from the 750 m offset VSP in a traveltimes inversion algorithm. The initial guess and layering of the velocity model are taken from the conventional and full-waveform sonic logs acquired in the well. The velocity model will be discussed in more detail in chapter three. The upgoing  $P$  and  $S$  wavefields after waveshaping deconvolution, gain recovery, and NMO correction are shown in Figure 2.22 and Figure 2.23, respectively. In both cases, the bottom 20 levels contain the more coherent data, while the upper levels have less coherency and more random noise. To attenuate random noise, a seven-trace median filter was applied to the NMO-corrected

upgoing  $P$  and  $S$  wavefields. The upgoing  $P$  wavefield after median filtering is shown in Figure 2.24, and the upgoing  $S$  wavefield after median filtering is shown in Figure 2.25.

The upgoing  $S$  wavefield (Figure 2.24) has less coherent energy than the upgoing  $P$  wavefield (Figure 2.25). A possible explanation is that the upgoing  $S$  wavefield contains  $P$ - $SV$ - $SV$  reflections.  $P$ - $SV$ - $SV$  reflections originate as downgoing  $P$ -wave energy, are converted to downgoing  $S$ -wave energy and then reflected as upgoing  $S$ -wave energy. This reflection mode has an apparent velocity similar to the  $P$ - $SV$  reflections and thus can not be clearly distinguished from the  $P$ - $SV$  reflections. There is strong downgoing  $S$ -wave energy in the raw radial channel (Figure 2.14) and the wavefield-separated downgoing  $S$  wavefield (Figure 2.17) to support this argument. This problem has also been observed by Geis et al. (1990), and should be a future research topic.

After NMO correction and median filtering, the data are stacked along a corridor between the first breaks and a later time. A 100 ms corridor was used, and the results are shown in Figures 2.26 and 2.27 for the upgoing  $P$  and  $S$  wavefields respectively. These corridor stacks are useful for correlation and event interpretation and will be addressed further in chapter three.

The final step in the processing flow is to map the upgoing  $P$  and  $S$  wavefields to the correct offset positions. The offset mapping is similar to NMO correction in that a model-based ray tracing algorithm is used that assumes flat layers. The  $P$ - $P$  and  $P$ - $SV$  data are binned into 6.25 m bins centered every 6.25 m. For the  $P$ -wave data, this process is termed VSPCDP mapping as the data are mapped to the common depth point; for the  $S$  wave data, the process is termed VSPCCP mapping as the data are mapped to the common conversion point. The VSPCDP and VSPCCP maps are shown in Figures 2.26 and 2.27. Note that there are gaps in both of the mappings due to missing geophone levels in the recording geometry.

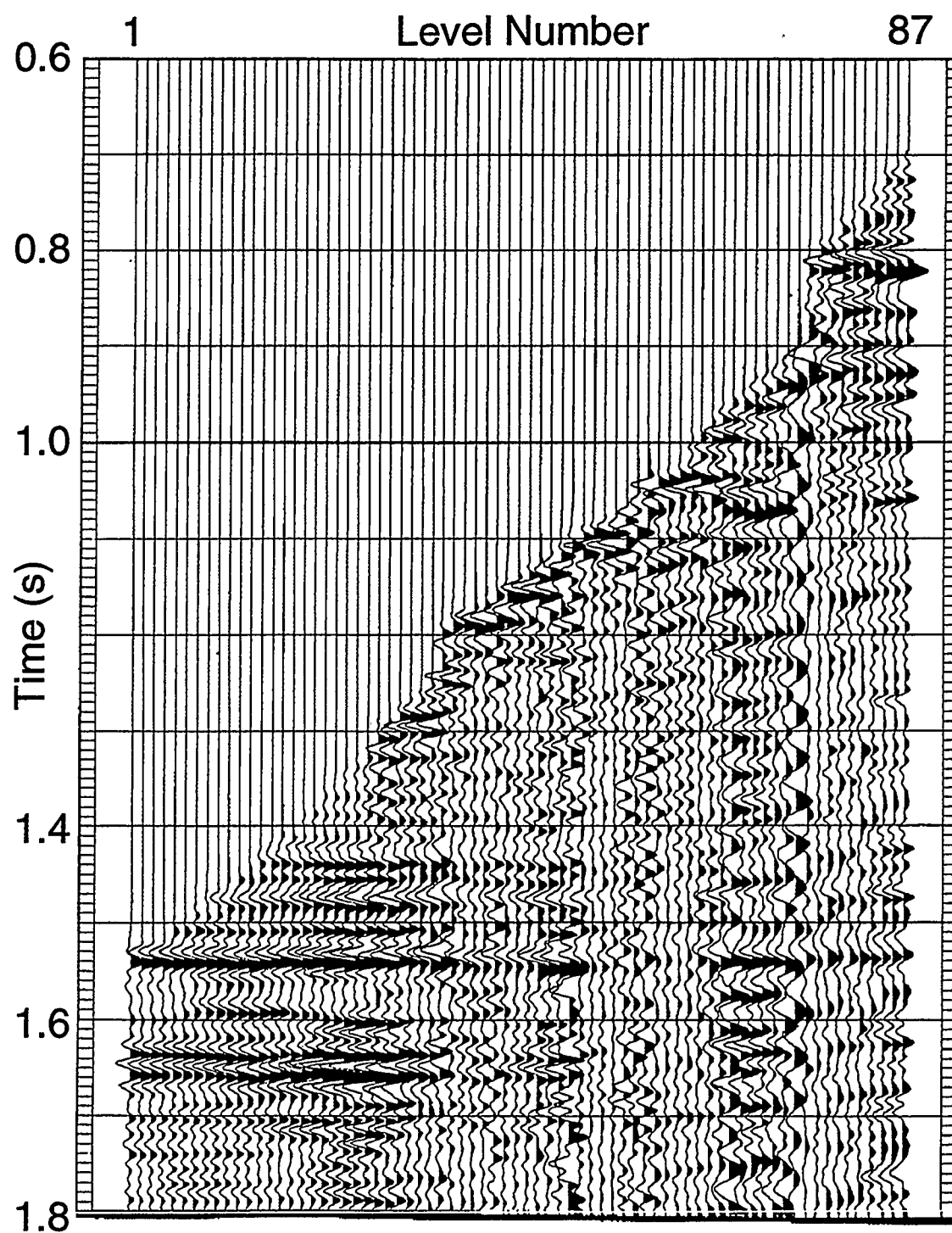


FIG 2.22. Upgoing  $P$  wavefield after waveshaping deconvolution, amplitude recovery, and NMO. The data are plotted file-normalized.

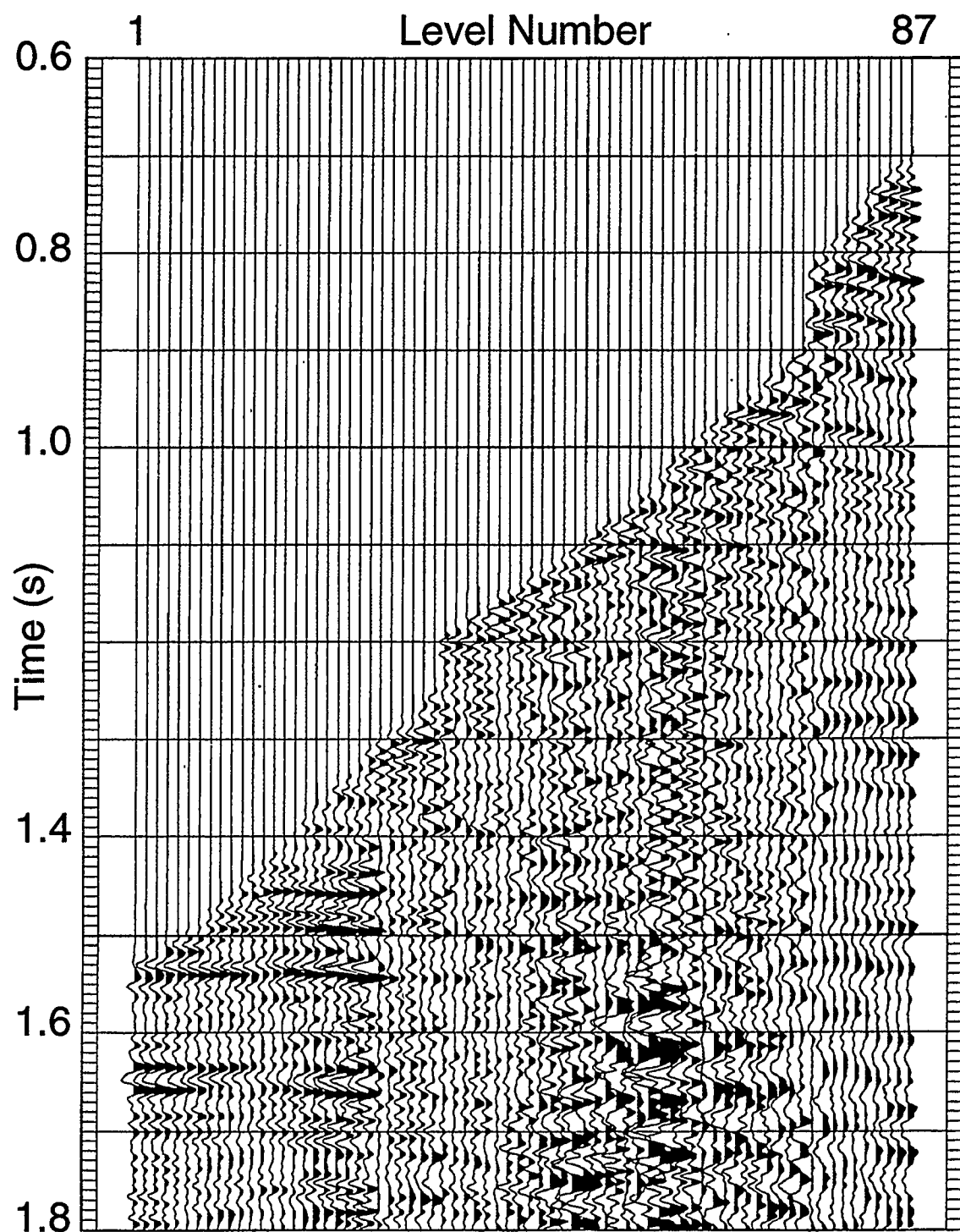


FIG 2.23. Upgoing  $S$  wavefield after waveshaping deconvolution, amplitude recovery, and NMO. The data are plotted file-normalized.

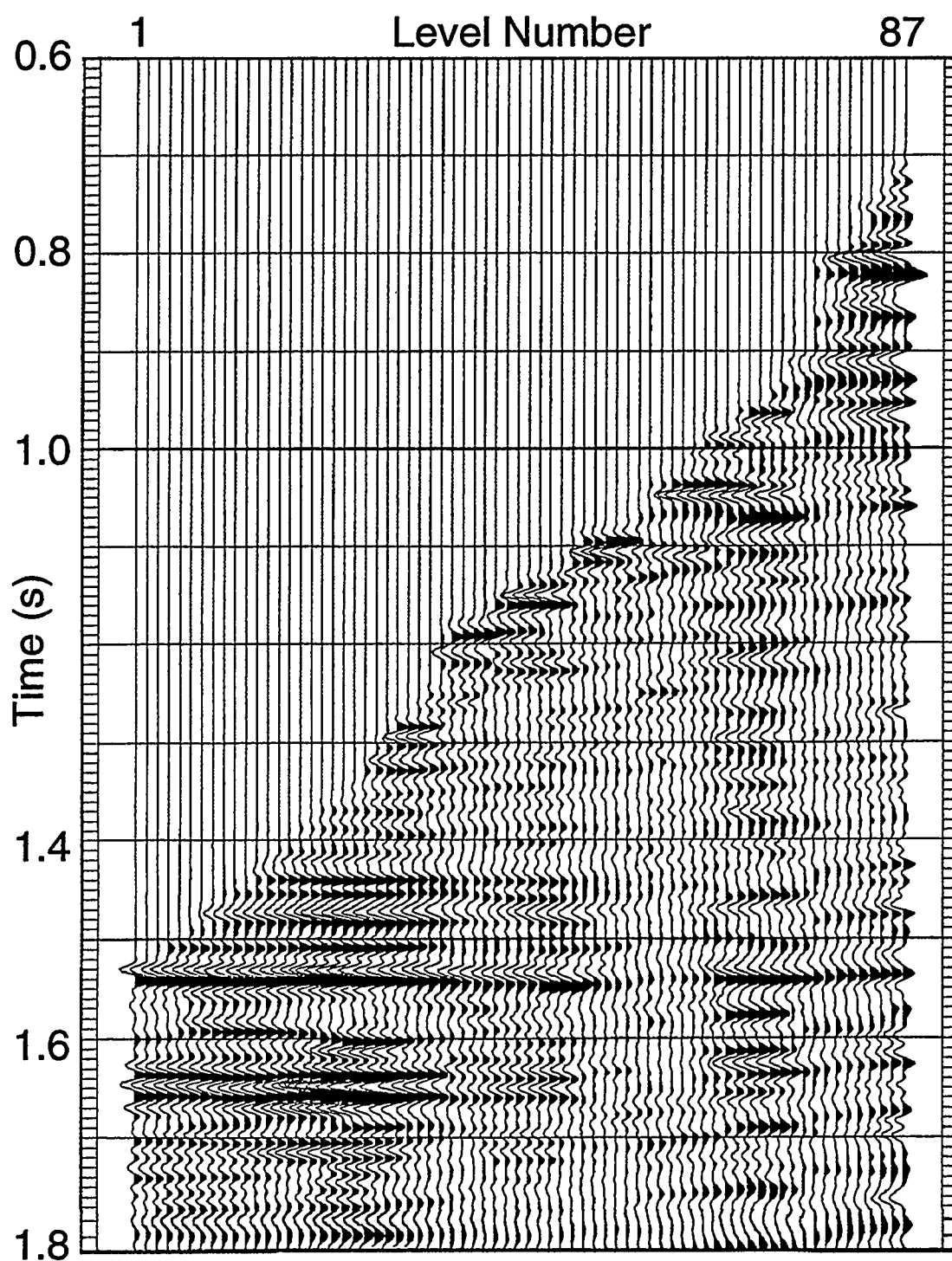


FIG 2.24. NMO-corrected upgoing  $P$  wavefield after a seven-trace median filter was applied. The data are plotted file-normalized.

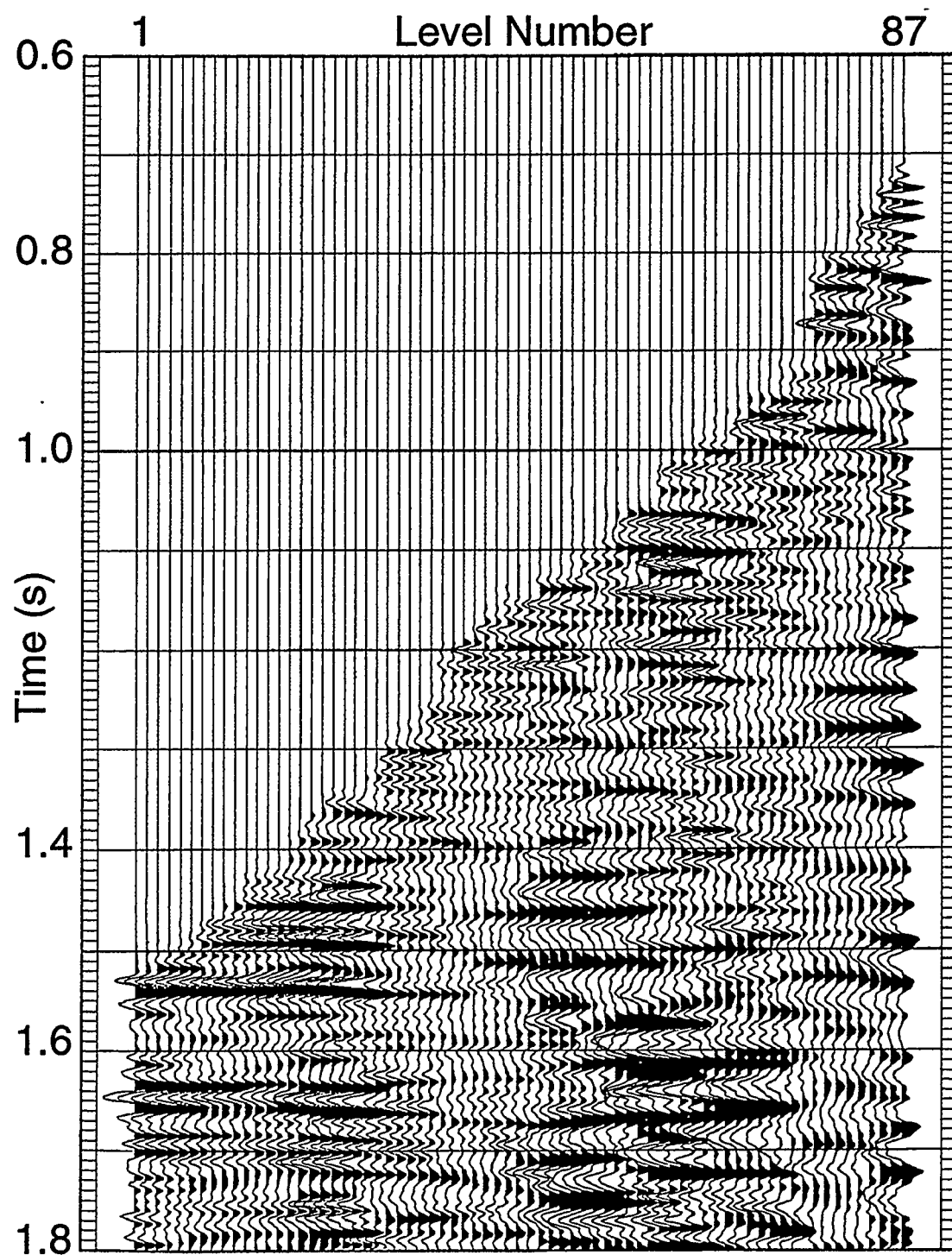


FIG 2.25. NMO-corrected upgoing  $S$  wavefield after a seven-trace median filter was applied. The data are plotted file-normalized.

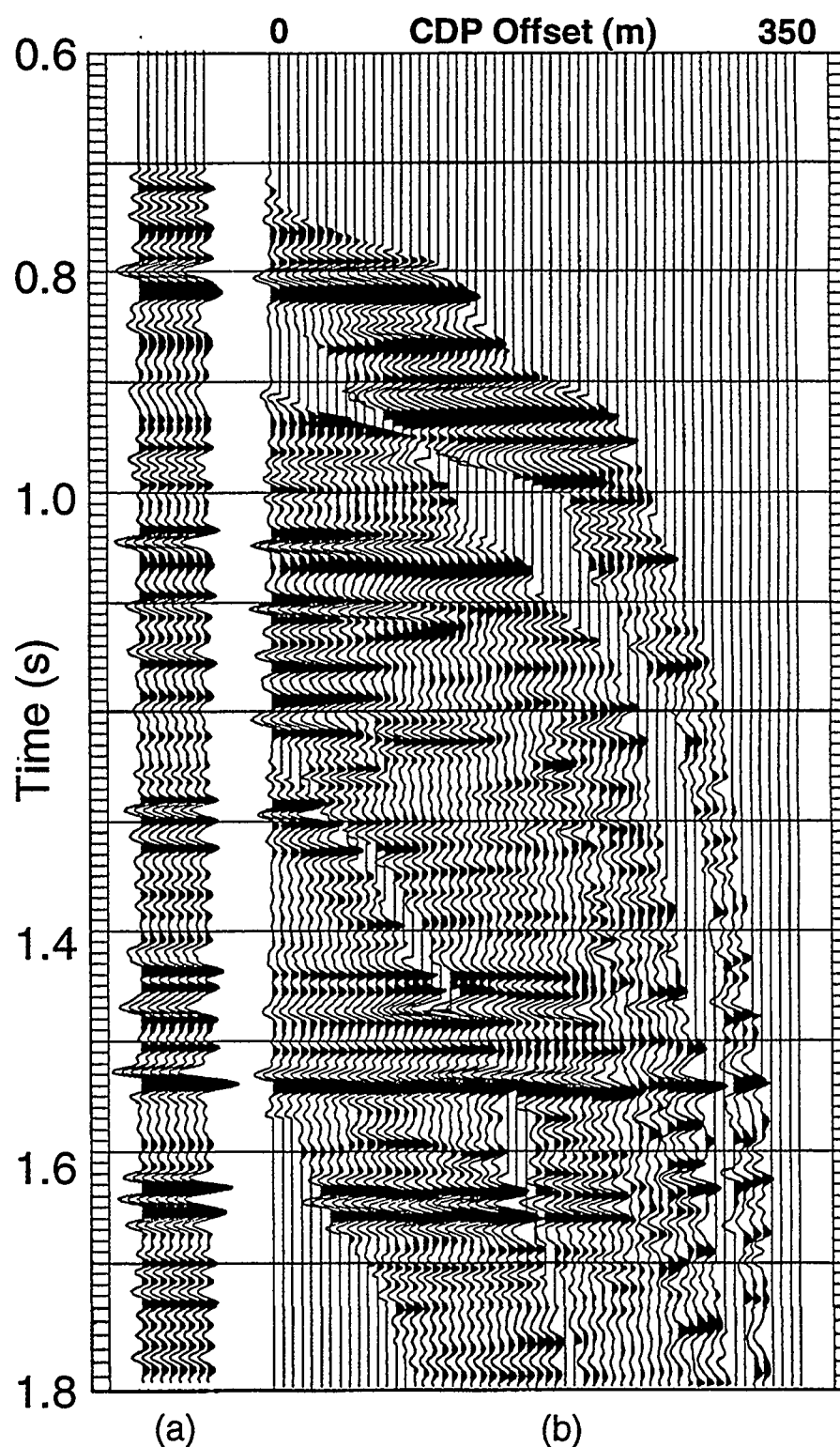


FIG 2.26. (a) 100 ms corridor stack of upgoing *P* wavefield plotted 8 times. (b) VSPCDP map of upgoing *P* wavefield. The data are plotted file normalized, and the trace spacing is 6.25 m.



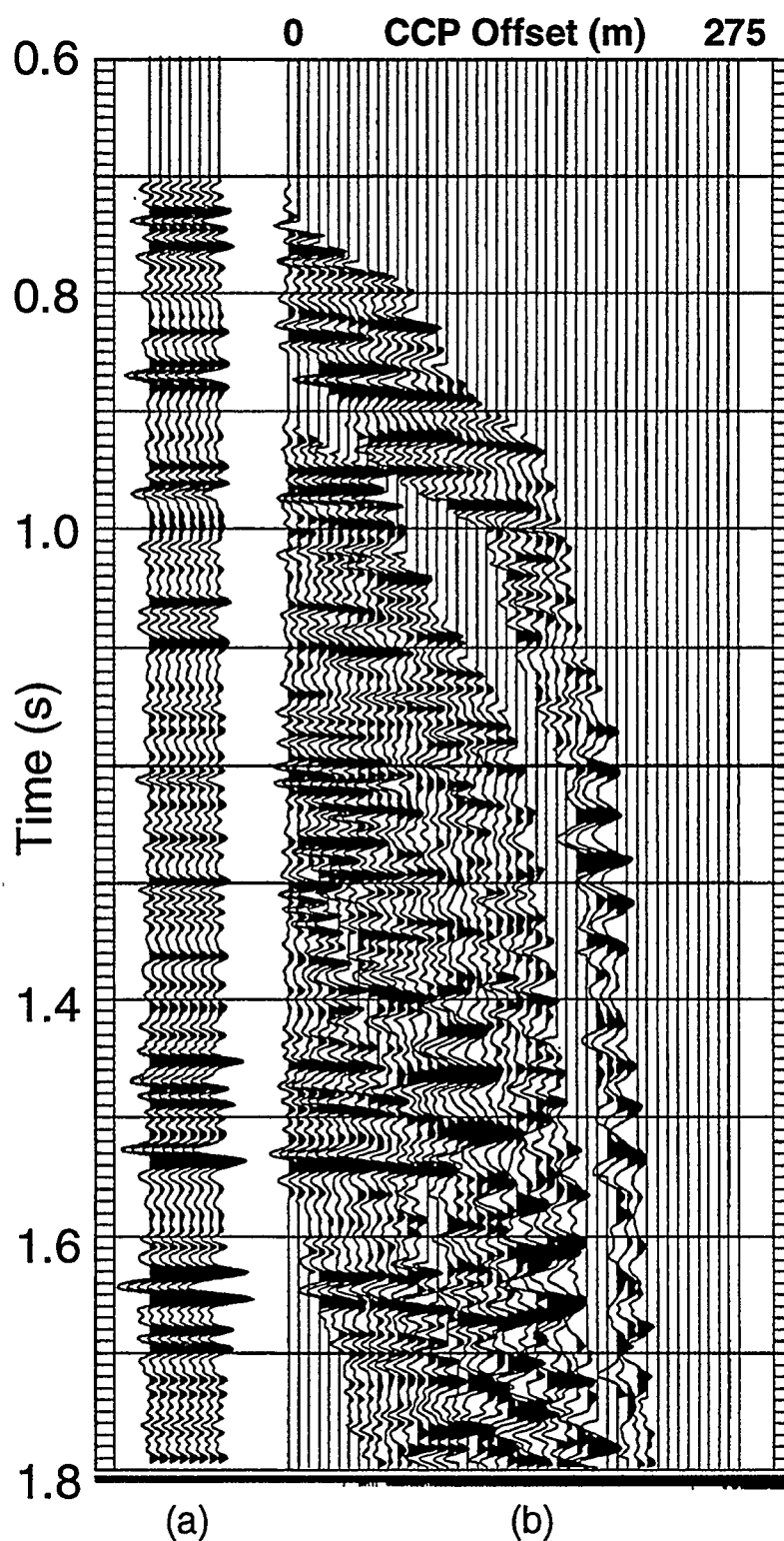


FIG 2.27. (a) 100 ms corridor stack of upgoing  $S$  wavefield plotted 8 times. (b) VSPCCP map of upgoing  $S$  wavefield. The data are plotted file normalized, and the trace spacing is 6.25 m.

### 2.3.3 Multioffset VSP Processing - Synthetic Data

A three-component processing flow has been developed to process the multioffset VSP data for AVO analysis. It is necessary to test this flow on synthetic data to insure that no relative amplitude changes are introduced between the upgoing and downgoing wavefields. Wavefield separation and waveshaping deconvolution are two important processes that must be tested. A brief overview of the processing flow will be given for the synthetic VSP data with a more detailed description following for the multioffset VSP field data.

The synthetic data were generated from the velocity model shown in Figure 2.28. The model is that of a gas-saturated sandstone encased in shale. The top of the sand is at 850 m and the base of the sand is at 1000 m. 11 geophone levels were modeled between depths of 745 m and 845 m for source offset positions of 50 m, 200 m, 400 m, and 600 m. The data were generated by ray tracing and convolution with a 35-Hz zero-phase Ricker wavelet. The synthetic data for the 400 m offset are shown in Figure 2.29. Several events are labeled on this diagram; the  $P$ - and  $S$ -wave direct arrivals (labeled  $P$  and  $S$ ),  $P$ - $P$  reflections (labeled  $P$ - $P$ ), and a  $P$ - $SV$  reflection (labeled  $P$ - $SV$ ). These data were used to test the amplitude recovery of the wavefield separation and waveshaping deconvolution processes.

The first step in processing the synthetic multioffset VSP data is wavefield separation. The wavefield separation algorithm used for processing the 750 m offset VSP data is also used for the multioffset VSP data. Wavefield separation is applied to the vertical and radial channels of each offset position individually. The results of wavefield separation of the 400 m offset are shown in Figure 2.30. These data are separated into the four modes of wave propagation; the downgoing  $P$  and  $S$  wavefields, and the upgoing  $P$  and  $S$  wavefields. The separation has worked well with the minor exception of some

noise introduced in the upgoing  $S$  wavefield. This noise only occurs in the wavefield separation for the 400 m offset VSP, and the cause is not understood.

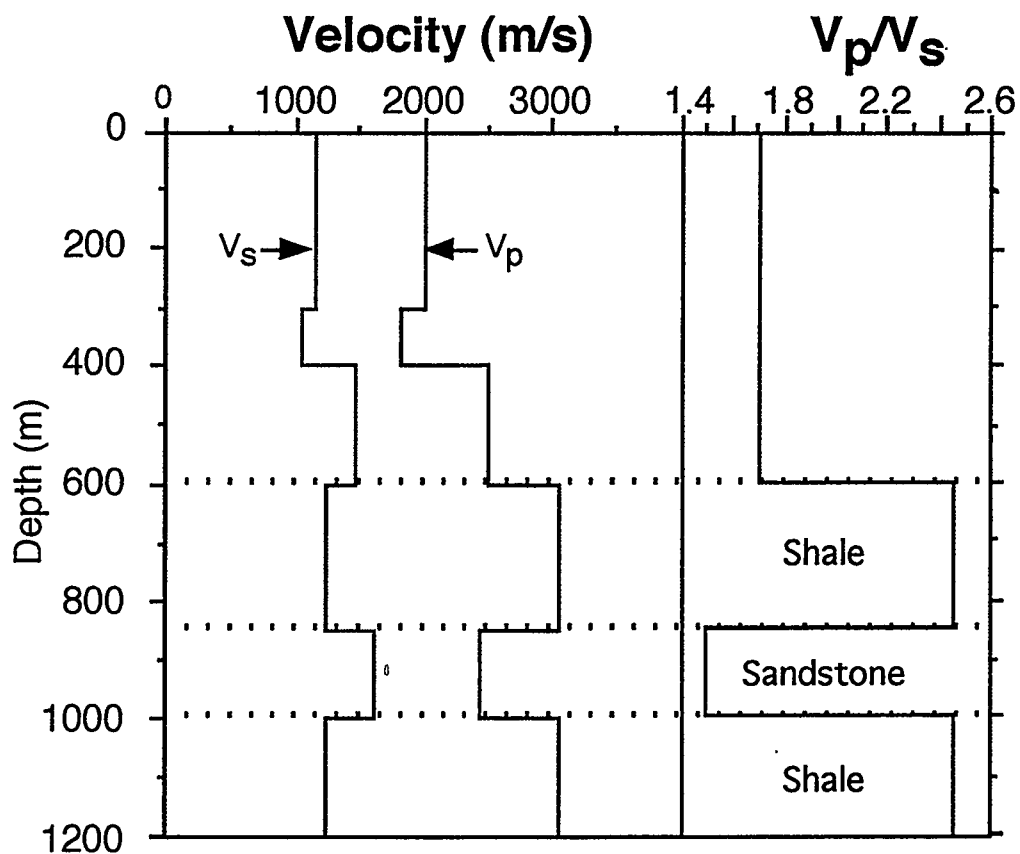


FIG 2.28. Velocity model used to generate the synthetic test data. The zone of interest between 850 m and 1000 m, and the velocities, are consistent with a gas-saturated sand encased in shale.

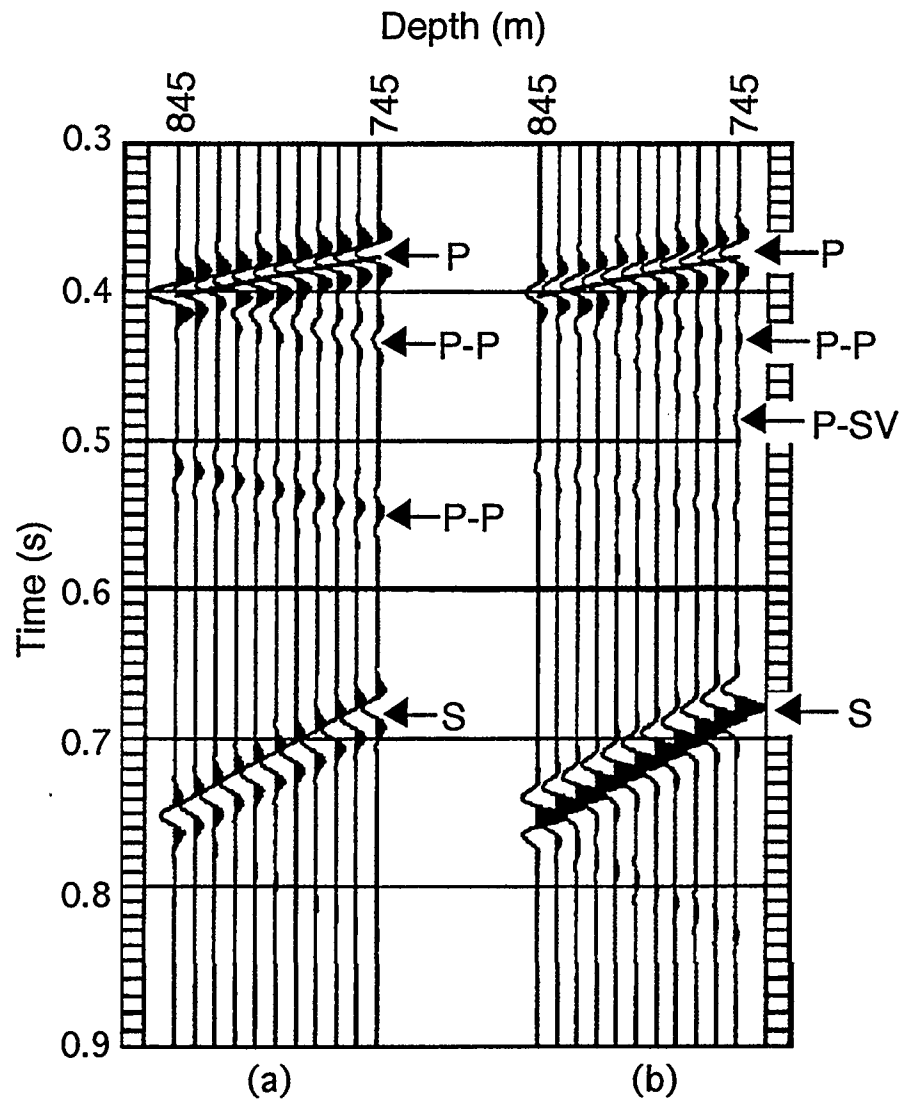


FIG 2.29. Raw synthetic data from the 400 m offset generated with a 35 Hz zero-phase wavelet; (a) vertical channel and (b) radial channel.

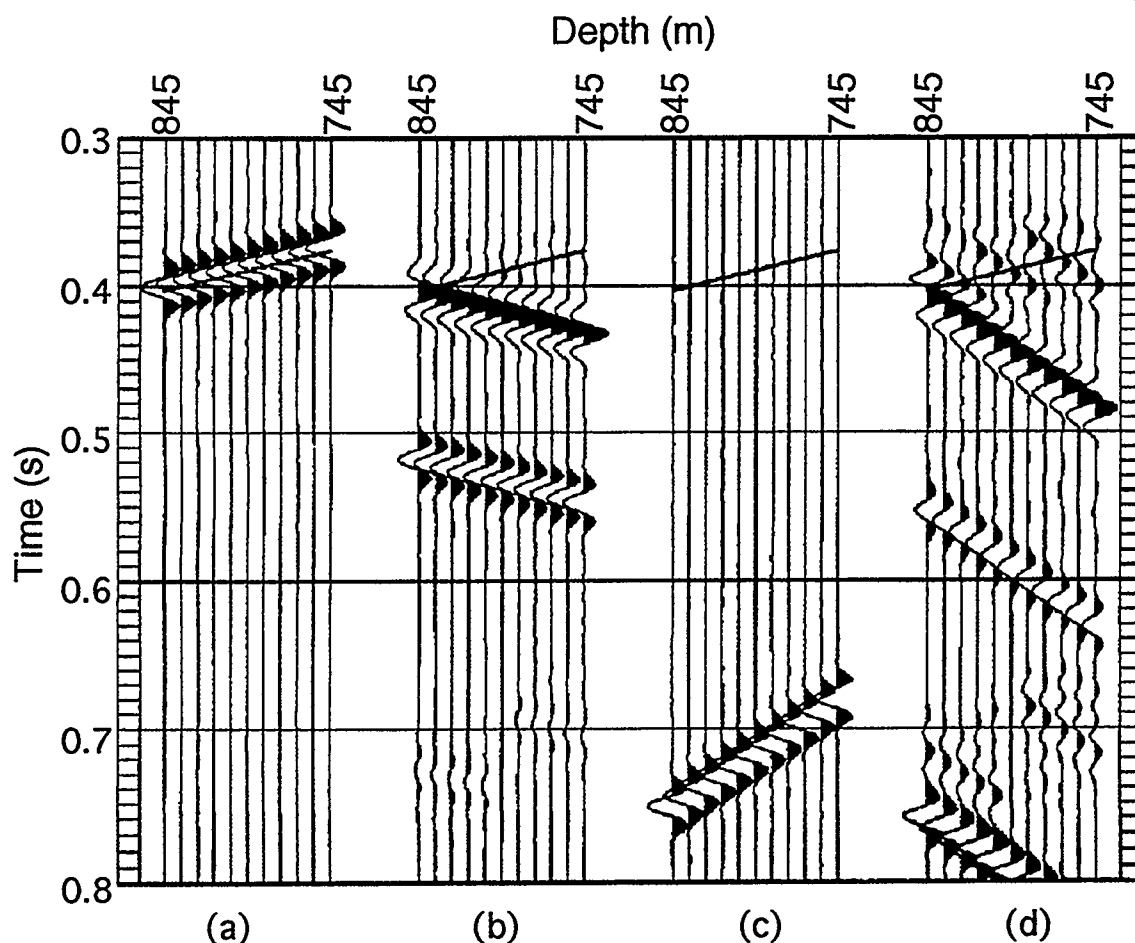


FIG. 2.30. The results of wavefield separation for the 400 m offset; (a) downgoing  $P$  wavefield, (b) upgoing  $P$  wavefield, (c) downgoing  $S$  wavefield, (d) upgoing  $S$  wavefield.

The other important process is waveshaping deconvolution. The downgoing  $P$  wavefield is trace equalized along the first breaks prior to waveshaping deconvolution to insure that the same amplitude operator is applied to each upgoing trace. As mentioned previously, the operator is calculated for each depth level of the downgoing  $P$  wavefield, and the operator is applied to both the upgoing  $P$  and  $S$  wavefields. After waveshaping deconvolution the upgoing  $P$  and  $S$  wavefields are flattened on an event. The flattened upgoing wavefields are shown in Figure 2.31, as shown in Figure 2.31 is the flattened waveshaping-deconvolved downgoing  $P$  wavefield.

The final steps in this processing flow are to stack the upgoing wavefields from each offset of the multioffset VSP data, gather the data into  $P$ - $P$ -reflectivity and  $P$ - $SV$ -reflectivity traces, and then correct the data for NMO. The NMO-corrected data are shown in Figure 2.32. These data show the true seismic AVO response of the model in Figure 2.28.

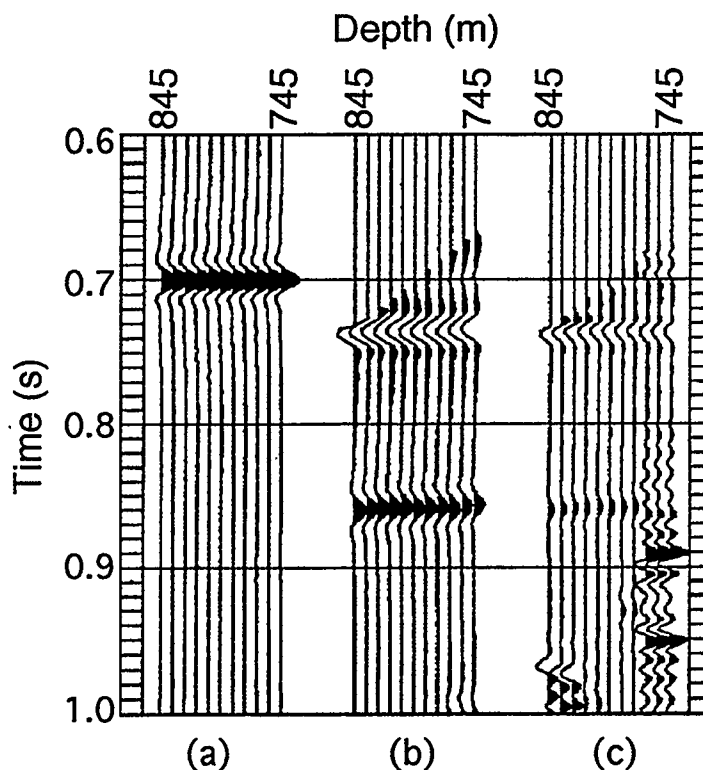


FIG. 2.31. Waveshaping deconvolved (a) downgoing  $P$  wavefield, and upgoing (b)  $P$ - $P$  and (c)  $P$ - $SV$  wavefields after waveshaping deconvolution and flattening.

The processing flow is tested for true amplitude recovery by comparing the picked amplitude from the top of the sand reflection with the theoretical Zoeppritz equation solution for the interface (Figure 2.33). There is reasonable agreement between the processed data amplitudes and the theoretical amplitudes showing that the processing flow extracts amplitudes accurately from multioffset VSP data.

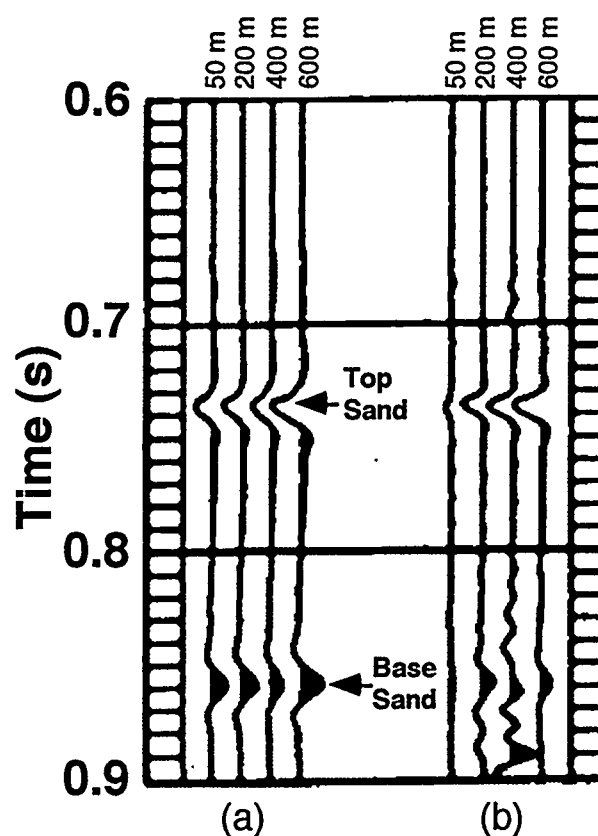


FIG 2.32. Final processed synthetic  $P$ - $P$  (a) and  $P$ - $SV$  (b) reflectivity gathers generated from the velocity model shown in Figure 2.28.

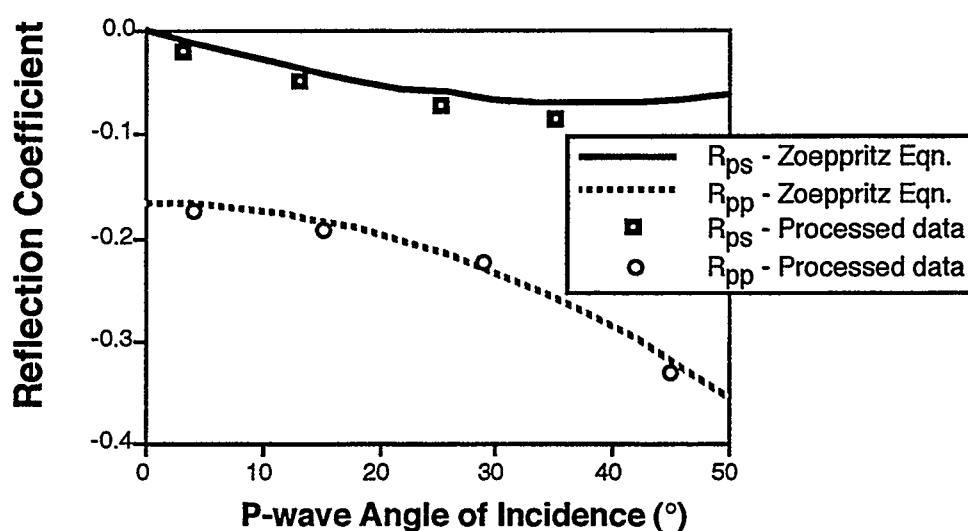


FIG 2.33. Picked amplitudes from the top of the gas-sand event, and the corresponding Zoeppritz-equation solution for the interface.

### 2.3.4 Multioffset VSP Processing - Field Data

The plan view of the well A VSP survey (Figure 2.3) shows that there are 10 source positions used for the multioffset VSP. The appropriate depth levels from the zero-offset VSP and the 750-m-offset VSP have been extracted and are included in the multioffset VSP survey.

The three-component processing flow for the multioffset VSP survey is unique in that each of the ten VSP surveys making up the multioffset VSP survey are processed individually through the wavefield separation and waveshaping deconvolution steps, and then each VSP is stacked and gathered into pseudo- $P$ - $P$  and  $P$ - $SV$  common-receiver gathers. NMO correction is then applied to the common-receiver gathers as the final stage of processing.

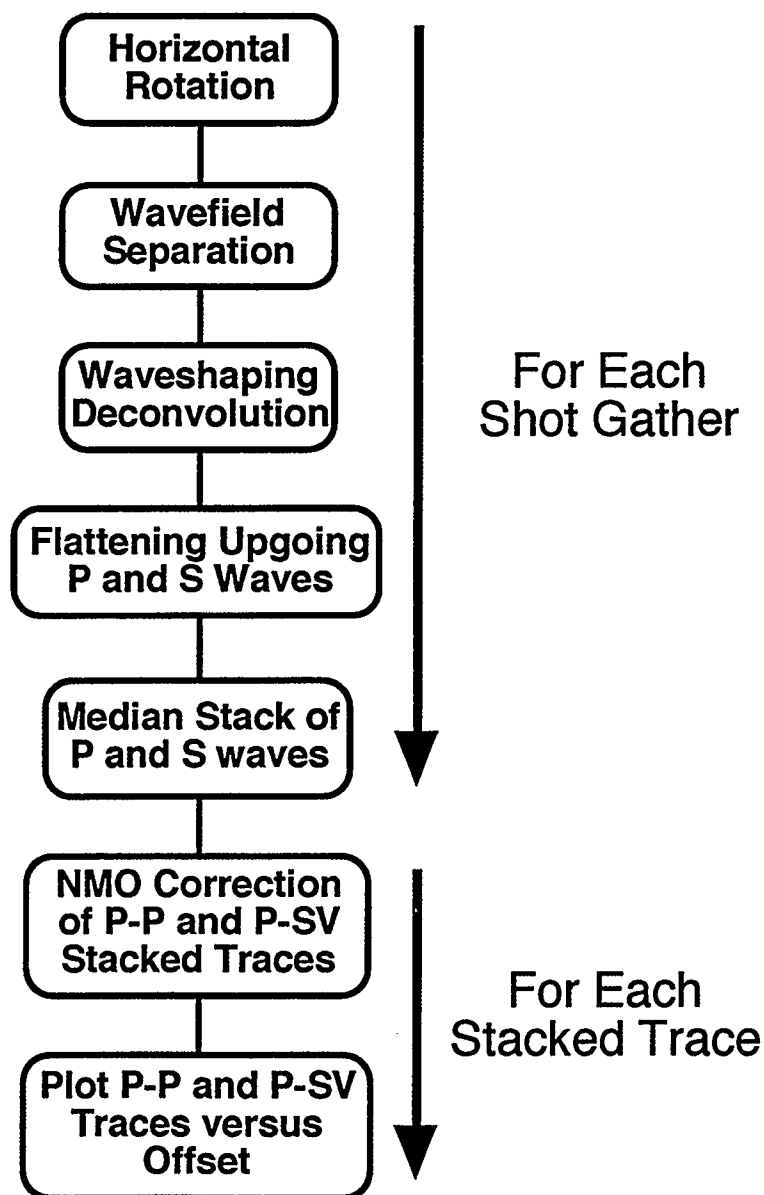


FIG. 2.34. Multioffset VSP three-component processing flow.



The results of processing the 2000 m offset of the multioffset VSP will be presented to illustrate the processing flow. The results of the synthetic data study suggest that multioffset VSP data acquired using the geometry shown in Figures 1.2 and 2.3 can be processed for true amplitudes using the proposed processing flow shown in Figure 2.34. The first step in processing the multioffset VSP field data is to rotate the horizontal channels into the radial and transverse directions. The radial and vertical channels of the 2000 m offset are shown

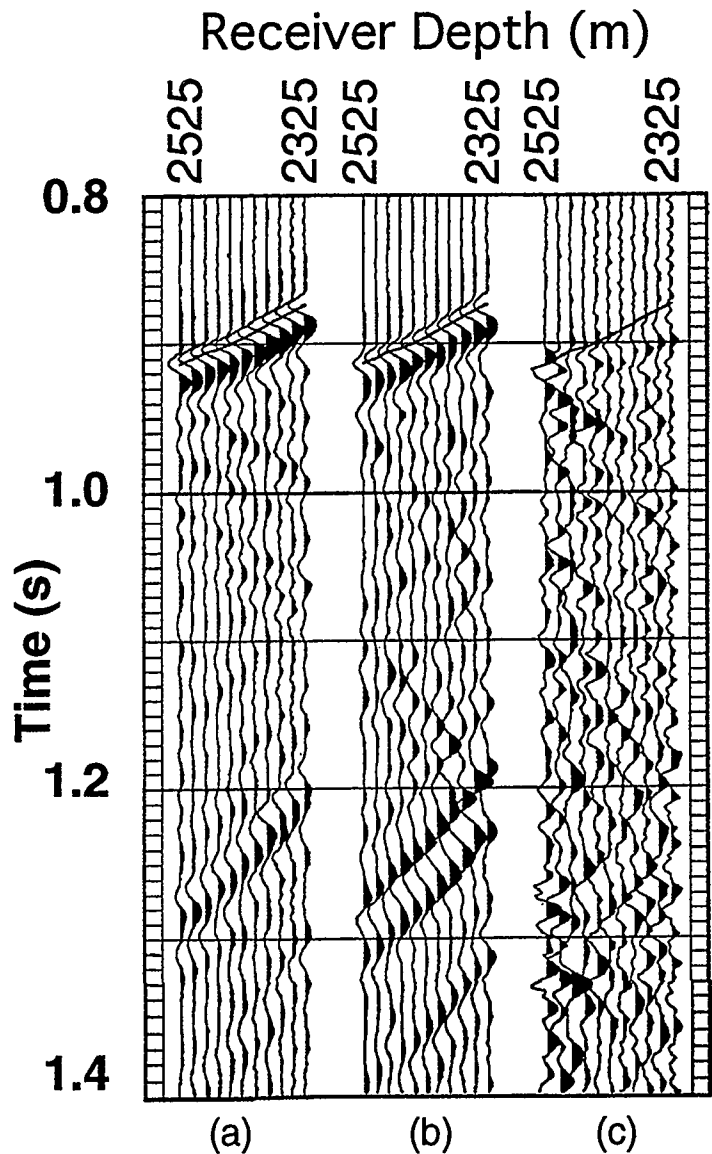


FIG. 2.35. (a) Raw vertical, (b) radial, and (c) transverse channels of 2000 m offset VSP.

in Figure 2.35. The *P*-wave

direct arrival is a strong event on both channels and there are relatively strong downgoing mode-converted *P-SV* waves (between 1.20 and 1.30 s) on the radial channel.

Following the horizontal rotations, the vertical and radial channels are separated into the four propagation modes using the parametric inversion technique used for the 750-m-offset VSP. The wavefield separation of the 2000 m offset is shown in Figure

2.36 as an example. The data are separated into the four propagation modes of which the downgoing  $P$  wavefield and the upgoing  $P$  and  $S$  wavefields are used in further processing.

After wavefield separation, the downgoing  $P$  wavefield, upgoing  $P$  wavefield, and upgoing  $S$  wavefield are trace equalized using a window along the downgoing  $P$  wavefield to determine the equalization factor. This step corrects for propagation losses along the downgoing travel path, and equalizes the downgoing  $P$  wavefield so the deconvolution operator designed from the downgoing  $P$  wavefield does not introduce any relative amplitude changes between the upgoing and downgoing wavefields.

After trace equalization the upgoing  $P$  and  $S$  wavefields are deconvolved using the operator designed from the downgoing  $P$  wavefield. The downgoing  $P$  wavefield contains reverberations that are reflected in the upgoing wavefields. The deconvolution operator eliminates these reverberations and shapes the seismic wavelet to zero phase. The downgoing  $P$  wavefield and upgoing  $P$  and  $S$  wavefields after waveshaping deconvolution of the 2000 m offset are shown in Figure 2.37. These data are now near zero phase and largely multiple free.

The next step in processing these data is to divide the upgoing  $P$  and  $S$  wavefield amplitudes by the peak amplitude of the downgoing  $P$  wavefield. This process results in true-amplitude reflection data as illustrated in Figure 1.2. The receivers are all immediately above the zone of interest, so the only major difference between the upgoing and downgoing wavefields is that the upgoing wavefields are reflected. Note in Figure 2.37(d) that the  $P$ - $SV$  reflection event that intersects the  $P$ -wave first-break curve at the bottom geophone level takes approximately 0.080 s to travel up to the top geophone level. If this event were corrected for spherical spreading and transmission losses using the  $n$  value of 1.70 that was applied to the zero-offset and offset VSPs, the  $T^n$  scaling difference between the top and bottom levels would be 1.4%. Furthermore, the correction

for the  $P$ - $P$  reflections would be even smaller as they take less time to travel up the borehole. This suggests that there is only a minor gain correction required over the small window of receivers used for the multioffset VSP geometry, and therefore a gain correction will not be applied to these multioffset VSP data. Thus, the bandlimited reflection coefficient can be determined by taking the ratio of the upgoing and downgoing wavefield amplitudes.

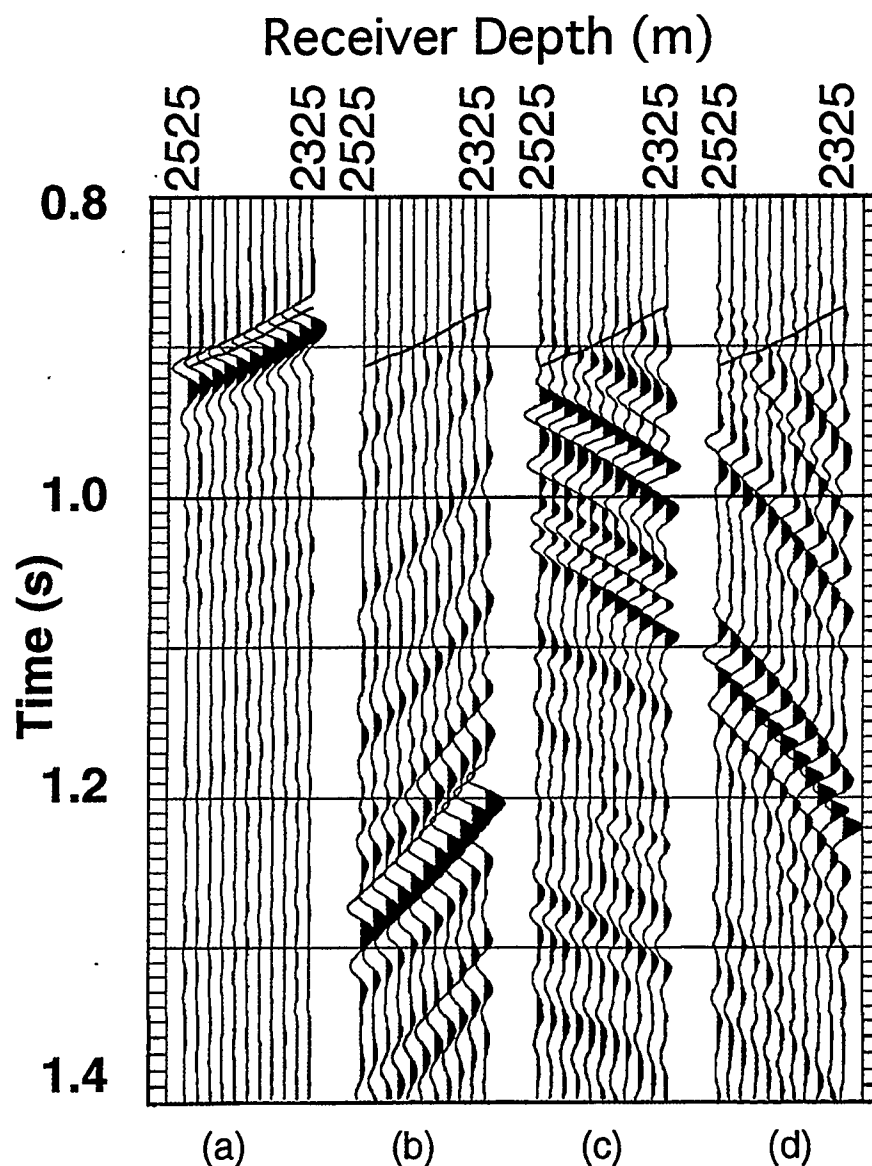


FIG. 2.36. Output of wavefield separation; (a) downgoing  $P$  wavefield, (b) downgoing  $S$  wavefield, (c) upgoing  $P$  wavefield, and (d) upgoing  $S$  wavefield.

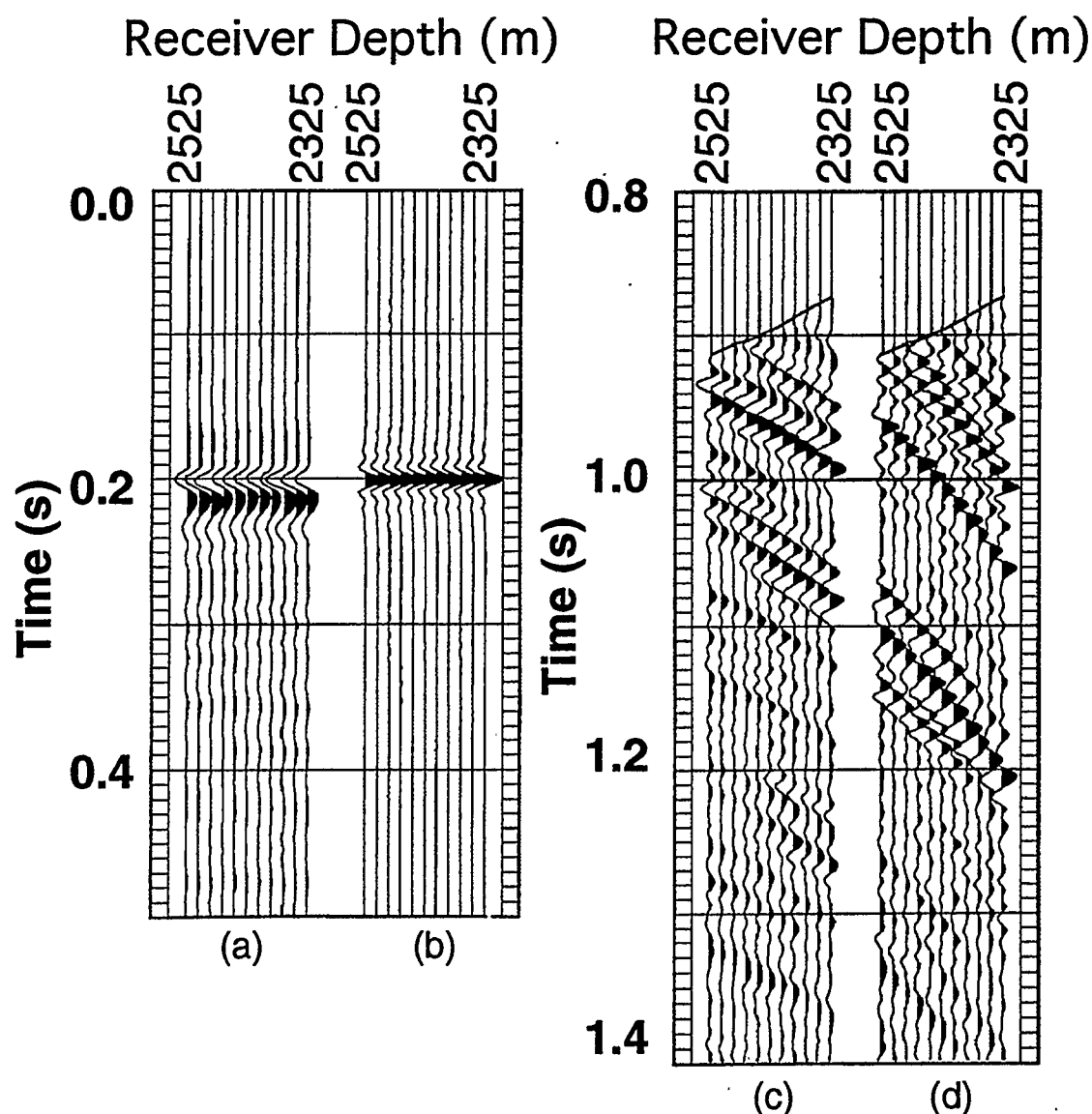


FIG. 2.37. (a) The downgoing  $P$  wavefield before waveshaping deconvolution, (b) the downgoing  $P$  wavefield after waveshaping deconvolution, and the upgoing  $P$  (c) and  $S$  (d) wavefields after waveshaping deconvolution.

The final steps in the processing flow are stacking the receiver traces together for each source position, gathering the stacked traces into common-receiver  $P$ - $P$  and  $P$ - $SV$  gathers, and correcting the data for NMO. In order to stack the receiver traces together, the events must be aligned. An event was picked on the upgoing  $P$  wavefield, for each of the source positions, and then the reflection events are aligned using this event (Figure 2.38a). The upgoing  $S$  wavefield was flattened in a similar manner (Figure 2.38b). Note

that the events over the window of receivers in Figure 2.38 are aligned so these traces can be stacked constructively.

After the events are aligned, each of the upgoing wavefields are median stacked, resulting in one  $P$ - $P$  reflectivity trace and one  $P$ - $SV$  reflectivity trace for each source position of the multioffset VSP survey. These traces are gathered into a pseudo-common-receiver  $P$ - $P$  and  $P$ - $SV$  reflectivity gathers (Figure 2.39). An interesting effect that is shown very clearly in the flattened  $P$ - $P$  gather is the change in tuning from the near to far offset. Note that the trough at 670 ms slopes down towards the trough at 700 ms. This is a very important effect when considering AVO, as it shows how much the offset traces must be stretched to correct the data for NMO. The change in tuning from the near to far offsets is discussed in previous work by Ostrander (1984), and Swan (1991).

The net result is a loss of information from the near to far-offset traces due to a decrease in the time thickness between each bed.

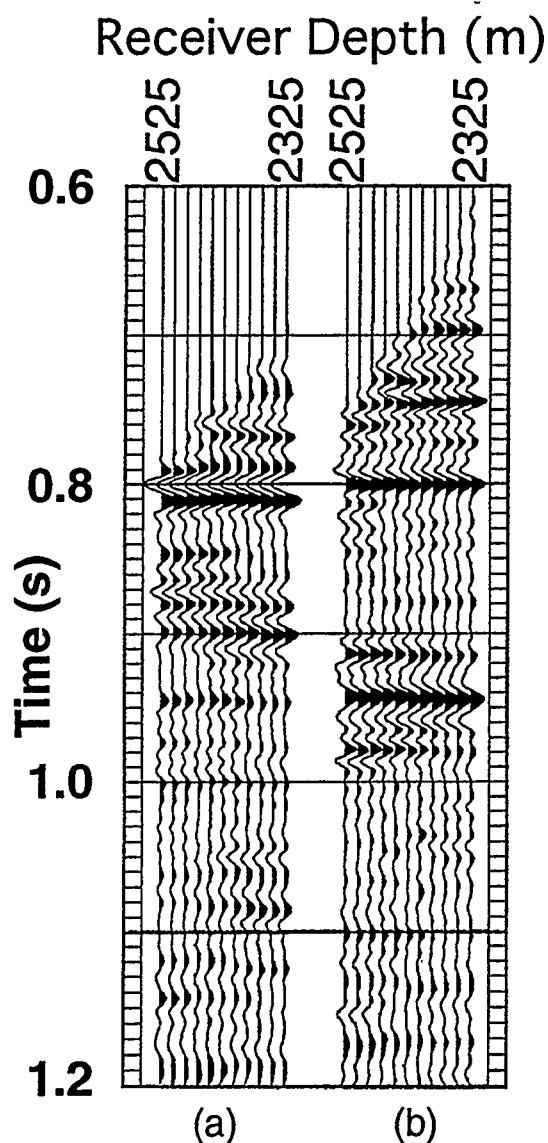


FIG. 2.38. Flattened wavefields; (a) upgoing  $P$  and (b) upgoing  $S$ .

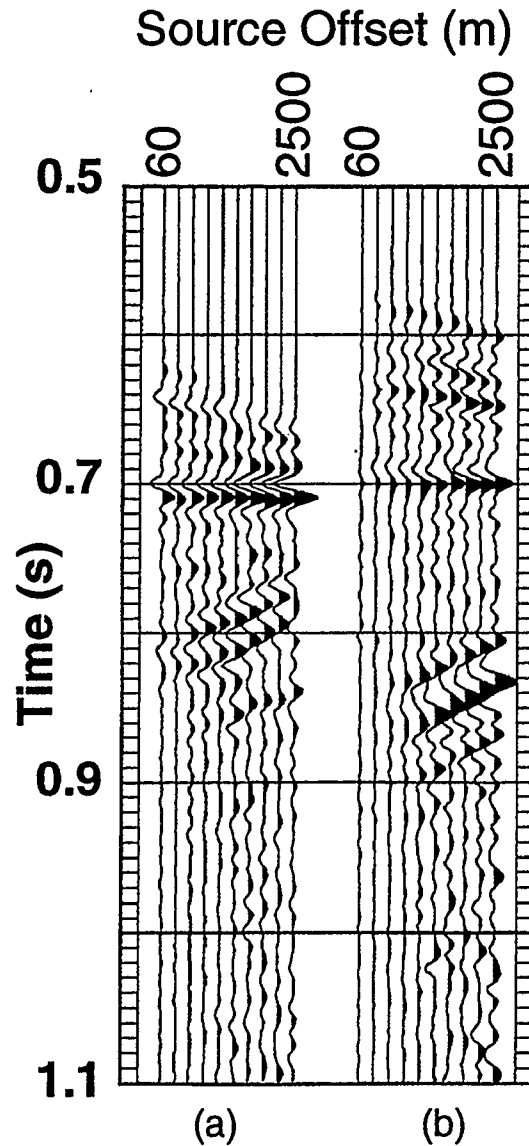


FIG. 2.39. Stacked and gathered reflectivity traces; (a)  $P$ - $P$  and (b)  $P$ - $SV$ .

Before NMO correction, the stacked traces must be returned to the correct traveltimes. The stacked traces shifted back to the correct traveltimes are shown in Figure 2.40. Static corrections are also applied at this stage. These statics are largely a correction for near-surface heterogeneities. The statics are determined by subtracting the observed direct-arrival traveltimes from the ray-traced direct-arrival times, and shifting the traces by the differences. This method assumes horizontal homogeneous layers with the exception of the near surface. These traces are then corrected for NMO using the

algorithm discussed in the offset VSP processing section. The NMO-corrected traces are shown in Figure 2.41. These traces shown the true seismic AVO response for the zone of interest (between 1.50 and 1.55 s).

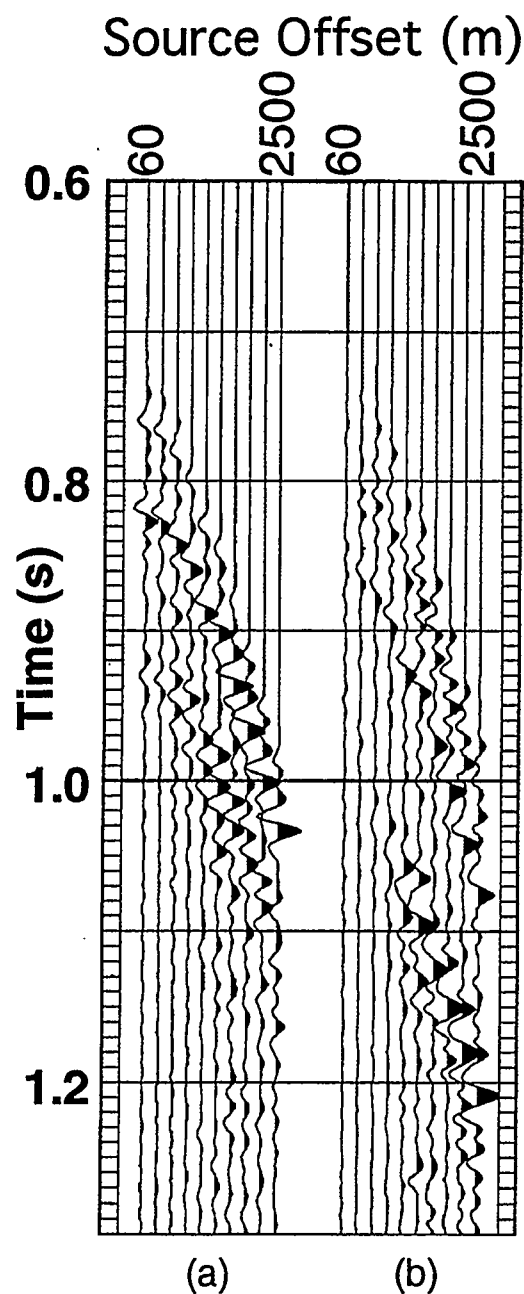


FIG. 2.40. (a)  $P$ - $P$  and (b)  $P$ - $SV$  reflectivities shifted back to the correct traveltimes.

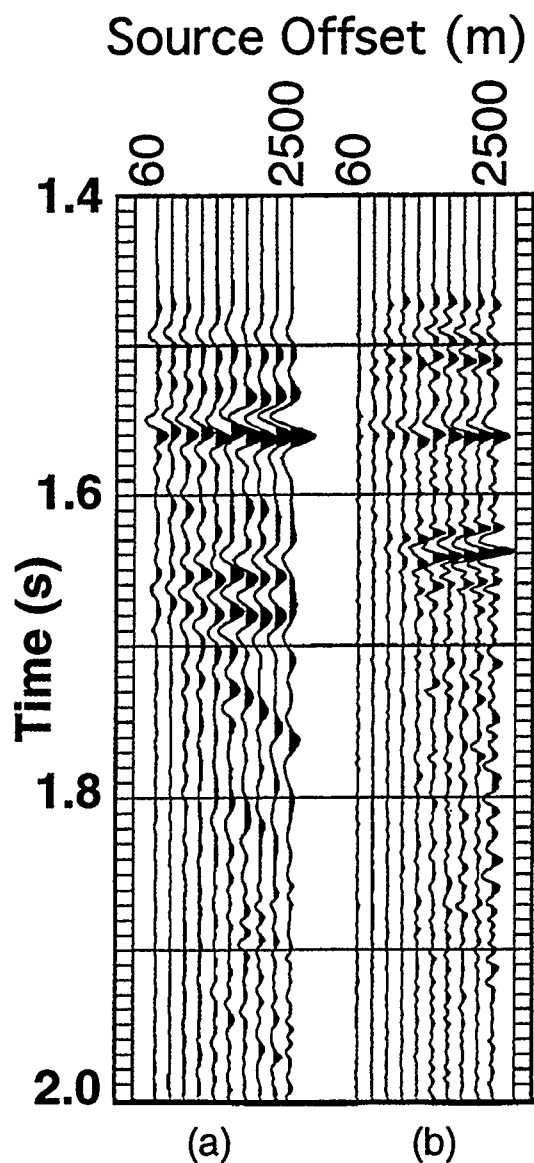


FIG. 2.41. NMO corrected (a)  $P$ - $P$  and (b)  $P$ - $SV$  reflectivity traces.

# Chapter 3

## VSP Interpretation

### 3.1 Introduction

The next step after processing the VSP data is interpretation. In this thesis, the well logs and the VSP data will be interpreted. The log interpretation involves blocking the logs and interpreting the blocked logs for lithology. The VSP interpretation is more complicated. First, the zero-offset VSP is interpreted using the synthetic seismogram generated from the well logs. The goal of this interpretation is to correlate the layers in the zone of interest from the well logs to the zero-offset VSP. Some issues to be addressed are the thin-bed interference effects and the VSP data polarity. Second, the zero-offset VSP is correlated with the offset VSP and the multioffset VSP. The purpose is to establish  $P$ - $P$  and  $P$ - $SV$  reflectivity correlations and to determine the polarity of the  $P$ - $SV$  events. Third, the  $P$ - $P$  and  $P$ - $SV$  AVO responses of the multioffset VSP data are interpreted. The goal of this interpretation is to understand the AVO response of the reservoir zone and to determine how well the forward-model data match the field data. The interpretation of these data is broad in scope. However, the approach is to start with a basic interpretation of the zero-offset VSP and build up to the more complex AVO interpretation of the multioffset VSP.

### 3.2 Well-Log/Zero-Offset VSP Interpretation

To form a basis for the VSP/well-log correlation, it is necessary to interpret the well logs. The well logs are interpreted to help understand the lithology and petrophysical parameters, such as porosity, near the well bore. When comparing well logs with seismic data, it is important to determine the vertical resolution of the two



measurements given the different frequency bandwidths of the data. A rough calculation of the seismic wavelength is made by looking at the waveshaping-deconvolved downgoing *P* wavefield from the zero-offset VSP (Figure 2.8). These deconvolved traces are approximately the VSP wavelet, and the wavelet period is about 20 ms (trough to trough time). A 20 ms period corresponds to a frequency ( $f$ ) of 50 Hz. The zone of interest is a carbonate, and an average velocity ( $v$ ) of carbonate rocks is 5500 m/s. The seismic wavelength ( $\lambda$ ) is calculated to be  $\lambda = v/f = 5500/50 = 110$  m. Seismic resolution can be up to about 1/8th of the wavelength (Widess, 1973), which in this case is 13.75 m. This suggests that any beds thinner than about 13 m will be unresolvable. Sonic logs have a vertical sampling of less than 1 m, and consequently there is a large discrepancy between the vertical resolution of the well log and VSP data.

### 3.2.1 Well A Log Blocking

The goal of this study is to recover the elastic parameters from the VSP AVO response of the reservoir. The first problem in the interpretation is to find a common layering of the Earth that satisfies both the well logs and the VSP data. A common method of addressing this problem is to average (block) the logs into larger depth intervals. The result of log-blocking is a simplified Earth model that retains the coarse information in the well logs, and dismisses the fine information that is unresolvable with seismic data. The simplified Earth model is also desirable as a starting point for the generalized-linear-inversion algorithm that will be introduced later. The main requirement of log blocking is that the blocked logs retain enough information for a good correlation of the synthetic seismogram generated from the blocked logs and VSP data. This implies that the significant seismic events are retained in the blocked logs.

The raw logs used for the VSP interpretation are the full-waveform sonic and bulk-density logs. The full-waveform sonic log measures the compressional- and shear-

wave slowness and the bulk-density log measures the electron density of the rocks which correlates with the bulk density. The raw sonic and density measurements in the zone of interest are shown in Figure 3.1. Notice that these measurements have a very fine sampling interval of less than 1 m. These logs are blocked using a compound median filtering technique (Leaney and Ulrych, 1987). This technique is automatic so there is no bias introduced by the interpreter. The technique uses a series of median filters starting with a filter width of three samples and ending with a filter width of the number of samples corresponding to 1/2 the maximum bed thickness. A maximum bed thickness of 25 m was used to filter the data. A comparison of the logs before and after median filtering is shown in Figure 3.2. The median filtered logs retain the main characteristics of the raw logs, and have little of the fine detail in the raw logs. The logs are now simplified and can be interpreted in terms of the bulk lithologies.

### 3.2.2 Well A Log Interpretation

The zone of interest in Well A is at a depth of about 2530 m. Note in Figure 3.2 that all of the log curves change substantially in this zone. The zone has been tested and is proven to be gas-saturated. The lithology and porosity of the gas zone and the zones above and below the gas zone are important for this interpretation. The blocked-log measurements for the three zones are listed in Table 3.1.

Table 3.1. Average log values in the zone of interest

Zone	<i>P</i> -wave Slowness ( $\mu\text{s/m}$ )	<i>S</i> -wave Slowness ( $\mu\text{s/m}$ )	Bulk Density $\text{kg/m}^3$	$V_p/V_s$ ratio
Upper zone	167	314	2660	1.88
Gas zone	193	337	2550	1.75
Lower zone	166	316	2688	1.90

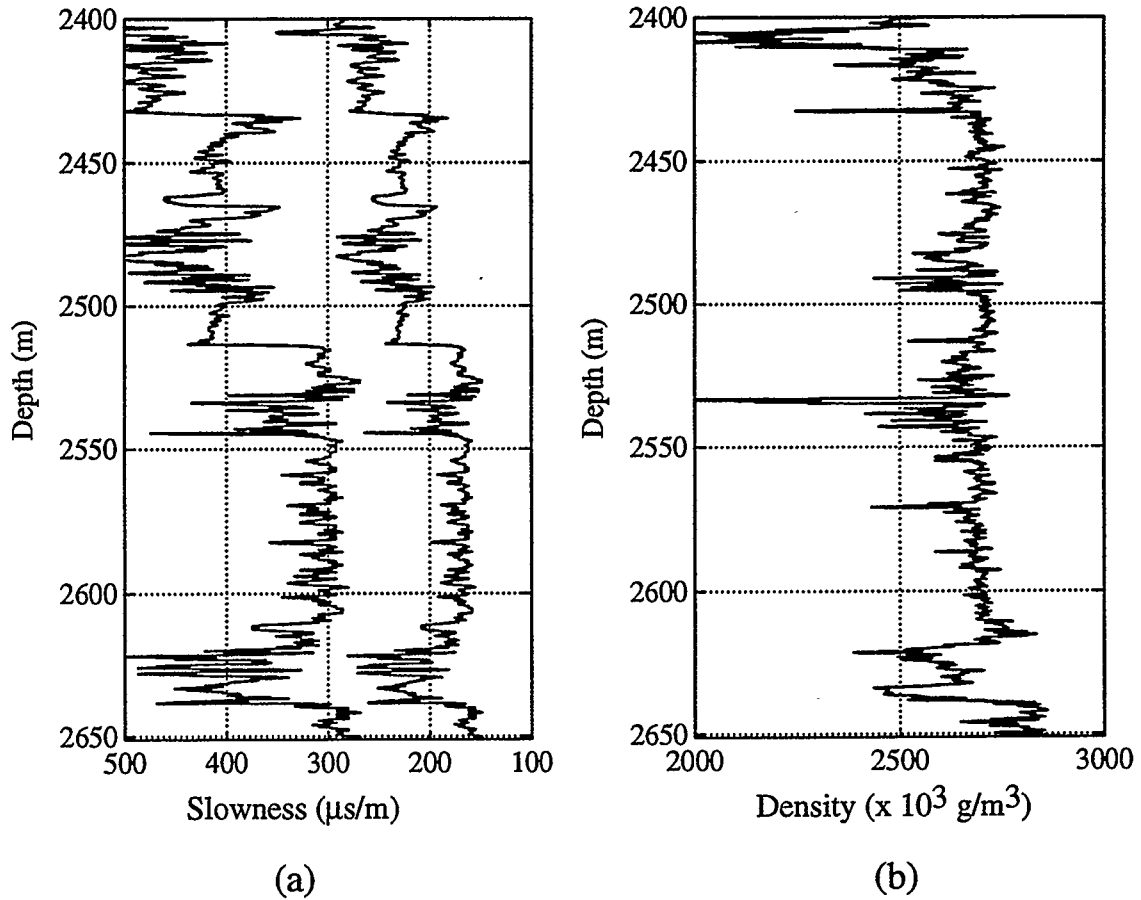


FIG. 3.1. Raw well logs in the zone of interest; (a) full waveform sonic log with compressional wave and shear wave slowness curves, and (b) bulk density log curve.

The measurements shown in Table 3.1 are used to determine the porosity and lithology of these zones by comparing crossplots of the  $P$ -wave transit time and the bulk density with published log-interpretation charts (Schlumberger, 1988). The upper zone crossplots as a limestone with 2.5% porosity, the gas zone crossplots between a limestone with 10% porosity and a dolomite with 17% porosity, and the lower zone cross plots as a limestone with 2% porosity.

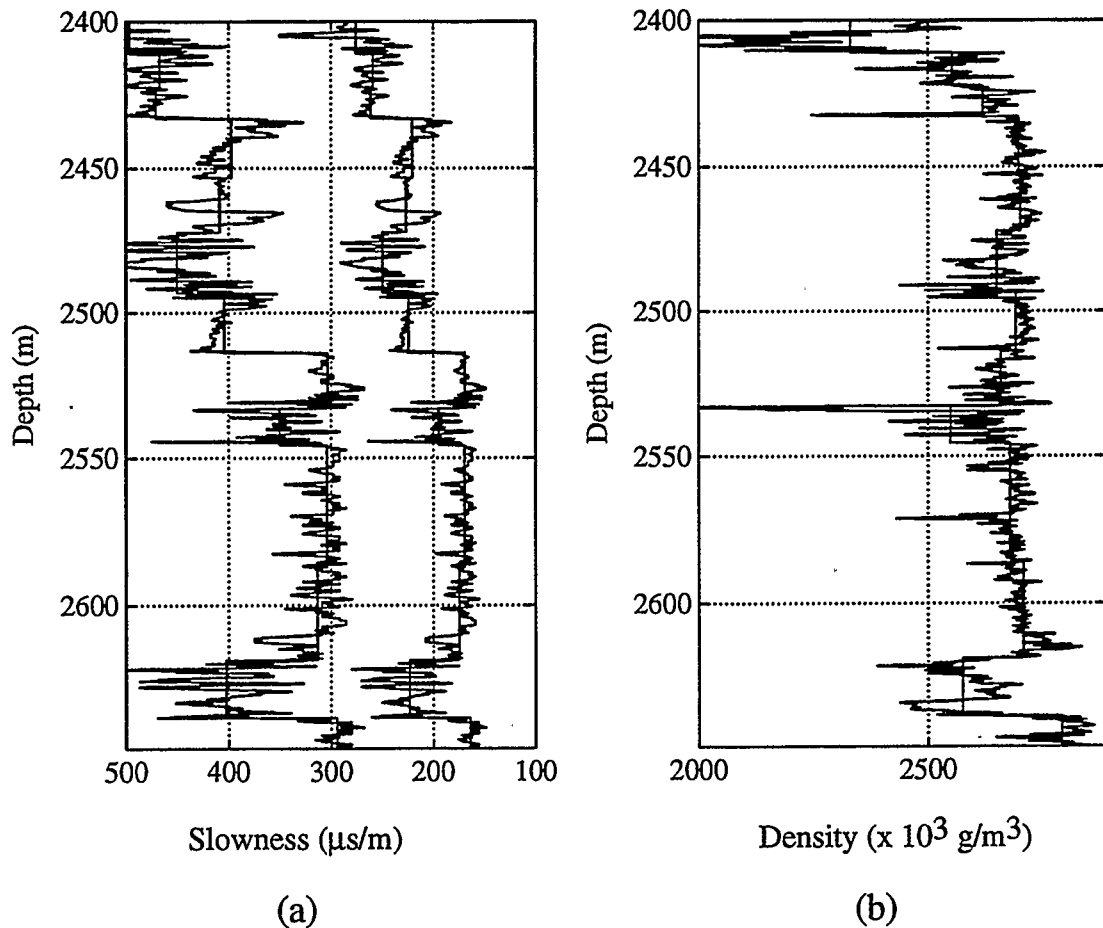


FIG. 3.2. Raw and blocked well logs in the zone of interest; (a) full-waveform sonic log with compressional- and shear-wave slowness curves before and after log blocking, and (b) bulk-density-log curve before and after log blocking.

Figure 3.3 shows the photoelectric cross-section (curve) through the zone of interest. The photoelectric cross-section log is measured using a gamma-ray source and two detectors. Gamma rays emitted from the source are scattered by the formation and lose energy until absorbed through the photoelectric effect. The number of gamma rays in the energy region of Compton scattering and the photoelectric effect are used to determine the photoelectric absorption index. Basically, the photoelectric cross-section index is related to the molecular weight of the minerals in the formation. The photoelectric cross-section log responds primarily to lithology and secondarily to porosity.

and pore fluid (Schlumberger, 1987). Limestone generally has a photoelectric cross-section of about 5 Barns/electron and dolomite generally has a photoelectric cross section of about 3 Barns/electron. The log curve in Figure 3.3 has a sharp decrease in photoelectric cross section at a depth of 2530 m corresponding to the top of the reservoir. The photoelectric cross-section log is approximately 3 Barns/electron in the reservoir zone between 2530 m and 2545 m, suggesting the zone is dolomite. The layers above and below the reservoir zone have values of approximately 5 Barns/electron, suggesting these zones are limestone. Because the photoelectric cross-section log responds primarily to lithology, the reservoir zone is interpreted to be dolomite, and the layers above and below to be limestone. The photoelectric cross-section log can also be crossplotted against bulk density. The upper zone cross plots as a limestone with 2 % porosity, the reservoir zone crossplots as a dolomite with 17% porosity, and the lower zone crossplots as a limestone with 1% porosity.

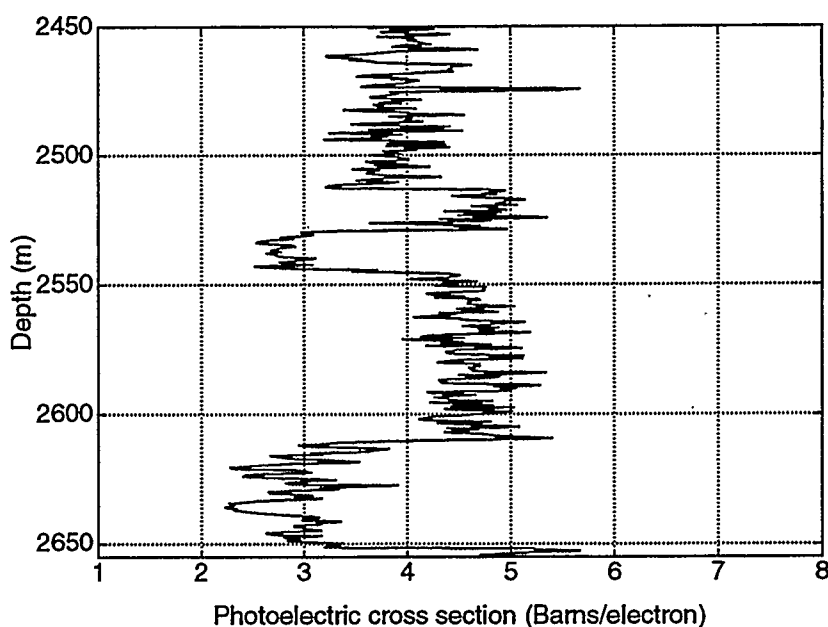


FIG. 3.3. Photoelectric cross-section log through zone of interest.

Once the lithology is established, the bulk-density log can be used alone to calculate the porosity. Assuming the bulk-density tool measures mainly the response of the invaded zone, the porosity can be calculated using a porosity-weighted average equation (Schlumberger, 1987)

$$\phi = \frac{\rho_{ma} - \rho_b}{\rho_{ma} - \rho_f} \times 100\%, \quad 3.1$$

where  $\rho_{ma}$  is the matrix density,  $\rho_b$  is the measured bulk density, and  $\rho_f$  is fluid density. The fluid density (from the well log-header) is 1.1 g/cm<sup>3</sup>, the matrix density for dolomite is 2.870 g/cm<sup>3</sup>, and the matrix density is 2.710 g/cm<sup>3</sup> for limestone. Inputting the bulk densities in Table 3.1 into equation 3.1 results in porosities of 3% for the upper zone, 18% for the gas-zone, and 1% for the lower zone.

Several methods have been used to determine the lithology and porosity of the reservoir zone. There are uncertainties in some of the log measurements due to the presence of gas in the reservoir. However, the photoelectric cross-section log discriminates very well between dolomite and limestone and thus the reservoir is clearly indicated to be a dolomite encased in limestone. The limestone units have very low porosities, and the reservoir dolomite has a porosity possibly as high as 18%.

The next stage of the interpretation is to compare the measured sonic velocities with the VSP velocities. The VSP velocities are determined using a traveltimes inversion algorithm similar to that of Stewart (1984). The first-break traveltimes from the zero-offset VSP were used to invert for the *P*-wave velocities, and the traveltimes from a downgoing *S*-wave event on the offset VSP were used to invert for the *S*-wave velocities. In both cases the blocked sonic-log velocities were used as an initial guess for the inversion algorithm. The blocked-sonic and VSP velocities are shown in Figure 3.4. Note that there is a constant  $V_p/V_s$  ratio for the sonic logs above the upper limestone layer. The full-waveform sonic log was only acquired below this depth, and the *S*-wave

transit times were estimated from the conventional sonic log using a constant  $V_p/V_s$  ratio of 1.88.

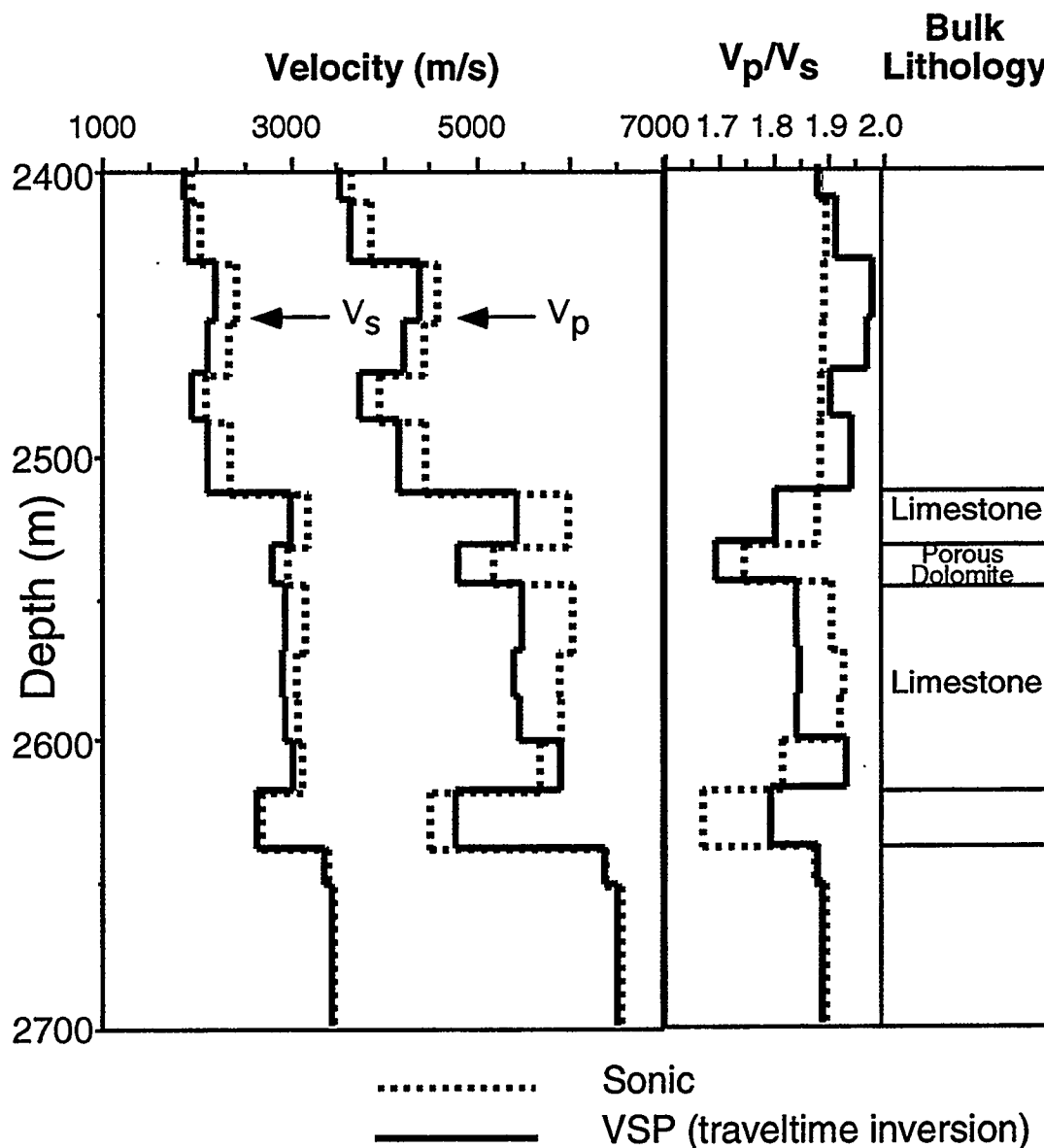


FIG. 3.4. Blocked-sonic and VSP velocities,  $V_p/V_s$  ratio, and bulk lithology from Well A. The zone of interest is at approximately 2530 m where there is a substantial decrease in the  $V_p/V_s$  ratio.

The comparison of the sonic and VSP velocities shows that the VSP velocities are generally lower than the sonic velocities. It has been documented (Stewart et al., 1984) that VSP velocities are generally lower than sonic velocities due to velocity dispersion.

The VSP data have lower frequencies than the sonic logs (10-70 Hz compared with  $\approx 10,000$  Hz). The VSP velocities will be used for all further analysis in this thesis for consistency of comparison with the VSP reflections.

### 3.2.3. VSP/Well-Log Correlation

The forward-modeled 1-dimensional (1-D) seismic response of the VSP velocity model can now be compared with the zero-offset VSP corridor stack. A favorable comparison would suggest that the velocity model is a valid representation of the Earth in a 1-D sense, and the layering of the model, based on the well logs, is reasonable. An unfavorable comparison would suggest that there are errors in either the layering or the acoustic parameters of the model. Thus, the correlation of the 1-D synthetic seismogram with the VSP corridor stack is an important test of the methods used in this analysis, especially the log blocking.

The 1-D synthetic was calculated using the convolution model. The polarity of the synthetic seismogram was calculated such that a positive reflection coefficient (impedance increase with time or depth) results in a peak when convolved with the wavelet. Both the bulk density and  $P$ -wave velocity were used to calculate the reflection coefficients. The reflection coefficients were transformed from the depth to the time domain using the VSP interval velocities and then convolved with the VSP wavelet. It is assumed here that the waveshaping deconvolution process has shaped the embedded seismic wavelet to match the waveshaping-deconvolved downgoing  $P$  waves (Figure 2.10). Thus, the VSP wavelet is determined by averaging the bottom 10 levels of the waveshaping deconvolved downgoing  $P$  waves, and scaling the result to a peak amplitude of 1.0. A comparison of the VSP corridor stack and the synthetic seismogram is shown in Figure 3.5. Note that the amplitudes and seismic character match reasonably well. No scaling has been applied to the corridor stack, so the zero-offset VSP data have been



processed to true seismic amplitudes. The match between the synthetic seismogram and the VSP corridor stack suggests that the Earth model is valid in the 1-D of the well bore.

There is a good correlation between the VSP corridor stack and the 1-D synthetic seismogram. The origin of the events on the synthetic seismogram can be determined easily and correlated with the VSP corridor stack. The first step in this analysis is to transform the well logs from depth to time using the VSP *P*-wave velocity (Figure 3.6). The zone of interest is between approximately 1.50 and 1.54 s.

The traveltimes of the seismic interfaces can be determined by overlaying the reflection-coefficient time series on the synthetic seismogram and VSP corridor stack traces (Figure 3.7). This display also shows how the events are corrupted by wavelet interference (tuning). To correlate the reflection coefficients back to the well logs, the acoustic-impedance curve is also plotted at the same scale in Figure 3.7. This display shows that the top of the limestone unit (at approximately 1.515 s) has a positive reflection coefficient that correlates with a peak on the seismic traces. The top of the porosity unit is a decrease in impedance resulting in a negative reflection coefficient that correlates fairly closely with a trough on the seismic traces. The base of the porosity unit has a positive reflection coefficient correlating approximately with a peak on the seismic traces. Note that the seismic waveforms in this interval exhibit thin-bed effects. The peaks and troughs of the synthetic seismogram and VSP corridor stack do not correlate exactly with the reflection coefficients. This effect is caused by wavelet interference from events above and below the reflectors.

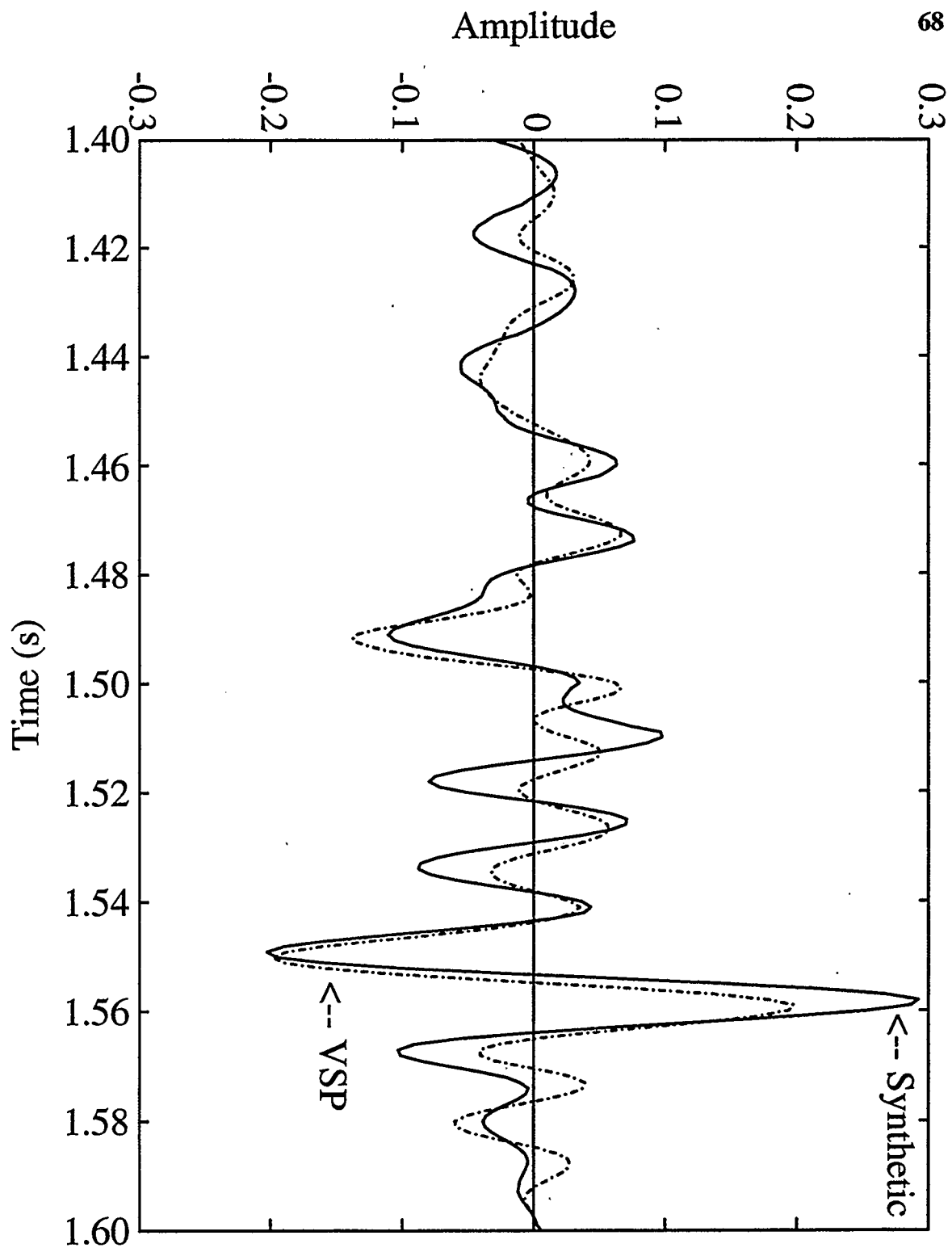


FIG. 3.5. Comparison of the synthetic seismogram generated from the blocked VSP  $P$ -wave velocity and blocked bulk-density log with the VSP corridor-stack trace. The synthetic trace is solid and the VSP trace is dashed.

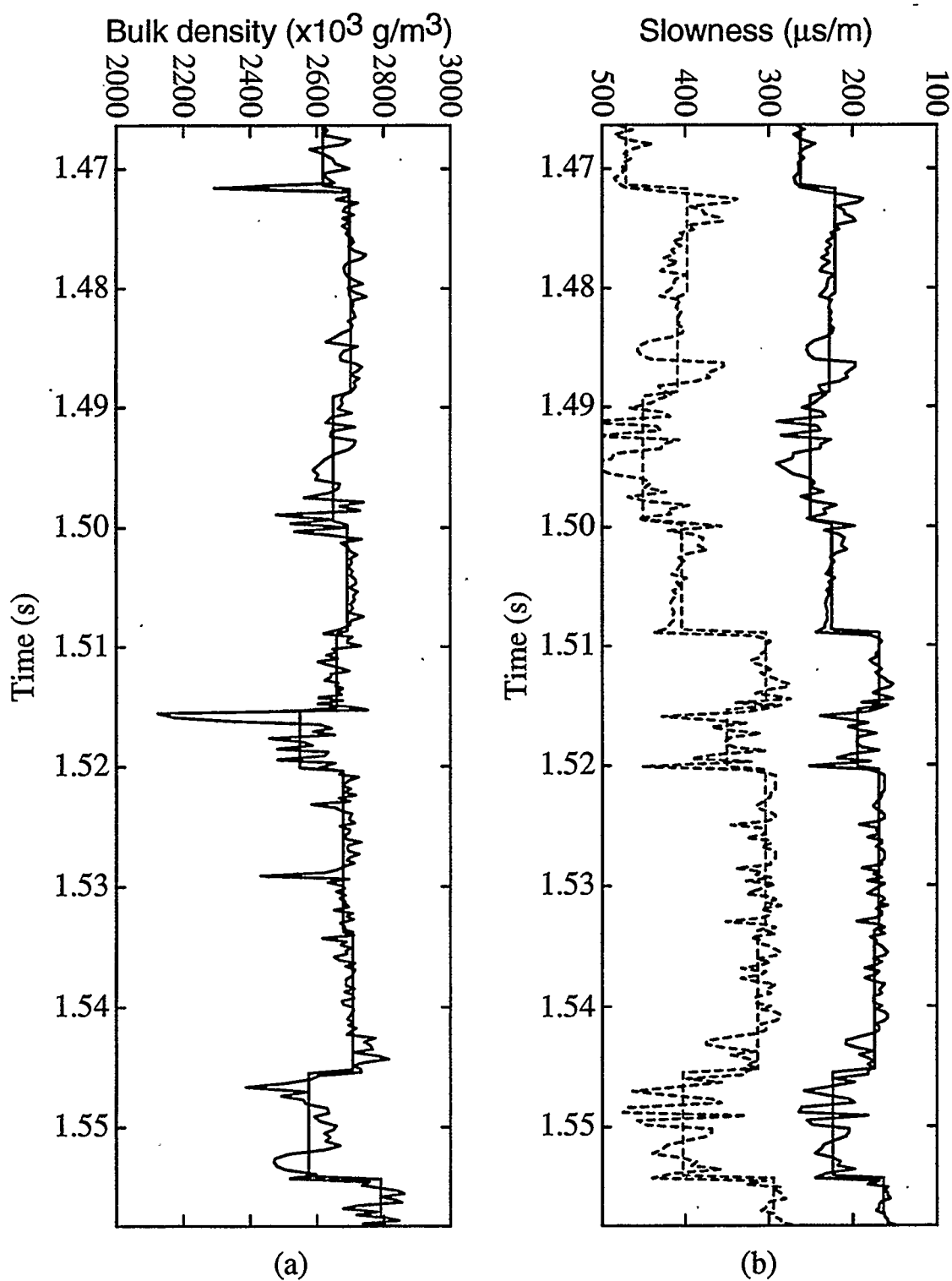


FIG. 3.6. Raw and blocked well logs in zone of interest in time; (a) bulk-density curve before and after log blocking, and (b) full-waveform sonic log with compressional- and shear-wave slowness curves before and after log blocking.

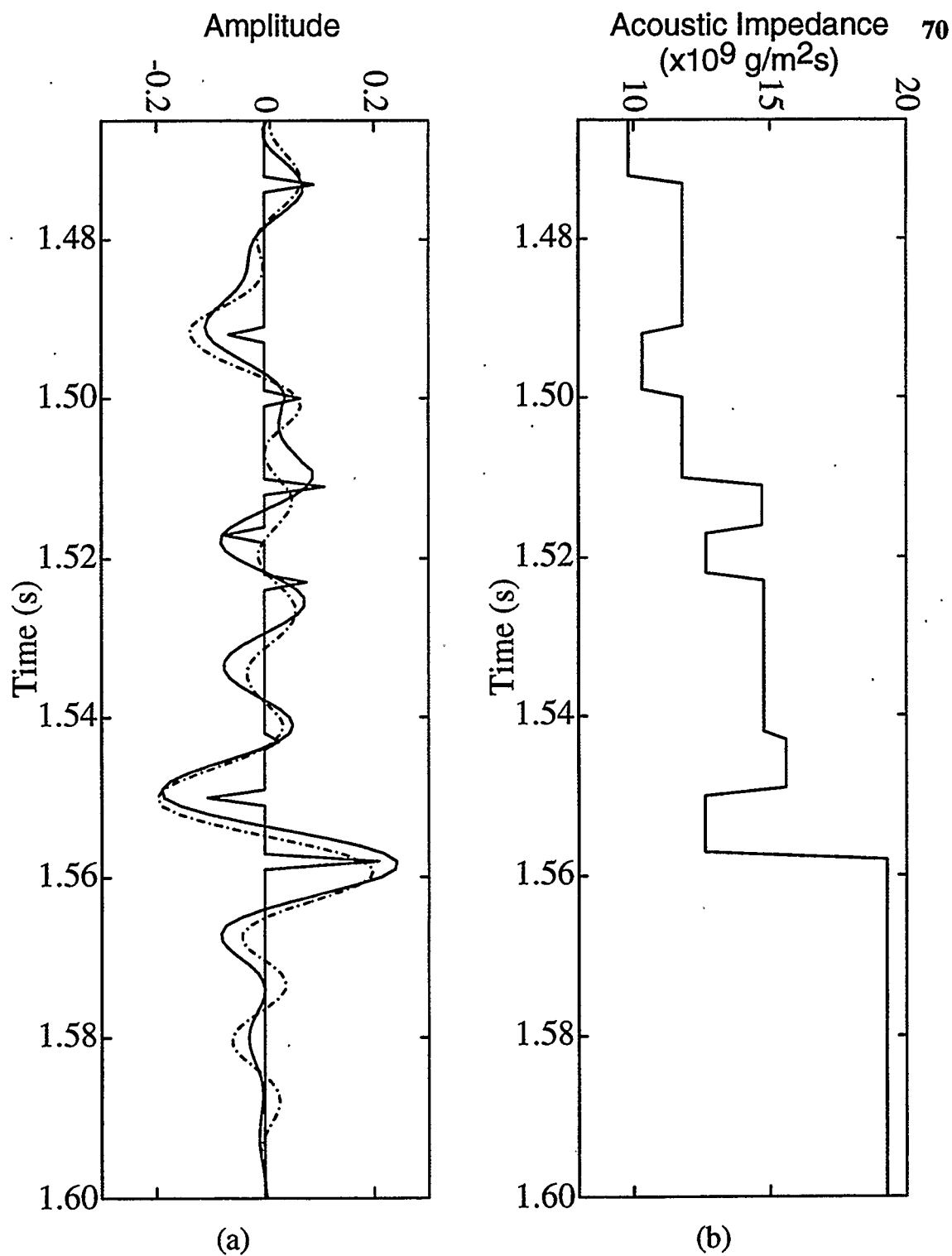


FIG. 3.7. Comparison of 1-D seismic with the acoustic-impedance log in time; (a) overlay of the reflection-coefficient time series (spiked trace), synthetic seismogram (solid trace), and corridor stack (dashed trace), and (b) blocked acoustic-impedance curve.

This interpretation has been limited to a very detailed analysis in the zone of interest, but there are other issues regarding the offset and multioffset VSPs that must be addressed. In particular, the correlations between the well logs, zero-offset VSP, offset VSP and multioffset VSP. One of the main issues for this part of the analysis is the correlation between the  $P$ - $P$  and  $P$ - $SV$  reflections on the offset and multioffset VSPs.

### 3.3 Integrated VSP Interpretation

Both the offset and multioffset VSP surveys have been processed for  $P$ - $P$  and  $P$ - $SV$  reflections. The VSP has been shown to be a good domain in which to correlate these reflections (Geis et al., 1990). The VSP yields a time-depth correlation that can be used to correlate  $P$ - $P$  and  $P$ - $SV$  reflections with well logs. This correlation can also be used to determine the polarity of the seismic data.

A composite plot of the zero-offset VSP corridor stack and the sonic log is shown in Figure 3.8. The lines on the composite plot indicate correlations between sonic-log character and seismic signatures. Event 1 is the top of a carbonate unit with a decrease in slowness (increase in velocity) on the sonic log, resulting in a positive reflection coefficient. The corresponding event on the zero-offset VSP is a peak, and therefore the polarity of the zero-offset VSP data is normal. That is, a peak represents an increase in impedance. Event 2 is the top of a shale unit with an increase in slowness on the sonic log corresponding to a trough on the zero-offset VSP. Event 3 is the top of another shale unit with an increase in slowness on the sonic log corresponding to a trough on the zero-offset VSP. Event 4 is the top of a shaly-carbonate unit with a decreases in slowness on the sonic log, corresponding to a peak on the zero-offset VSP. Event 5 is the top of a carbonate unit that decreases in slowness on the sonic log corresponding to a peak on the zero-offset VSP. Event 5 is the top of the limestone unit that overlays the porous dolomite reservoir. So, using the VSP and sonic log to correlate events has resulted in an

unambiguous interpretation of both the seismic events and the polarity of the zero-offset VSP data.

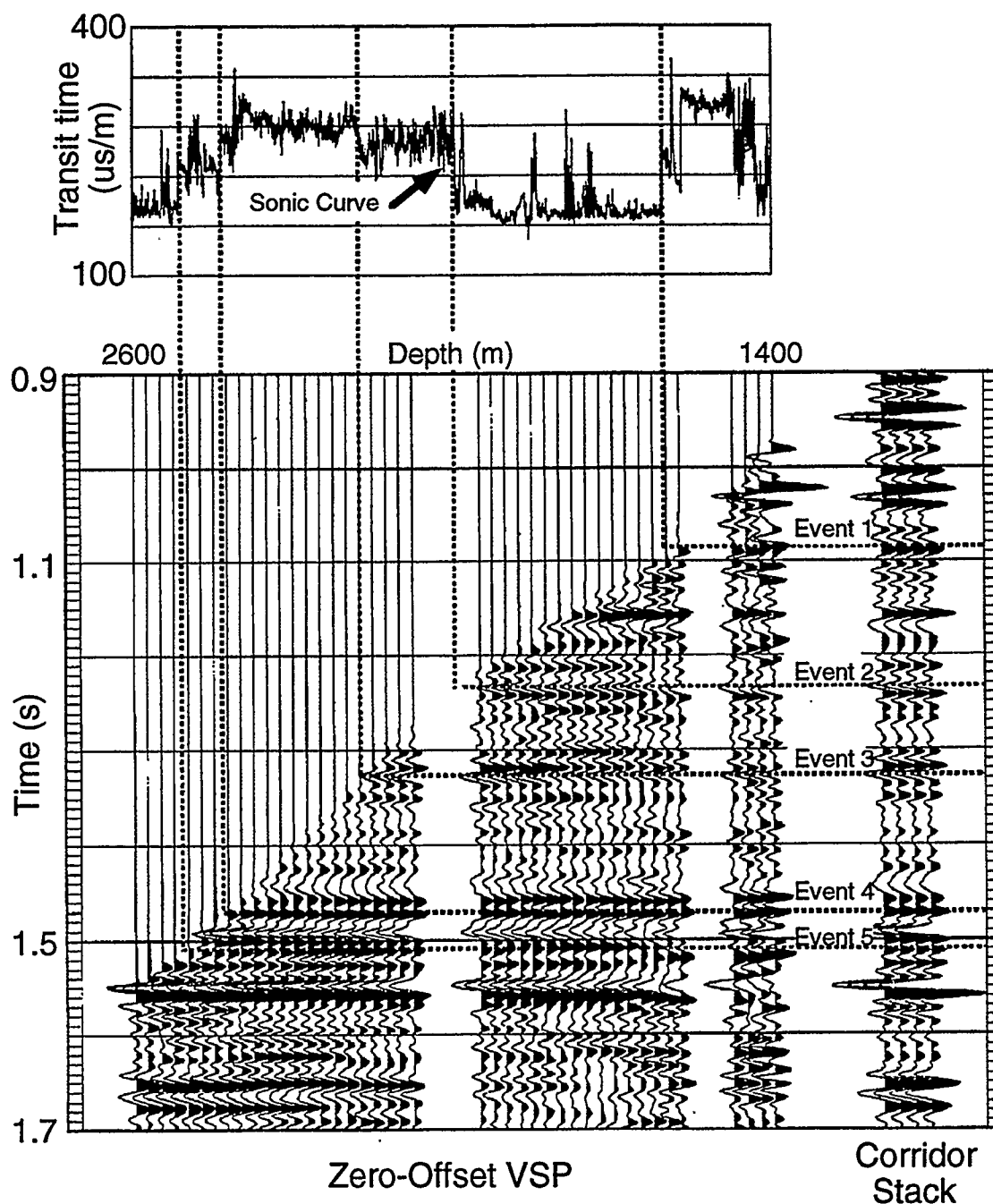


FIG. 3.8. Composite plot of the sonic log, zero-offset VSP, and the zero-offset VSP corridor stack showing correlations of 5 events from the sonic log recorded in depth with the VSP recorded in time.

The correlation between the zero-offset VSP corridor stack, the multioffset  $P$ - $P$  reflectivity gather, the offset VSP  $P$ - $P$  corridor stack, the multioffset  $P$ - $SV$  reflectivity gather, and the offset VSP  $P$ - $SV$  corridor stack is shown in Figure 3.9. The correlation is generally good; however there are some interesting observations. The offset VSP  $P$ - $SV$  corridor stack correlates better with the zero-offset VSP corridor stack than the offset VSP  $P$ - $P$  corridor stack correlates with the zero offset VSP corridor stack.

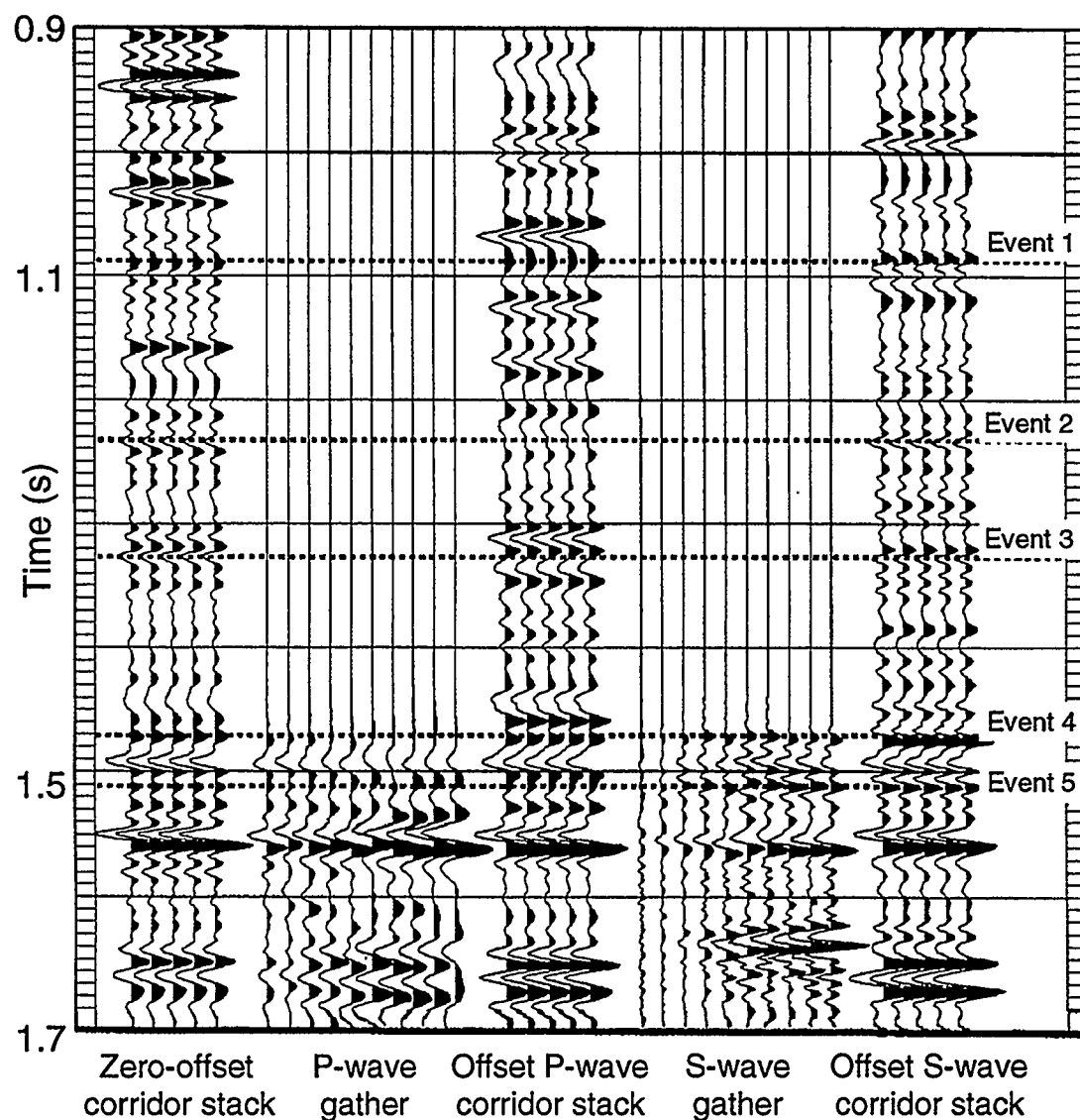


FIG 3.9. Correlation of 5 events across the VSP corridor stack, the  $P$ -wave gather, the offset VSP  $P$ -wave corridor stack, the  $S$ -wave gather, and the offset VSP  $S$ -wave corridor stack.

The *S*-waves in the *P-SV* corridor stack have traveled for a small time (less than 100 ms) after mode-conversion. The offset VSP *P-SV* corridor stack has the same frequency band as the offset VSP *P-P* corridor stack because they were both generated by the downgoing *P* wavefield. The *P-SV* waves have a shorter wavelength than the *P-P* waves, but a similar period, and are plotted at the same time scale as the *P-P* waves. The result is that the *P-SV* waves have a higher resolution and apparently higher frequencies than the *P-P* waves. The offset VSP data travel further than the zero-offset VSP data, causing more attenuation of the high frequencies. Therefore, the apparent higher frequencies in the *P-SV* data result in a better match with the zero-offset VSP corridor stack than the *P-P* data. The *P-SV* data correlate very well with the *P-P* data as there is generally a good match between peaks and troughs through the zone of interest. The *P-SV* data are thus reverse polarity using the Aki and Richards (1980) convention.

### 3.4 AVO Interpretation and Modeling

The multioffset VSP data have been acquired and processed for AVO analysis. The first step in understanding the AVO response of the reservoir zone is to calculate the single-interface Zoeppritzequation solution for some of the events near the reservoir zone. This step is important in developing an understanding of the AVO response of each of the layers near the reservoir zone. The next step is to calculate the multilayer forward model of the reservoir zone. This step is used to analyze the composite AVO response of the reservoir zone.

For single-interface AVO analysis, the Zoeppritz equations for *P-P* and *P-SV* displacement have been solved for the top of the limestone interface, the top of the reservoir interface, and base of the porosity interface. The VSP *P*- and *S*-wave velocities and bulk densities were used as the input parameters. The results of these calculations are shown in Figure 3.10. These curves are plotted such that amplitudes with a phase term  $\pm$



180 degrees are multiplied by -1.0. Note that in each case the  $P$ - $SV$  reflection coefficient is zero at normal incidence, increases to a peak at an intermediate angle of incidence, and then drops in amplitude at larger angles of incidence. The  $P$ - $P$  reflection coefficient for the top of the limestone decreases with incident angle up to about 35 degrees, and then increases at the larger angles due to critical-angle effects. The  $P$ - $P$  reflection coefficient for the top of the reservoir increases in amplitude with incident angle due to the decrease in  $V_P/V_S$  ratio and a negative normal-incidence reflection coefficient. The  $P$ - $P$  reflection coefficient for the base of the porosity increases in amplitude with incident angle due to the increase in  $V_P/V_S$  ratio and a positive normal-incidence reflection coefficient. An increase in amplitude with incident angle is used in this thesis to express that the absolute value of the reflection coefficient increases with increasing incident angle. This means that a positive reflection increases in a positive sense, and a negative reflection increases in a negative sense. The  $P$ - $P$  reflection-coefficient curves for the top and base of the reservoir unit are consistent with Koefoed's rules.

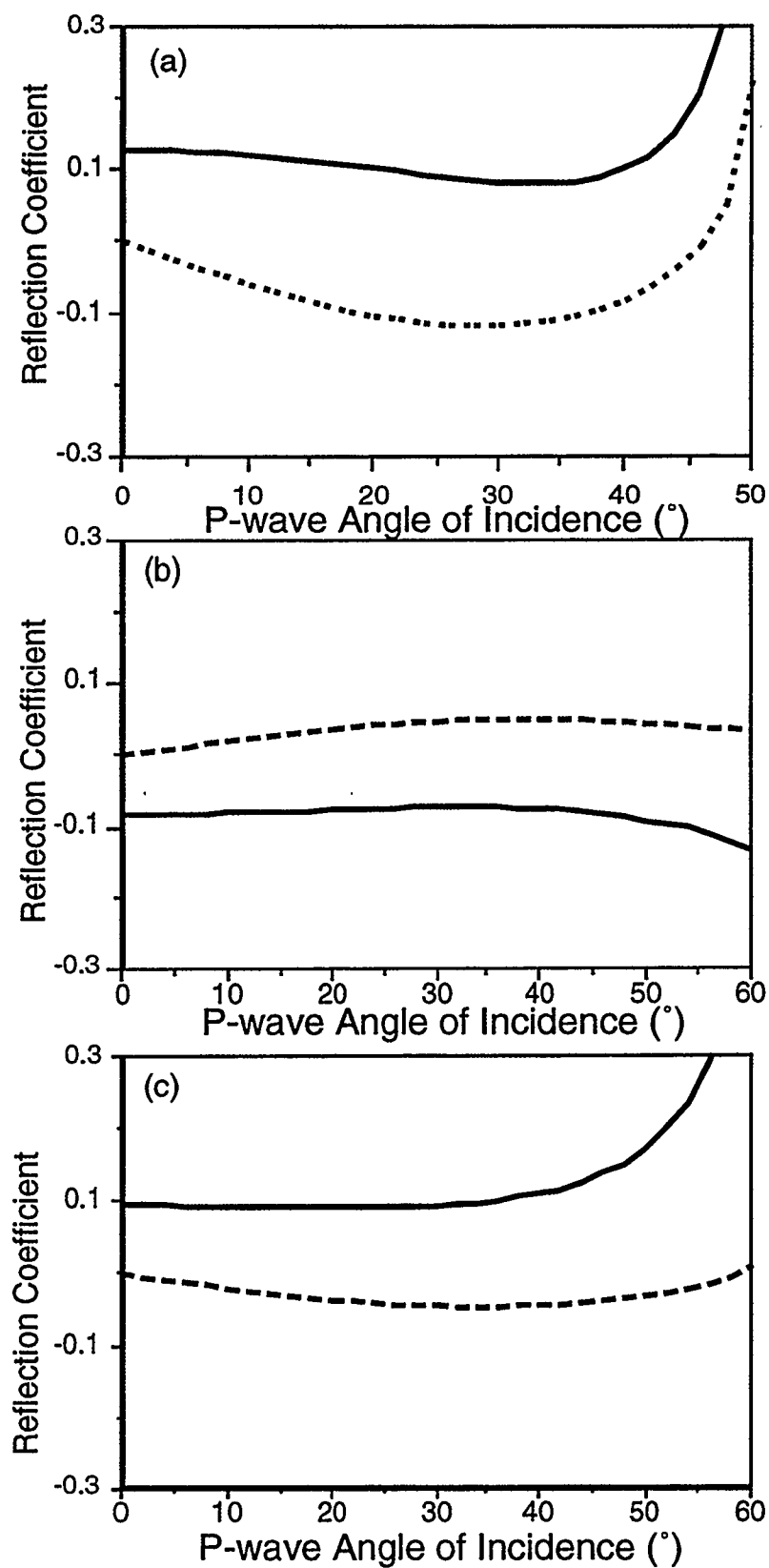


FIG. 3.10. Solution of the single interface Zoeppritz equations for  $P$ - $P$  (solid line) and  $P$ - $SV$  waves (dashed line); (a) top of the limestone interface, (b) top of the porosity interface, and (c) base of the porosity interface.

Unfortunately for AVO analysis, seismic data are bandlimited; so the seismic AVO response from a particular interface is complicated by wavelet interference from surrounding events. Generally, there is wavelet interference when reflections are within  $1/2$  a seismic wavelength of each other. Therefore, it is necessary in this case to model the seismic AVO response from all the layers near the reservoir zone because the reservoir thickness is less than  $1/2$  of the seismic wavelength. The forward-model data were generated by: (i) ray tracing through the VSP velocity model for the event traveltimes and angles of incidence; (ii) solving the Zoeppritz equations for the reflection coefficients; (iii) convolving with a 40-Hz zero-phase Ricker wavelet; (iv) and correcting for NMO using the algorithm that was used in the multioffset VSP processing section for the field data. For tuned events it is important to include NMO in the modeling to account for the wavelet stretch that is in the real data. The effects of wavelet stretch have been quantified in other work (Ostrander, 1984; Swan, 1990) and this study reinforces how important this effect is for AVO analysis. As shown in Figure 2.39, approximately 15 ms of stretch must be applied to the far offset traces during NMO. This is significant considering that the amount of stretch is greater than the time thickness of the reservoir. The correlation of the  $P$ - $P$  and  $P$ - $SV$  forward models with the field  $P$ - $P$  and  $P$ - $SV$  reflectivity gathers are shown in Figure 3.11. All the  $P$ - $P$  and  $P$ - $SV$  data are both true relative amplitude to each other in Figure 3.11. The two-way  $P$ -wave traveltimes of the top of the limestone, top of the porosity, and base of the porosity events are also drawn (dashed lines) on this plot. Generally, the event correlation between the field and the model data is good, although there are some differences in seismic character. The  $P$ - $SV$  correlation is slightly better than the  $P$ - $P$  correlation. The modeled  $P$ - $P$  data have a strong peak at 1.56 s that has a strong AVO effect. The size of this peak is much larger than the corresponding peak on the real data. This is a critical-angle effect that probably is not modeled properly with the method that was used.

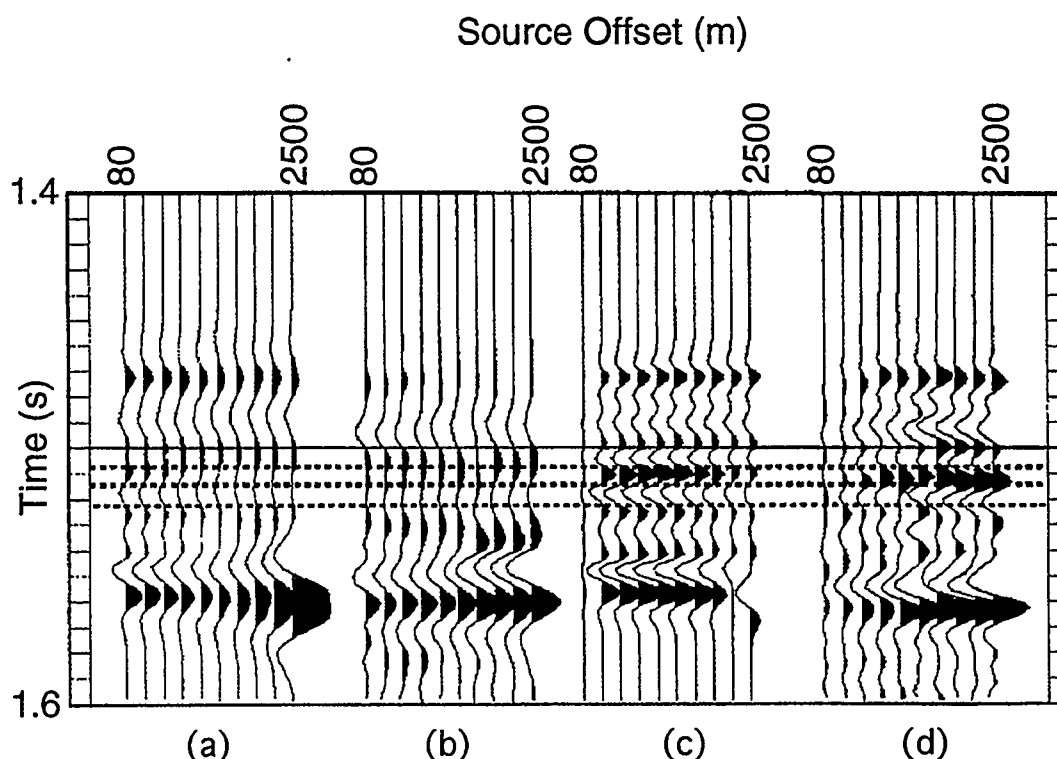


FIG 3.11. Correlation of multilayer forward-modeled (a)  $P$ - $P$  and (c)  $P$ - $SV$  gathers with the field (b)  $P$ - $P$  and (d)  $P$ - $SV$  gathers. Three events (dashed lines) are correlated, the top event is the top of the limestone interface, the middle event is the top of the porosity interface, and the bottom event is the base of the porosity interface.

The event correlations (dashed lines) also show how extreme the wavelet interference (tuning) effects are in these data. The  $P$ - $P$  data display the events at near offsets, but the correlations change at far offsets. This suggests that the effect of tuning changes with offset. The  $P$ - $SV$  data correlate better across the range of offsets than the  $P$ - $P$  events. The reflected  $P$ - $SV$  waves have approximately the same frequency band and travel at lower velocities than the  $P$ - $P$  waves. Thus the  $P$ - $SV$  waves have a shorter wavelength (or higher resolution) than the  $P$ - $P$  waves. So, the tuning effects are smaller for the  $P$ - $SV$  reflections than for the  $P$ - $P$  reflections.

The wavelet-interference effects versus offset are complicated phenomena that affect the AVO response of the real and modeled  $P$ - $P$  and  $P$ - $SV$  data. One method of studying this effect is to model the interfaces independently, and then study the effects of

adding the response of the different interfaces together. Figure 3.12 is a summary of this analysis for the  $P$ - $P$  reflections. Each panel is an AVO model generated as previously, except fewer events are used. In Figure 3.12(a) only the top of the limestone interface is modeled. This event is highlighted in the schematic impedance profile plotted above the seismic response for reference. The hatched area of the impedance profile is the porous reservoir zone. Figure 3.12(a-c) are the AVO modeled responses of the top of the limestone, top of the porosity, and base of the porosity interfaces respectively. Figure 3.12(d) is the composite AVO response from the top and base of the porosity, and Figure 3.12(e) is the composite AVO response from all 3 interfaces.

The combined AVO response of the top and base of the porosity is close to a 90 degree wavelet that is consistent with Widess (1973) for two tuned reflections of approximately equal strength and opposite polarity. The AVO response of these two interfaces is tuned, but there is still an AVO response similar to that of the individual interfaces (Figure 3.12(b) and Figure 3.12(c)). Interestingly, the AVO response from the top of the porosity changes completely when the top of the limestone event is included in the modeling (Figure 3.12(e)). The top of the porosity AVO response changes from an increase in amplitude with offset to a decrease in amplitude with offset. Figure 3.12(f) is the AVO model of the same three interfaces plus the interface above the top of the limestone. In this model response, the top of the porosity event appears to have returned at the far offsets. However, this is likely side-lobe interference from the additional event. The AVO response from the base of the porosity is relatively unchanged from the single interface response in this case.

The remaining AVO model responses (Figures 3.12(g-k)) are each calculated with an additional lower event. The AVO response from the base of porosity changes considerably in Figure 3.12(i) and Figure 3.12(j), suggesting that the AVO response from the base of porosity is also tuned and does not show the true AVO response of the

individual event. In summary, this detailed AVO analysis shows that the AVO response of the reservoir zone is complicated by wavelet-interference (tuning) effects that make it difficult to understand the exact AVO contribution of each layer independently.

The analysis for the  $P$ - $SV$  reflections is shown in Figure 3.13. In this case, as discussed previously, these data have higher resolution than the  $P$ - $P$  reflection data due to the shorter wavelength of the  $P$ - $SV$  waves. Therefore, there is less tuning in these data than in the  $P$ - $P$  reflection data. There are differences other than the amount of tuning. Figure 3.13(e) shows that the  $P$ - $SV$  reflection from the base of the porosity contributes less to the  $P$ - $SV$  AVO response than the  $P$ - $P$  reflection in Figure 3.12(e). It is also apparent that the  $P$ - $SV$  reflection from the top of the limestone is more dominant than the  $P$ - $P$  reflection. This detailed analysis of the  $P$ - $SV$  AVO model response shows that there is less tuning overall. Furthermore, the degree of tuning at each interface is not consistent between the  $P$ - $P$  and  $P$ - $SV$  data as shown by the difference in relative strengths of the  $P$ - $P$  and  $P$ - $SV$  reflections from the top of limestone and base of porosity.

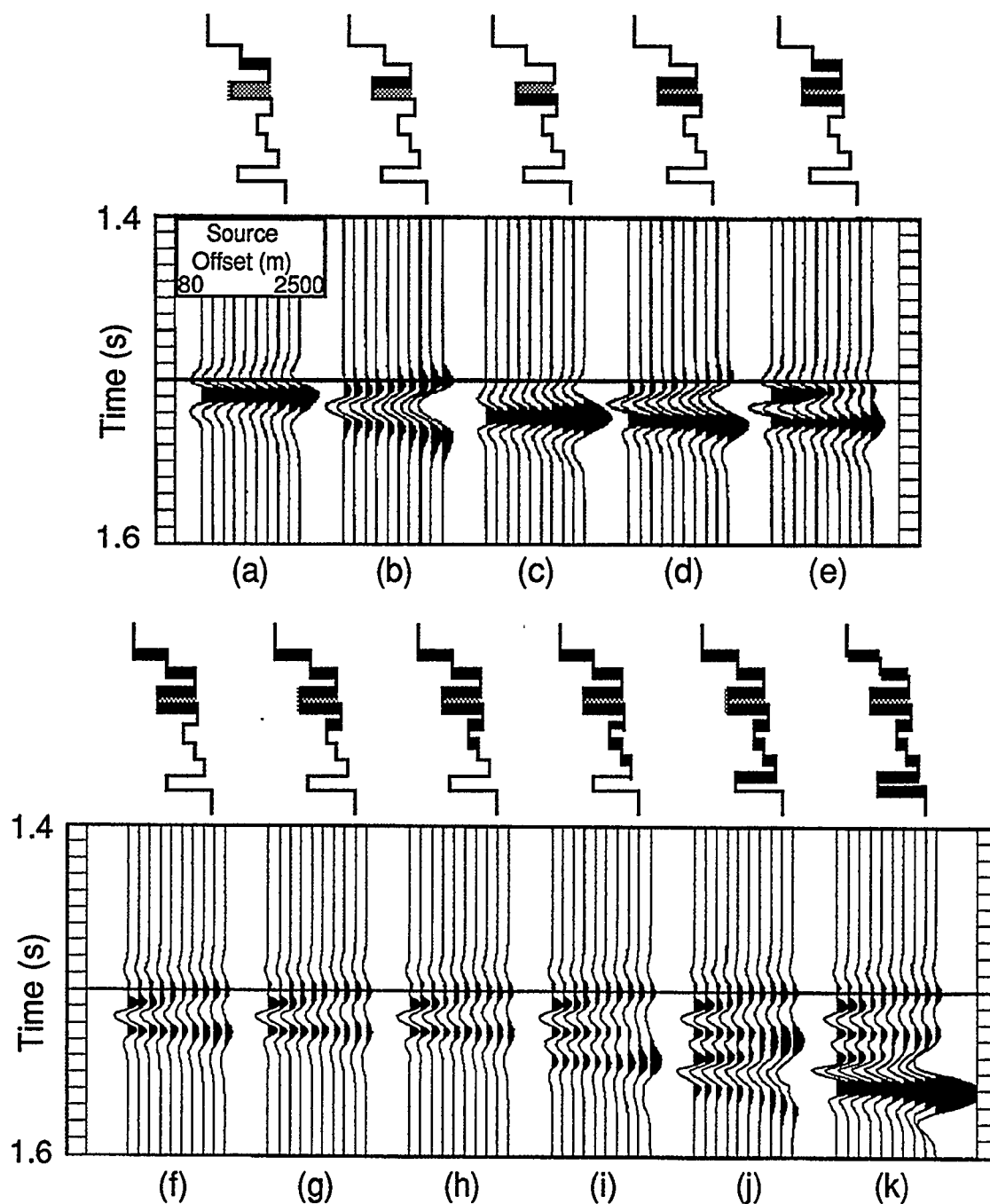


FIG. 3.12. *P-P* forward models generated using a 40-Hz Ricker wavelet. Each model contains reflections from the bold reflectors of the schematic impedance profile plotted above. The gray area is the reservoir zone. (a) AVO model of the top of the limestone. (b) AVO model of the top of the porosity. (c) AVO model of the base of the porosity. (d) AVO model of the top and base of the porosity. (e) AVO model of the top of the limestone, top of the porosity, and base of the porosity. (f)-(k) AVO models of the bold interfaces.

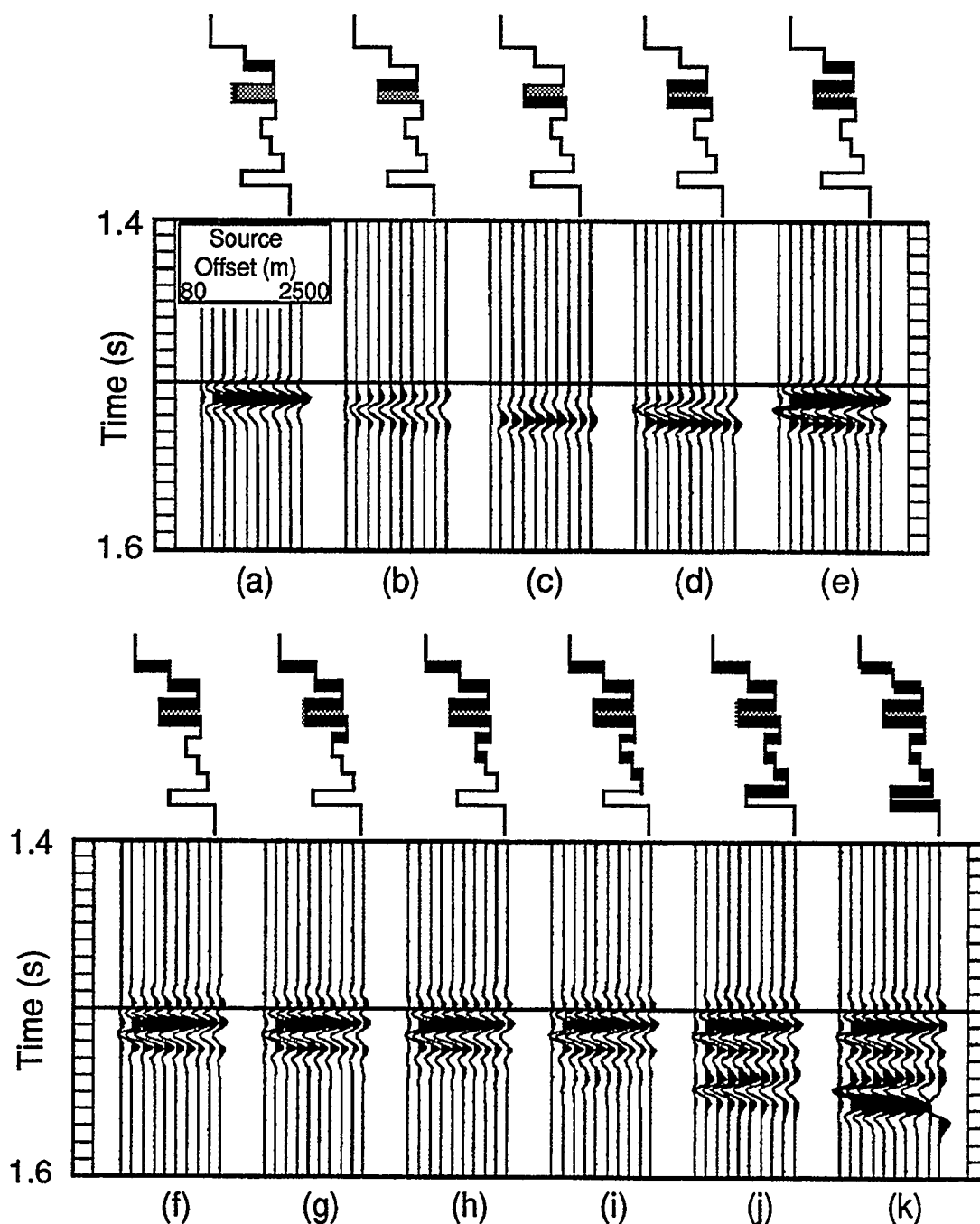


FIG. 3.13. *P*-*SV* forward models generated using a 40-Hz Ricker wavelet. Each model contains reflections from the bold reflectors of the schematic impedance profile plotted above. The gray area is the reservoir zone. (a) AVO model of the top of the limestone. (b) AVO model of the top of the porosity. (c) AVO model of the base of the porosity. (d) AVO model of the top and base of the porosity. (e)-(k) AVO models of the bold interfaces.



The next step in the AVO analysis is to try to estimate the reservoir parameters ( $V_P$ ,  $V_S$ , and  $\rho$ ) using the multioffset VSP data. The approach used here is to visually compare the model and seismic responses and update the model until there is a better visual match. This approach is very qualitative in nature, and thus there is no guarantee that the match is the best that can be found. Figures 3.14 and 3.15 show the results of this analysis for the  $P$ - $P$  and  $P$ - $SV$  data respectively. The  $P$ - $SV$  data have a lower signal-to-noise ratio than the  $P$ - $P$  data, and the comparison of the field and model data (Figure 3.11) is better for the  $P$ - $SV$  data than the  $P$ - $P$  data. Thus the  $P$ - $P$  data will be emphasized in this analysis.

Figure 3.14(a) is the AVO forward model using a 100 Hz wavelet. This plot shows AVO response for the reservoir that is largely uncomplicated by wavelet-interference affects, and is used here for event correlation. The top of the porosity event in this plot is the trough at 1.517 s. Figure 3.14(b) is the AVO forward model using a 40 Hz Ricker wavelet. In Figure 3.14(c) the  $P$ -wave velocity was lowered incrementally in the reservoir until a better qualitative match between the model and field data was found in the reservoir zone for the far-offset traces. The velocity was lowered further until the modeled AVO response began to deviate from the VSP field data. Figure 3.14(d) is the field  $P$ - $P$  gather. The reservoir zone velocities used in this modeling are listed in Table 3.2. A better model/field data match was obtained by perturbing the  $P$ -wave velocity in the reservoir zone. In this case, the reservoir  $P$ -wave velocity estimated from the  $P$ - $P$  field data is lower than from the VSP traveltime inversion (Section 3.2.2). This also raises the issue of justifying a change in the VSP velocities to obtain a better seismic reflection model.

Table 3.2. VSP and perturbed velocities.

Lithology	VSP Velocities			Perturbed Velocities		
	$V_p$ (m/s)	$V_s$ (m/s)	$V_p/V_s$	$V_p$ (m/s)	$V_s$ (m/s)	$V_p/V_s$
Limestone	5469	3026	1.81	5469	3026	1.53
Dolomite	4817	2833	1.70	4333	2833	1.53
Limestone	5444	2937	1.85	5444	2937	1.85

The VSP interval velocities are determined from the traveltimes of the downgoing  $P$  and  $S$  waves of the zero-offset and 750 m offset VSPs respectively. These traveltimes were measured in the borehole at depth intervals of 20 m. It has been shown that the limit of seismic resolution for these data is about 13 m. Therefore, the resolution of the two methods are different, and this may account for the discrepancy observed using AVO analysis and VSP traveltimes.

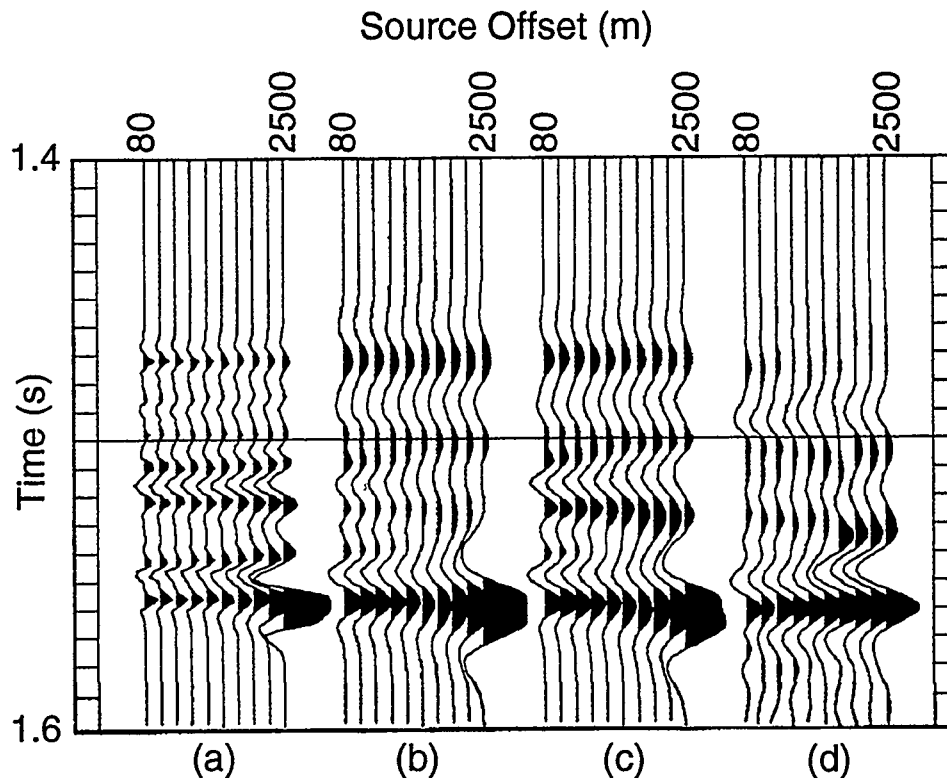


FIG 3.14.  $P$ - $P$  multilayer forward models and field-data comparison; (a) forward model with 100 Hz wavelet, (b) forward model with 40 Hz wavelet, (c) perturbed model with 40 Hz wavelet, and (d) field  $P$ -wave gather.

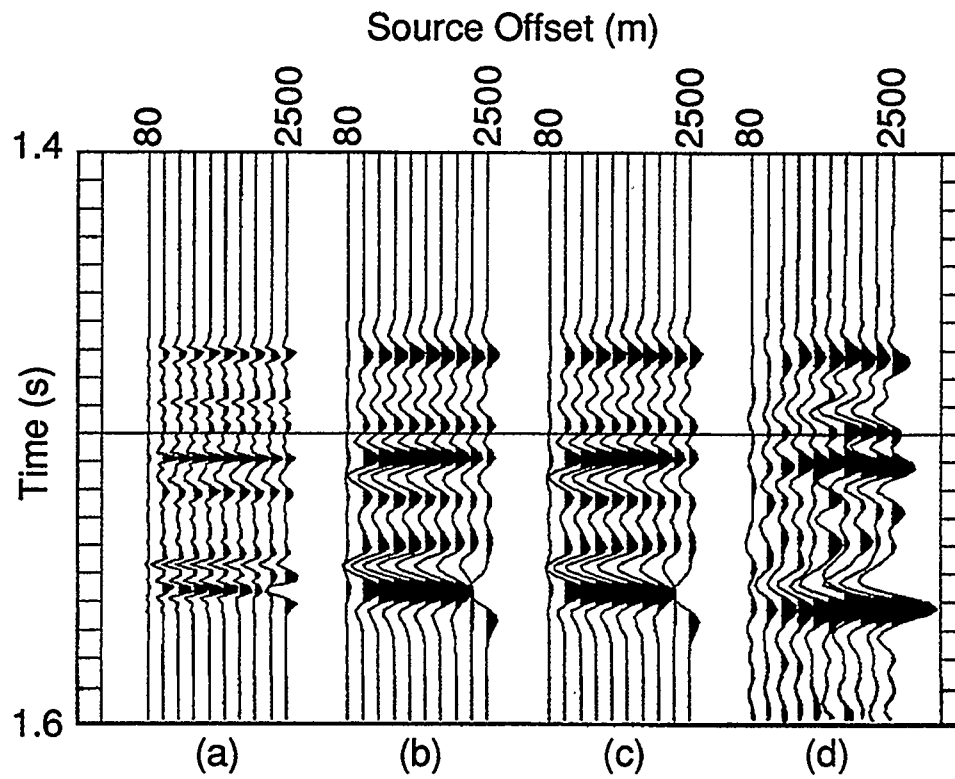


FIG. 3.15. *P-SV* multilayer forward models and field-data comparison; (a) forward model with 100-Hz wavelet, (b) forward model with 40-Hz wavelet, (c) perturbed model with 40-Hz wavelet, and (d) field S-wave gather.

# Chapter 4

## VSP Inversion

### 4.1 Introduction

The ultimate objective of AVO analysis is to estimate the subsurface rock properties using seismic measurements. Several methods have been proposed to meet this goal, ranging from the relatively simple  $A*B$  (intercept\*gradient) method (Treadgold, et al., 1990) to complex full wave-equation techniques (Carazzone and Srnka, 1992) and genetic-algorithm solutions (Sen and Stoffa, 1992). All of these methods have applications in some environments and exploration strategies, and, of course, they vary in computational cost and complexity. To solve the AVO inversion problem in this thesis, a generalized-linear-inversion (GLI) approach is developed. The GLI method is first applied in this chapter to the zero-offset VSP corridor stack to find a 1-D solution for the  $P$ -wave impedance. The method is then expanded to the offset domain, where the  $P$ - $P$  and  $P$ - $SV$  multioffset VSP field gathers are inverted for the three elastic parameters  $V_p$ ,  $V_s$ , and  $\rho$ .

### 4.2 1-D Generalized Linear Inversion

Several methods can be used to obtain a reflectivity series from a seismic trace and then invert the reflectivity series back to an impedance log or pseudo-sonic log (e.g., Lindseth, 1979; Oldenburg et al., 1983; Chi et al., 1984). These methods usually involve a wavelet-estimation algorithm and a reflectivity estimation algorithm. For the case of VSP data, where we assume that the wavelet is well known and the data are largely multiple free, the inversion problem is simpler than for the surface-seismic case. Furthermore, well-log measurements can be used to obtain a good initial estimate of the

reflectivity. This problem is therefore well posed for the GLI inversion technique as outlined by Cooke and Schneider (1983).

The initial step in developing a GLI algorithm is to define the forward problem. Shown in Figure 4.1 is a schematic diagram for a stack of  $n$  layers, plotted in time, with an acoustic impedance  $Z$  assigned to each layer. The  $n$  layers can be represented by an impedance curve,  $Z(t)$ , and a reflectivity series  $R(t)$  (Equation 4.1). The forward-model seismic trace,  $S(t)$ , is the result of convolving the reflectivity series  $R(t)$  with a wavelet. The inverse problem is to find the acoustic impedance curve  $Z(t)$  and corresponding forward model trace  $S(t)$  that most closely matches the zero-offset VSP corridor stack. A flowchart of the GLI inversion process is shown in Figure 4.2 (Russell, 1988).

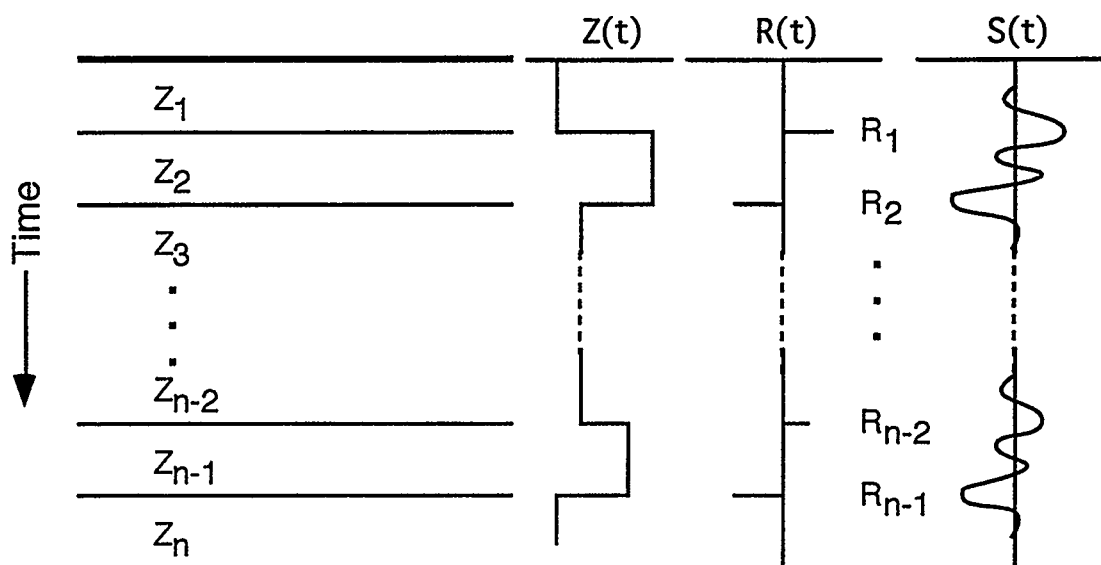


FIG 4.1. Schematic diagram of a stack of layers and the resulting forward modeled seismic trace.

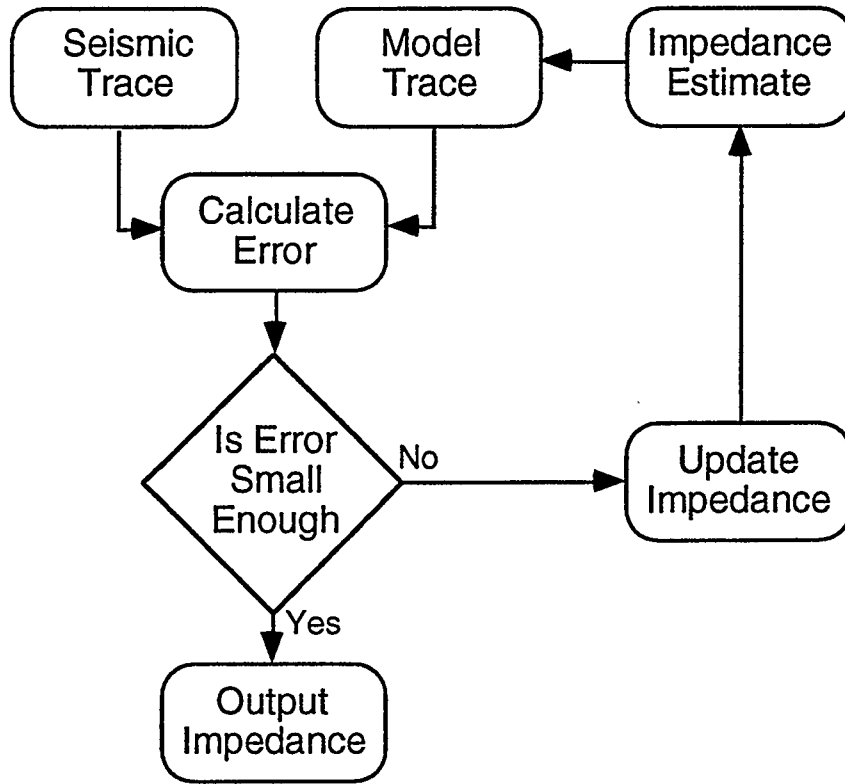


FIG 4.2. Flowchart of GLI inversion method.

The primary reflection coefficients (no multiples) can be calculated simply as

$$R_i = \frac{Z_{i+1} - Z_i}{Z_{i+1} + Z_i}, \quad i = 1, n. \quad (4.1)$$

The traveltimes are known for each of the reflectors because the velocities from the VSP traveltimes inversion can be used to convert the well log measurements from depth to time, allowing  $R_n$  to be expressed as a time series  $R(t)$ . The convolution of the reflectivity series  $R(t)$  with a wavelet  $w(t)$  of duration  $l$  is the forward-modeled seismic trace, that can be expressed as

$$S(t) = R(t) \sum_{\tau=-l}^l w(\tau) \delta(t-\tau). \quad (4.2)$$

The forward modeling function defined by Equation 4.2 is quite simple, and can be used to formulate a GLI solution to the inverse problem.

Using the GLI technique, a Taylor series expansion of the forward model (Cooke and Schneider, 1983) is formed.

$$F(\mathbf{I}) = F(\mathbf{IG}) + \left[ \frac{\partial F(\mathbf{I})}{\partial \mathbf{I}} \right]_{\mathbf{I}=\mathbf{IG}} (\mathbf{I}-\mathbf{IG}) + \dots \quad (4.3)$$

where

$\mathbf{I}$	=	the impedance profile to be solved for,
$\mathbf{IG}$	=	an initial guess of the impedance profile,
$(\mathbf{I}-\mathbf{IG})$	=	error in above guess,
$F$	=	forward modeling function,
$F(\mathbf{I})$	=	observed seismic trace,
$F(\mathbf{IG})$	=	forward modeled seismic trace, and
$\frac{\partial F(\mathbf{I})}{\partial \mathbf{I}}$	=	partial-derivative matrix of the forward modeling function with respect to the model parameters.

Equation 4.3 can be simplified by assigning

$$\mathbf{b} = F(\mathbf{I}) - F(\mathbf{IG}), \quad (4.4)$$

$$\mathbf{A} = \left[ \frac{\partial F(\mathbf{I})}{\partial \mathbf{I}} \right]_{\mathbf{I}=\mathbf{IG}}, \quad (4.5)$$

$$\mathbf{x} = (\mathbf{I}-\mathbf{IG}), \quad (4.6)$$

truncating the series after the linear term, and rearranging to give

$$\mathbf{Ax} = \mathbf{b}. \quad (4.7)$$

Equation 4.7 is a linear system of equations that can be solved for the model updates  $\mathbf{x}$ . It is generally necessary to introduce a damping factor to stabilize the inversion as  $\mathbf{A}$  can be singular. The system can be rewritten as

$$(\mathbf{A}^t \mathbf{A} + k^2 \mathbf{I}) \mathbf{x} = \mathbf{A}^t \mathbf{b} \quad (4.8)$$

where  $k$  is the least-squares damping factor. Equation 4.8 is the general GLI system of equations for any problem that can be formulated as in Equation 4.3. The solution of this system using matrix algebra is (Cooke and Schneider, 1983)

$$\mathbf{x} = (\mathbf{A}^t \mathbf{A} + k^2 \mathbf{I})^{-1} \mathbf{A}^t \mathbf{b}. \quad (4.9)$$

The inversion problem can initially be formulated using a four-layer Earth model where we assume that the wavelet is a spike. Also, the inversion will be constrained by the impedance of the top layer and the traveltimes of the events. The inversion problem, in this case, is to determine the impedance in the three layers below the top layer, and thus the partial derivatives with respect to these impedances are solved for.

Equation 4.2 for the seismic trace becomes

$$S(t) = \frac{Z_2 - Z_1}{Z_2 + Z_1} \delta(t - \tau_1) + \frac{Z_3 - Z_2}{Z_3 + Z_2} \delta(t - \tau_2) + \frac{Z_4 - Z_3}{Z_4 + Z_3} \delta(t - \tau_3), \quad (4.10)$$

where  $\tau_i$  are the event times for the  $i$ th event. Taking the partial derivatives with respect to the impedance  $Z_i$  gives

$$\frac{\partial S(t)}{\partial Z_2} = \frac{2Z_1}{(Z_2 + Z_1)^2} \delta(t - \tau_1) - \frac{2Z_3}{(Z_3 + Z_2)^2} \delta(t - \tau_2), \quad (4.11)$$

$$\frac{\partial S(t)}{\partial Z_3} = \frac{2Z_2}{(Z_3 + Z_2)^2} \delta(t - \tau_2) - \frac{2Z_4}{(Z_4 + Z_3)^2} \delta(t - \tau_3), \text{ and} \quad (4.12)$$

$$\frac{\partial S(t)}{\partial Z_4} = \frac{2Z_3}{(Z_4 + Z_3)^2} \delta(t - \tau_3). \quad (4.13)$$

The seismic trace has three spiked events at the appropriate traveltimes and can be expressed as  $R(t) = (R_1, R_2, R_3)$ ; the forward model trace can be expressed as  $S(t) = (S_1, S_2, S_3)$ . Equation 4.7 becomes

$$\begin{pmatrix} S_1 - R_1 \\ S_2 - R_2 \\ S_3 - R_3 \end{pmatrix} = \begin{pmatrix} \frac{2Z_1}{(Z_2 + Z_1)^2} & 0 & 0 \\ \frac{-2Z_3}{(Z_3 + Z_2)^2} & \frac{2Z_2}{(Z_3 + Z_2)^2} & 0 \\ 0 & \frac{-2Z_4}{(Z_4 + Z_3)^2} & \frac{2Z_3}{(Z_4 + Z_3)^2} \end{pmatrix} \begin{pmatrix} \Delta Z_2 \\ \Delta Z_3 \\ \Delta Z_4 \end{pmatrix}. \quad (4.14)$$

The model updates  $\Delta Z_i$  can be calculated from Equation 4.14 using a matrix inversion algorithm.



### 4.2.1 Synthetic Data Examples

The 1-D algorithm was tested using several synthetic data sets. The test data were generated from the VSP interval velocities and bulk densities used for forward modeling in Chapter 3. The four layers modeled included the gas-bearing porous layer (shown in Figure 3.4). The top layer of the model is the layer immediately above the top limestone unit, and the bottom layer of the model is the limestone layer immediately below the porous zone. The first test data were generated using a spike wavelet and the model mentioned above.

The algorithm results are shown in Figure 4.3. Figure 4.3(a) has four traces plotted; trace 1 is the initial guess forward model, trace 2 is the forward model trace after inversion, trace 3 is the true seismic trace, and trace 4 is the difference between the inverted trace (trace 2) and the true seismic trace (trace 3). Figure 4.3(b) is a comparison of the initial guess impedance profile (dashed line) with the inverted impedance profile (dotted), and the true impedance profile (solid line). The inverted impedance profile is overlain by the true impedance profile as the inversion is exact for these data; this is also shown by trace 4 in Figure 4.3(a). A damping factor of 0.001 and three iterations were required to reach the final solution.

The algorithm was then tested on synthetic data generated using the same model and the VSP wavelet. The algorithm results for these data are shown in Figure 4.4. Again, the inversion is virtually exact as the residual trace is zero, and the inverted impedance profile exactly matches the true impedance profile. The same damping factor (0.001) was used for this inversion, and three iterations were necessary to reach the final solution. Tuning occurs in these data, and the algorithm performed as well as in the previous case where there was no tuning. If the traveltimes of the events and the wavelet are known, one can invert for the acoustic impedance with noise-free data.

The algorithm was then tested for the case where the upper impedance of the initial guess is incorrect; the results are shown in Figure 4.5. The error trace (trace 4 in Figure 4.5(a)) shows that there is zero error in the inversion. So, the algorithm has converged to a solution with zero error despite the incorrect upper impedance. The upper impedance was not changed by the inversion algorithm because it is a constraint on the solution. The inverted impedance profile is bulk shifted from the true impedance profile by the difference between the true and guess upper impedance. The relative changes in impedance for the four layers are correct, as the normal-incidence reflection coefficient is dependent primarily on the changes in impedance and not the absolute impedance values. Therefore, the inversion has performed correctly for the relative changes in impedance. This example also illustrates the nonuniqueness problem with inversion methods. The final impedance model matches the data with zero error, but the impedances are bulk shifted. There are many solutions for these data depending on the constraint of the upper impedance.

The algorithm was further tested using an initial guess with an incorrect traveltimes for one of the events. The traveltimes of the top of porosity event (second event) has been shifted down 1 ms. The results of this test are shown in Figure 4.6, and again three iterations were required to converge to the solution. Trace 4 in Figure 4.6 shows some residual error for this test, indicating that incorrect event traveltimes inhibit the performance of the algorithm. The algorithm does not converge to the correct impedance for the second or third layers; however, surprisingly, the algorithm does converge very close to the correct impedance for the fourth layer. The fourth layer is less affected because it is slightly removed from the incorrect traveltimes event. These results suggest that an initial-guess impedance profile with incorrect event traveltimes will inhibit the performance of the algorithm, although the results are still close to true impedance curve.

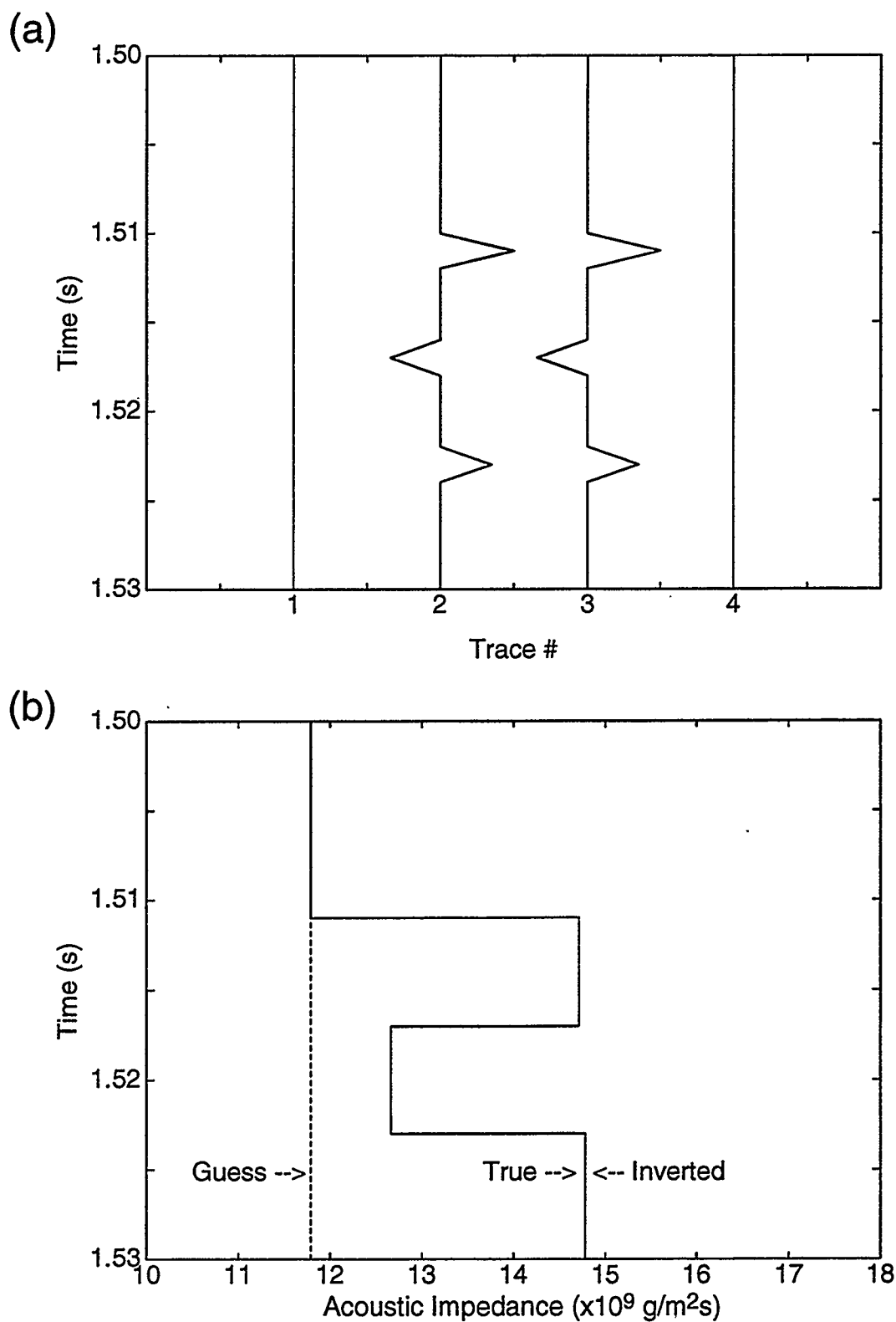


FIG 4.3. Synthetic data-inversion results for spiked data traces; (a) initial guess, inverted, real seismic, and difference traces, and (b) initial, inverted, and real impedance profiles.

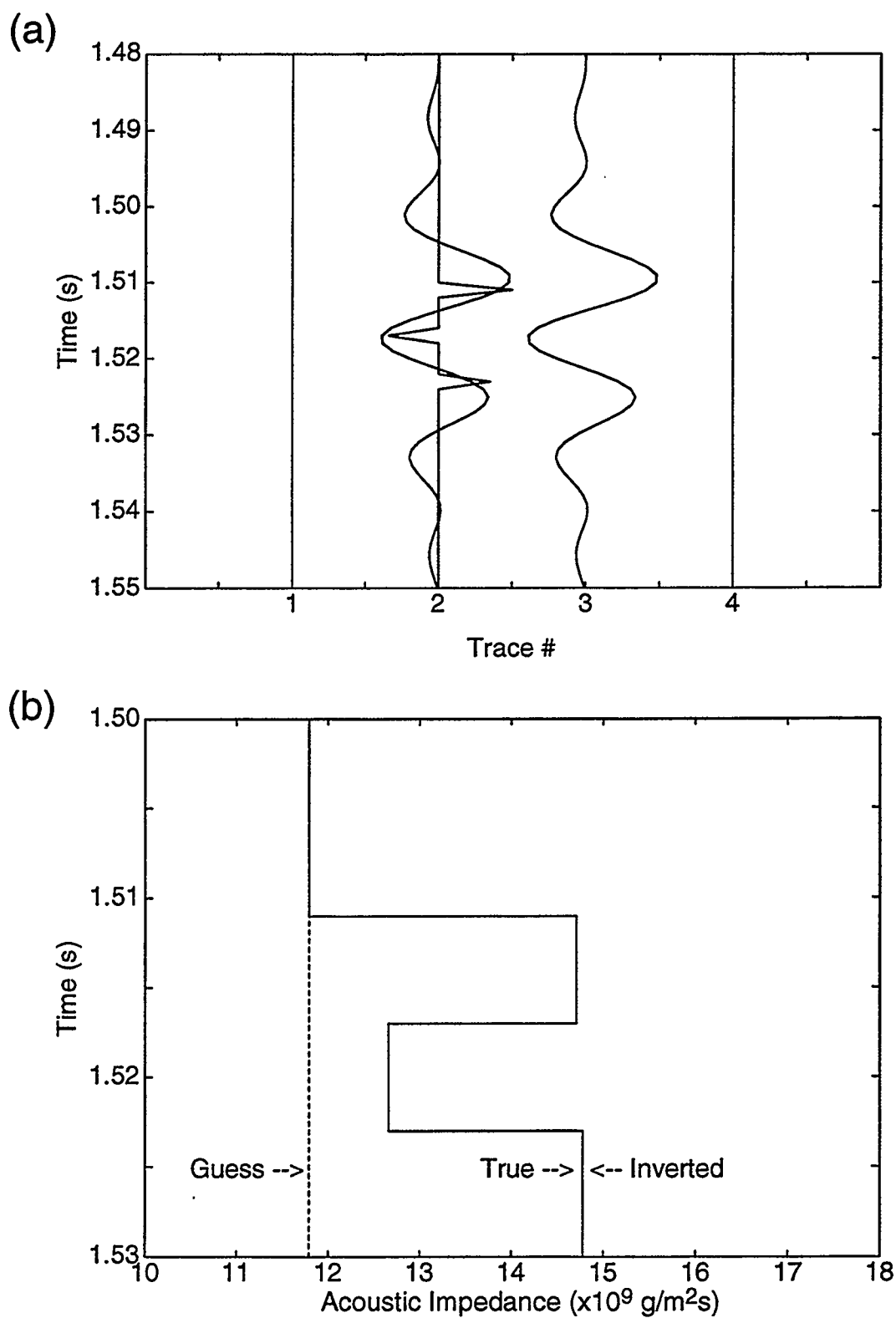


FIG 4.4. Synthetic data-inversion results for VSP wavelet traces; (a) initial guess, inverted, real seismic, and difference traces, and (b) initial, inverted, and real impedance profiles.

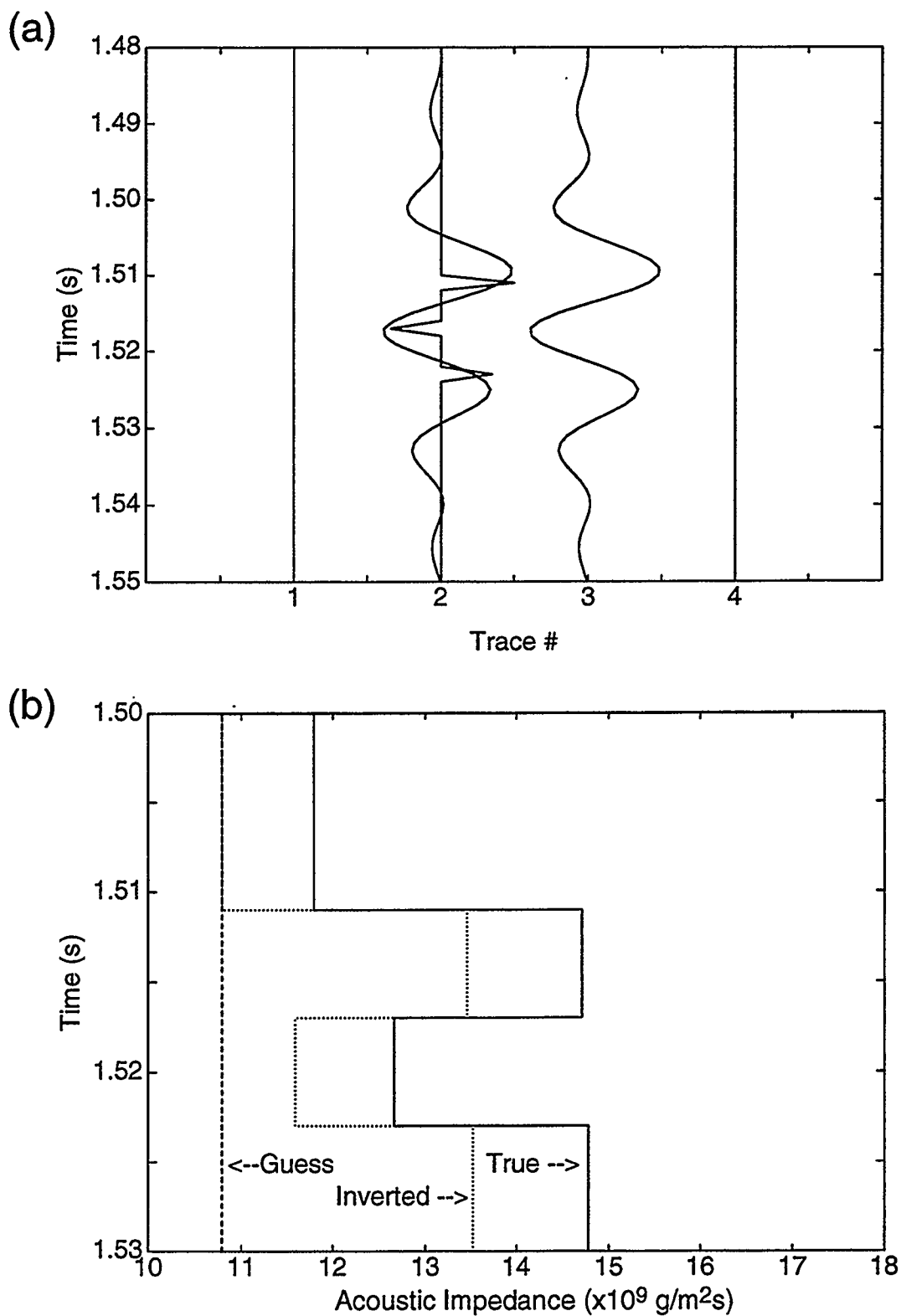


FIG 4.5. Synthetic data-inversion results for VSP wavelet traces with incorrect top impedance; (a) initial guess, inverted, real seismic, and difference traces, and (b) initial, inverted, and real impedance profiles.

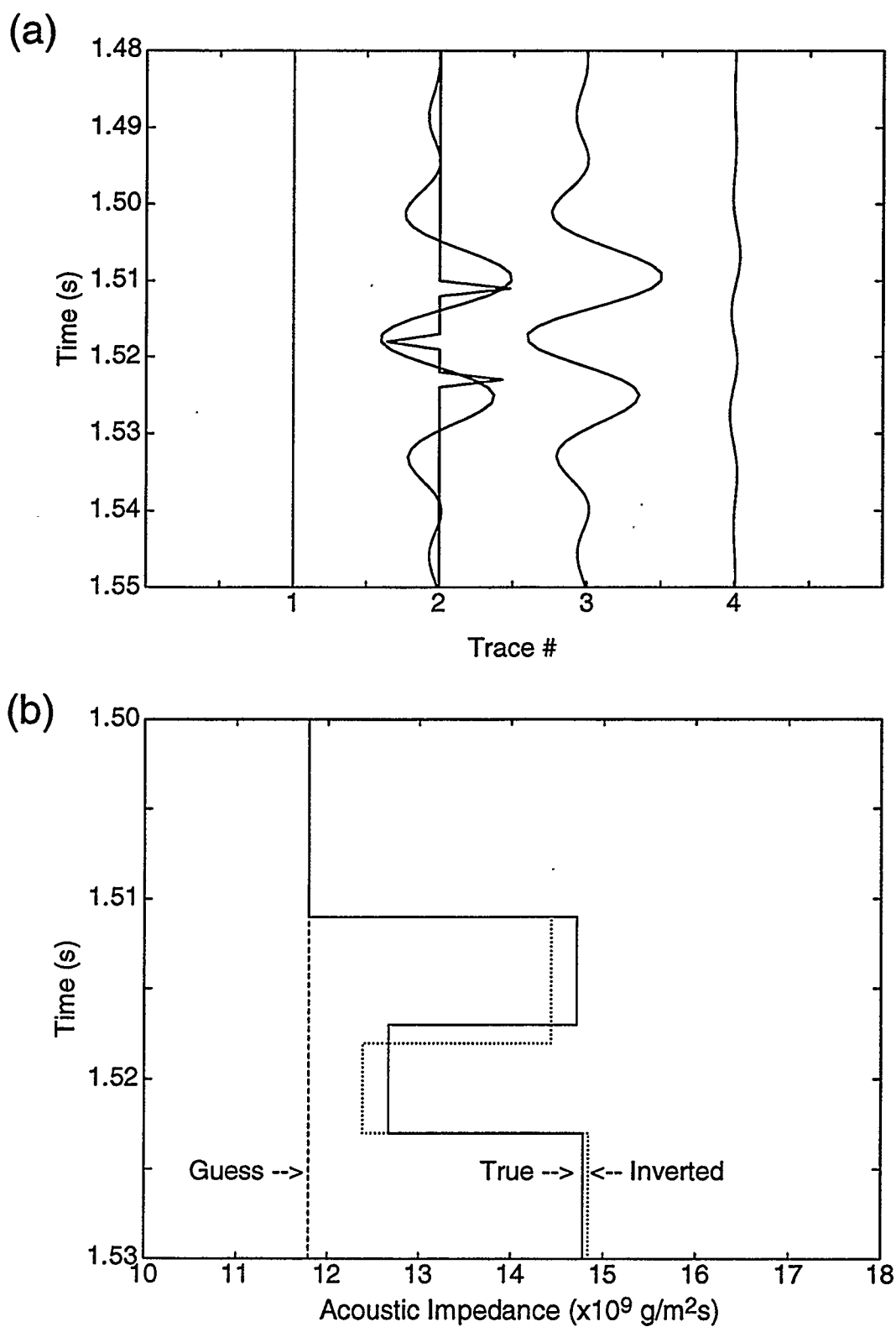


FIG 4.6. Synthetic data-inversion results for VSP wavelet traces with second event at the wrong time; (a) initial guess, inverted, real seismic, and difference traces, and (b) initial, inverted, and real impedance profiles.

The final test of the algorithm was to add random noise to the original data trace. In the first case random noise with a normal distribution and an RMS value of 0.0279 was added to the seismic trace. The noise-free seismic data over the window of 1.480 s to 1.530 s has an RMS value of 0.0420. The results of the algorithm performance on these data are shown in Figure 4.7. Three iterations were again required to converge to the final solution. The inverted impedance curve for these data is closer to the true impedance curve than the initial guess curve, indicating that the algorithm has converged towards the true solution. There is an extreme amount of noise added to these data as shown by the difference trace in Figure 4.7(a), and the algorithm has still resulted in a fairly good solution. The algorithm has also been tested using noise with a lower RMS value of 0.0064, and the results are shown in Figure 4.8. The algorithm performs better with lower energy noise, as the algorithm converges very close to the true solution. The effects of noise on the algorithm vary with the amount of noise added to the true seismic trace.

Overall, the algorithm performs well when the imposed assumptions are met. For relatively noise-free data with known event traveltimes and a known wavelet the algorithm performs very well, and can invert for thin beds. When the assumptions are not met the algorithm does not perform perfectly; however it always was found to converge to a better solution than the initial guess. With VSP data where the signal-to-noise ratio is generally high, the traveltimes of the events can be accurately determined, and the seismic wavelet is well known, this inversion algorithm is appropriate.

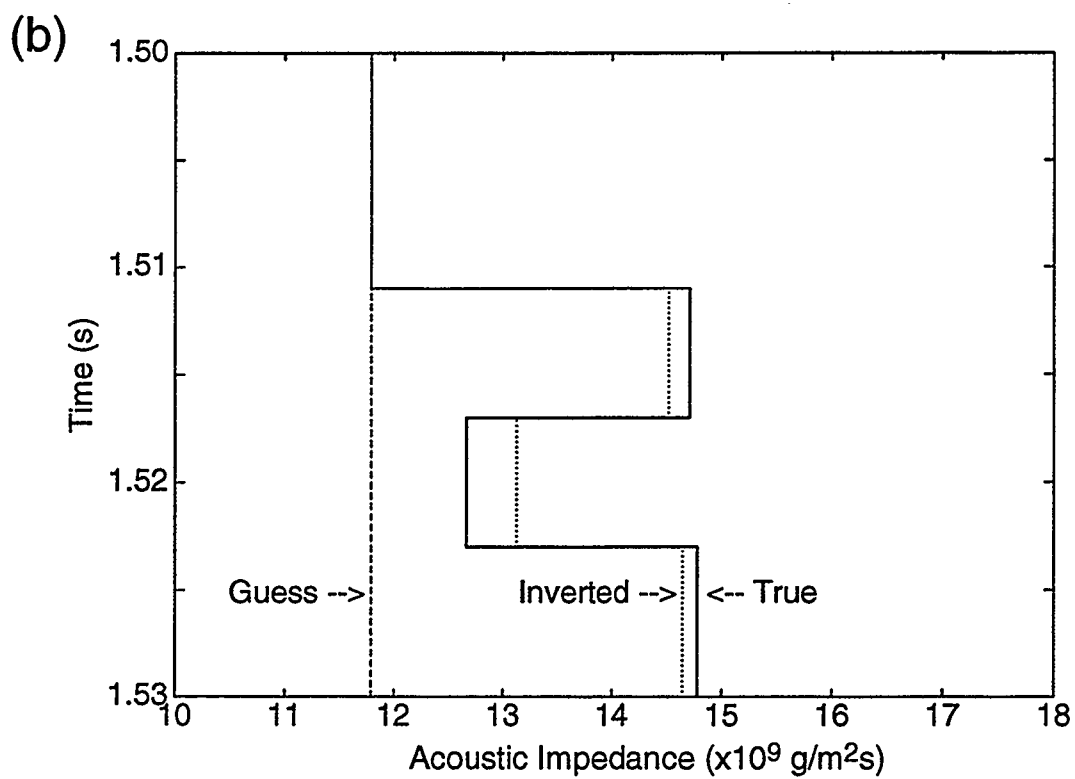
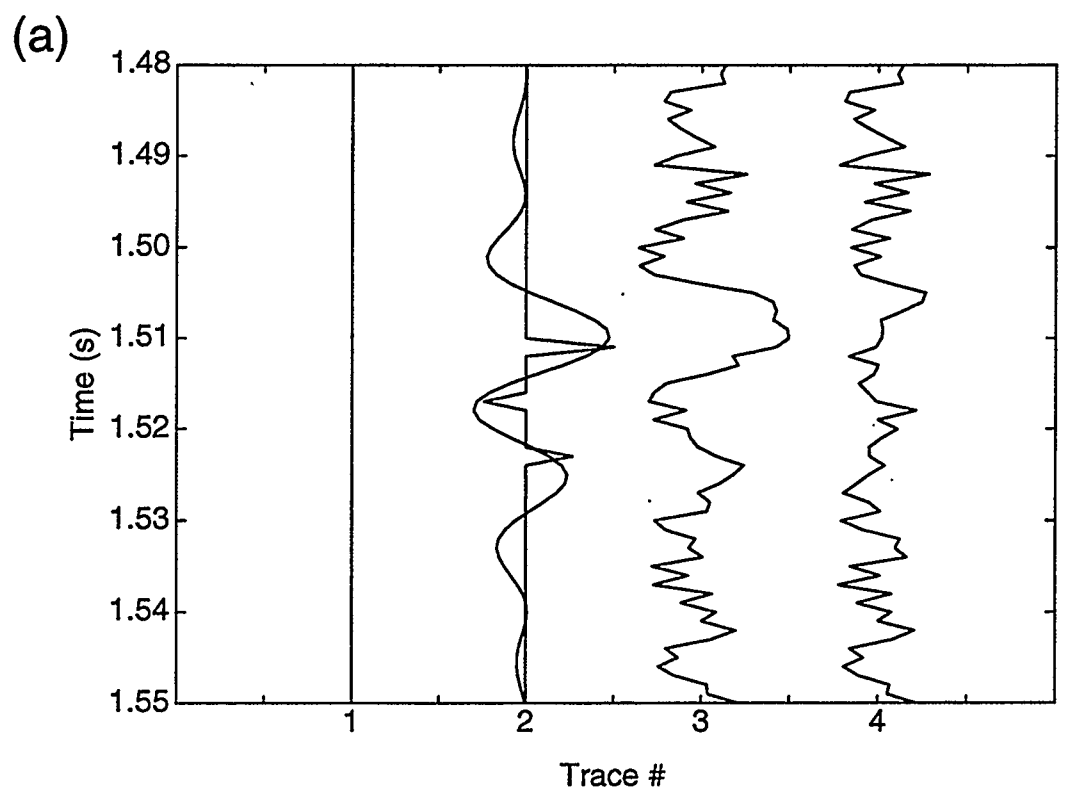


FIG 4.7. Synthetic data-inversion results for VSP wavelet traces with random noise with a uniform distribution; (a) initial guess, inverted, real seismic, and difference traces, and (b) initial, inverted, and real impedance profiles.



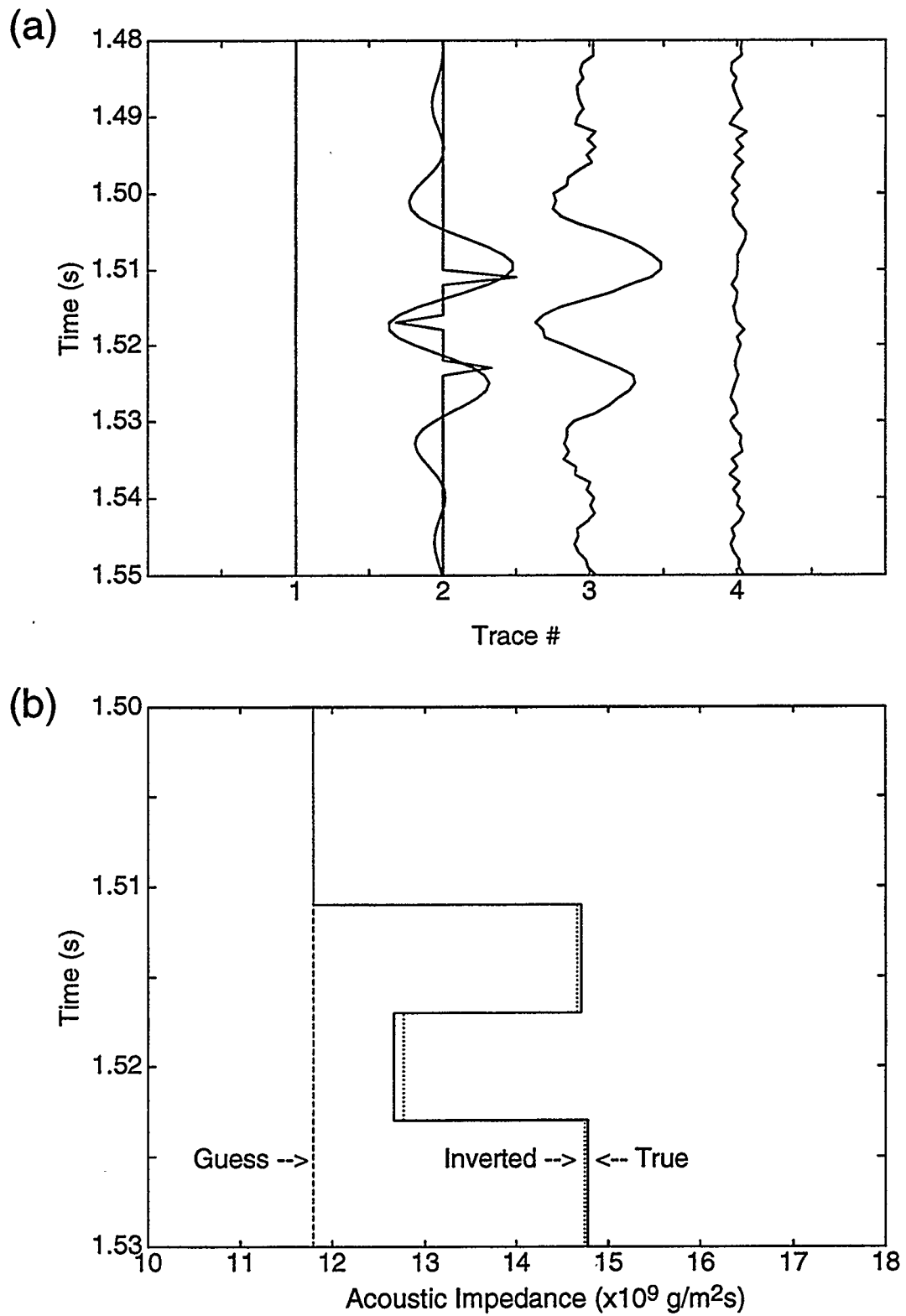


FIG 4.8. Synthetic data-inversion results for VSP wavelet traces with random noise with a uniform distribution; (a) initial guess, inverted, real seismic, and difference traces, and (b) initial, inverted, and real impedance profiles.

### 4.2.2 Real Data Example

The 1-D inversion algorithm has been tested using synthetic data, and shown to be suitable for zero-offset VSP data. The results of the inversion of the Well A VSP corridor stack are shown in Figure 4.9. Figure 4.9(a) shows the forward-model seismic response for the initial guess (trace 1), the inverted seismic response (trace 2), the VSP corridor stack (trace 3), and the difference between the inverted trace and the VSP corridor stack (trace 4). Figure 4.9(b) shows the initial-guess impedance profile (solid curve) and the inverted impedance profile (dashed curve). The initial-guess impedance is from the well-log bulk density and VSP interval velocities. The inverted trace matches the VSP trace better than the original model trace, indicating that the inversion algorithm has performed well. The error trace does have some residual energy; however, the residual trace has a cyclical nature and does not appear to correlate with any events. The cyclical trace appearance may be due to small frequency-bandwidth differences between the VSP wavelet and the reflected data, or to small-amplitude events that are not in the original model. Overall, the inverted-impedance curve has the same high-frequency trends as the initial-guess impedance curve with the exception of the event at approximately 1.545 s, for which the inversion has changed the polarity. The low-frequency trend of the initial guess and inverted impedance profiles do not match. As shown by Lindseth (1979) the seismic data are bandlimited with no frequencies under about 10 Hz, so the low frequency component of the impedance profile can not be extracted from the data. Another interesting result is the smaller relative impedance change at the top of the porosity at 1.517 s. This suggests that the impedance of the top limestone layer is lower than that determined from bulk-density log and VSP *P*-wave velocity. This effect may also be due to the limestone unit thinning away from the borehole, so that the average thickness of the layer over the VSP Fresnel zone is less than the thickness at the well bore. It may also be explained by the rock properties of the upper limestone unit

upper limestone unit changing away from the borehole. In summary the inversion of the VSP corridor stack gives a reasonable result, which suggests that the method may be expanded to the joint  $P$ - $P/P$ - $SV$  AVO inversion problem.

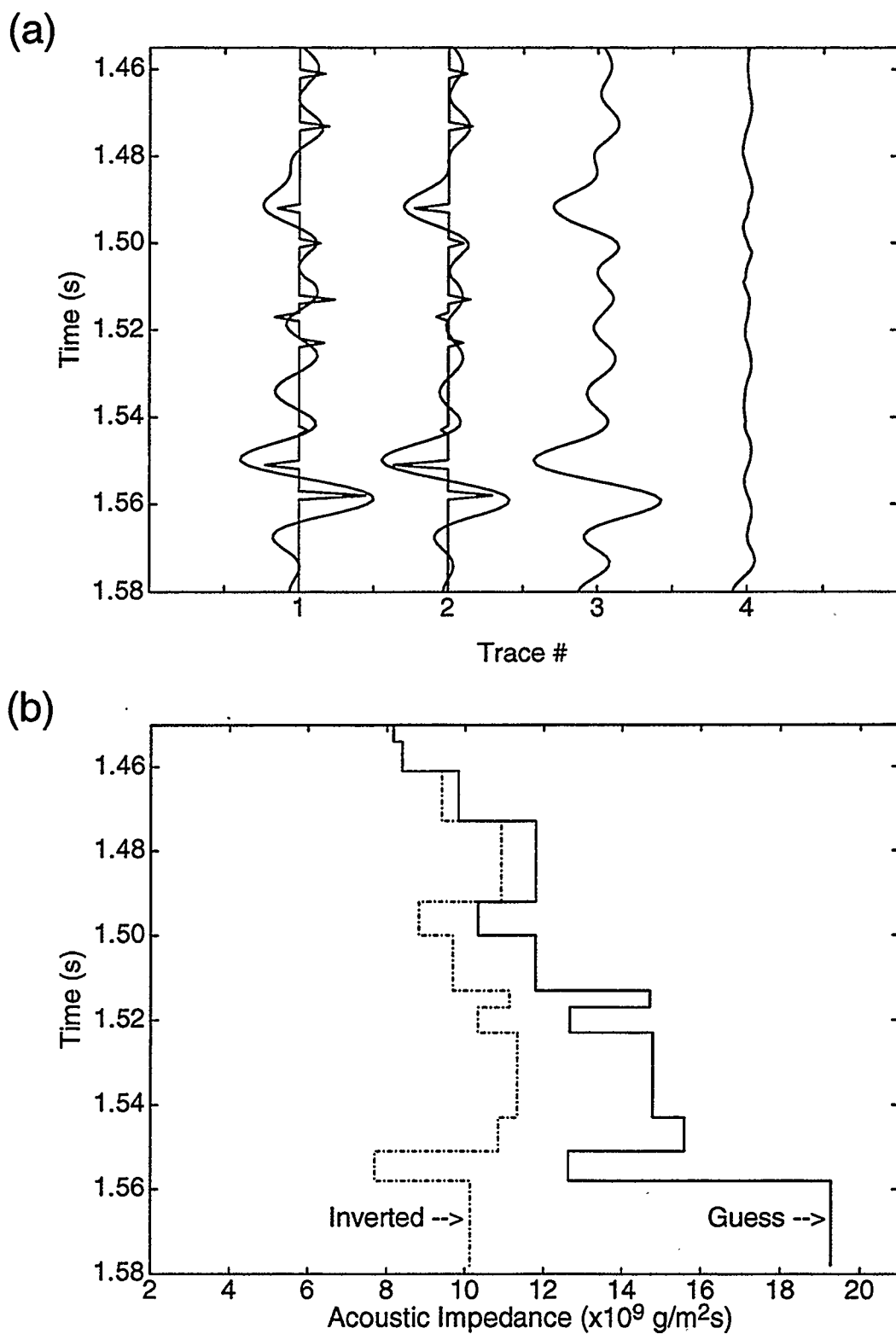


FIG 4.9. Field data-inversion results; (a) initial guess, inverted, real seismic and difference traces, and (b) initial guess (solid) and inverted (dashed) impedance profiles.

### 4.3 Joint *P-P/P-SV* AVO Inversion

There are several methods to approach the inversion of offset-dependent seismic data. In the loose sense of inversion problems, any method that can be used to obtain an estimate of some model parameters from the seismic data applies. A GLI approach is used in this thesis to obtain a quantitative estimate of the subsurface properties  $V_p$ ,  $V_s$ , and  $\rho$ . The GLI method has advantages when there is a good initial guess of the model parameters. A disadvantage is that there is no guarantee of a unique solution. Nonuniqueness is a concern with most inversion problems (Russell, 1988), and it was shown previously in Figure 4.5 that the results of this inversion method are nonunique and dependent on the constraints placed on the inversion.

#### 4.3.1 AVO Inversion GLI Algorithm

An approach similar to that used for the zero-offset VSP inversion is applied to the multioffset VSP *P-P* and *P-SV* traces (Figure 2.37). Equation 4.7 is the inversion formula for the GLI method, where  $\mathbf{A}$  is the partial derivative matrix,  $\mathbf{b}$  is the difference column vector, and  $\mathbf{x}$  is the parameter-update column vector. For the AVO inversion case, the equations become more complicated. To invert the multioffset VSP data, there are twenty traces as the input data vector, ten *P-P* reflectivity traces and ten *P-SV* reflectivity traces. The model parameters are  $V_p$ ,  $V_s$ , and  $\rho$ , and the partial-derivative and update matrices also become more complicated.

The GLI algorithm has been formulated by expressing the *P-P* reflectivity traces as a column vector  $\mathbf{P}=[P_1, P_2, P_3, \dots, P_n]^t$ , where  $P_n$  is the  $n$ th offset *P-P* reflectivity trace. Each  $P_n$  can also be written as a column vector,  $P_n=[Rpp_1, Rpp_2, Rpp_3, \dots, Rpp_m]^t$ , for  $m$  reflectors. Similar expressions can be written for the *P-SV* reflectivity traces;  $\mathbf{S}=[S_1, S_2, S_3, \dots, S_n]^t$ , and  $S_n=[Rps_1, Rps_2, Rps_3, \dots, Rps_m]^t$ . The *P*- and *S*-wave

reflectivity  $P$  and  $S$  can be expanded as a truncated Taylor series about the model parameters

$$\Delta P = \left[ \frac{\partial P}{\partial V_p} \right]_{V_p=V_{0p}} \Delta V_p + \left[ \frac{\partial P}{\partial V_s} \right]_{V_s=V_{0s}} \Delta V_s + \left[ \frac{\partial P}{\partial \rho} \right]_{\rho=\rho_0} \Delta \rho, \quad (4.15a)$$

and

$$\Delta S = \left[ \frac{\partial S}{\partial V_p} \right]_{V_p=V_{0p}} \Delta V_p + \left[ \frac{\partial S}{\partial V_s} \right]_{V_s=V_{0s}} \Delta V_s + \left[ \frac{\partial S}{\partial \rho} \right]_{\rho=\rho_0} \Delta \rho. \quad (4.15b)$$

These equations can be solved simultaneously for the model parameter updates  $M_0(V_p, V_s, \rho)$

$$\begin{pmatrix} \Delta P \\ \Delta S \end{pmatrix} = \begin{pmatrix} \frac{\partial P}{\partial M_0} \\ \frac{\partial S}{\partial M_0} \end{pmatrix} (M - M_0), \quad (4.16)$$

where  $\Delta P$  and  $\Delta S$  are the difference between the forward modeled and field  $P$ - $P$  and  $P$ - $SV$  traces.

As in the case of formulating the zero-offset inversion, insight into the offset inversion algorithm can be developed by first considering a simple model. For a two-layer model inversion constrained by the model parameters in the top layer,  $V_{p2}$ ,  $V_{s2}$ , and  $\rho_2$  of the lower layer are the inversion parameters. If the true model parameters are defined as  $V_{p'}$ ,  $V_{s'}$  and  $\rho'$ , Equation 4.16 becomes

$$\begin{pmatrix} \Delta P \\ \Delta S \end{pmatrix} = \begin{pmatrix} \frac{\partial P}{\partial V_{p2}} & \frac{\partial P}{\partial V_{s2}} & \frac{\partial P}{\partial \rho_2} \\ \frac{\partial S}{\partial V_{p2}^2} & \frac{\partial S}{\partial V_{s2}} & \frac{\partial S}{\partial \rho_2} \end{pmatrix} \begin{pmatrix} V_{p'} - V_{p2} \\ V_{s'} - V_{s2} \\ \rho' - \rho_2 \end{pmatrix} \quad (4.17)$$

Equation 4.17 is of the form  $\mathbf{Ax}=\mathbf{b}$  and can be solved for  $\mathbf{x}$  (the model updates) using damped least squares (Equation 4.8). Further analysis of Equation 4.17 shows that to expand the problem to a multilayer case, the number of columns in  $\mathbf{A}$ , and the number

of rows in **b** are increased to the number of unknown parameters in the problem. Note that the **A** matrix in Equation 4.17 contains partial derivatives of the *P-P* and *P-SV* reflectivities with respect to the model parameters. The forward modeling algorithm uses the Zoeppritz equations to compute the offset reflection coefficients, and it is necessary to analytically or numerically calculate these partial derivatives. Because the analytical solution of the Zoeppritz equation partial derivative is not trivial, a numerical derivative is calculated here.

The partial derivatives in Equation 4.17 are calculated numerically from the Zoeppritz equations using first differences. It is important to test the stability of this process. The derivative is stable if there is a linear change in *P-P* and *P-SV* reflection coefficients with changes in one of the layer parameters at a constant angle of incidence. To test this the reflection coefficients have been calculated for a two-layer model with  $V_P = 5500$  m/s,  $V_S = 2800$  m/s and  $\rho = 2650$  g/m<sup>3</sup> in the upper half space. The parameters in the lower half space were varied by  $\pm 100$  (m/s or g/m<sup>3</sup>) stepping by 1 unit, starting at  $V_P = 4000$  m/s,  $V_S = 2000$  m/s and  $\rho = 2450$  g/m<sup>3</sup>. One parameter was varied at a time, and both the *P-P* ( $R_{pp}$ ) and *P-SV* ( $R_{ps}$ ) reflection coefficients were calculated for a constant 30 degree angle of incidence; the results are shown in Figure 4.10. Figure 4.10(a) shows the change of  $R_{pp}$  and  $R_{ps}$  versus changes in *P*-wave velocity in layer two;  $R_{pp}$  decreases linearly and  $R_{ps}$  increases linearly with increasing *P*-wave velocity. Figure 4.10(b) shows  $R_{pp}$  and  $R_{ps}$  versus changes in *S*-wave velocity in layer two. In this case both  $R_{pp}$  and  $R_{ps}$  increase linearly with increasing *S*-wave velocity in the lower half space. Figure 4.10(c) shows the change of reflection coefficient versus changes in density in layer two; this case mirrors the case of increasing *P*-wave velocity in the second layer where  $R_{pp}$  decrease and  $R_{ps}$  increase linearly with increasing density. This analysis shows that *P-P* and *P-SV* reflection coefficients calculated using the Zoeppritz

equations change linearly with respect to the layer parameters  $V_P$ ,  $V_S$ , and  $\rho$ . Therefore, the partial derivatives in Equation 4.17 can be calculated numerically.

The partial derivatives of the Zoeppritz equations show how the variation of reflection coefficient versus angle of incidence changes with respect to each parameter, at what angle of incidence these changes are significant, and the sensitivity of the reflection coefficient curves to each parameter. Figure 4.11(a) is a plot of the  $P$ - $P$  reflection-coefficient partial derivative with respect to the elastic parameters of the lower half space using the same model used to calculate the curves in Figure 4.10. The solid curve is the partial derivative with respect to the  $P$ -wave velocity, the dashed curve is with respect to the  $S$ -wave velocity, and the dotted curve is with respect to density. The  $S$ -wave velocity curve and the density curve both increase with angle of incidence, while the  $P$ -wave velocity curve decreases with angle of incidence. This graph also shows that the  $P$ - $P$  reflection coefficient is dependent entirely on  $V_P$  and  $\rho$  at normal incidence. The  $P$ - $P$  reflection coefficient dependence on  $V_S$  becomes significant at a  $P$ -wave angle of incidence of approximately 20 degrees, and this dependence continues to increase with increasing angle of incidence. This implies that  $P$ -wave angles of incidence of at least 20 degrees are necessary to extract any useful  $V_S$  information.

The partial derivatives of the  $P$ - $SV$  reflection coefficient with respect to the parameters in the lower half space are shown in Figure 4.11(b). The  $P$ - $SV$  partial derivatives approach zero at normal incidence. The partial derivatives with respect to  $V_S$  and  $\rho$  are coupled together up to angles of incidence of approximately 25 degrees and then diverge. At angles greater than 25 degrees the dependence on  $\rho$  falls off and the dependence on  $V_S$  increases. The partial derivative with respect to  $V_P$  is smaller, but does increase with increasing angles of incidence.

This analysis shows the promise of using both  $P$ - $P$  and  $P$ - $SV$  reflections in a joint inversion. The  $P$ - $SV$  reflections are dependent mainly on  $V_S$  and  $\rho$ , while the  $P$ - $P$



reflections are only significantly dependent on  $V_S$  at  $P$ -wave angles of incidence greater than 25 degrees. Using both  $P$ - $P$  and  $P$ - $SV$  measurements in a joint inversion should therefore, give better results than the  $P$ - $P$  inversion alone, especially for  $V_S$  information.

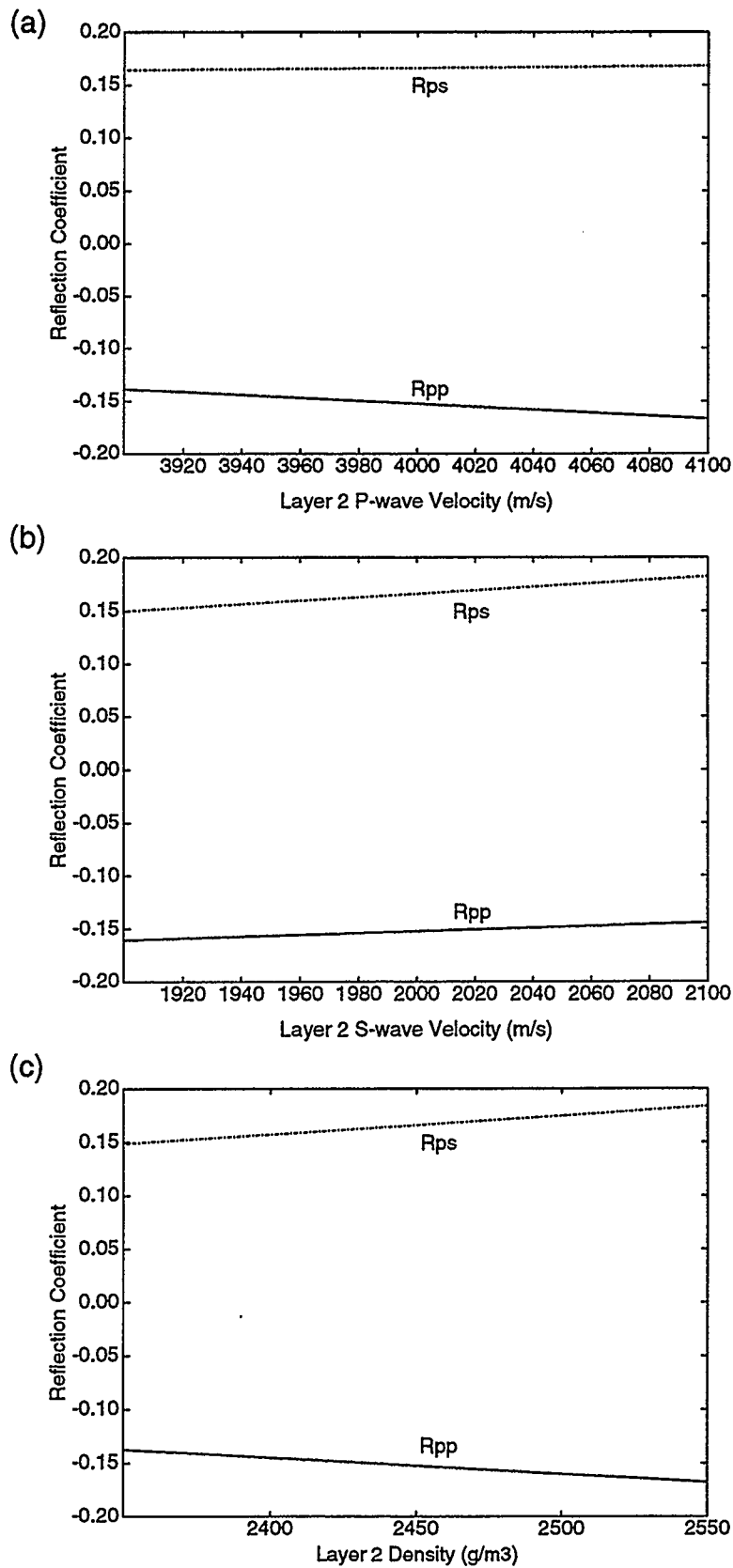


FIG 4.10.  $P$ - $P$  and  $P$ - $SV$  reflection coefficient versus (a)  $P$ -wave velocity, (b)  $S$ -wave velocity, and (c) density of the lower half space for a constant angle of incidence of 30 degrees.

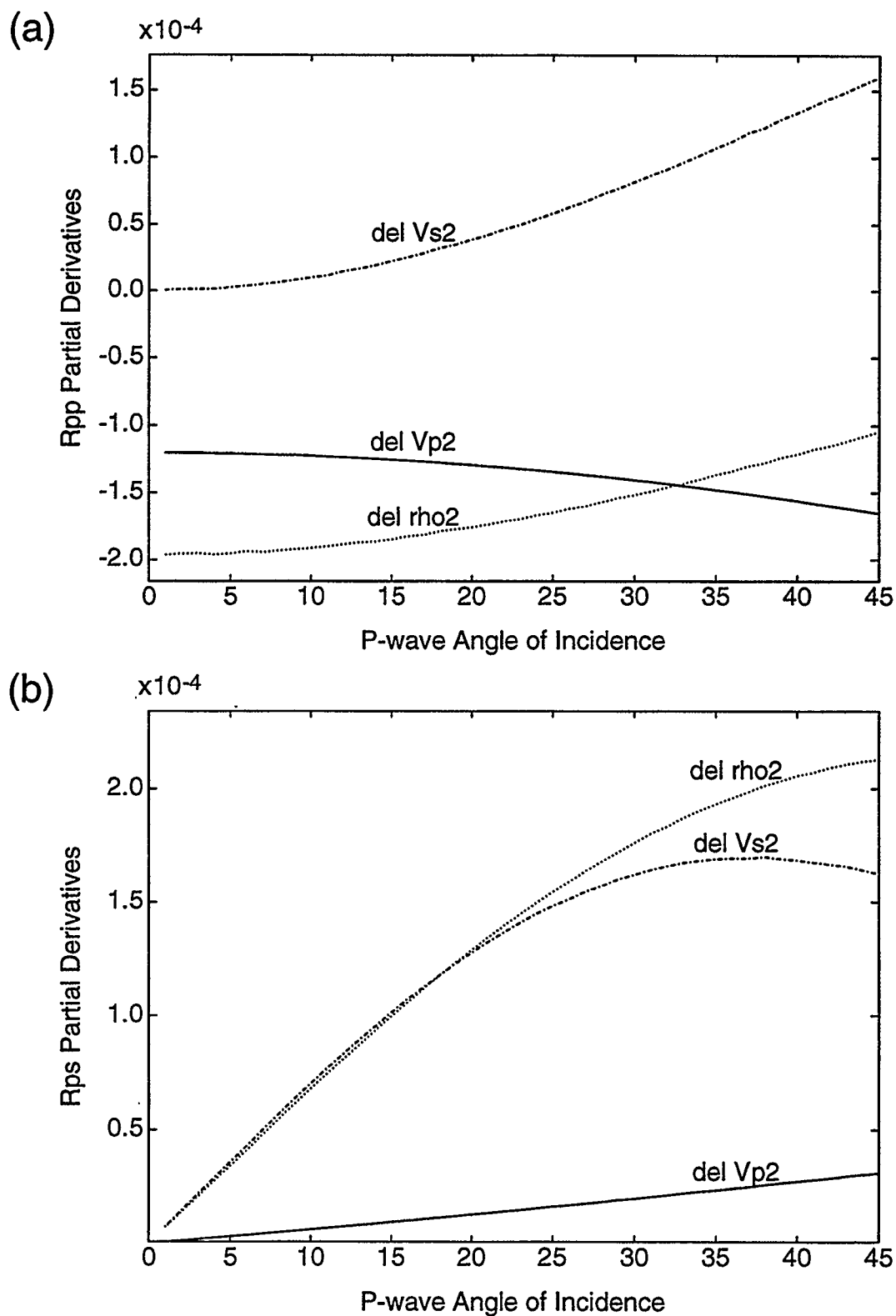


FIG 4.11. Partial derivatives of (a)  $P$ - $P$  and (b)  $P$ - $SV$  Zoeppritz equations. The solid curve is with respect to  $V_p$  in the lower half space, the dotted curve is with respect to  $\rho$ , and the dashed curve is with respect to  $V_s$ .

### 4.3.2 Synthetic Data Inversion

A four-layer model was generated for testing the inversion algorithm using the VSP interval velocities and log bulk densities in the zone of interest. The model data consist of the reflection coefficients and angles of incidence, and are shown in Figure 4.12. These data traces show reflections aligned at time 100, 200, and 300 ms; this is only for display purposes, as the inversion algorithm ignores the non-data points and deals only with the amplitudes of the reflections. The results of inputting an incorrect initial guess into the inversion are shown in Figure 4.13. The  $P$ -wave velocity,  $S$ -wave velocity and density curves are plotted for three models; the initial-guess model (dashed line), the inverted model (dotted line), and the true model (solid line). The inverted model and the true model agree exactly in this case, so that only the solid curve shows up on the display. This agreement means that in the perfect case, the Zoeppritz equations can be inverted exactly for the reservoir parameters  $V_p$ ,  $V_s$ , and  $\rho$ . This solution is constrained by the parameters in the top layer, which are correct in the initial guess. The performance of the algorithm under certain unfavorable conditions needs to be tested before applying the algorithm to real data. The effects of; incorrect parameters in the top layer, incorrect angles of incidence, and noise are all important.

This inversion technique uses the upper layer as a constraint on the lower layers, so it is necessary to test the effects of an incorrect upper layer on the inversion. The log curves of the inversion results for an incorrect upper layer are shown in Figure 4.14. These results show that the inverted layer parameters are dependent on the upper-layer parameters. The inverted parameters (dotted curves) are bulk shifted from the true parameters by the error in the upper-layer parameters. The relative changes in parameters are very close to correct, so the inversion has resolved the changes in parameters, but not the absolute parameters in this case.

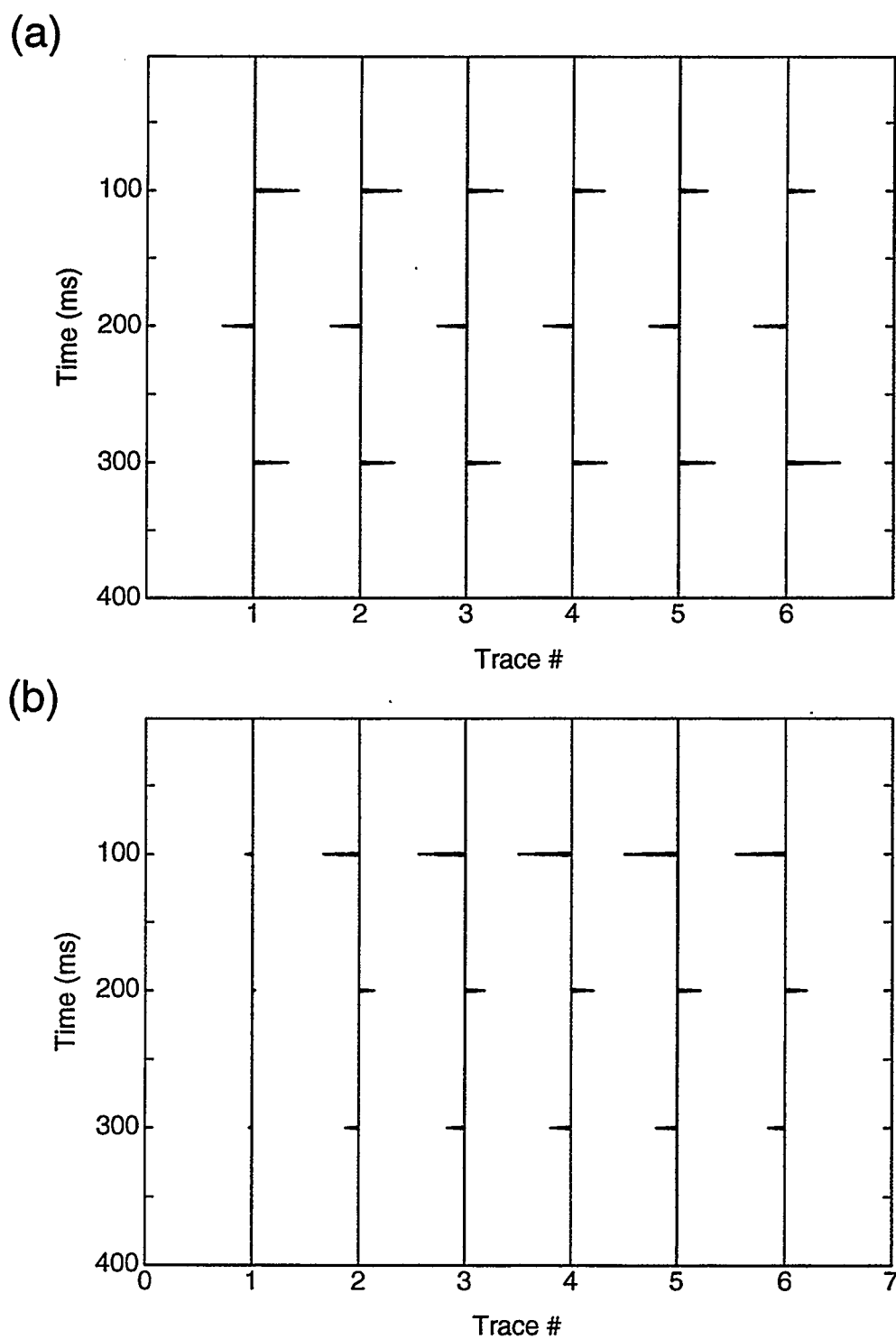


FIG 4.12. Synthetic AVO model data; (a)  $P$ - $P$  reflection coefficient traces, and (b)  $P$ - $SV$  reflection coefficient traces.

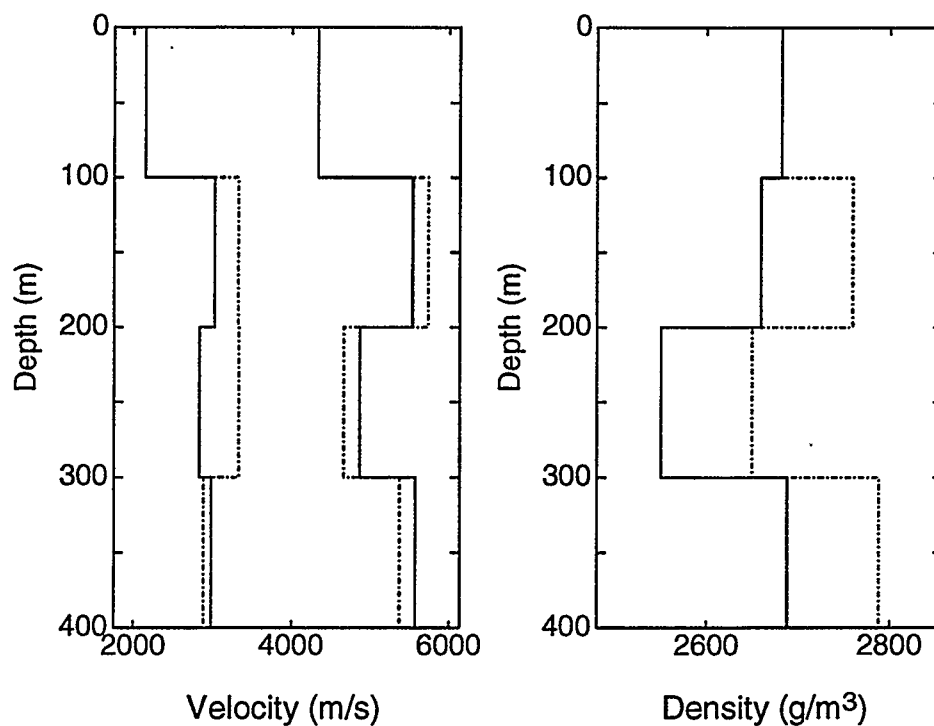


FIG 4.13. Initial-guess (dashed line), inverted (dotted line), and true (solid line) model parameter curves.

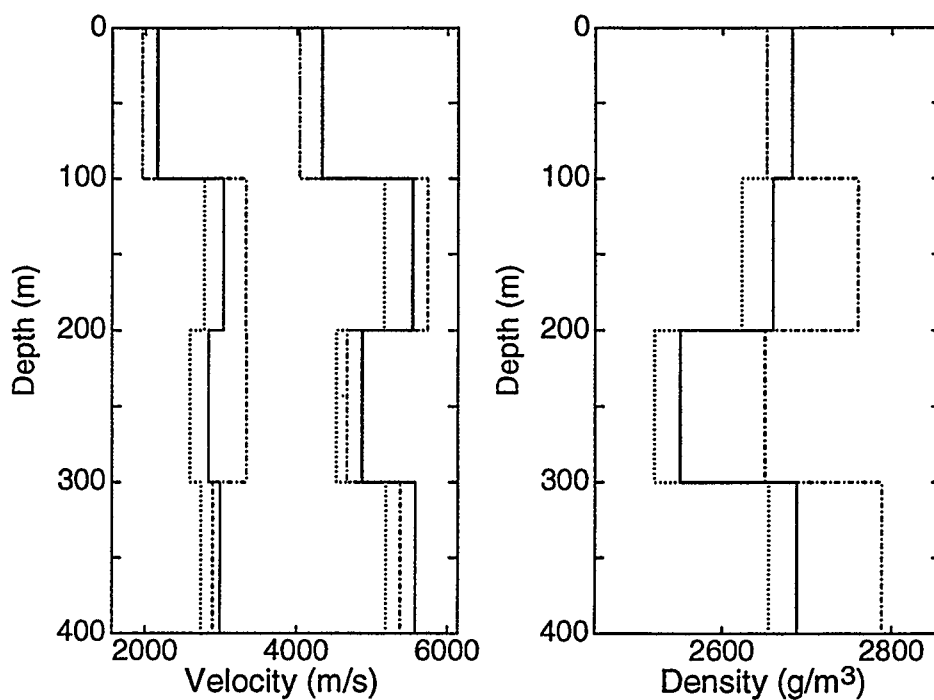


FIG 4.14. Initial-guess (dashed line), inverted (dotted line), and true (solid line) model parameters for an initial guess with incorrect upper layer parameters.

In the previous examples, the correct angles of incidence have been input into the inversion algorithm. These angles of incidence are accurate to four decimal places (in degrees). Another important aspect of the inversion is the effect of less accurate and incorrect angles of incidence. The results of using angles of incidence rounded to the nearest whole number are shown in Figure 4.15. This Figure shows that the density is affected more by the angles of incidence than the  $P$ - and  $S$ -wave velocities are. The velocity inversion is nearly exact, but there are residual errors in the inverted density curve. So, these results imply that accurate angles of incidence are necessary to optimally invert for all the layer parameters. The  $P$ - and  $S$ -wave velocities are less dependent on the angles of incidence than the density. The effect of incorrect angles of incidence is tested further by adding random noise with a normal distribution and RMS value of 1.57 to the angles of incidence. These results show (Figure 4.16) again that the inversion is sensitive to the angles of incidence. All the layer parameters are closer to the true parameters than the initial guess, which indicates that the inversion does converge under these circumstances. However, the convergence is not perfect and there are residual errors in the final solution.

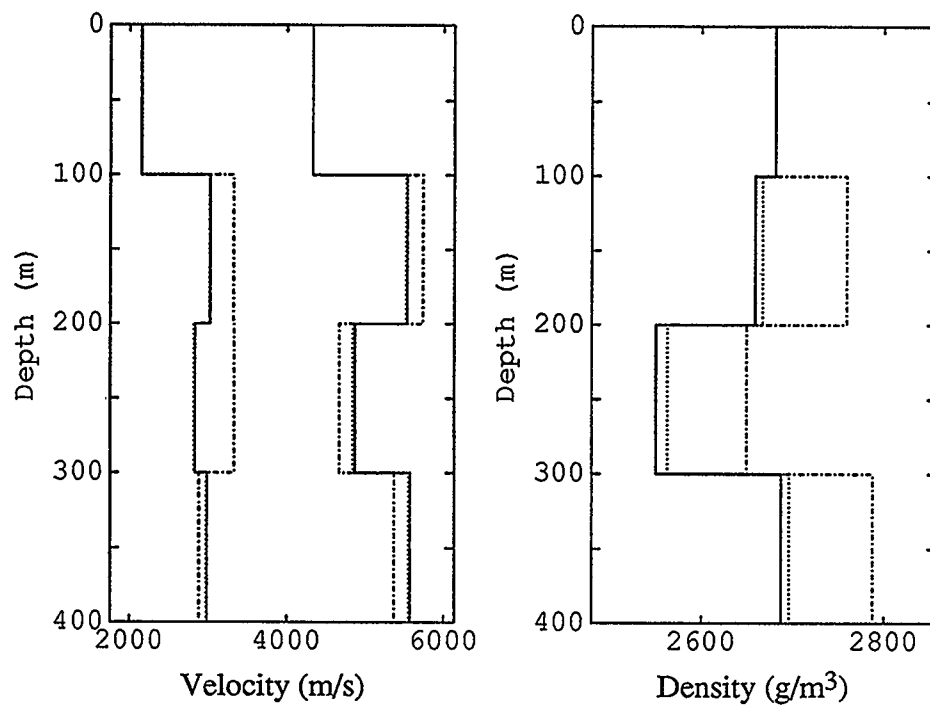


FIG 4.15. Initial-guess (dashed line), inverted (dotted line), and true (solid line) model parameters for rounded angles on incidence.

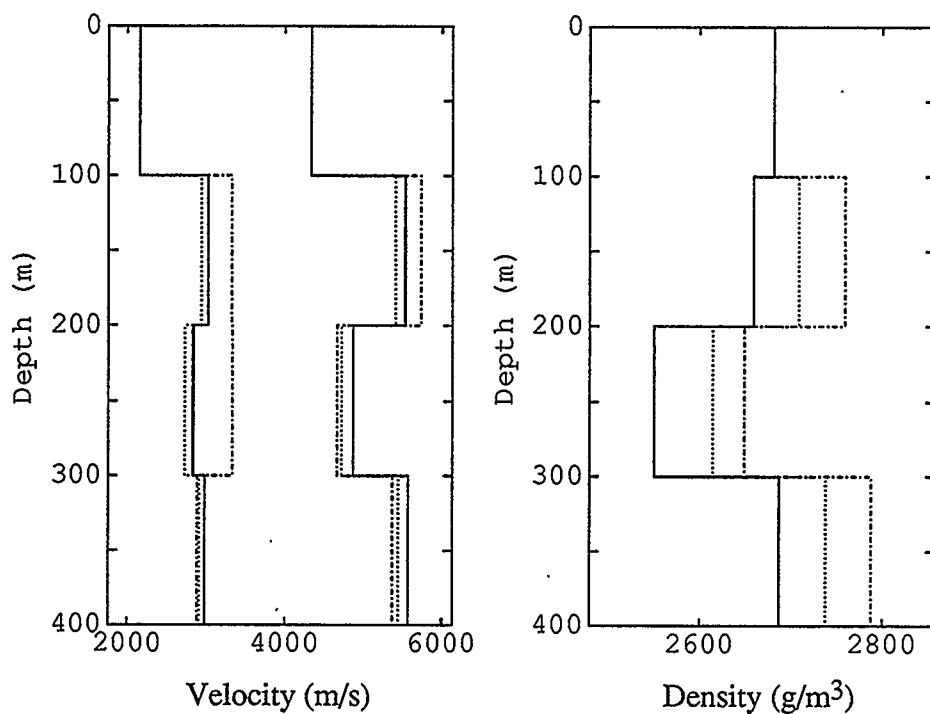


FIG 4.16. Initial-guess (dashed line), inverted (dotted line), and true (solid line) model parameters for random noise added to angles of incidence.



To test the algorithm further, random noise with an RMS value of 0.0124 is added to the data. The RMS value of the noise-free  $P$ -wave data is 0.0931 and the RMS value of the noise-free  $S$ -wave data is 0.0634; this gives a the signal-to-noise ratio for the  $P$ - $P$  data of 7.51:1, and a signal-to-noise ratio for the  $P$ - $SV$  data of 5.11:1. The results of this test (Figure 4.17) show that the inversion is sensitive to noise in the data. The inversion has diverged from the initial guess for the lower two layers. The effect is more extreme for the density, as the density contrast changes polarity at the second event. The changes in  $P$ - and  $S$ -wave velocity are in the correct direction, but the convergence is poor. The results of adding noise with an RMS value of 0.00124 ( $P$ - $P$  signal-to-noise ratio of 75.1:1 and  $P$ - $SV$  signal-to-noise ratio of 51.1:1) to the data are shown in Figure 4.18. These results are much better than in the previous case, as expected. The convergence is good for all the parameters, and very close to exact.

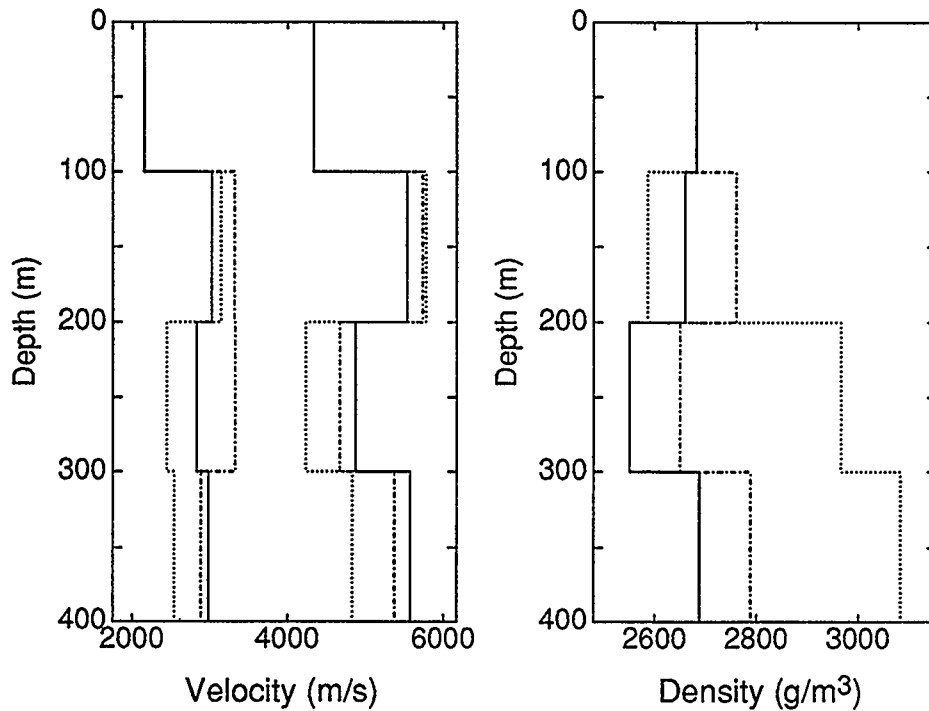


FIG 4.17. Model parameter curves with noise added to data; initial-guess (dashed line), inverted (dotted line), and true (solid line) model parameters.

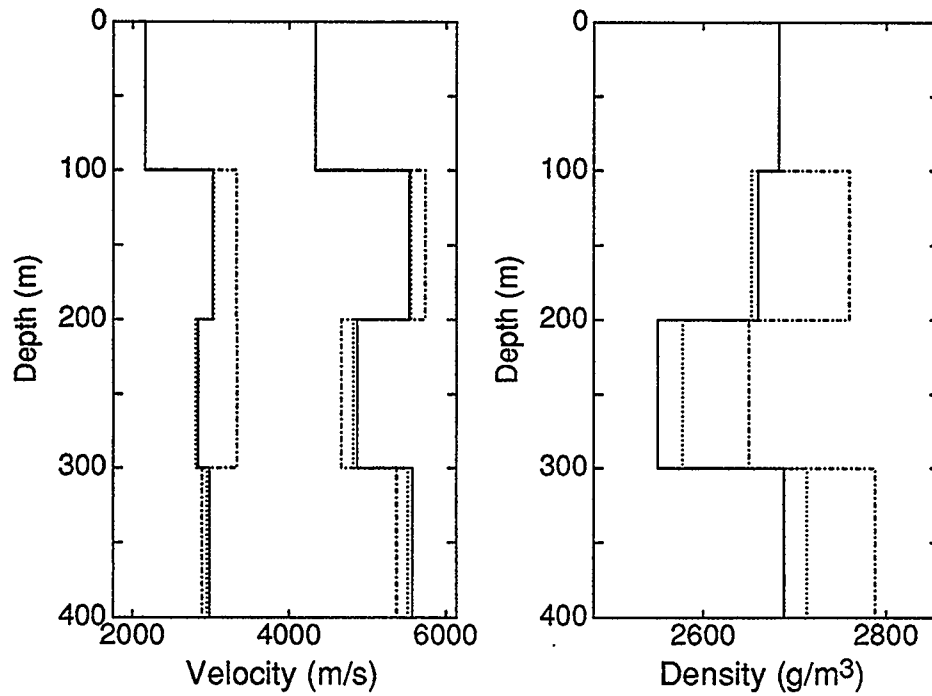


FIG 4.18. Model parameter curves with random noise added to data; initial-guess (dashed line), inverted (dotted line), and true (solid line) model parameters.

The straight inversion of the Zoeppritz equations is a stable process, inverting the data reasonably well under the above conditions. The algorithm can now be expanded to consider real data situations. The  $P$ -wave reflectivity trace is expressed as previously  $P_n = [R_{pp1}, R_{pp2}, R_{pp3}, \dots, R_{ppm}]^t$ , for  $m$  reflectors. The  $P$ -wave trace can be considered as a time series with the reflectivity events at known transit time  $tt_m$ . After convolution with a wavelet of length  $2l+1$ , each  $P$ -wave trace can be expressed as

$$P_n(t) = \sum_{i=1}^m R_{ppi} \sum_{\tau=-l}^l w(\tau) \delta(t - \tau - tt_m). \quad (4.18)$$

Similarly each  $S$ -wave trace can be expressed as

$$s_n(t) = \sum_{i=1}^m R_{psi} \sum_{\tau=-l}^l w(\tau) \delta(t - \tau - tt_m). \quad (4.19)$$

Equations 4.18 and 4.19 can be substituted into Equation 4.16 and the resulting system can be solved using matrix inversion as before.

This more complex algorithm is first tested on synthetic data. These data are generated from the Well A geometry and Earth model. The data are then convolved with a spike wavelet. The input data are the  $P$ - $P$  reflectivity traces (Figure 4.19) and the  $P$ - $SV$  reflectivity traces (Figure 4.20). These data have been flattened on an event and are not NMO corrected. An incorrect Earth model is input into the algorithm as the initial guess. The partial derivative matrix ( $A$ ) for the first iteration is shown in Figure 4.21. Each column is the partial derivative with respect to one of the layer parameters: columns 1, 4, and 7 are the partial derivatives with respect to  $V_p$  in layers 2, 3, and 4 columns 2, 5, and 8 are the partial derivatives with respect to  $V_s$  in layers 2, 3, and 4 columns 3, 6, 9 are the partial derivatives with respect to  $\rho$  in layers 2, 3, and 4. Layer 1 is the upper layer that the inversion is constrained by, and  $V_p$ ,  $V_s$ , and  $\rho$  are being inverted for in layers 2, 3, and 4. The results of the inversion are shown in Figure 4.22, in which the initial guess, inverted and true model parameters are plotted. The algorithm converges to the true model parameters as there is a direct overlap of the final inverted and true model parameters. The algorithm converged in three iterations with no damping applied. For the case where there is no tuning (a spike wavelet) the inversion algorithm converges exactly. The inversion is stopped when the total change in the model parameters is less than 1.0, where velocities (units of m/s) are summed with densities (units of  $\text{g/m}^3$ ), or the algorithm stops converging (the residual error stops decreasing)

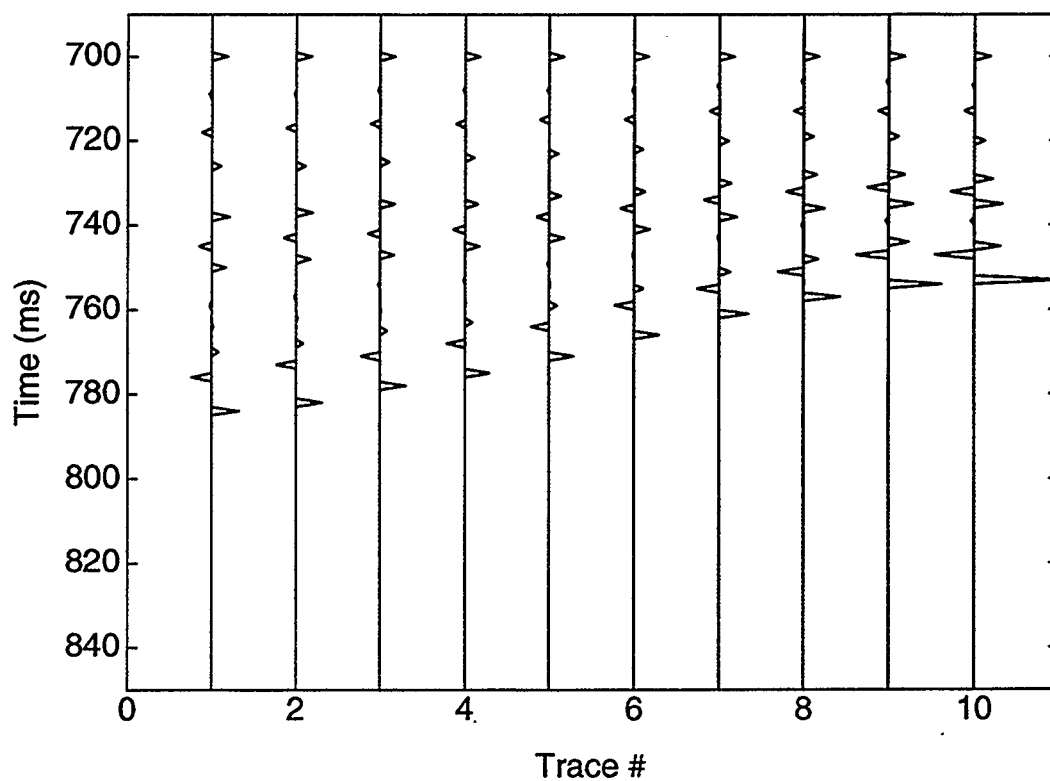


FIG 4.19. *P-P* reflectivity synthetic traces; with one trace for each offset, trace 1 is the near offset (80 m) and trace 10 is the far offset (2500 m).

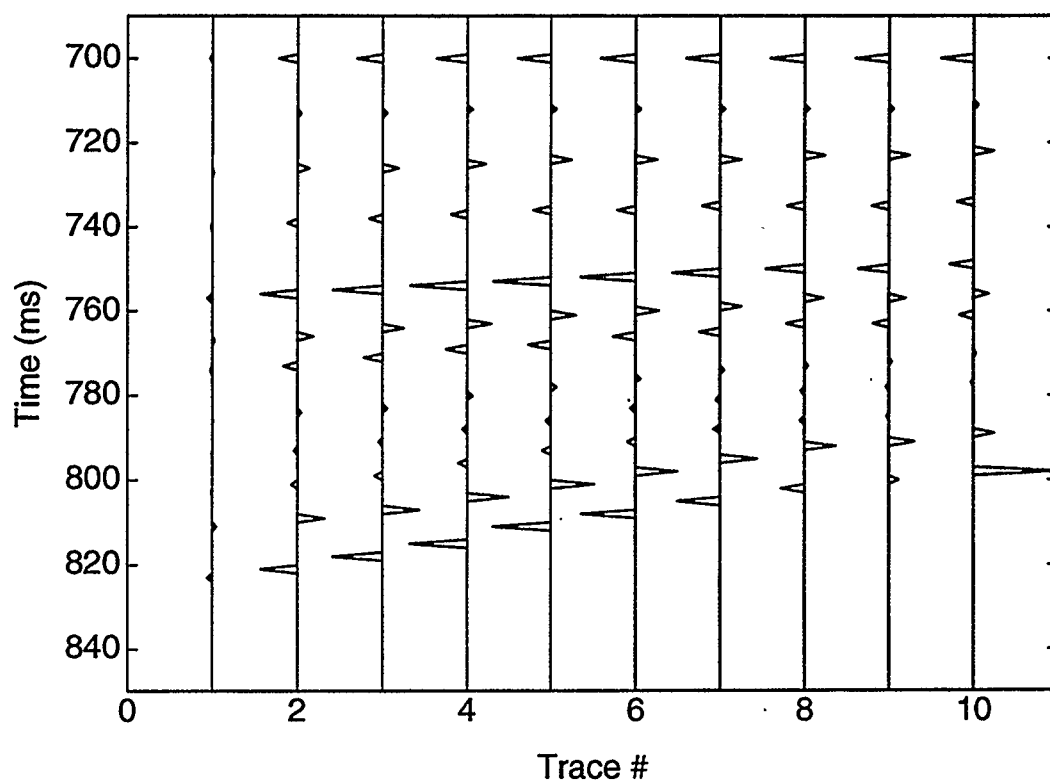


FIG 4.20. *P-SV* reflectivity synthetic traces; with one trace for each offset, trace 1 is the near offset and trace 10 is the far offset.

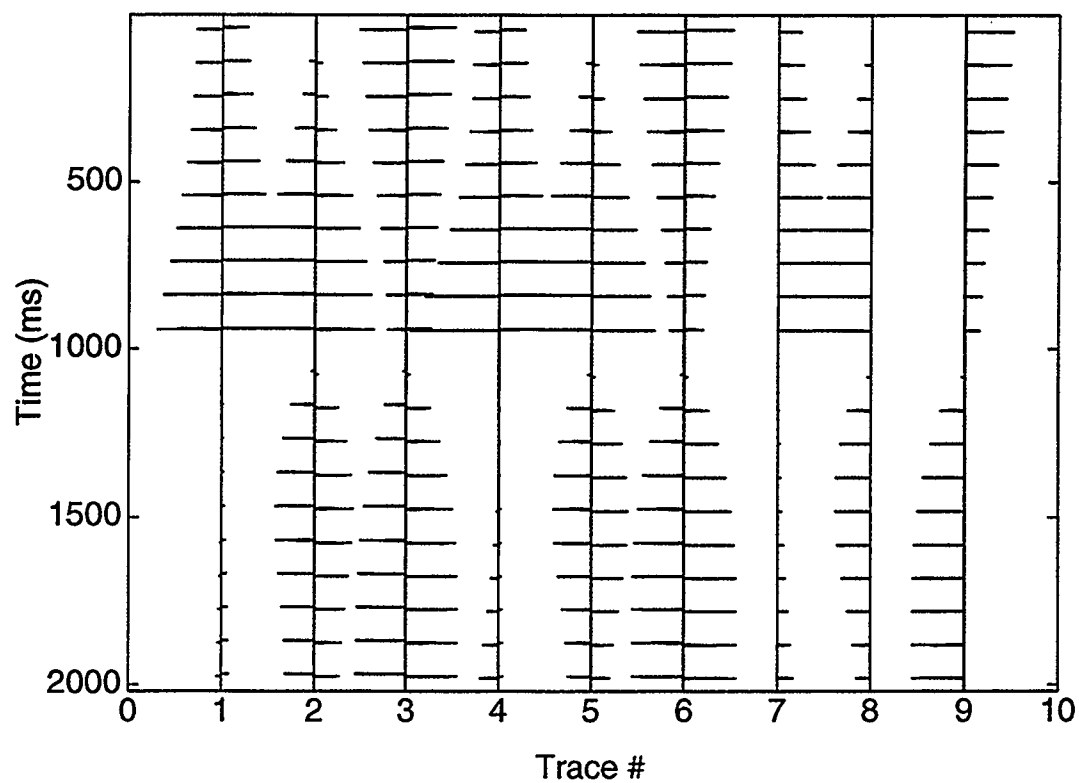


FIG 4.21. Partial derivative matrix  $A$  for the first iteration.

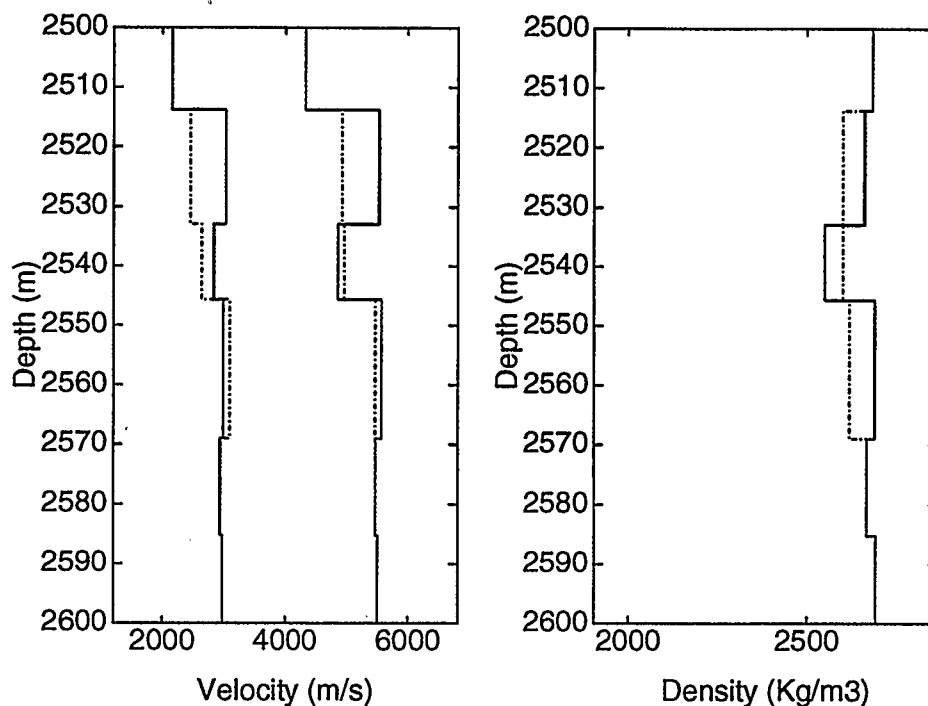


FIG 4.22. Initial-guess (dashed line), inverted (dotted line), and true (solid line) model parameter curves for the inversion with a spike wavelet. The inverted and true parameters are superimposed.

Notice that the traveltimes of the spike events converge at the far offsets in Figure 4.19 and Figure 4.20. These data are not NMO corrected and have been flattened on an event at 700 ms. There is a loss of information with increasing offsets due to a decrease in the traveltime difference between reflectors. This also causes an increase in tuning versus offset. This is a major concern when considering the AVO problem. As shown in Figure 4.10, the  $P$ - $P$  reflection coefficient becomes significantly dependent on the  $S$ -wave velocity at angles of incidence greater than 20 degrees. The increase in tuning versus offset limits the offset information and, thus, the  $S$ -wave velocity information in the  $P$ - $P$  reflections. The  $P$ - $SV$  reflections are more dependent on the  $S$ -wave velocity and thus this joint-inversion approach may help to invert for the  $S$ -wave velocity.

The convergence of events-versus-offset is an effect that is important to consider before inputting the data into the inversion algorithm. If the data were corrected for NMO, the event convergence would be corrected for by stretching the far-offset traces to

match the zero-offset traces. This would cause a time-varying change of the wavelet versus offset. NMO is not applied to the data prior to inversion so the wavelet is constant versus offset. The increase in tuning versus offset is modeled, so that the real and model data are comparable in the inversion.

The final test of the algorithm is to use synthetic data with a real wavelet. The VSP wavelet from the zero-offset VSP, and the velocity model shown in Figure 3.4 were used to generate the synthetic data. The initial-guess, inverted and true model parameters are shown in Figure 4.23. An initial-guess (dashed curves) with no reflections was input into the algorithm. The inverted model parameters overlay the true model parameters, so the algorithm has converged to the exact solution. The initial-guess and true (synthetic data)  $P$ - $P$  and  $P$ - $SV$  reflectivity traces are shown in Figure 4.24 and Figure 4.25. The initial-guess traces are dashed and the true-reflectivity traces are solid. The traces are plotted true relative amplitude to each other. The inverted and true  $P$ - $P$  and  $P$ - $SV$  traces are shown in Figure 4.26 and 4.27. Both sets of traces appear to be solid in this case as the convergence is exact and the dashed inverted traces overlap the true traces. A damping factor of  $1.0 \times 10^{-8}$  was used in this inversion, and 15 iterations were required to reach the exact solution. The true  $P$ - $P$  data have an energy (the sum of the amplitudes squared) of 6.91616, and the initial-guess  $P$ - $P$  data have an energy of 4.41755. The true  $P$ - $SV$  data have an energy of 2.35698, and the initial-guess  $P$ - $SV$  data have an energy of 2.72526. The initial error was 4.81805, measured as the sum of the squares of the difference between the true and initial-guess traces. The algorithm converged to a very small error  $7.19289 \times 10^{-9}$  before the stopping criteria of a total change of less than 1.0 was met. Thus the algorithm performs equally well with tuned data provided the wavelet and timing of the events are known.



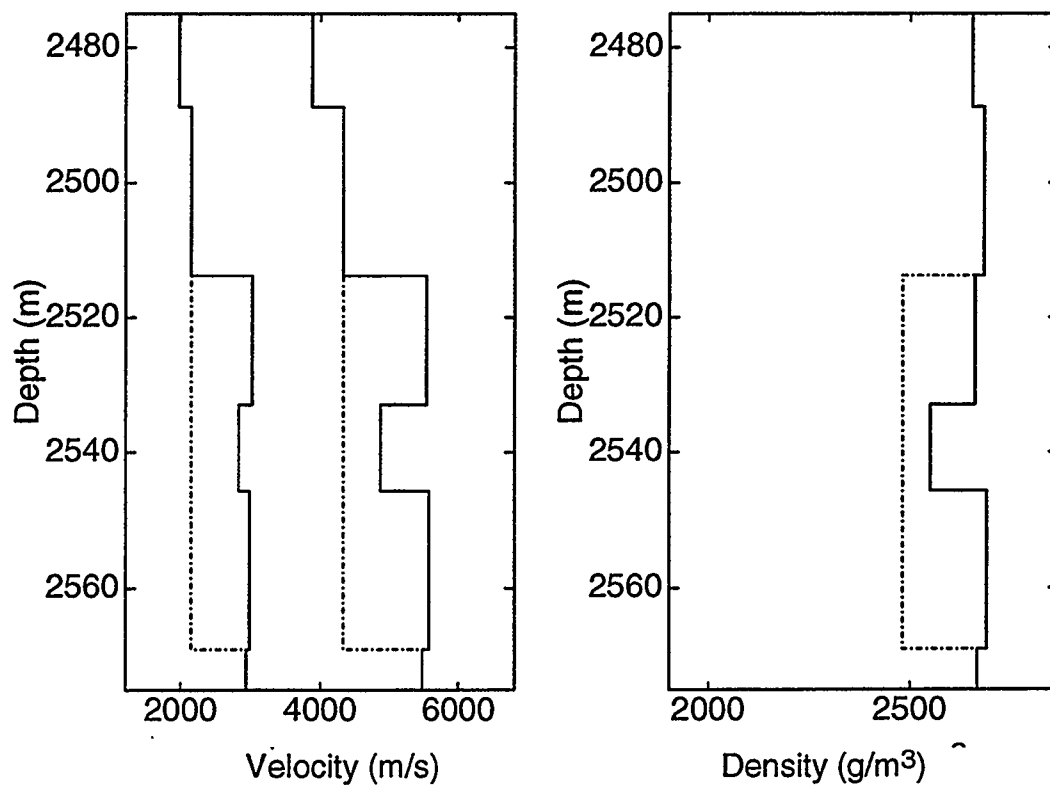


FIG 4.23. Initial-guess (dashed line), inverted (dotted line), and true (solid line) model parameters for the inversion results with the VSP wavelet.

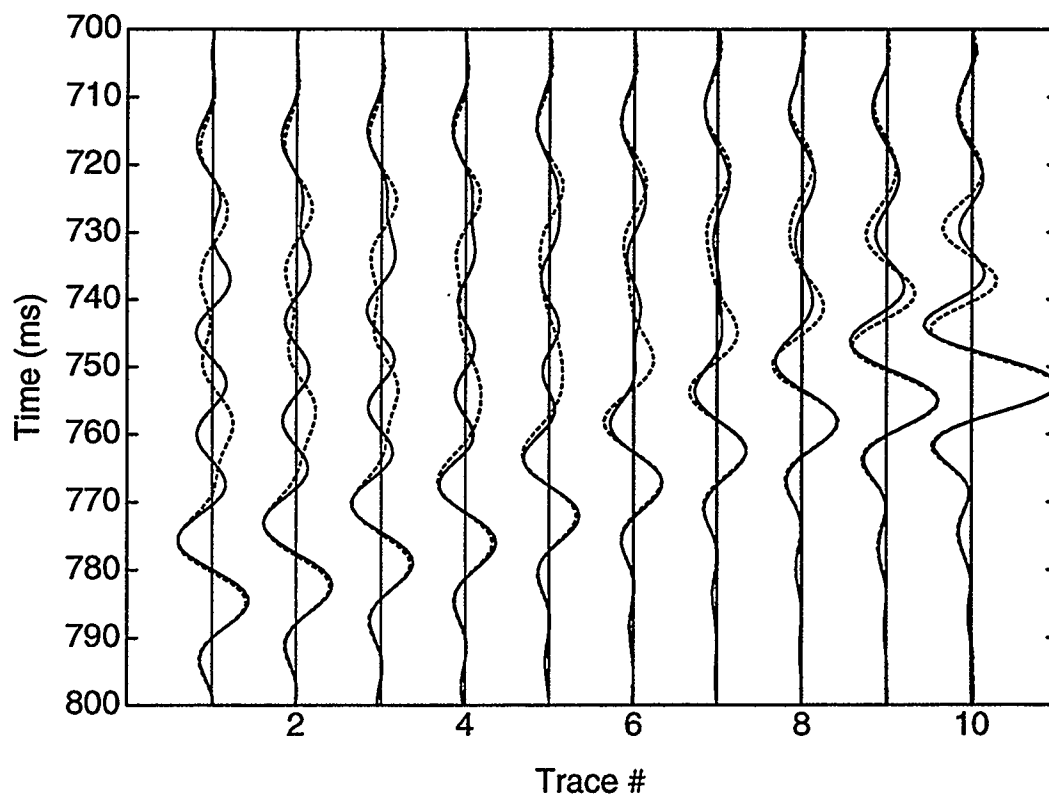


FIG 4.24. Synthetic real (solid) and initial-guess (dotted)  $P$ - $P$  reflectivity traces.

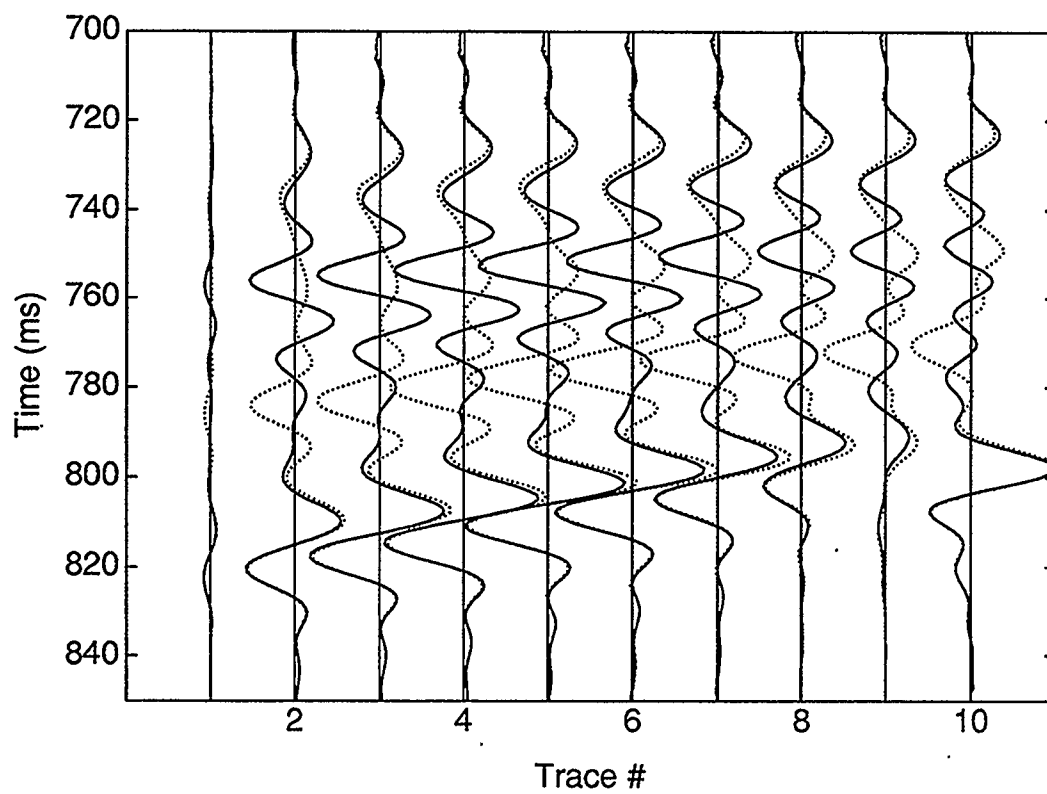


FIG 4.25. Synthetic real (solid) and initial-guess (dotted)  $P$ - $SV$  reflectivity traces.

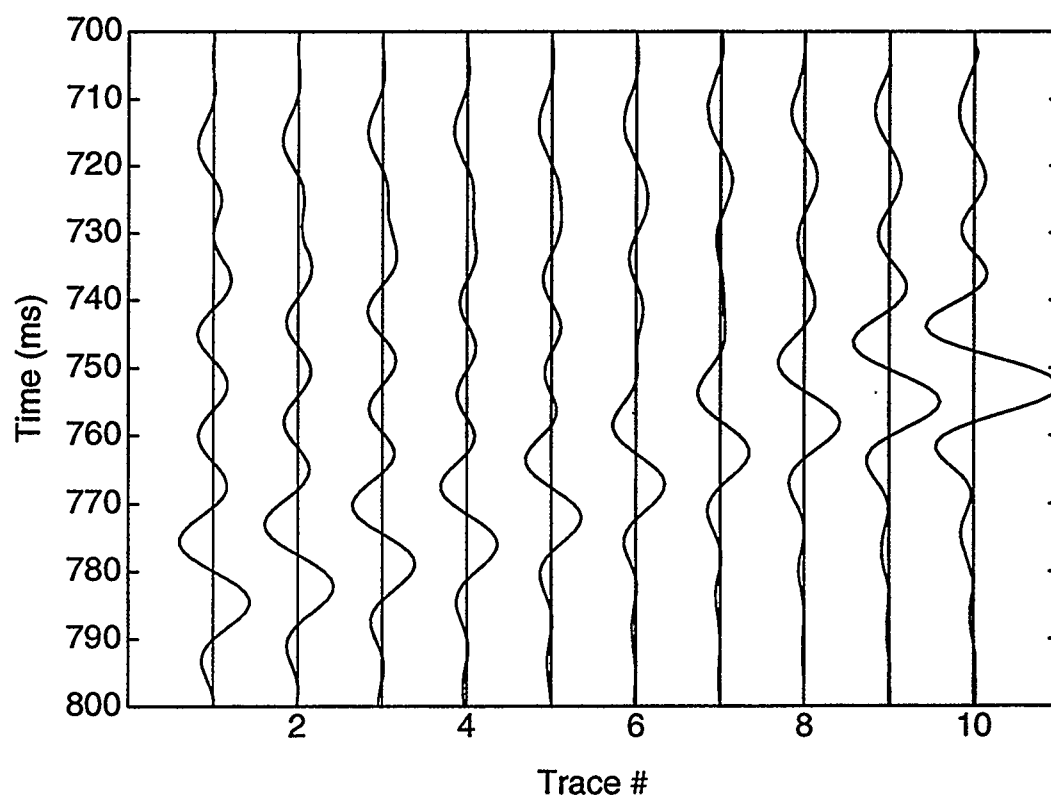


FIG 4.26. Synthetic real (solid) and inverted (dotted)  $P$ - $P$  reflectivity traces.

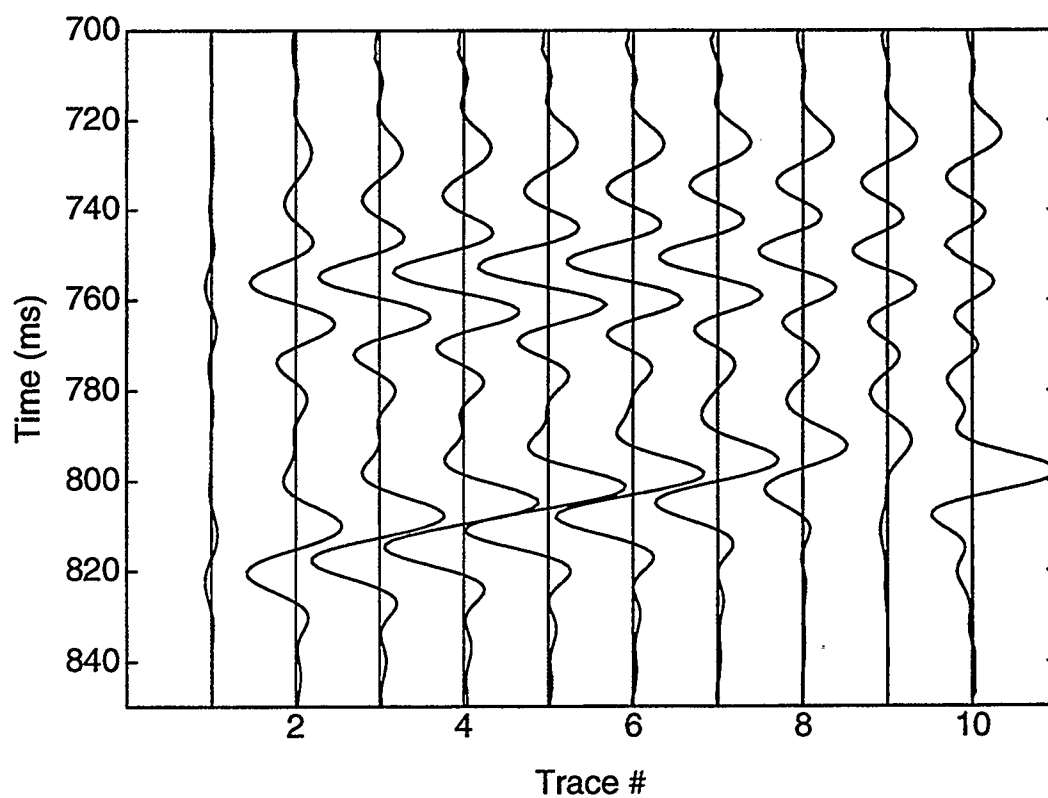


FIG 4.27. Synthetic real (solid) and inverted (dotted)  $P$ - $SV$  reflectivity traces.

### 4.3.3 Field-Data Inversion

The algorithm has been applied to the multioffset VSP field data processed in Chapter 2 and interpreted in Chapter 3. The geometry of the VSP survey is shown in Figure 1.2, and the details of the geometry are shown in Figure 2.3. There are 10 offsets ranging from 60 to 2500 m. NMO has not been applied to these data, as it has been determined that the amount of stretch required to shift the data to two-way time would distort the wavelet. The data have been flattened on an event, and cross-correlated with the initial-guess synthetic data to align the events. A window of the data is used in the inversion; both the input and model data are windowed between  $\pm 15$  ms from the top and bottom events used in the inversion and a 10 ms cosine taper is applied to the edges of the window.

The inversion algorithm has been tested for two scenarios. In the first scenario it is assumed that the initial-guess velocity model is very close to the true velocity model and that the traveltimes of the events determined from this model are correct. In this case the traveltimes of the events are held constant through each iteration of the inversion. In the second scenario it is assumed that the initial guess is a good estimate, but the updates to the model parameters will cause significant changes in the traveltimes of the events. In this case, the traveltimes of the events are updated after a number of iterations of the inversion. In both cases, ray tracing is used to calculate the angles of incidence and the traveltimes of the events.

The inversion results of the first scenario are shown in Figure 4.28. The dolomitized porosity zone is at a depth of approximately 2530 m. The inverted  $V_P$  and  $V_S$  curves follow the same trends as the initial-guess curves while the inverted  $\rho$  curve does not follow the same trends as the initial-guess curves. The initial-guess and field  $P$ - $P$  reflectivity traces are shown in Figure 4.29, and the initial-guess and field  $P$ - $SV$  reflectivity traces are shown in Figure 4.30. The inverted and field  $P$ - $P$  and  $P$ - $SV$

reflectivity traces are shown in Figure 4.31 and 4.32 respectively. Four layers were simultaneously inverted for in this case. The algorithm stopped converging after nine iterations with a final error of 0.926973. The initial error was 1.50694, and a damping of  $1.0 \times 10^{-5}$  was used. The energy of the *P-P* field data within the window is 1.43534, and the energy of the *P-SV* field data within the window is 0.395739. The initial-guess *P-P* data have an energy of 2.19095, and the inverted *P-P* data have an energy of 2.02772. The initial-guess *P-SV* data have an energy of 0.841584, and the inverted *P-SV* data has and energy of 0.352902.

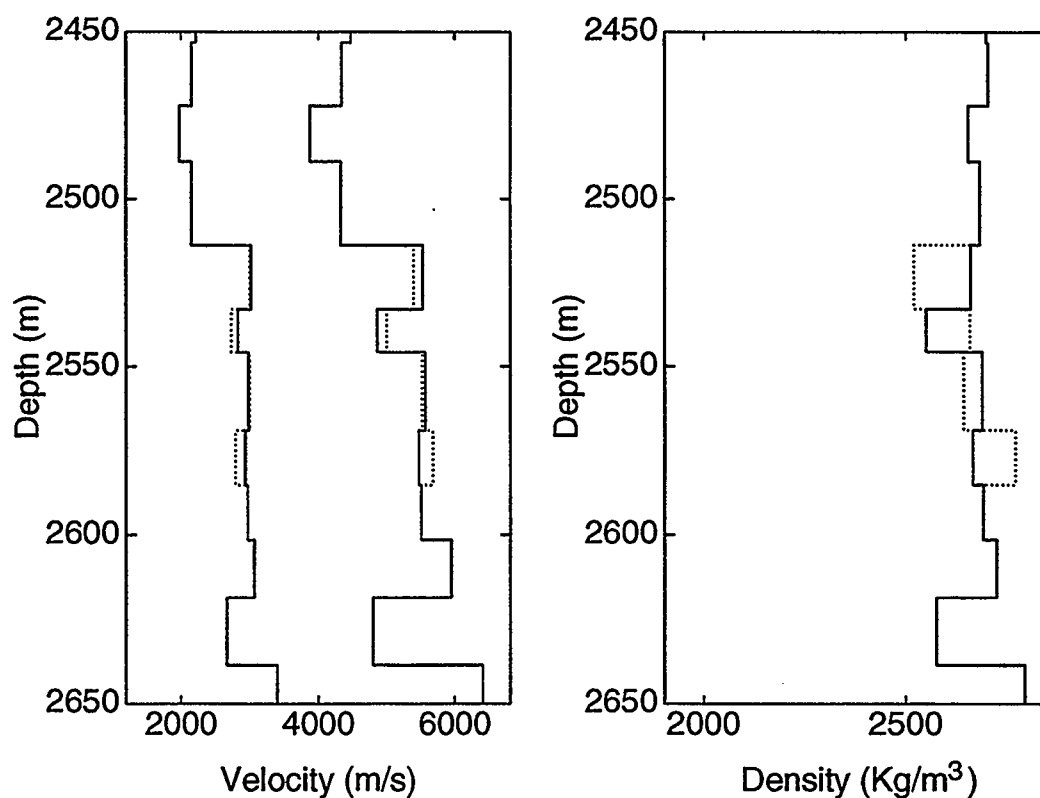


FIG 4.28. Initial guess (dashed) and inverted (dotted) model parameter curves.

These inversion results are not exact, as there is fairly significant residual error. There are several possible explanations for this residual error. The assumptions built into the algorithm may not be correct. The angles of incidence calculated by ray tracing may not match the angles of incidence in the real data. This is realistic explanation as the velocity model is calculated from the *P*-wave direct arrival and a near-surface mode-

velocity model is calculated from the  $P$ -wave direct arrival and a near-surface mode-converted  $P$ - $SV$  downgoing event. These velocities can only be calculated at depths between the topmost and bottommost geophones from the zero-offset and 750-m offset VSPs. So, the velocity above the top geophone is the average velocity for that medium. This means that the near-surface velocity structure is not known, which may lead to errors in calculating angles of incidence at the zone of interest. This is a significant problem for AVO analysis, and future work is necessary to determine the most appropriate method of calculating the angles of incidence. With VSP data, the polarization angle of the downgoing wavefields could be used as a constraint when determining the velocity model. This would be extra information in the traveltime inversion, and may help in alleviating some of the uncertainties of the near-surface velocity structure.

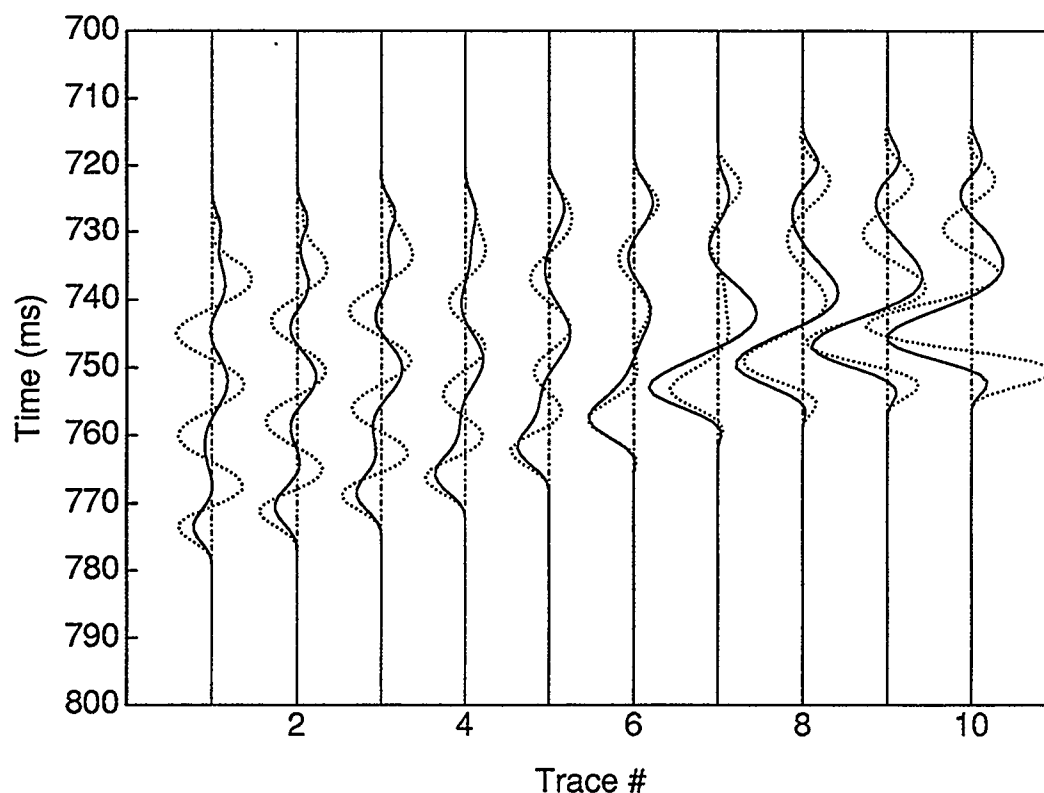


FIG 4.29. Real (solid) and initial-guess (dotted)  $P$ - $P$  reflectivity traces.



The assumption that the traveltimes of the events calculated by raytracing are not correct may also cause some of the residual error. Again, this is a realistic explanation of the error; however there is a good match between the synthetic and real data, and the error appears to be small. The assumption that the wavelet is constant for each offset of the multioffset VSP may not be correct. The VSP data have been processed to maintain this assumption. Each of the multioffset VSPs were waveshaping deconvolved using the downgoing *P* wavefield to design the deconvolution operator, with the same desired output wavelet. In principle this assumption should be met; however, there is a large difference in travel path between the near-offset and far-offset traces. The far-offset wavelet has likely been attenuated more than the near offsets, and thus may have lower high frequency energy that can not be corrected for by deconvolution. So, it is possible that the frequency band of the wavelet changes from the near to the far offsets. This has not been studied, and would be interesting for future work. Also for future work, an interesting study could be made of the source signal versus offset. The amplitude, phase, attenuation, and source directivity of the source signal could be studied. This would perhaps lend some insight into some of the problems that are trying to be addressed by the surface-consistent deconvolution algorithms that are currently being applied to surface seismic data (Yilmaz, 1987).

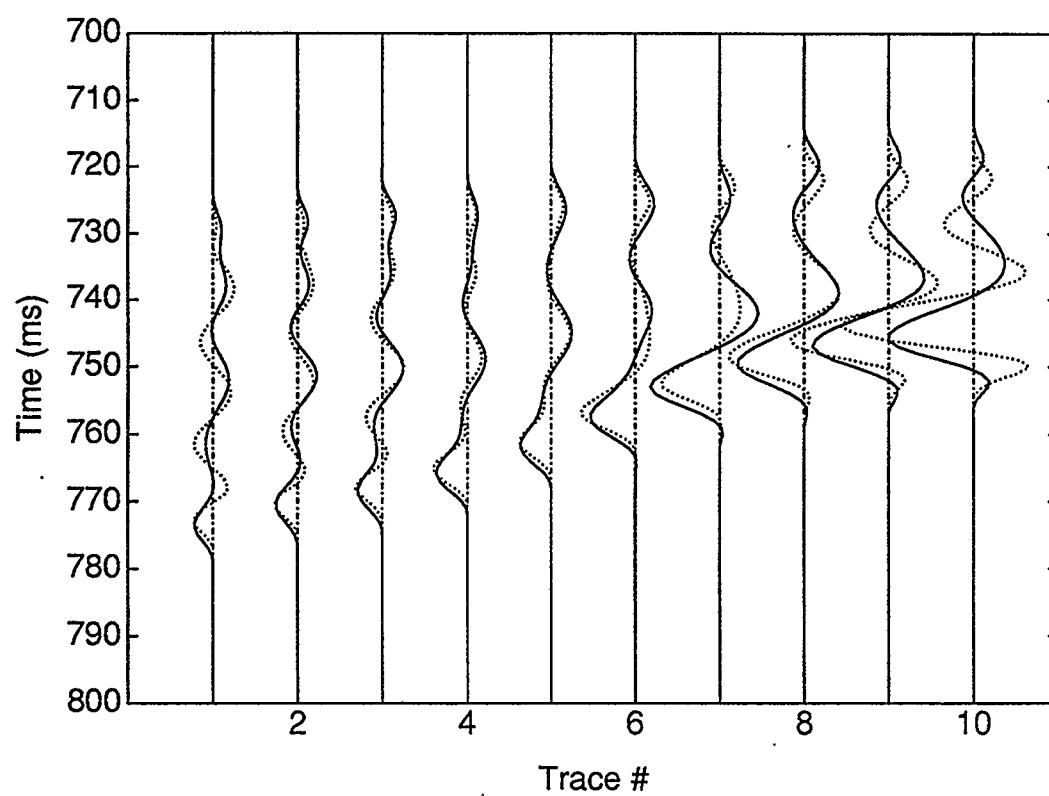


FIG 4.30. Real (solid) and inverted (dotted)  $P$ - $P$  reflectivity traces.

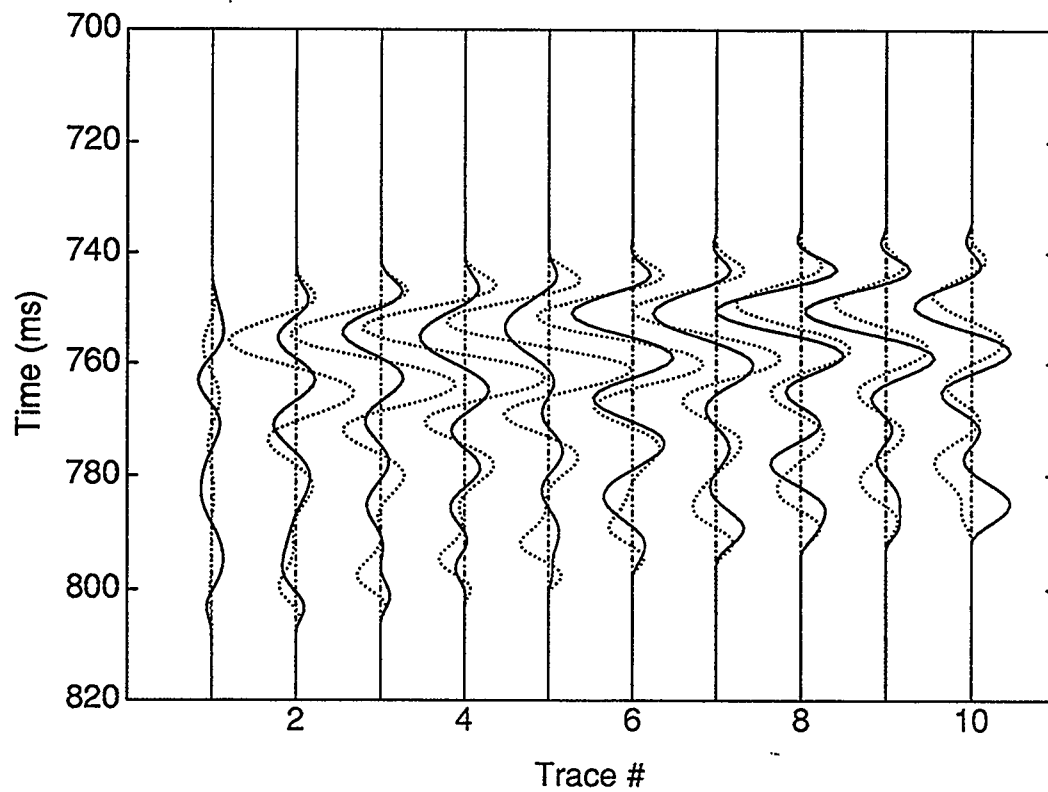


FIG 4.31. Real (solid) and initial-guess (dotted)  $P$ - $SV$  reflectivity traces.

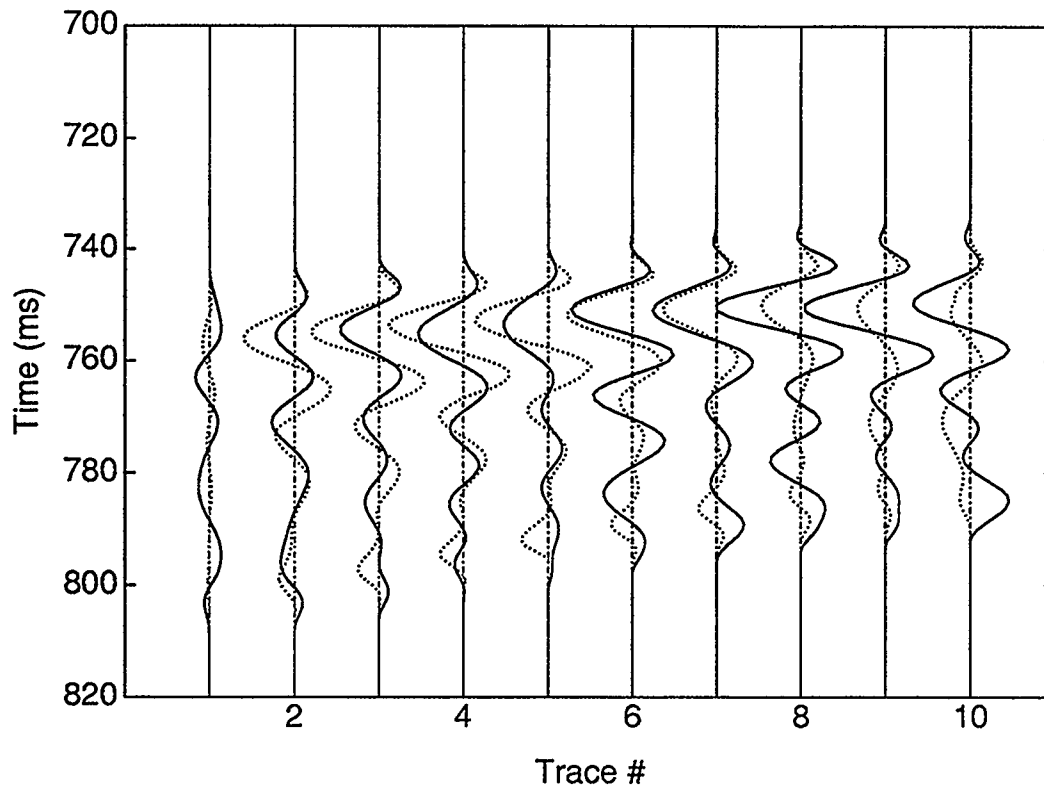


FIG 4.32. Real (solid) and inverted (dotted)  $P$ - $SV$  reflectivity traces.

The joint inversion algorithm has also been applied to the data for the case where the traveltimes of the events are updated during the inversion. In the previous inversion, the traveltimes of the events were calculated before the first iteration, and then held constant for the remaining iterations until the inversion stopped converging. In the second approach, the traveltimes are recalculated after four iterations using the updated velocity model. This was done to give the algorithm a number of iterations to converge before updating the traveltimes. The inversion is an iterative approach, so it is reasonable to recalculate the traveltimes after a number of iterations. The initial-guess and final inverted model parameters for this inversion scheme are shown in Figure 4.33. The initial-guess  $P$ - $P$  and  $P$ - $SV$  traces are the same as in the previous trial (Figure 4.29 and Figure 4.31). The final-inverted (dashed)  $P$ - $P$  and field  $P$ - $P$  (solid) traces are shown in Figure 4.34, and the final-inverted (dashed)  $P$ - $SV$  and field (solid)  $P$ - $SV$  traces are shown

in Figure 4.35. The initial error was 1.50694, the error after four iterations is 1.00796, and the final error after 8 iterations is 0.892280. The  $P$ - $P$  field-data energy within the inversion window is 1.43531, the initial-guess  $P$ - $P$  model-data energy is 2.02772, and the inverted  $P$ - $P$  model energy is 2.126. The  $P$ - $SV$  field-data energy within the inversion window is 0.395739, the initial-guess  $P$ - $SV$  model-data energy is 0.841584, and the inverted  $P$ - $S$  model energy is 0.348444. The final error for this inversion is slightly smaller than in the previous case (0.926973) where there was no raytracing between iterations. This method keeps the velocity model and traveltimes consistent during the inversion, and appears to provide a better solution.

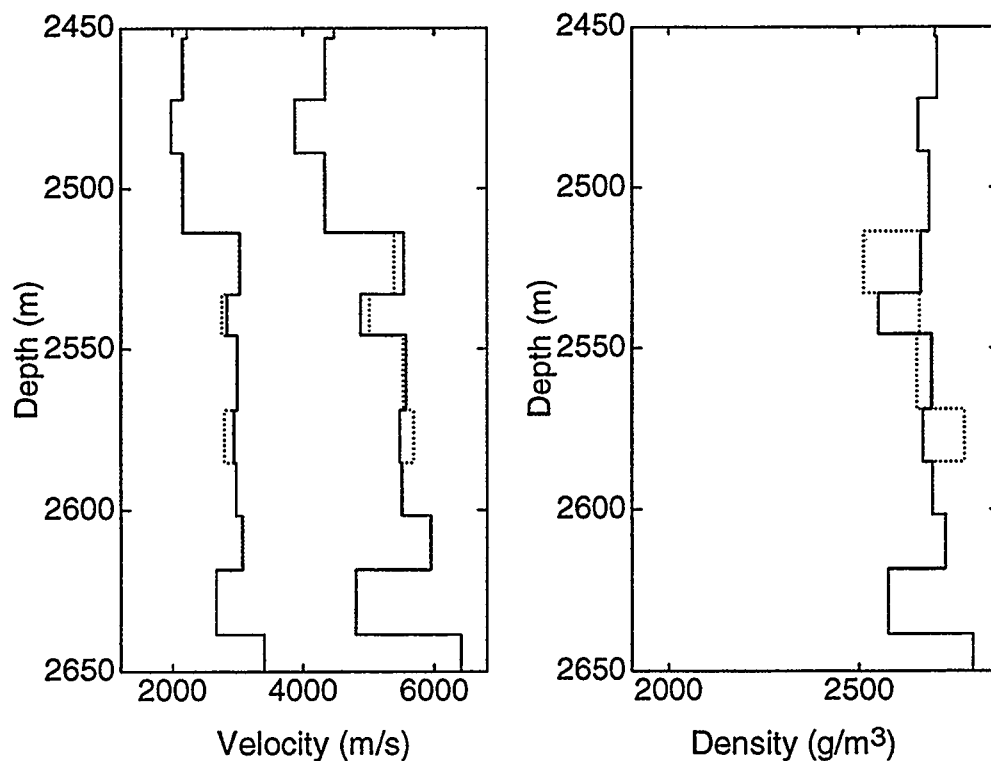


FIG 4.33. Initial-guess (solid) and inverted (dotted) model parameter curves.

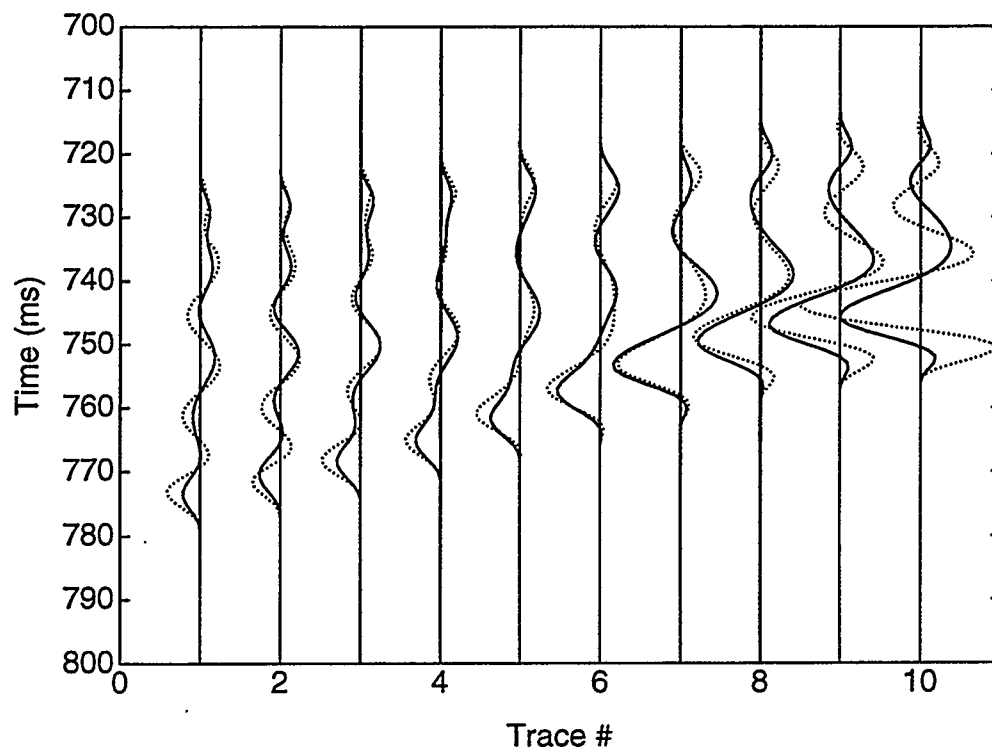


FIG 4.34. Real (solid) and inverted (dotted)  $P$ - $P$  reflectivity traces.

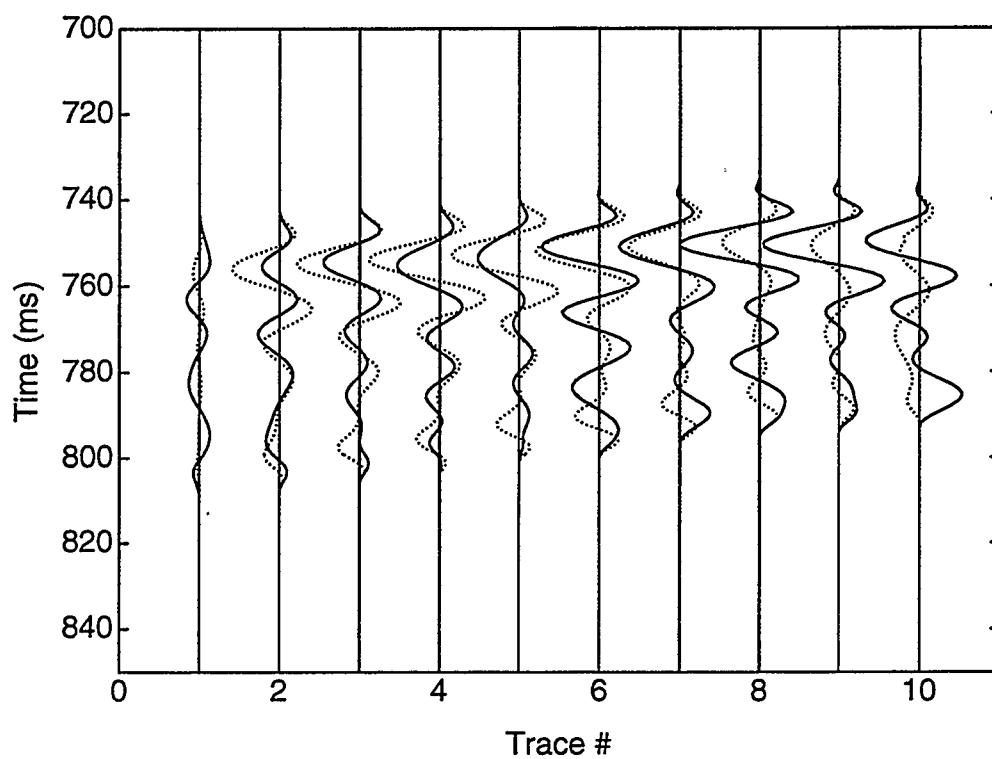


FIG 4.35. Real (solid) and inverted (dotted)  $P$ - $SV$  reflectivity traces.

The joint  $P$ - $P/P$ - $SV$  inversion has been shown theoretically to have the promise of producing better results than a  $P$ - $P$  inversion alone, suggesting that it is worthwhile to compare a  $P$ - $P$  inversion with the joint inversion. The  $P$ - $P$  inversion results of the field VSP data are shown in Figure 4.36. The initial and final error of the inversion are 1.47424 and 0.830355 respectively. Nine iterations were required before the inversion stopped converging, and a damping factor of  $1.0 \times 10^{-5}$  was applied. The comparison of the initial-guess and field  $P$ - $P$  traces is the same as in the previous two examples (shown in Figure 4.29). The final-inverted and field  $P$ - $P$  traces are shown in Figure 4.37. The inversion has converged to match the  $P$ - $P$  field data better than the initial guess. The inversion results of the joint  $P$ - $P/P$ - $SV$  (Figure 4.33) and the  $P$ - $P$  inversion (Figure 4.36) are different. The  $P$ - $P$  inversion and joint inversion density curves are quite different. The  $P$ -wave velocity curves are similar, but the  $S$ -wave velocity curves vary. There is more fluctuation in the  $S$ -wave velocity for the  $P$ - $P$  inversion than in the joint inversion. The inverted  $S$ -wave velocity in the zone of interest is much lower for the  $P$ - $P$  case than for the joint  $P$ - $P/P$ - $SV$  case. This suggests that the  $S$ -wave velocity is better constrained in the joint-inversion case than in the  $P$ - $P$  inversion case.

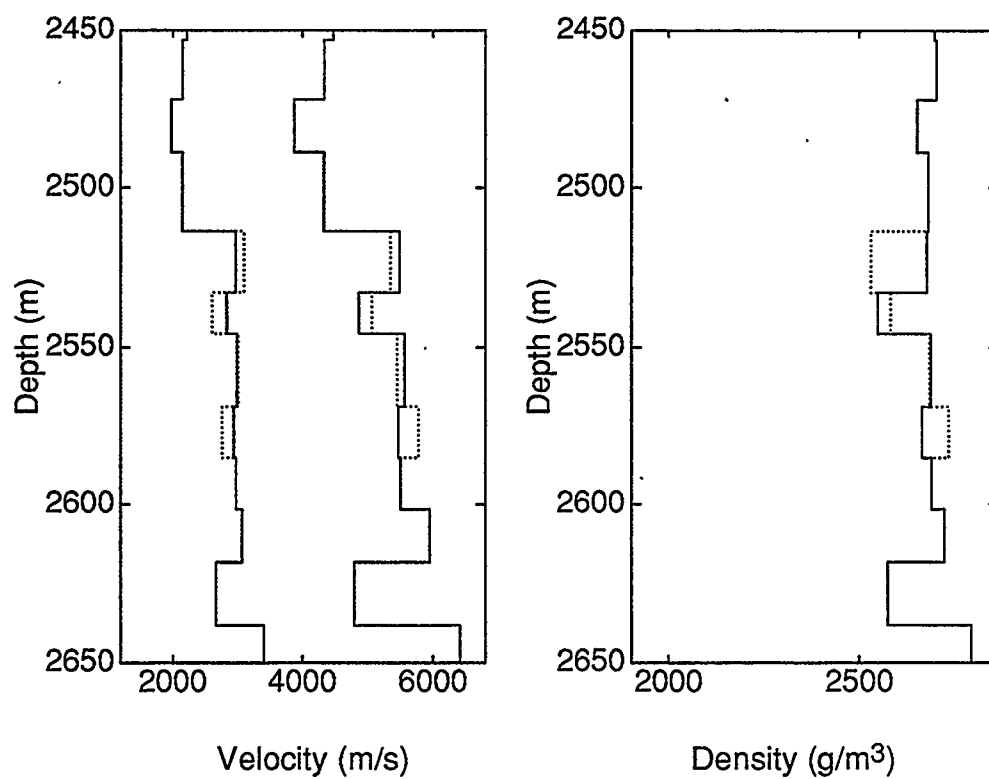


FIG 4.36. Initial-guess (solid) and inverted (dotted) model parameter curves.

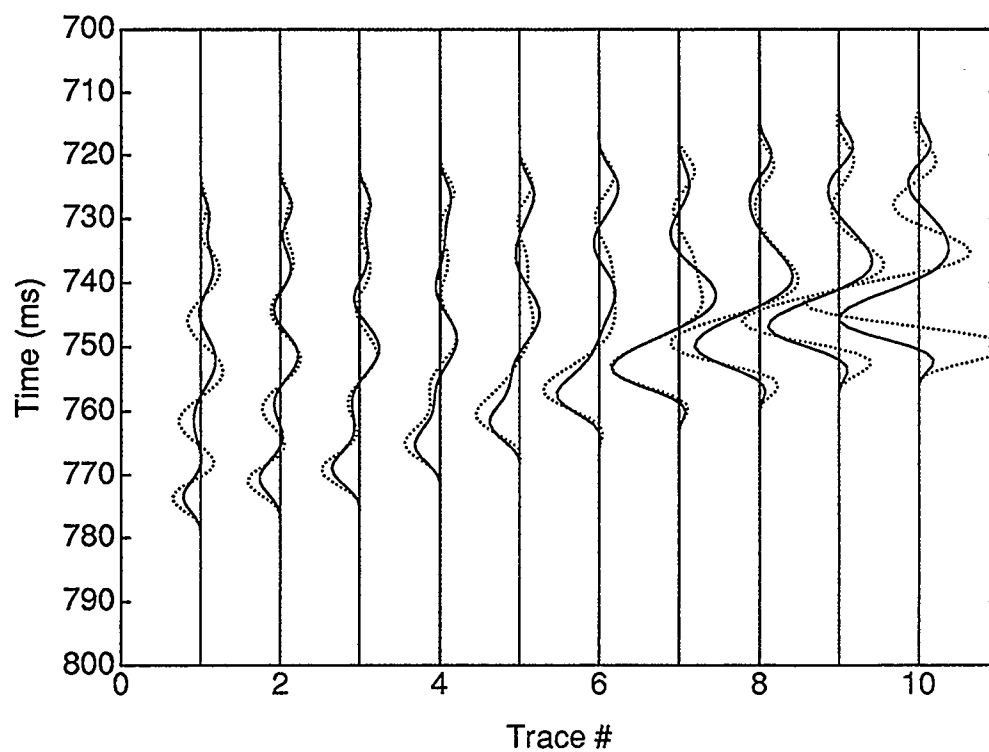


FIG 4.37. Real (solid) and inverted (dotted)  $P$ - $P$  reflectivity and traces.



The joint  $P$ - $P/P$ - $SV$  inversion has been shown to give different results than a  $P$ - $P$  inversion. Using the additional information in the converted wavefield has resulted in a more constrained inversion than using the  $P$  wavefield alone. Because two separate measurements are used in the inversion, more confidence may be placed in the joint inversion, although in this case, the results are not dramatically different.

These inversion results all suggest a higher  $P$ -wave velocity in the reservoir zone than the initial guess. In Chapter 3, a qualitative forward-modeling approach resulted in a lower  $P$ -wave velocity in the reservoir zone. This disagreement suggests that predicting the reservoir parameters using a visual qualitative comparison may not improve the match of the model data to the real data. The inversion approach eliminates the interpretive nature of the forward modeling, and produces a model that is qualitatively a better match with the real data given the modeling constraints.

These results show that VSP data acquired using the geometry shown in Figure 1.2 can be used to obtain estimates of the elastic parameters  $V_p$ ,  $V_s$ ,  $\rho$  in the subsurface. The inversion algorithm developed here assumes: the seismic velocities are well known on a macroscale; the wavelet is known; and the seismic wavefield can be explained by raytracing for traveltimes and solving the Zoeppritz equations for amplitudes. The inversion results are reasonable given that they are close to the initial guess, which is itself assumed to be close to the true parameters.

# Chapter 5

## Conclusions

### 5.1 Thesis Summary

Several objectives have been met in this thesis. The main objective to use the multioffset VSP geometry to analyze and understand the AVO behavior of a subsurface reservoir zone has been met to varying degrees using several different methods. The areas of VSP data acquisition, processing, modeling, and inversion have all been developed and discussed for the multioffset VSP geometry. The results and conclusions of this analysis can be summarized as follows.

The multioffset VSP geometry has many advantages over surfaces seismic when considering AVO. The uncertainties of; source directivity, near-surface effects, multiples, wavelet phase, can be eliminated or greatly reduced using the VSP geometry and VSP processing methods. So, the multioffset VSP geometry can be used to acquire accurate data for AVO analysis.

The VSP data acquired have the promise of high quality and accuracy, however the algorithms used in processing may introduce artifacts into the data. The VSP data have been processed with care, and a unique processing flow has been introduced in Chapter 2 that results in true seismic amplitudes. The flow has been tested using synthetic data to insure that there are no uncertainties introduced by the processes applied to the data. Thus the VSP data have been processed to true seismic amplitudes with a known zero-phase wavelet, and can be interpreted with confidence.

In Chapter 3 several levels of interpretation have been used to understand the elastic parameters, lithology, and seismic response of the reservoir zone. The well logs have been interpreted in terms of lithology and porosity. The reservoir zone has been

determined to be dolomite with a porosity as high as 18%. The log velocities have been compared with the seismic velocities from the VSP data. The comparison shows that the sonic velocities are generally lower than the VSP velocities. This difference has been attributed to velocity dispersion. It is also shown in Chapter 3 that the normal-incidence synthetic seismogram compares well with the zero-offset VSP corridor stack indicating that the  $P$ -wave velocity and density model is valid. The zero-offset VSP, 750 m offset VSP, and multioffset VSP are integrated with the sonic log in a configuration that led to an unambiguous interpretation of several seismic events and the polarity of these different data. The AVO forward modeling of the  $P$ - $P$  and  $P$ - $SV$  field data shows that there is a fairly good comparison of the synthetic and field data, verifying the validity of the Earth model. However, the match between the synthetic and the field data was improved by lowering the  $P$ -wave velocity in the reservoir zone.

Both normal-incidence and joint  $P$ - $P$ / $P$ - $SV$  AVO inversion algorithms are developed to compare quantitatively the match between synthetic and field data in Chapter 4. The normal-incidence inversion showed that the impedance contrasts in the reservoir zone is smaller than the well logs indicate. The AVO inversion showed that the data could be inverted using a complete Zoeppritz equation inversion with no approximations. The inversion results match the initial guess fairly closely; however, it was not clear to what degree the joint inversion outperformed the  $P$ - $P$  inversion. The inversion results do show that the  $P$ -wave velocity is higher in the reservoir zone than the initial guess. This result is opposite to the forward modeling results where a better qualitative match was found by lowering the  $P$ -wave velocity in the reservoir zone. This suggests that qualitative analysis of forward modeling may not produce the best interpretation results, and that a quantitative approach is more robust as it gives a direct numerical measurement of the goodness of fit of the field and model data.

## 5.2 Future Work

There are several areas that have been introduced in this thesis and not fully analyzed. In Chapter 2 it was shown that some of the  $P$ - $SV$  data were of lower quality than the  $P$ - $P$  data. It appears that the  $P$ - $SV$  data are contaminated with  $P$ - $SV$ - $SV$  events. These events are converted from  $P$  waves to downgoing  $S$  waves and the reflected as  $S$  waves. The  $P$ - $SV$ - $SV$  events have the same apparent velocity as the  $P$ - $SV$  events, and thus can not be uniquely identified. A possible approach to attenuating these events is to use the downgoing  $S$ -wave energy to model the  $SV$ - $SV$  reflections and then subtract these reflections from the data.

The multioffset VSP geometry used in this thesis provides a means of directly measuring the seismic-source signature. This geometry could be used to study the near-surface, source-directivity, and source-array effects on the source signature. Also, the attenuation of the source-signal versus offset could be studied. Evaluating these source-signal variations could lead to the design of offset dependent operators that could be applied to surface seismic data.

It was suggested in Chapter 4 that the traveltimes inversion method used in this thesis ignored the polarization angle of the downgoing wavefields. The polarization angle could be used to further constrain the traveltimes inversion algorithm, and lead to a better near surface-velocity model.

Another area for future work is to expand the joint  $P$ - $P$ / $P$ - $SV$  inversion algorithm to the surface seismic case. Some important considerations are determining the seismic wavelet, and correlating  $P$ - $P$  and  $P$ - $SV$  events.

## REFERENCES

- Aki, K., and Richards, P.G., 1980, Quantitative seismology: Theory and methods, V.1: W.H. Freeman and Co.
- Burnett, R., 1990, Seismic amplitude anomalies and AVO analysis at Mestena Grande Field, Jim Hogg Co., Texas, *Geophysics*, 55, 1015-1025.
- Carazzone, J.J., and Srnka, L.J., 1992, Elastic inversion of Gulf of Mexico data: Joint SEG/EAEG Summer Research Workshop - How useful is AVO analysis?, Technical Program and Abstracts, 526-544.
- Carron, D., 1987, Optimal Layer definition by simultaneous VSP inversion and log squaring: Presented at 57th Ann. Int. Mtg. Soc. Expl. Geophys.
- Chacko, S., 1989, Porosity identification using amplitude variations with offset: examples from South Samatra: *Geophysics*, 54, 942-951.
- Cheng, S., Hron, F., and Daley, P.F., 1992, Determination of shear wave velocities from P-wave amplitudes in VSP data: *J. Can. Soc. Expl. Geophys.*, 28, 19-29.
- Chi, C., Mendal, J.M., and Hampson, D., 1984, A computationally fast approach to maximum-likelihood deconvolution: *Geophysics*, 49, 560-565.
- Cooke, D.A., and Schneider, W.A., 1983, Generalized linear inversion of reflection seismic data: *Geophysics*, 48, 665-676.
- Dankbaar, J.W.M., 1987, Vertical seismic profiling separation of P and S waves: *Geophys. Prosp.*, 35, 803-814.
- DiSiena, J.P., Gaiser, J.E., and Corrigan, D., 1984, Horizontal component and shear wave analysis of three component VSP data. in Toksoz, N.N., and Stewart, R. R., Eds., *Vertical seismic profiling Part B: Advanced concepts*: Geophysical Press.
- Ferry, R.M., 1989, Geophysical Atlas of Western Canadian Hydrocarbon pools: *Can Soc. Expl. Geophys./Can. Soc. Petrol. Geol.*

- Frazier, C.W., and Zaengle J.F., 1992, Correlation and interpretation of P-P and P-SV reflections across the Zamora Gas Field in Yolo County, California: Joint SEG/EAEG Summer Research Workshop - How useful is AVO analysis?, Technical Program and Abstracts, 66-77.
- Gaiser, J.E., DiSiena, J.P., and Fix, J.E., 1984, VSP: Fundamentals of the downgoing wavefield and applications that improve CDP data interpretation, in Toksoz, N.N., and Stewart, R. R., Eds., Vertical seismic profiling Part B: Advanced concepts: Geophysical Press.
- Geis, W.T., Stewart, R.R., Jones, M.J., and Katapodis, P.E., 1990, Processing, correlating, and interpreting converted shear waves from borehole data in southern Alberta: Geophysics, 55, 660-669.
- Jolly, R.N., 1953, Deep-hole geophone study in Garvin County, Oklahoma: Geophysics, 18, 662-670.
- Koefoed, O., 1955, On the effect of Poisson's ratios of rock strata on the reflection coefficients of plane waves: Geophys. Prosp., 3, 381-387.
- Lawton, D.C., and Nazar, B.D., 1992, Thin bed tuning and AVO: a case history of coupled P-P and P-SV interpretation: SEG/EAEG AVO Workshop, Expanded Abstracts, 90-96.
- Leany, S.W. and Esmersey, C., 1989, Parametric wavefield decomposition of offset VSP wave fields: 59th Ann. Int. Mtg. Soc. Expl. Geophys., Expanded Abstracts, 26-29.
- Leaney, S.W., and Ulrych, T.J., 1987, Compound median filtering applied to sonic logs: 57th Ann. Int. Mtg. Soc. Expl. Geophys., Expanded Abstracts, 23-26.
- Lee, M.W., and Balch, A.H., 1983, Computer processing of vertical seismic profile data: 48, 272-287.
- Lindseth, R.O., 1979, Synthetic sonic logs - A process for stratigraphic interpretation: Geophysics, 44, 3-26.
- Mazzotti, A., 1991, Amplitudes, phase, and frequency versus offset applications, Geophys. Prosp. 39, 863-886.

- Morris R.G. and MacGregor M.D., 1991, An examination of amplitude versus offset attributes of a Middle Devonian Carbonate Bank Margin, at the Caroline Giant Gas Pool, Alberta, Canada: 60th Ann. Int. Mtg. Soc. Expl. Geophys., Expanded Abstracts, 1058-1061.
- Muskat, M. and Meres, M.W., 1940, Reflection and transmission coefficients for plane waves in elastic media: *Geophysics*, 5, 149-155.
- Oldenburg, D.A., Schuer, T., and Levy, S., 1983, Recovery of the acoustic impedance from reflection seismograms: *Geophysics*, 48, 1318-1337.
- Ostrander, W.J., 1984, Plane wave reflection coefficients for gas sands at non normal angles of incidence: *Geophysics*, 49, 1637-1648.
- Ross, C.P., 1992, Incomplete AVO near salt structure: *Geophysics*, 57, 543-553.
- Russell, B.H., 1988, Introduction to seismic inversion methods (S.N. Domenico ed.): SEG Course Notes Series, Vol. 2.
- Rutherford, S.R., and Williams, R.H., 1989, Amplitude-versus-offset variations in gas sands: *Geophysics*, 54, 680-688.
- Schlumberger, 1987, Log interpretation principles/applications: Schlumberger Educational Services.
- Schlumberger, 1988, Log interpretation charts: Schlumberger Educational Services.
- Sen, M.K., and Stoffa, P.L., 1992, Multilayer AVO inversion by genetic algorithms: Joint SEG/EAEG Summer Research Workshop - How useful is AVO analysis?, Technical Program and Abstracts, 581-589.
- Stewart, R.R., 1984, Vertical-seismic-profile (VSP) interval velocities from traveltimes inversion. *Geophys. Prosp.*, 32, 608-628.
- Stewart, R.R., 1985, Median filtering - review and a new F/K analogue design: *J. Can. Soc. Expl. Geophys.*, 21, 54-63.
- Stewart, R.R., and DiSiena, J.P., 1989, The values of VSP in interpretation: The Leading Edge - *Geophys.*, 8, 16-23.

- Stewart, R.R., Huddleston, P.D., and Kan, K.T., 1984, Seismic versus sonic velocities: a vertical seismic profiling study: *Geophysics*, 49, 1153-1168.
- Swan, H.W., 1991, Amplitude-versus-offset measurement errors in a finely layered medium: *Geophysics*, 56, 41-49.
- Tatham, R.H., and Krug, E.H., 1985, *Vp/Vs Interpretation: Developments in Geophysical Methods - 6.*, Ed. A.A. Fitch, Elsevier Applied Science Publications, London, New York.
- Treadgold, G.E., Dey-Sarkar, S.K., Smith, S.W., and Swan, H.W., 1990, Amplitude versus offset and thin beds: 60th Ann. Int. Mtg. Soc. Expl. Geophys., Expanded Abstracts, 1463-1466.
- Walden, A.T., 1991, Making AVO sections more robust: *Geophys. Prosp.* 39, 915-942.
- Widess, M.B., 1973, How thin is a thin bed?: *Geophysics*, 38, 1176-1180.
- Yilmaz, O., 1987, *Seismic Data Processing*, Soc. of Expl. Geophys., pp 506.
- Young, B.G., and Braile, L.W., 1976, A computer program for the application of Zoeppritz's amplitude equations and Knott's energy equations: *Seismological Society of America Bulletin*, 66, 1881-1885.



# APPENDIX A

## Well B AVO Analysis

### Introduction

A second multioffset VSP data set has been evaluated using the methods discussed in Chapters 2 and 3. These data were acquired to evaluate a gas-bearing carbonate zone as were the data used previously in this thesis. These data differ in that the zone of interest is much deeper at a depth of approximately 3800 m, and the maximum source offset is 1750 m, so the angles of incidence are smaller.

### Experiment Design and Acquisition

The field VSP survey was acquired to test the AVO VSP method. The survey consists of three VSP types; a zero-offset VSP, a 720 m offset VSP, and a multioffset VSP. The geometry of the survey is shown in Figure A.1. All the VSPs were recorded using a single-level three-component mechanically-clamped geophone. The source consisted of two Hemi-44 vibrators with an 8 to 90 Hz 16 s linear sweep. The zero-offset VSP consists of 99 levels recorded between depths of 3850 m and 1500 m with a level spacing of 25 m. The offset VSP consists of 94 levels recorded between depths of 3825 m and 1500 m with a 25 m level spacing. The multioffset VSP consists of 6 VSPs; 11 levels each recorded between depths of 3825 m and 3575 m with a 25 m level spacing.

The multioffset VSP data are processed with the same flow used in Chapter 2. The results of processing these data are the  $P$ - $P$  and  $P$ - $SV$  reflectivity gathers shown in Figure A.2. Note that the  $P$ - $SV$  data are plotted normal polarity (Aki and Richards, 1980) that is the opposite to the polarity used in Chapter 3.

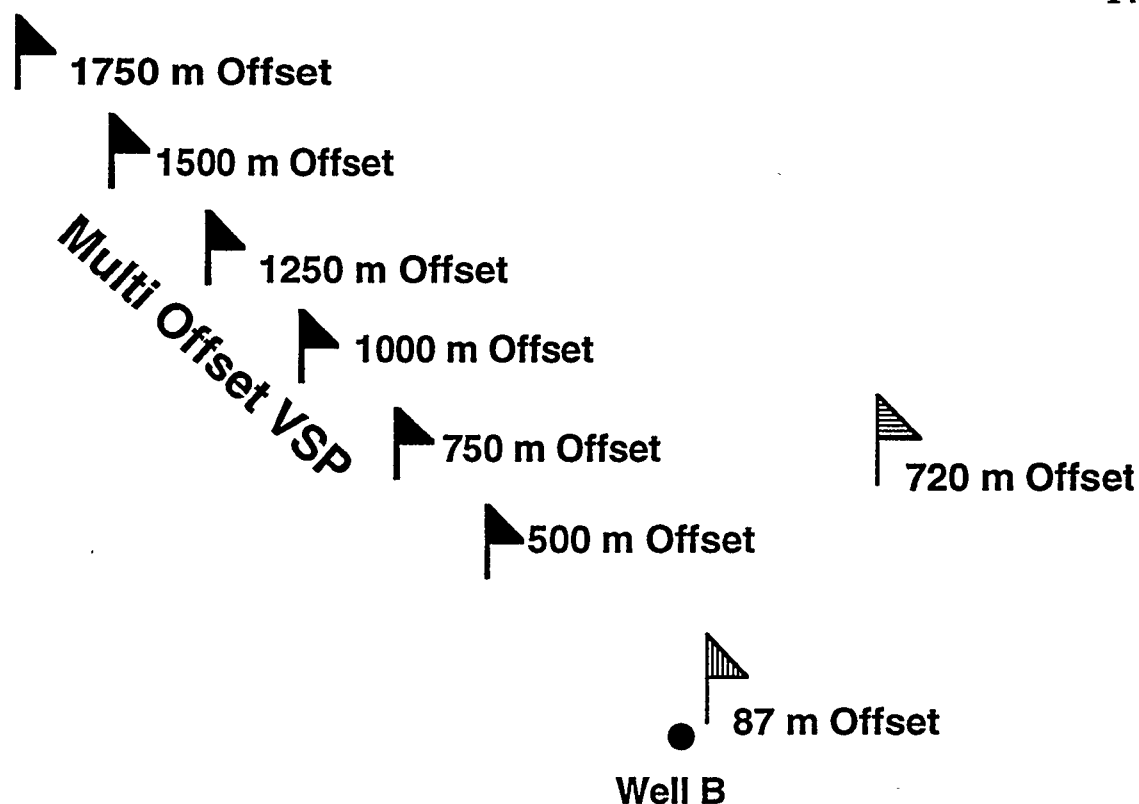


FIG. A.1. Plan view of the multioffset VSP geometry.

### Data Analysis and Forward Modeling

The  $P$ - $P$  and  $P$ - $SV$  reflectivity gathers show the true seismic AVO response of the gas-bearing carbonate zone. The inverse problem is to use the amplitudes in these gathers to obtain an estimate of the  $V_P/V_S$  ratio in the gas-bearing zone. A forward-modeling approach was used to analyze the amplitudes in the gathers.

Along with the VSP, several other borehole measurements were acquired. A full-waveform sonic log and a bulk density log are two directly related to seismic reflection amplitudes. The logs were blocked with the constraint that the output blocked logs (Figure A.3) contain the minimum number of interfaces necessary to faithfully reproduce the spectrum of the input logs within a given bandwidth (Carron, 1987). This technique

was chosen because it is automatic, and the results could not be biased by the interpreter's expectations.

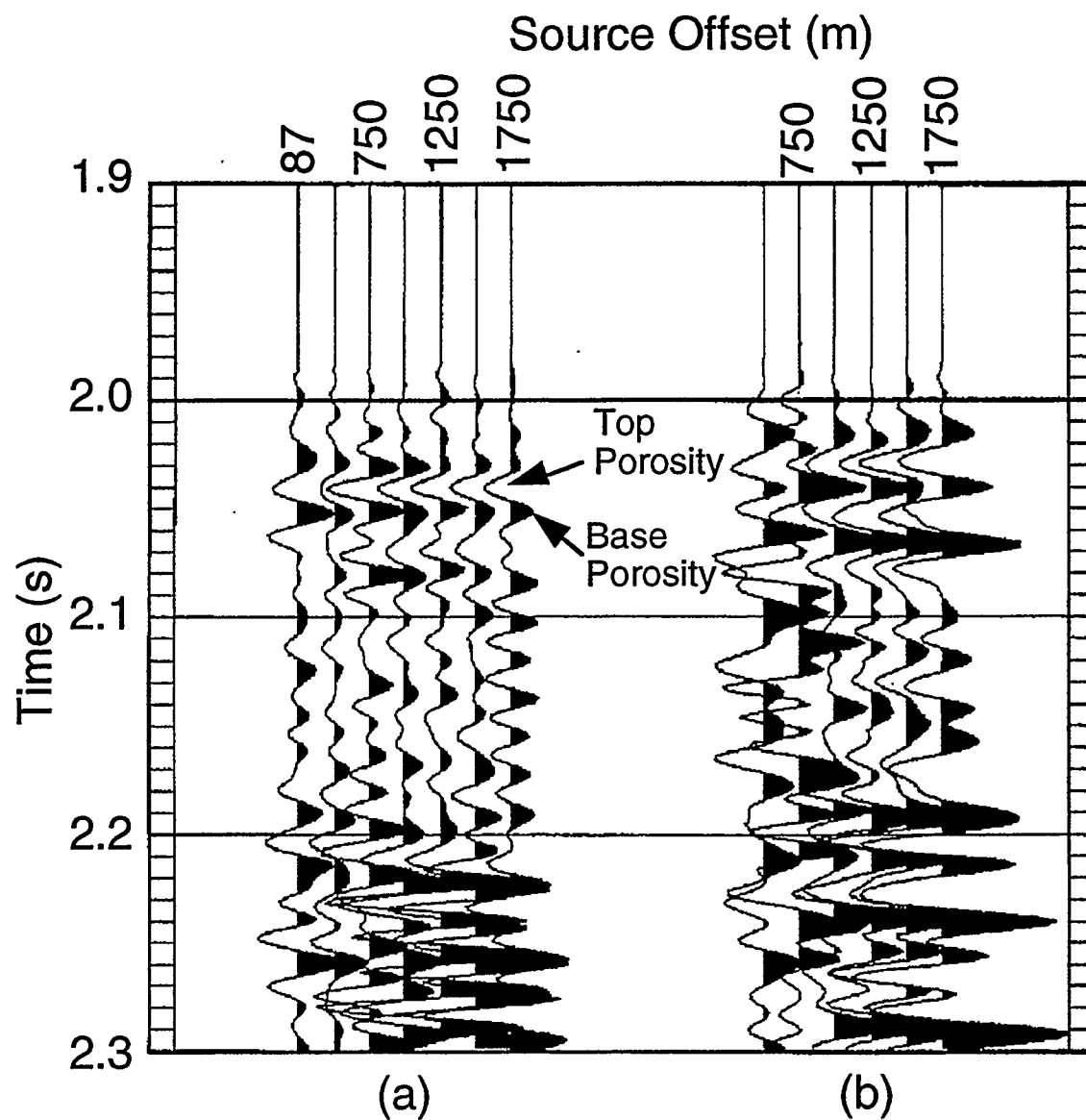


FIG. A.2. (a) Processed  $P$ - $P$  and (b)  $P$ - $SV$  reflectivity traces from the multioffset VSP survey.

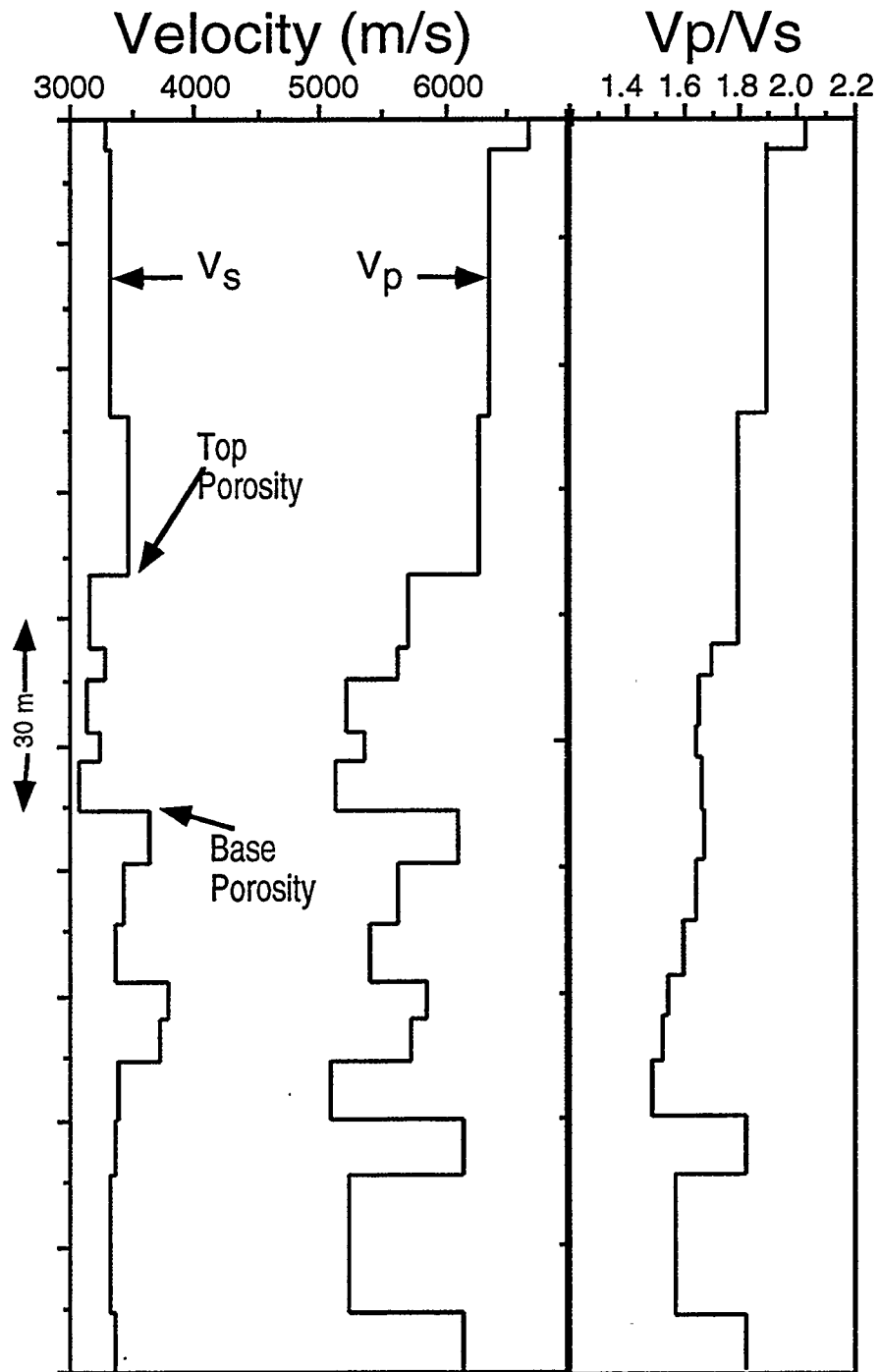


FIG. A.3. Blocked well logs through the zone of interest.

The inputs into the forward modeling algorithm are the blocked full-waveform sonic and bulk-density logs in the zone of interest, and the VSP interval velocities above

the zone of interest. Ray-tracing was used to obtain the time reflectivity series, and the reflection coefficients were calculated using the Zoeppritz equations. The reflectivity series was convolved with the waveshaping-deconvolved downgoing  $P$  wavefield (the recorded seismic wavelet), and then corrected for NMO, resulting in the  $P$ - $P$  and  $P$ - $SV$  reflectivity synthetic gathers (Figure A.4). The downgoing  $P$  wavefield was convolved with the reflectivity series to maintain a consistent wavelet between the real and modeled data.

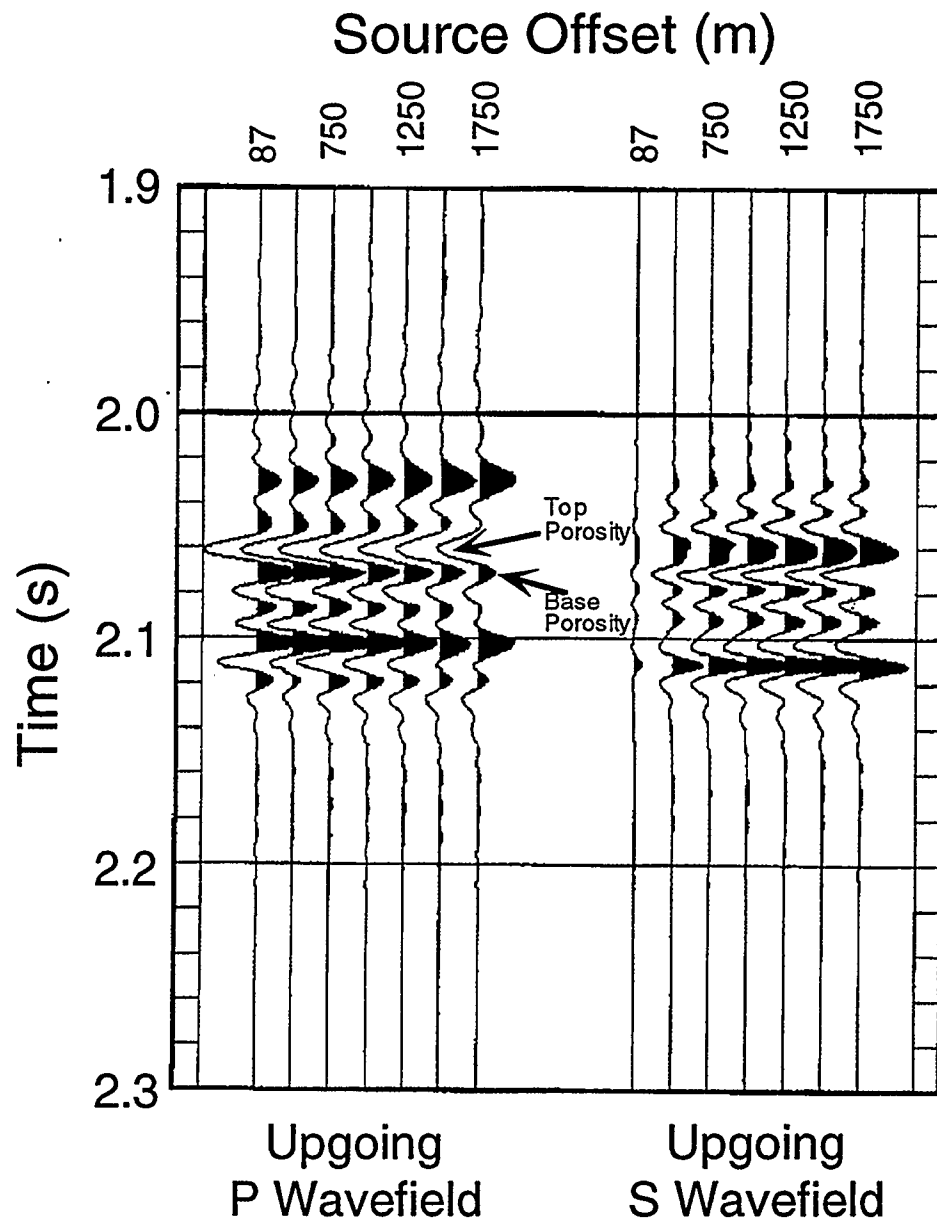


FIG. A.4. Synthetic (a)  $P$ - $P$  and (b)  $P$ - $SV$  reflectivity gathers.

The picked amplitudes of the top and base of porosity events from the real and forward-modeled  $P$ - $P$  and  $P$ - $SV$  reflectivity traces are shown in Figure A.5 and Figure A.6. Also plotted are the theoretical Zoeppritz equation curves for the respective interfaces. There is a good correlation between the forward-modeled and the real-data amplitudes. The irregularities that do exist between the real and forward-modeled data can be attributed to noise, as the overall match is good, and the mismatches occur at the same  $P$ -wave angle of incidence (same offset position). The good correlation of the picked amplitudes suggests that the processing flow is successful in extracting the true seismic amplitudes from these data. The poor correlation between the theoretical (Zoeppritz equation) curves and the real and synthetic data points are an interesting result of this study. This poor correlation can be attributed to the limited bandwidth of the seismic data and the thin bed nature of the gas bearing zone. The base of the porosity event has a significant event immediately below it causing thin bed tuning for both the  $P$ - $P$  and  $P$ - $SV$  reflections. The top of porosity event is more isolated and thus the amplitudes correlate better as there is less tuning.

The picked  $P$ - $P$  reflection amplitudes from the top of the porosity event (Figure A.3) are higher amplitude than the Zoeppritz equation amplitudes. This suggests that there is constructive wavelet interference for this event. The measured  $P$ - $P$  reflection amplitudes from the base of the porosity (Figure A.3) and the measured  $P$ - $SV$  reflection amplitudes from both the top and base of the porosity (Figure A.3) are all lower amplitude than the theoretical curves suggesting that there is destructive wavelet interference at these events. Thus for this case, single interface AVO analysis does not adequately describe the AVO behavior of the gas-bearing zone, and complete multilayer modeling is necessary.

## Conclusions

Processing multioffset VSP data using a 3-component processing flow can recover the true reflection coefficients of seismic reflections by calculating the amplitude ratio of the incident to reflected waves. Full multilayer modeling was required to match the AVO response of the gas-bearing carbonate zone. In this case, single interface AVO analysis was not adequate to describe either the  $P$ - $P$  or  $P$ - $SV$  AVO behavior of the reservoir zone.

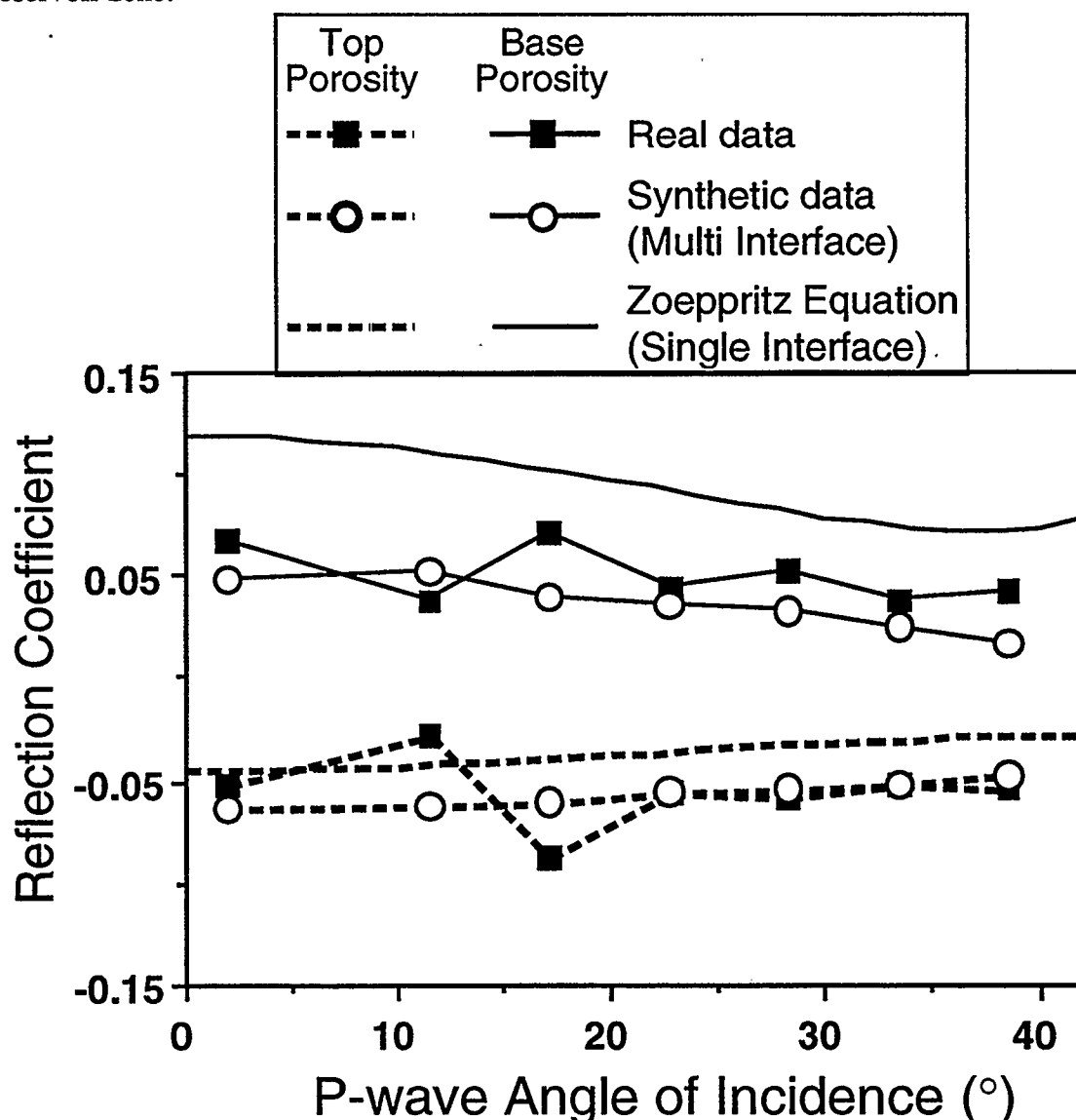


FIG. A.5. Picked amplitudes of the top and base of the porosity events from the  $P$ - $P$  field and synthetic reflectivity gathers, along with the Zoeppritz equation curve calculated from the blocked well log parameters.

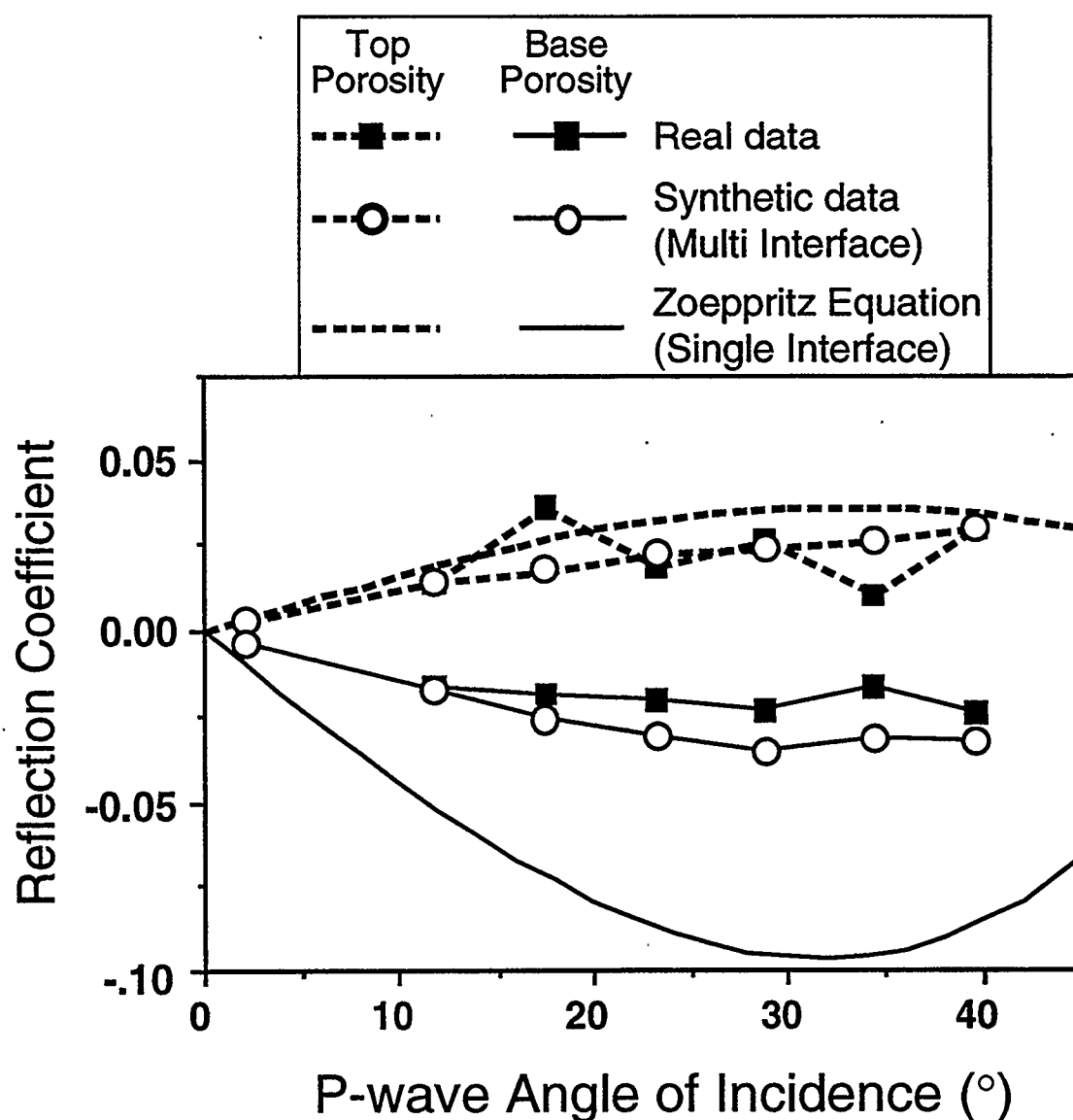


FIG. A.6. Picked amplitudes of the top and base of the porosity events from the *P-SV* field and synthetic reflectivity gathers, along with the Zoeppritz equation curve calculated from the blocked well log parameters.